

Novel porous coatings for performance benefits and cost reduction of polymer exchange membrane water electrolyzer

Von der Fakultät Energie-, Verfahrens- und Biotechnik der Universität
Stuttgart zur Erlangung der Würde eines Doktors der Ingenieurwissenschaften (Dr.-Ing.)

genehmigte Abhandlung

Vorgelegt von

Svenja Isabell Stiber

aus Owen

Hauptberichter: Prof. Dr. rer. nat. K. Andreas Friedrich

Mitberichter: Prof. Dr. Pierre Millet

Tag der mündlichen Prüfung: 03.04.2023

Universität Stuttgart

Institut für Gebäudeenergetik, Thermotechnik und Energiespeicherung

2023

The greatest enemy of knowledge is not ignorance,
it is the illusion of knowledge.

- Stephen Hawking

Acknowledgement

First and foremost, I would like to thank Prof. Dr. K. Andreas Friedrich, who gave me the opportunity to pursue my doctoral thesis at the German Aerospace Center (DLR). I appreciated a lot the interesting scientific discussions, but also your support during the whole work. I am grateful that you made it easy for me to develop into a scientific expert while being a caring, loving mother. Furthermore, I would like to thank Prof. Dr. Pierre Millet for taking over the co-examination of this thesis.

I would also like to thank Dr. Aldo Gago for his continuous support, motivation and inspiration. Thank you for the intense time that challenged and pushed me to always get the best possible out of my work.

I would like to thank my dear colleagues who accompanied me on my way and without whom this work would not have been possible. Many thanks to Dr. Asif Ansar and Günther Roth for sharing their expertise on VPS coating with me as well as for their technical support. I would also like to acknowledge Dr. Noriko Sata for sharing her experience on mercury porosimetry. Ina Plock, it was my great pleasure to get an introduction to the scanning electron microscope from you. Thank you for your support, patience and the coffee. I would also like to express my gratitude to Dr. Indro Biswas and Dr. Pawel Gazdzicki for performing the XPS measurements. I thank Tobias Morawietz for fruitful discussions and measurements at the AFM, and Frederik Heger for technical support. Also, I would like to express my gratitude to Jörg Bürkle for technical work, full material cabinets and of course not to forget the "Lab-Talk".

Both for the successful project work, the productive project meetings and the fun get-togethers after the meetings, I would like to express my gratitude to my project partners of the EU project PRETZEL. Thank you so much for the nice time we had together. I would like to specifically thank Prof. Aimy Bazylak for the collaboration beyond my time in your TEAM at the University of Toronto. I am also very grateful for the fruitful and interesting discussions with Dr. Sebastian Proch and his colleagues from Sandvik. Thank you for your support and interest in my work, as well as your open-mindedness towards new approaches.

To my office colleagues Dr. Regine Reißner, Dr. Daniel Sanchez Garcia and Olivier Garrot, thank you for the professional discussions, many conversations and suggestions over the years. My thanks also go to my PhD colleagues Vincent Wilke and Benjamin Kimmel for their help and open ears. It has been a pleasure and an absolutely valuable experience to accompany, support, guide and share my knowledge with my four very enthusiastic bachelor and master students Ana Gloria Moutinho Goncalves, Abissaid Martínez Séptimo, Aleyna Üstün and Bárbara Lopes Costa Gomes.

My extraordinary thanks also go to my family for their everlasting love, encouragement, motivation, patience and support in our special situation. Through your care I was able to grow into the person I am today and fulfil my dreams.

Last but not least, I thank my loving husband who supported me wherever possible, had my back and all his understanding. I would also like to thank my wonderful children for their patience, their calm participation in the one or other conference call and above all for showing me every day what is important.

Therefore, I dedicate my thesis to my grandiose family.

Declaration

I would like to confirm herewith that this submitted dissertation was written independently and that no other aids were used than those indicated. I have acknowledged and properly referenced the published work of others. This thesis partly contains experimental contributions by supervised students; whereas the idea of the whole thesis as well as the experiments are designed by myself.

Erklärung

Ich möchte hiermit bestätigen, dass diese eingereichte Dissertation selbstständig verfasst wurde und keine anderen Hilfsmittel verwendet wurden, als die angegebenen. Ich habe die veröffentlichten Arbeiten anderer anerkannt und ordnungsgemäß referenziert. Diese Arbeit enthält teilweise experimentelle Beiträge von betreuten Studenten; wobei die Idee der gesamten Arbeit sowie die Experimente von mir selbst entworfen sind.



Svenja Stiber

Owen, 11.05.2023

Abstract

To produce hydrogen from renewable energy (green hydrogen), polymer electrolyte membrane water electrolysis is the most promising technology due to the highly dynamic operation, the safety of the overall system as well as the scalability to relevant plant sizes at least in the MW range. However, due to the use of titanium for manufacturing stack components such as bipolar plates and porous transport layers as well as the requirement of precious metal based protective coatings, polymer electrolyte membrane water electrolysis is still too expensive to compete with current state of the art technologies for hydrogen production. Since the bipolar plates and porous transport layers made of titanium account for about 2/3 of the overall stack cost depending on the cell configuration, a significant cost reduction could be achieved in this technology if they could be manufactured from low-cost materials. Additionally, a cost reduction is also conceivable by establishing new operating parameters such as high current densities, temperature and pressure, which result in an increased hydrogen production rate. With this the operational cost of polymer electrolyte membrane water electrolysis can be reduced.

The main objective of this dissertation is to develop high-performance, durable and cost-effective polymer electrolyte membrane water electrolysis cell components as well as investigating extreme operating conditions for polymer electrolyte membrane water electrolysis. For this purpose, previous research work was followed up and coated stainless steel bipolar plates were investigated for their stability on the anode side for polymer electrolyte membrane water electrolysis use. Therefore, a polymer electrolyte membrane water electrolysis stack with niobium and niobium/titanium coated stainless steel and uncoated stainless steel bipolar plates for the anode and cathode side, respectively, was operated for 14,000 hours. The niobium/titanium coated bipolar plate was manufactured using two different coating procedures: first on top of plasma-sprayed titanium, niobium was applied *via* magnetron sputtered physical vapor deposition. In contrast, the niobium coated bipolar plate only required a single coating process *via* plasma spraying. In this long-term test, the aforementioned coatings were investigated in comparison to commercially available bipolar plates. The cells were analyzed regularly using polarization curves and post-test characterizations were performed by measuring ICR, SEM/EDX, AFM and XPS. These analysis methods showed that both applied coatings are suitable for use in polymer electrolyte membrane water electrolysis. A remarkable degradation rate of only $5.5 \mu\text{V h}^{-1}$ for all tested cells was achieved. These results indicate that stainless steel is a real alternative to pure titanium bipolar plates for commercial use and contributes to a significant cost reduction of the polymer electrolyte membrane water electrolysis technology.

To achieve further cost reduction for polymer electrolyte membrane water electrolysis, the also very expensive porous transport layers was optimized by material substitution to compete with current state-of-the-art technologies in hydrogen production. So far, the use of uncoated stainless steel components in the polymer electrolyte membrane water electrolysis cell is not possible due to strongly increasing cell potentials. Therefore, the approach was pursued to apply non-precious metal coatings of titanium and niobium/titanium to both the stainless steel bipolar plates and a stainless steel porous transport layers, so that the current density could be increased by a factor of 13 for the same cell potential. Once again, the components used were comprehensively characterized physically and electrochemically, which, supported by modelling of the pore network, shows that the niobium/titanium coating on the stainless steel porous transport layers leads to efficient water and gas transport. In addition, the polymer electrolyte membrane water electrolysis cell with coated stainless steel components was tested in an accelerated stress test for more than 1000 hours. After the test, no signs of iron contamination were detected in either the membrane or the electrodes. Finally, the polymer electrolyte membrane water electrolysis cell with stainless steel-based components was investigated up to 6 A cm^{-2} at 80°C to cope with future operating strategies. A remarkable performance of 4 A cm^{-2} at 1.91 V was achieved, which is comparable to the highest performances reported in the literature by reknown institutes.

Likewise, the cost of green hydrogen can be reduced by changing the operating parameters of the polymer electrolyte membrane water electrolysis. For this purpose, the current density, the temperature and the hydrogen pressure of the polymer electrolyte membrane water electrolysis have been significantly increased. However, this requires the use of components optimized with regard to media transport. A porous transport layer for polymer electrolyte membrane water electrolysis was developed that allows operation up to 6 A cm^{-2} , 90°C and 90 bar hydrogen outlet pressure. For this purpose, a porous sintered layer of titanium was deposited on a low-cost titanium mesh by diffusion bonding. This novel approach eliminates the need for a flow field in the bipolar plate. Comparatively, the mesh porous transport layer without porous sintered layer was tested, but its cell potential increases significantly due to mass transport losses, reaching about 2.5 V at 2 A cm^{-2} and 90°C . In contrast, the polymer electrolyte membrane water electrolysis with the porous sintered layer/mesh porous transport layers has shown 6 A cm^{-2} at the same cell potential, which significantly extends the operating range of the electrolyser. The behaviour of the porous transport layer during cell operation was extensively investigated by means of physical characterization and pore network simulations, which showed that the porous sintered layer/mesh porous transport layer leads to efficient gas/water management in the polymer electrolyte membrane water electrolysis. Finally, the porous sintered layer/mesh porous transport layer was validated in an industrial-sized and

containerized polymer electrolyte membrane water electrolysis stack operating at 90 bar hydrogen outlet pressure.

Therefore, key findings of my research were that the most expensive components, namely the bipolar plates and porous transport layer, can be made of stainless steel by coating them with non-precious metals to fully protect against corrosion and brings an efficiency increase of 12 % for the coated stainless steel porous transport layer in comparison to the reference material. The conduction of the, to date longest polymer electrolyte membrane water electrolysis test in academy, of a novel plasma sprayed coating revealed neglectable degradation rates. This test demonstrated that uncoated stainless steel can be used on the cathode side resulting in further cost reduction. In conclusion, it can be said that titanium as a base material can be replaced by stainless steel as the new standard material. Furthermore, a novel porous transport layer was developed which achieves a 31 % higher efficiency compared to the reference material during operation under extreme conditions. High permeabilities for the media ensures effective two-phase transport what makes the flow-field structure of the bipolar plates obsolete. Thereby new operating parameters suggested can be established as future state-of-the-art.

Zusammenfassung

Zur Erzeugung von Wasserstoff aus erneuerbaren Energien (grüner Wasserstoff) ist die Polymerelektrolytmembran-Wasserelektrolyse aufgrund des hochdynamischen Betriebs, der Sicherheit des Gesamtsystems sowie der Skalierbarkeit auf relevante Anlagengrößen mindestens im MW-Bereich die vielversprechendste Technologie. Allerdings ist die Polymerelektrolytmembran-Wasserelektrolyse aufgrund der Verwendung von Titan für die Herstellung von Stack-Komponenten wie den Bipolarplatten und porösen Transportschichten sowie des Bedarfs an edelmetallbasierten Schutzbeschichtungen noch zu teuer, um mit dem derzeitigen Stand der Technik bei der Wasserstoffherzeugung konkurrieren zu können. Da die Bipolarplatten und die porösen Transportschichten aus Titan je nach Zellkonfiguration etwa 2/3 der Gesamtkosten des Stacks ausmachen, könnte bei dieser Technologie eine erhebliche Kostensenkung erzielt werden, wenn sie aus kostengünstigen Materialien hergestellt werden könnten. Zusätzlich ist eine Kostensenkung auch durch die Etablierung neuer Betriebsparameter wie hohe Stromdichten, Temperatur und Druck denkbar, die zu einer erhöhten Wasserstoffproduktionsrate führen. Damit können die Betriebskosten der Wasserelektrolyse mit Polymerelektrolytmembranen gesenkt werden.

Das Hauptziel dieser Dissertation ist die Entwicklung von leistungsstarken, langlebigen und kostengünstigen Polymerelektrolytmembran-Wasserelektrolysezellenkomponenten sowie die

Untersuchung extremer Betriebsbedingungen für die Polymerelektrolytmembran-Wasserelektrolyse. Zu diesem Zweck wurde an frühere Forschungsarbeiten angeknüpft und beschichtete Bipolarplatten aus Edelstahl auf ihre Stabilität für den anodenseitigen Einsatz in Polymerelektrolytmembran-Wasserelektrolysen untersucht. Dazu wurde ein Polymerelektrolytmembran-Wasserelektrolysestack mit Nb- und Nb/Ti-beschichteten Bipolarplatten aus Edelstahl und unbeschichteten Bipolarplatten aus Edelstahl für die Anoden- bzw. Kathodenseite 14.000 Stunden lang betrieben. Die Niob/Titan-beschichtete Bipolarplatte wurde mit zwei verschiedenen Beschichtungsverfahren hergestellt: auf das plasmagespritzte Titan wurde zunächst Niob durch physikalische Gasphasenabscheidung mittels Magnetronzerstäubung aufgebracht. Für die Niob-beschichtete Bipolarplatte war dagegen nur ein einziger Beschichtungsvorgang durch Plasmaspritzen erforderlich. In diesem Langzeittest wurden die vorgenannten Beschichtungen im Vergleich zu handelsüblichen Bipolarplatten untersucht. Die Zellen wurden regelmäßig anhand von Polarisationskurven analysiert, und nach dem Test wurden Charakterisierungen mittels ICR-, SEM/EDX-, AFM- und XPS-Messungen durchgeführt. Diese Analysemethoden zeigten, dass beide aufgetragenen Beschichtungen für den Einsatz in der Wasserelektrolyse mit Polymerelektrolytmembranen geeignet sind. Es wurde eine bemerkenswerte Degradationsrate von lediglich $5,5 \mu\text{V h}^{-1}$ für alle getesteten Zellen erreicht. Diese Ergebnisse zeigen, dass Edelstahl eine echte Alternative zu reinen Titan-Bipolarplatten für den kommerziellen Einsatz ist und zu einer erheblichen Kostenreduzierung der Polymerelektrolytmembran-Wasserelektrolyse-Technologie beiträgt.

Um eine weitere Kostenreduzierung für die Polymerelektrolytmembran-Wasserelektrolyse zu erreichen, wurden die ebenfalls sehr teuren porösen Transportschichten durch Materialsubstitution optimiert, um mit dem aktuellen Stand der Technik bei der Wasserstoffherzeugung konkurrieren zu können. Bisher ist der Einsatz von unbeschichteten Edelstahlkomponenten in der Polymerelektrolytmembran-Wasserelektrolysezelle aufgrund stark steigender Zellpotentiale nicht möglich. Daher wurde der Ansatz verfolgt, sowohl auf die Bipolarplatten aus Edelstahl als auch auf eine poröse Transportschicht aus Edelstahl Nichtedelmetallbeschichtungen aus Titan und Niob/Titan aufzubringen, so dass die Stromdichte bei gleichem Zellpotential um den Faktor 13 erhöht werden konnte. Auch hier wurden die verwendeten Komponenten umfassend physikalisch und elektrochemisch charakterisiert, was, unterstützt durch die Modellierung des Porennetzwerks, zeigt, dass die Nb/Ti-Beschichtung auf den porösen Transportschichten aus Edelstahl zu einem effizienten Wasser- und Gastransport führt. Darüber hinaus wurde die Wasserelektrolysezelle mit Polymerelektrolytmembran und beschichteten Edelstahlkomponenten in einem beschleunigten Alterungstest über mehr als 1000 Stunden getestet. Nach dem Test wurden weder in der Membran noch in den Elektroden Anzeichen einer Eisen-Kontamination festgestellt. Schließlich wurde die Polymerelektrolytmembran-Wasserelektrolysezelle mit

Komponenten auf Edelstahlbasis bis zu 6 A cm^{-2} bei 80°C untersucht, um zukünftigen Betriebsstrategien gerecht zu werden. Es wurde eine bemerkenswerte Leistung von 4 A cm^{-2} bei 1.91 V erreicht, die mit den höchsten von namhaften Instituten in der Literatur berichteten Leistungen vergleichbar ist.

Ebenso können die Kosten für grünen Wasserstoff durch Änderung der Betriebsparameter der Polymerelektrolytmembran-Wasserelektrolyse gesenkt werden. Zu diesem Zweck wurden die Stromdichte, die Temperatur und der Wasserstoffdruck der Polymerelektrolytmembran-Wasserelektrolyse deutlich erhöht. Dies erfordert jedoch den Einsatz hinsichtlich des Medientransports optimierter Komponenten. Es wurde eine poröse Transportschicht für die Polymerelektrolytmembran-Wasserelektrolyse entwickelt, die einen Betrieb bis zu 6 A cm^{-2} , 90°C und 90 bar Wasserstoffaustrittsdruck ermöglicht. Zu diesem Zweck wurde eine poröse gesinterte Schicht aus Titan auf einem kostengünstigen Titan-Gitter durch Diffusionsbindung abgeschieden. Dieser neuartige Ansatz macht ein Strömungsfeld in der Bipolarplatte überflüssig. Im Vergleich dazu wurde die poröse Transportschicht in Form einer Gitterstruktur ohne poröser Sinterschicht getestet, deren Zellpotential jedoch aufgrund von Massentransportverlusten deutlich ansteigt und bei 2 A cm^{-2} und 90°C etwa 2.5 V erreicht. Bei der Wasserelektrolyse mit Polymerelektrolytmembran und poröser Sinterschicht/poröser Transportschicht wurden dagegen 6 A cm^{-2} bei gleichem Zellpotential erreicht, was den Betriebsbereich des Elektrolyseurs deutlich erweitert. Das Verhalten der porösen Transportschicht während des Zellbetriebs wurde mittels physikalischer Charakterisierung und Porennetzwerksimulationen eingehend untersucht, was zeigte, dass die poröse Sinterschicht/poröse Transportschicht zu einem effizienten Gas/Wasser-Management in der Polymerelektrolytmembran-Wasserelektrolyse führt. Schließlich wurde die poröse Sinterschicht/poröse Transportschicht in einem industrietauglichen und Container integrierten Polymerelektrolytmembran-Wasserelektrolysestack validiert, der mit 90 bar Wasserstoffausgangsdruck arbeitet.

Die wichtigsten Ergebnisse meiner Arbeit waren daher, dass die teuersten Komponenten, nämlich die Bipolarplatten und die poröse Transportschicht, aus Edelstahl hergestellt werden können, indem sie mit Nichtedelmetallen beschichtet werden, um sie vollständig vor Korrosion zu schützen, und dass die beschichtete poröse Transportschicht aus Edelstahl eine Effizienzsteigerung von 12% gegenüber dem Referenzmaterial aufweist. Die Durchführung des bisher längsten Wasserelektrolyse-Tests mit Polymerelektrolytmembranen einer Forschungseinrichtung mit einer neuartigen plasmagespritzten Beschichtung ergab vernachlässigbare Degradationsraten. Dieser Test hat gezeigt, dass unbeschichteter Edelstahl auf der Kathodenseite verwendet werden kann, was zu einer weiteren Kostenreduzierung führt. Zusammenfassend kann gesagt werden, dass Titan als

Basismaterial durch Edelstahl als neues Standardmaterial ersetzt werden kann. Darüber hinaus wurde eine neuartige poröse Transportschicht entwickelt, die im Betrieb unter extremen Bedingungen eine 31 % höhere Effizienz als das Referenzmaterial erreicht. Hohe Permeabilität für die Medien sorgt für einen effektiven Zweiphasentransport, was die Strömungsfeldstruktur der Bipolarplatten obsolet macht. Damit können die vorgeschlagenen neuen Betriebsparameter als zukünftiger Stand der Technik etabliert werden.

List of publications

This is a cumulative thesis based on three scientific articles listed hereinafter,

Article I: Long-term Operation of Nb-Coated Stainless Steel Bipolar Plates for Proton Exchange Membrane Water Electrolysers.

Svenja Stiber, Michael Hehemann, Marcelo Carmo, Martin Müller, Katherine E. Ayers, Christopher Capuano, Nemanja Danilovic, Tobias Morawietz, Indro Biswas, Pawel Gazdzicki, Jan F. Heger, Aldo Saul Gago, K. Andreas Friedrich.

Advanced Energy and Sustainability Research, 2022. <https://doi.org/10.1002/aesr.202200024>

Article II: High-performance, Durable and Low-Cost Proton Exchange Membrane Electrolyser with Stainless Steel Components.

Svenja Stiber, Noriko Sata, Tobias Morawietz, S. Asif Ansar, Thomas Jahnke, Jason K. Lee, Aimy Bazylak, Arne Fallisch, Aldo Saul Gago, K. Andreas Friedrich.

Energy & Environmental Science, 15, 109-122, 2021. <https://doi.org/10.1039/D1EE02112E>.

Article III: Porous Transport Layers for Proton Exchange Membrane Electrolysis under Extreme Conditions of Current Density, Temperature and Pressure.

Svenja Stiber, Harald Balzer, Astrid Wierhake, Florian J. Wirkert, Jeffrey Roth, Ulrich Rost, Michael Brodmann, Jason K. Lee, Aimy Bazylak, Wendelin Waiblinger, Aldo Saul Gago, K. Andreas Friedrich.

Advanced Energy Materials, 33(11),2100630, 2021. <https://doi.org/10.1002/aenm.202100630>.

Table of Content

Acknowledgement.....	III
Declaration.....	V
Erklärung.....	V
Abstract.....	VII
Zusammenfassung	IX
List of publications	XIII
Table of Content	XV
Abbreviation.....	XVII
Symbol definition and unit.....	XIX
1. Introduction	1
1.1 Motivation.....	1
1.2 Thesis Outline	5
2. Fundamentals	9
2.1 Polymer Electrolyte Membrane (PEM) Water Electrolysis Principle	9
2.2 Thermodynamics	12
2.3 Overpotentials.....	14
2.3.1 Ohmic Overpotential	15
2.3.2 Kinetic Overpotential.....	15
2.3.3 Mass Transport Overpotential	16
2.4 Components.....	18
2.4.1 Catalyst Coated Membrane (CCM)	18
2.4.2 Bipolar Plate (BPP).....	19
2.4.3 Porous Transport Layer (PTL).....	21
2.4.4 Component Cost.....	28
2.5 Operating Conditions	29
3. Experimental Work and Methods.....	31

3.1	Experimental	31
3.1.1	Testbench	31
3.1.2	PEM electrolysis cell	33
3.1.3	Porous Structure Layer Coating	34
3.1.4	Materials	37
3.2	Methods	38
3.2.1	SEM - scanning electron microscope	38
3.2.2	MIP - Mercury Intrusion Porosimetry	38
3.2.3	ICR - Interfacial Contact Resistance	39
3.2.4	Electrochemical Characterization	41
3.2.5	Capital cost estimation for upscaling the developed materials	44
4.	Discussion	50
4.1	Discussion of the Results	50
4.2	Overall Context	55
5.	Conclusion	58
5.1	General Conclusion	58
6.	General Outlook	60
7.	Bibliography	64
8.	List of Figures	83
9.	List of Tables	85
10.	Scientific Articles	87
10.1	Article I	87
10.2	Article II	97
10.3	Article III	111

Abbreviation

AC	alternating current
AST	accelerated stress test
AWE	alkaline water electrolysis
BoP	balance of plant
BPP	bipolar plates
BSE	backscattered primary electrons
CAPEX	capital expenditures
CCM	catalyst coated membrane
CL	catalyst layer
CO ₂	carbon dioxide
EDX	energy dispersive X-ray spectroscopy
EIS	electrochemical impedance spectroscopy
EoT	end of test
EW	equivalent weight
H ₂	hydrogen
HER	hydrogen evolution reaction
HHV	higher heating value
ICR	interfacial contact resistance
Ir	iridium
KPI	key performance indicator
LSC	long side chain

XVIII

MIP	mercury intrusion porosimetry
OER	oxygen evolution reaction
OPEX	operational expenditures
PEM	proton exchange membrane
PEMFC	proton exchange membrane fuel cell
PEMWE	proton exchange membrane water electrolysis
PFSA	perfluorosulfonic acid
PGM	platinum group metal
Pt	platinum
PTFE	polytetrafluorethylene
PTL	porous transport layer
PVD	physical vapour deposition
SA	sulphuric acid
SE	secondary electrons
SEM	scanning electron microscope
SoA	state of art
SOE	solid oxide electrolysis
SSC	short side chain
Ti	titanium
VPS	vacuum plasma spraying

Symbol definition and unit

Description	Symbols	Unit
Activity of species	a	/
Active cell area	a_{cell}	cm ²
Concentration	c	mol m ⁻³
Concentration at standard conditions	c_0	mol m ⁻³
Specific investment cost	$CAPEX$	€ kW ⁻¹
Cost for maintenance and operation	$C_{M/O}$	€ kW ⁻¹
Hydrogen production costs	C_{H_2}	€ kg ⁻¹
Cost of a product at a given time	C_P	€ kW ⁻¹
Initial cost of a reference product	C_R	€ kW ⁻¹
Pore diameter	d_P	μm
Reversible cell voltage	E_0	V
Cell voltage	E_{Cell}	V
Faraday constant	F	C mol ⁻¹
Hydrogen production rate	f_{H_2}	Nm ³ h ⁻¹
Gibb's free enthalpy	ΔG_R^0	J mol ⁻¹
Reaction enthalpy	ΔH_R^0	J mol ⁻¹
Rate of interest	i	%
Current	I	A
Current density	j	A cm ⁻²
Exchange current density	j_0	A cm ⁻²
Learning rate	LR	%
Lower heating value	LHV	kWh Nm ⁻³
Depreciation period	n	a
Cell number	n_{cell}	/
Cell efficiency	η_{cell}	/

XX

Faraday efficiency	η_F	%
Nominal system efficiency	η_{ges}	%
Kinetic loss	η_{kin}	V
Mass transport loss	η_{MTL}	V
Ohmic loss	η_{Ω}	V
Partial pressure	p	Pa
Capillary pressure	P_C	Pa
Specific electricity price	P_E	€ kWh ⁻¹
Gas phase pressure	p_g	Pa
Liquid phase pressure	p_l	Pa
Normal gas constant	R	J K ⁻¹ mol ⁻¹
Resistance	R_i	Ω
Interfacial contact resistant	R_C	Ω
Throat radius	r_c	m
Entropy	S	J mol ⁻¹
Reaction entropy	ΔS_R^0	J mol ⁻¹
Time	t	s
Annual full load hours	t_o	h
Volume	V	m ³
Ratio of produced oxygen to supplying water flow rate	\dot{V}_r	/
Required pore diameter to ensure transport path	\dot{V}_c	/
Number of electrons	z	/
Transfer coefficient	α	/
Surface tension	γ	N m ⁻¹
Contact angle	θ	rad
Phase shift	φ	/

Angular frequency	ω	s^{-1}
Cumulative production at a given time	X	/
Cumulative production at reference time	X_R	/

1. Introduction

1.1 Motivation

In recent years, carbon dioxide (CO₂) emissions have increased worldwide by more than 60 % from 1990 to 2021,^[1] clearly showing that related global warming is one of the greatest challenges of the 21st century. It has also become apparent that the current political agreements and efforts based on the Paris agreement of 2015 are unlikely to contribute to a sufficient reduction of CO₂ emissions. Likewise, the current shortage of energy sources, which is leading to an increasing demand for oil due to the shortage of coal and gas, shows that we need to find a way to store electricity from renewable sources more quickly in order to become independent of fossil fuels.^[2]

Besides energy and heat generation, the chemical industry and the mobility sector are one of the largest emitters of the globally emitted 36.3 Gt of CO₂ in 2021.^{[3],[1]} Alternatives to the use of fossil fuels must be found for the respective sectors and integrated into the processes in order to stop the steady upward trend. It is therefore essential to tighten up the already ambitious targets set out in the political agreements and to push ahead the green transformation.

In 2020, the global hydrogen demand was 87.1 Mt,^[4] with the largest share of 46% required in refineries for hydrocracking and desulphurization of fuels. The second largest consumer is the chemical industry with 35% for the production of ammonia and plastics, while methanol, steel and iron production require the remaining quantities. From this point of view, emissions could be drastically saved if hydrogen were produced green. Energy supply based on renewable energy entails dependence on weather conditions and geographical locations. Both wind and sun are not necessarily available when and where the energy is needed. Here, hydrogen production by water electrolysis with renewable electricity (green hydrogen)^{[5],[6]} can separate energy production from actual demand over time, making the energy storable and thus an attractive option in many respects. Figure 1 shows how green generated hydrogen can couple the respective sectors.

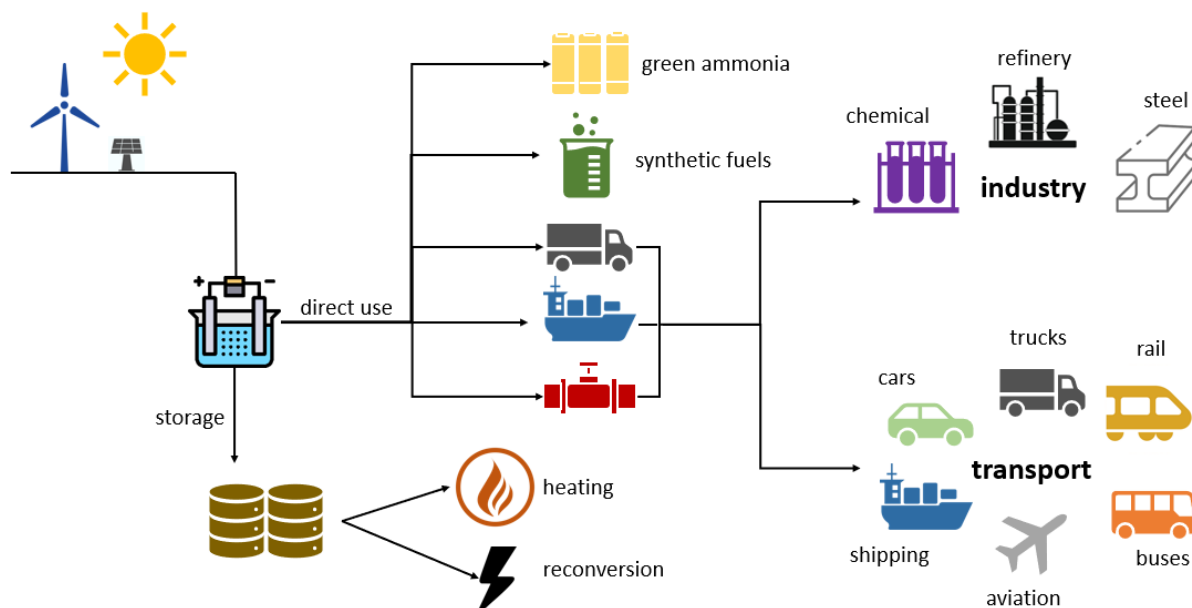


Figure 1. Potential sector coupling by green hydrogen adapted from [4]

Currently, about 48 % of today's hydrogen demand is produced from steam methane reformation, 30 % from crude oil cracking and 18 % from coal gasification, 3 % as chlor-alkali by-product while only 1% is produced by water electrolysis.^[7] Mainly three electrolysis technologies are available to produce hydrogen today. These are alkaline water electrolysis (AWE), proton exchange membrane water electrolysis (PEMWE) and solid oxide electrolysis (SOE), whose properties are classified in Table 1.

Table 1. Classification and parameters of state of art of the respective electrolysis technologies ^{[5],[8-11]}

Technology	AWE	PEMWE	SOE
Electrolyte	aqueous solution (25-30% KOH/NaOH)	proton exchange membrane (e.g. Nafion®)	proton conducting ceramics (Nickel/yttria stabilized zirconia)
Current Density / A cm ⁻²	0.2 – 0.8	1.0 – 3.0	0.3 – 1.0
Cell Voltage / V	1.4 – 3.0	1.4 – 2.3	1.0 – 1.5
Temperature / °C	60 – 90	50 – 80	500 – 900
Pressure / bar	10 – 30	20 – 50	1 – 15
Voltage efficiency / %	62 – 82	67 – 82	>95 (when external heat provided)
Degradation rate / µV h ⁻¹	< 3	< 14	
Max. nominal power per stack / MW	6	2	< 0.01
CAPEX / € kW ⁻¹	800 – 1500	1400 – 2100	>2000

In its report from July 2021, the EU emphasized the importance of action and resolved the ambitious targets to reduce net emissions by at least 55% by 2030 compared to 1990 and to be the first climate-neutral continent by 2050.^[12] For this, on the one hand, the share of renewable energies must be increased to 40%,^[13] on the other hand, hydrogen as a key energy carrier is to be used particularly in sectors such as industry or transport, where emissions are difficult to reduce.^[14] Therefore, large-scale electrolysis implementation of 2 x 40 GW electrolyzer capacity are planned by 2030.^[15]

Due to the compact design, pressurized operation as well as the possibility of varying the production rate over the entire load range, PEMWE offers advantages over others for this purpose^[8] but is still expensive mainly due to the use of titanium for manufacturing stack components such as bipolar plates (BPP) and porous transport layers (PTL) and protective precious metal coatings. Therefore, large-scale plants can hardly achieve the FCH-JU key performance indicators (KPI)^[16] in terms of cost but also in efficiency, lifetime and operability at present. Accordingly, not only capital expenditures (CAPEX) must be reduced, but savings must also be made in operational expenditures (OPEX).

As the BPPs and PTLs made of titanium are the most expensive components of the electrolyser stack, accounting for about 2/3 depending on the cell configuration,^{[17],[18]} these promise a significant potential savings in terms of their cost if they could be manufactured from low-cost materials. A cost analysis from 2019 shows, based on optimization measures in component production depending on the plant sizes as well as the number of installed plants, that BPP and PTL together still account for around 40 % of the entire stack costs.^[19] It becomes also clear for these components that the larger and the more systems are installed, the more the cost share shifts towards the substrate and coating material costs.

Moreover, the precious metals used also limit the installed plant capacities. These are used for the coating of the interconnecting components (BPP and PTLs), but are essentially needed for the production of the catalyst coated membrane (CCM), where they serve as catalyst materials for the electrodes. While a platinum loading of 0.2 mg cm^{-2} is sufficient on the cathode side due to the fast reaction kinetics, 2 mg cm^{-2} of iridium is required on the anode side. In particular iridium, which is one of the rarest metals in the earth's crust curtail PEMWE to 2 GW capacity per year,^[20] assuming an annual production rate of between 3.5 and 4 tons of iridium.^[21] Therefore, increased utilization of catalysts is sought to conserve resources while minimizing costs.

Ultimately, hydrogen levelized cost for large-scale PEMWE published in 2021 by H2NEW consortium shows that almost 50 % of the hydrogen production costs can be allocated to electricity costs, about 15 % to operating costs and more than 30 % to investment costs. By improving efficiency, increasing lifetime and reducing costs, these should be almost halved in the medium term, reaching a price of about 1.82 €/kg hydrogen.^[22] While electricity costs remain almost unchanged in their midterm target, investment costs as well as operating and maintenance costs are reduced by more than 50 %, shifting the cost dominance further towards electricity costs, which then account for a share of almost 80 % of the hydrogen production cost. Here, cell efficiency plays a key role, which can be increased by optimizing cell components and operating conditions to reduce OPEX. The PTL in particular, which is responsible for several functions like media transport (water and gases), electrical conductivity and mechanical stability in the cell, must be designed with this in mind. Often, however, materials are used for this purpose that have been taken from other areas (e.g. from the food industry, filters, etc.) and are not optimized for use in PEMWE. Thus, these components offer a high optimization potential.

1.2 Thesis Outline

Depending on the cell configuration in PEMWE, e.g., with or without flow field in the BPP, the PTL and the BPP together account for about 70%^[17] and 60%^[18] of the PEMWE stack cost. Due to their large cost share, a reduction in these component costs can contribute significantly to the widespread use of PEMWE and thus make green hydrogen available at competitive prices more quickly. According to the calculations of BNEF in 2020, green hydrogen can currently be provided at 2-5 € kg⁻¹ compared with cost for grey hydrogen of about 1-2.8 € kg⁻¹.^[23] To overcome this gap costs for electrolysis technologies need to be reduced.

Basically, the two following approaches can be considered:

- (i) replacement of Ti by low-cost materials such as stainless steel protected from corrosion by non-precious metal coatings,
- (ii) optimized Ti-based PTLs with increased H₂ production rate by operating them under extreme conditions (temperature, current density, pressure) and thus higher cell efficiency can be achieved.

The first approach highlights cost reduction by replacing high-cost materials^[24] such as Pt, Ir or Ti. Among other things, these materials are used as standard for the manufacture and coating of the BPP as well as PTLs. First, therefore, titanium was replaced for the BPP and stainless steel was used, which was coated with Nb and Nb/Ti to protect against corrosion. A long-term test was to verify the stability of the material. While more than 50,000 hours of operation must be demonstrated for commercial implementation, the longest test performed by academia to date was realized here. The stainless steel BPPs were tested for 14,000 h and analyzed afterwards by different physical characterization methods. The substitution of titanium in the PTL, due to its proximity to the electrode and its porous structure, represents a greater challenge. Local corrosion measurements showed that significant polarization of the component takes place particularly at the interface layer between the electrode and PTL on the anode side.^[25] For this purpose, multi-layered stainless steel mesh structures were coated with Nb/Ti by plasma spraying and investigated in cell tests. Subsequently, the cell components were examined, using imaging analysis as well as physical methods and pore network modelling.

The other approach is to operate the electrolyzer under new operating standards with the goal of achieving higher efficiencies and hydrogen production rates.^{[26],[27]} For this purpose, a titanium-based PTL was optimized to withstand these new and demanding operating parameters. Cell tests up to 6 A cm⁻², 90 °C and 100 bar were used for the study. In addition to physical analysis methods, the transport properties of the components were modelled using a pore network model.

In this way, the highest requirements for H₂ production from renewable energies can be met for vehicle refuelling, grid stabilisation and the reserve energy market, as well as for various industrial applications. To carry out the present work, which is summarized in Figure 2, the first step was basically to prepare the respective components for use in PEMWE by applying the coating.

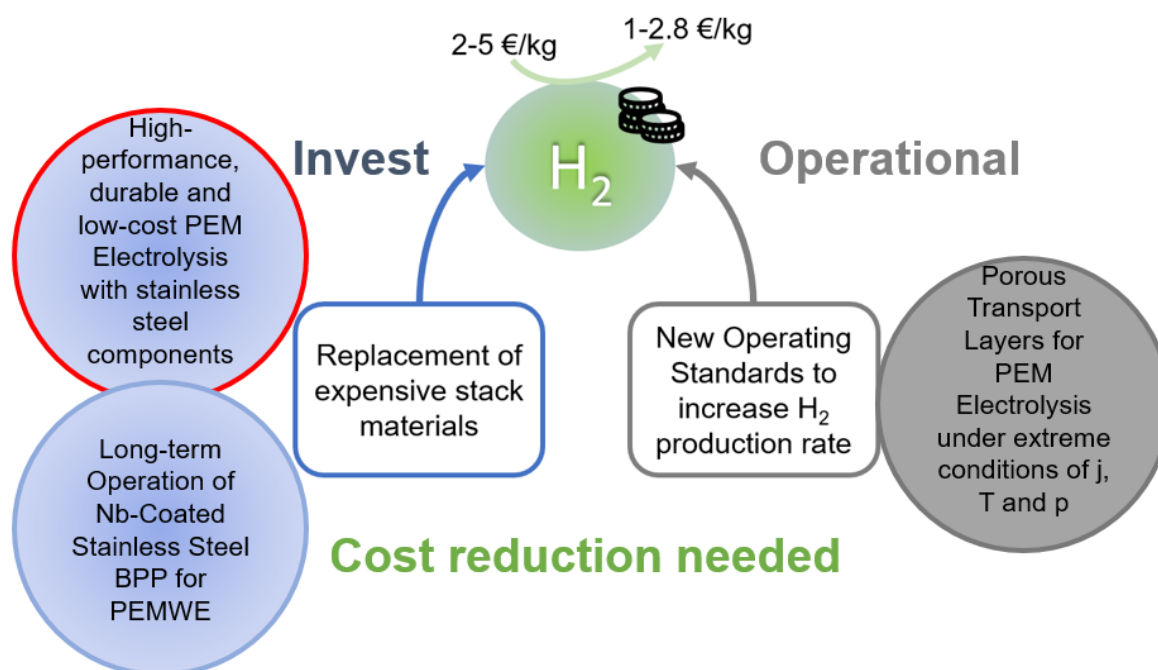


Figure 2. The present work in brief with the three areas of investigation belonging to the two categories with potential cost savings

Secondly, their quality and suitability were tested by pre-test analyses. Electrochemical characterization and a rapid aging test were among the methods chosen to investigate the performance parameters in the cell as well as its durability and to compare it with the state of the art. Followed by post-test analyses to explain the observed phenomena and results, new materials for PEMWE could be developed, which could represent the new standard in the future. The followed methodology is shown in Figure 3.

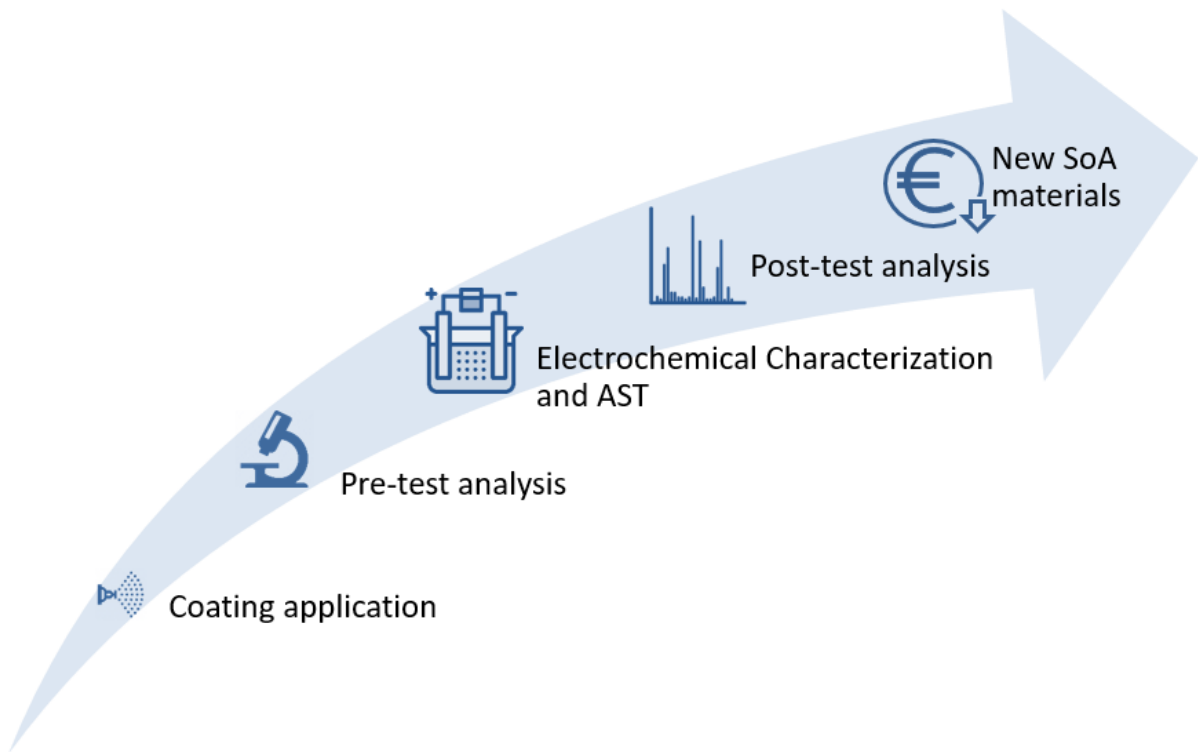


Figure 3. Summarized methodology of the thesis showing the individual steps for conducting the experiments and achieving the results

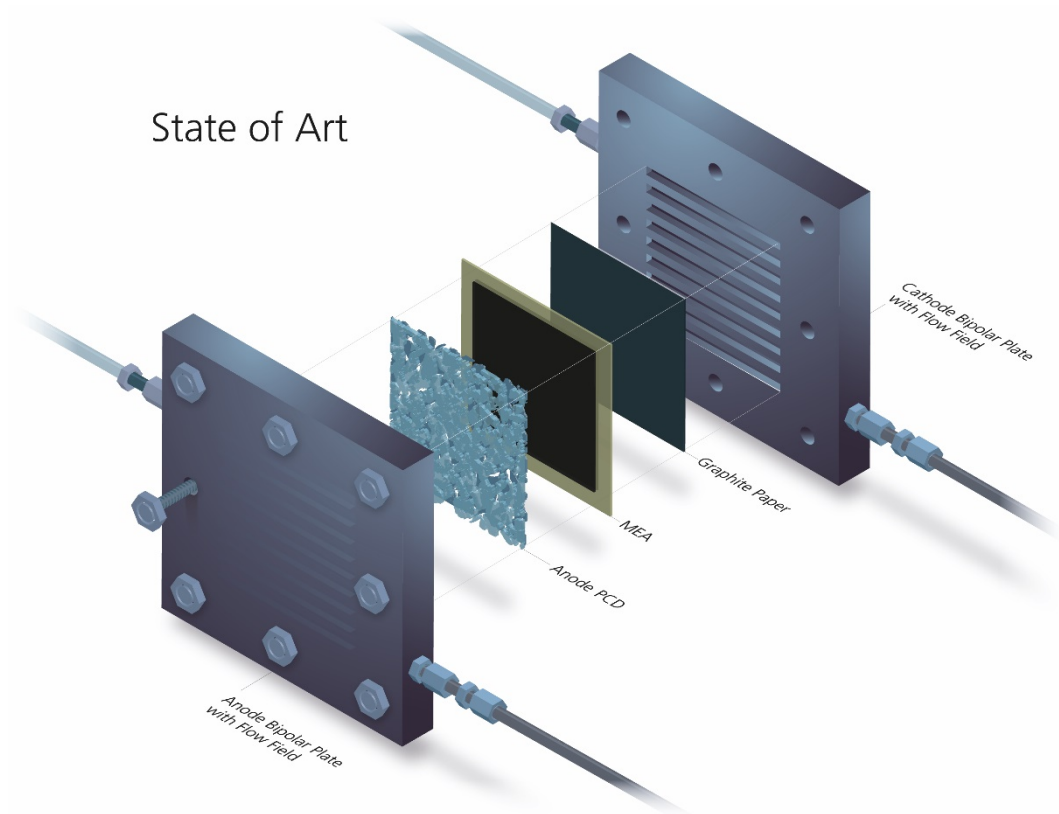
2. Fundamentals

2.1 Polymer Electrolyte Membrane (PEM) Water Electrolysis Principle

Proton exchange membrane water electrolysis (PEMWE) was first introduced by General Electric in the 1960s to overcome the disadvantages of AWE.^[28] At present, these two different types of commercial electrolyzer technologies are available for low temperature operation. Basically, the technologies in the field of electrolysis can be distinguished with regard to their electrolyte or separator, which significantly influences the applicability of the operating parameters. Considering the main factors for the widespread use of water electrolysis for hydrogen production such as performance, durability, cost, operating range, current density and pressure level,^[29] PEMWE^{[9],[30],[31]} with solid electrolyte offers advantages over AWE^[8] based on a liquid electrolyte concept, especially for the use with intermittent renewables like wind and solar.

When electricity is applied to a PEMWE cell, it splits water electrochemically into hydrogen and oxygen according to equation (2.1-1), thus converting electrical in chemical energy. In recent years, installed electrolyzer capacity has increased rapidly, with electrolyzer manufacturers currently realizing projects with plant sizes in the 100 MW range, with GW plants currently being planned. State of art (SoA) design for an electrolysis cell is shown in Figure 4 a) with BPP having a flow field structure, while b) demonstrates a novel cell design which enables the use of flat plates as BPP. For the present work, mainly the novel concept was used, with cells based on the state of art concept serving for comparative measurements. In this novel concept, the flow field structure, which is intended to provide an efficient water supply or to remove product gases from the cell, is omitted in the BPP. This task is additionally performed here by the adjacent PTL which has a gradient structure, specifically mesh or several layered meshes coated with a porous structure, to ensure efficient media transport. The water flows via pipes to the BPP where it is fed through holes in the plate surface to the PTL, which distributes it evenly over the active cell surface and transports it to the active centres of the catalyst. The gases produced are discharged again via the PTL on each side of the respective half-cell and leave the cell again through a hole opposite the inlet. Sealings around the components ensure that no media escape. One advantage of this approach is the lower manufacturing costs for the BPP. The reason for this is that the very hard titanium is used as the standard material for the BPP and thus the time-consuming and processing-intensive insertion of the channel structure can be dispensed with.

a)



b)

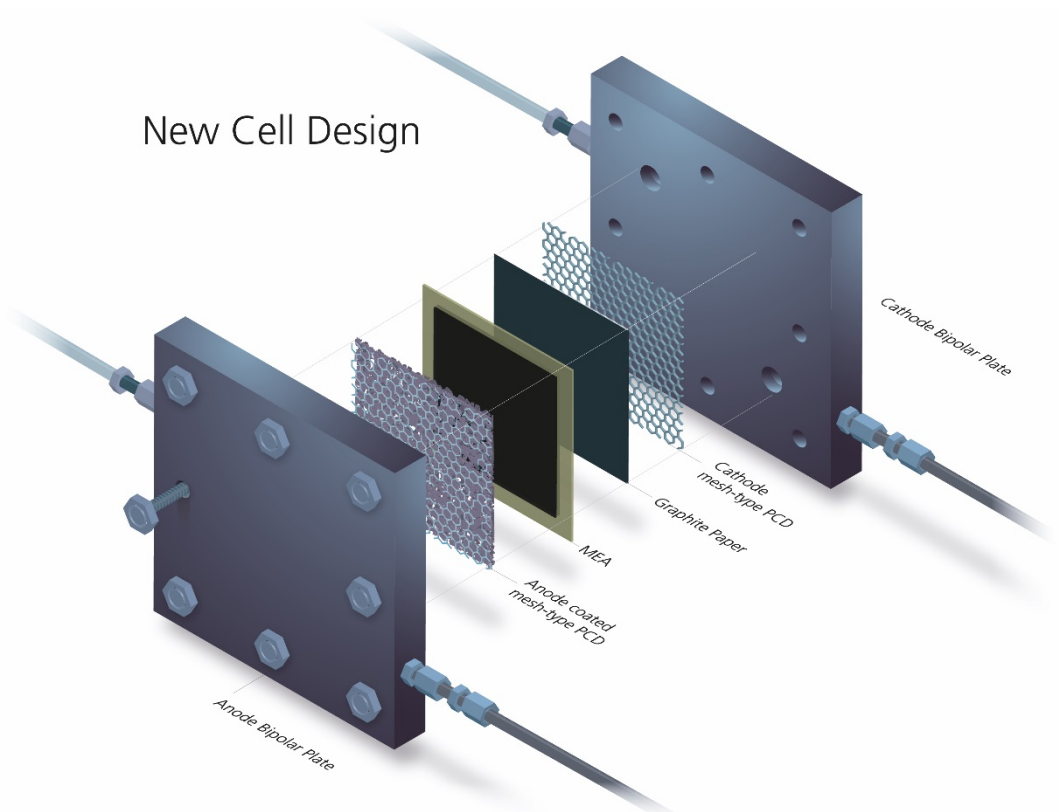


Figure 4. Sketch of electrolysis cell design a) State of Art, b) New Cell Design

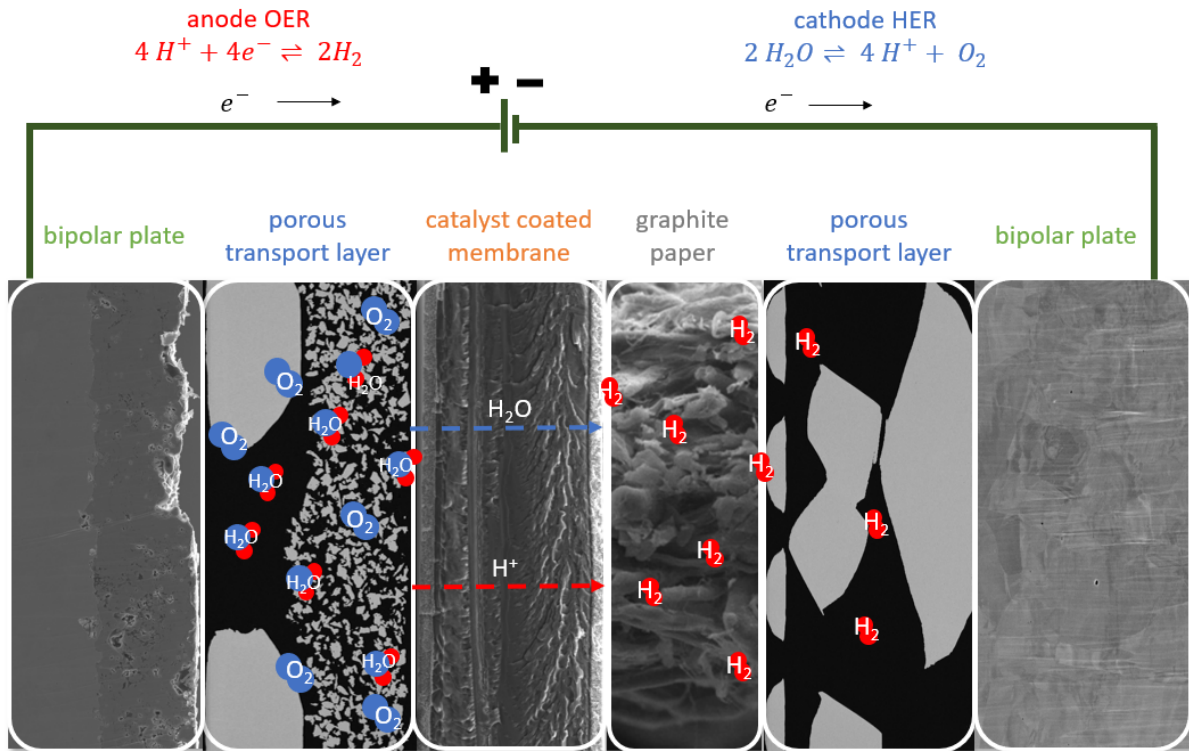


Figure 5. Schematic illustration of PEM electrolysis cell components showing their electrochemical and mechanical interactions. The demonstrated components are represented by SEM images. However, the scale is different for the respective components and serves only to schematic representation.

The cell reaction is composed of the two half-cell reactions of the anode and cathode, also known as the oxygen evolution reaction (OER) and hydrogen evolution reaction (HER), respectively. At standard conditions, the reversible cell voltage is 1.229 V, at which the reaction can theoretically occur. The electrochemical reactions of a PEMWE cell and the corresponding potentials are given in Table 2.

Table 2. Reaction equations and the particular potentials of electrochemical water splitting for PEMWE at standard conditions.

Overall Reaction	$2 H_2O + \text{electricity} + \text{heat} \rightleftharpoons 2 H_2 + O_2$	1.229 V	(2.1-1)
OER	$2 H_2O \rightleftharpoons 4 H^+ + O_2 + 4e^-$	-1,229 V	(2.1-2)
HER	$4 H^+ + 4e^- \rightleftharpoons 2H_2$	0 V	(2.1-3)

Figure 5 shows the key components of a PEMWE cell in which oxidative and reductive half-cell reactions are kept separated in detail. The component separating the two electrodes, namely the polymer electrolyte membrane, consists of a proton conducting perfluorosulfonic acid (PFSA) proton exchange membrane ionomer. Standard catalysts used are Iridium oxide for the anode and platinum for the cathode. The combination of the catalytic layers and membrane is also known as the catalyst coated membrane (CCM). The CCM is connected in

series with the other two important components, namely the PTLs and BPPs, each on both halves of the cell. The PTL is responsible to provide effective transport of reactants and products between the electrodes and the BPP. Similarly, the BPP must enable uniform electrical connection to the PTL, as well as effective transport of water to and removal of the reaction gases from the PTL.

Water is normally supplied to the anode, where it flows during operation through a pump via the flow field of the BPP to the pores of the PTL towards the porous catalyst layer (CL). Here, the water is oxidized into oxygen, protons, and electrons at the active sites according to equation 2.1-2. Oxygen exits the cell via the pores of the PTL (two-phase flow) toward the BPP, where it is removed through the flow field. The protons then migrate from the anode CL through the membrane to the cathode CL. This process is always accompanied by the simultaneous transport of water due to the electro-osmotic drag. Electrons are transferred via the external circuit from the anode CL through the anode PTL and BPP in reverse order to the cathode CL, where the protons are reduced to hydrogen correspondingly to equation 2.1-3. The produced hydrogen gas has a purity of 99.999 % and leaves the cathodic cell compartment via the PTL and the flow field of the BPP.

By default, quite thick PFSA membranes (Nafion 115: 127 μm , Nafion 117: 183 μm) are used in PEMWE cells, as they exhibit low gas crossover with good mechanical robustness. This occurs due to concentration differences between the two halves of the cell and is exacerbated by operation under pressure. In addition, the use of thicker membranes mitigates the effect of potential phenomena such as membrane thinning due to chemical decomposition, while thinner membranes result in lower ohmic losses, allowing higher efficiencies to be achieved. Whereas mechanical stability can be maintained by using reinforced membranes, $\text{H}_2\text{-O}_2$ recombination catalysts address the problem of crossover. Nevertheless, the Faraday losses associated with gas crossover remain.

To achieve high hydrogen production rates, the individual cells are connected in series to form a stack which is compressed by the end plates. If the cells are viewed from this mechanical aspect, the membrane with the applied catalyst layer is particularly prone to deformation or even damage, since incompressible components such as the PTL are in contact with it. But this arrangement results in a compact design and reduces the investment costs, which can be counted among the advantages of the PEMWE.

2.2 Thermodynamics

The amount of energy required for the electrolytic splitting of 1 mol of water under standard conditions is called Gibbs free energy which is given according to the following equation:

$$\Delta G_R^0 = \Delta H_R^0 - T\Delta S_R^0 \quad (2.2-1)$$

The Gibbs free energy is a measure of the driving force of a chemical process and is determined by the reaction enthalpy ΔH_R^0 and entropy ΔS_R^0 . It is used to determine whether a reaction takes place spontaneously or requires energy. Positive values for ΔG_R^0 due to high endothermic reaction enthalpy and entropy, allocates the water splitting as non-spontaneous and can therefore also be called an endergonic reaction. Thus, the electrolysis cell can be classified as an electrolytic cell.

The reversible cell voltage can be calculated for liquid and gaseous water with 1.228 and 1.184 V at standard conditions, respectively, according to equation 2.2-2 with ΔG_R^0 (liquid water: 237.14 kJ mol⁻¹, gaseous water: 228.57 kJ mol⁻¹), z the number of transferred electrons ($z=2$), F the Faraday constant ($F=96485$ C mol⁻¹) and E_0 the standard reversible cell voltage.

$$E_0 = \frac{\Delta G_R^0}{zF} \quad (2.2-2)$$

However, if the conditions deviate from the standard conditions, ΔG_R^0 must be considered as a function of temperature or pressure to determine the equilibrium voltage. Equations 2.2-3 and 2.2-4 show how the change in reversible cell voltage can be expressed as a function of temperature and pressure, respectively, where ΔS is the change in entropy, ΔV is the change in volume, R is the normal gas constant and Δn_g is the change in the number of moles of the gas.

$$p = \text{const.} \quad \left(\frac{dE}{dT}\right)_p = -\frac{\Delta S}{zF} \quad (2.2-3)$$

$$T = \text{const.} \quad \left(\frac{dE}{dp}\right)_T = \frac{\Delta V}{zF} = \frac{\Delta n_g RT}{zFp} \quad (2.2-4)$$

For this purpose, the Gibbs free energy is related to the cell voltage, this equation is known as the Nernst equation (2.2-5).

$$E = E_0 + \frac{RT}{zF} \ln \frac{a_{H_2} a_{O_2}^{0.5}}{a_{H_2O}} \quad (2.2-5)$$

Under non-standard conditions, this considers the correction of the standard reversible cell voltage E_0 by the temperature or pressure and the activity of participating species. For changing temperatures, the following applies from 2.2-3 and Nernst equation 2.2-5:

$$E = E_0 - \frac{\Delta S_R^0}{zF} + \frac{RT}{zF} \ln \frac{a_{H_2} a_{O_2}^{0.5}}{a_{H_2O}} \quad (2.2-6)$$

Since hydrogen and oxygen have a low solubility in water, their activity a from equation 2.2-5 can also be calculated as their concentration c normalized to the concentration c_0 at standard conditions. Furthermore, according to Henry's law, the concentration of dissolved gases is proportionally dependent on their partial pressures p . The cell voltage increases with increasing pressure considering 2.2-4 and 2.2-5.

$$E = E_0 + \frac{\Delta n_g RT}{zFp} + \frac{RT}{zF} \ln \frac{p_{H_2} p_{O_2}^{0.5}}{a_{H_2O}} \quad (2.2-7)$$

However, in order to split 1 mol of water, not only electricity ($237.14 \text{ kJ mol}^{-1}$) is required, but also heat ($48.69 \text{ kJ mol}^{-1}$), i.e. energy of $285.83 \text{ kJ mol}^{-1}$. This required heat is supplied during electrolysis by additionally produced heat through internal resistances. This means that a cell voltage of 1.481 V - the so-called standard or thermoneutral voltage - is theoretically needed for water splitting and corresponds to the higher heating value (HHV) calculated by equation 2.2-7.

$$E_{HHV} = \frac{\Delta H_R^0}{zF} \quad (2.2-7)$$

It thus provides a resilient value for calculating cell and stack voltage efficiency. The formula for calculating the cell efficiency consists of the quotient of the thermoneutral cell voltage and the cell voltage at the specified operating conditions and can be expressed as follows:

$$\eta_{Cell} = \frac{E_{HHV}}{E_{Cell}(p,T,i)} \quad (2.2-8)$$

2.3 Overpotentials

Basically, there are three main factors in PEMWE that reduce the efficiency of the cell. These are also called overpotentials or voltage losses and consist of the ohmic η_{Ω} , kinetic η_{kin} and mass transport losses η_{MTL} . The cell voltage E_{Cell} during PEMWE operation can be given according to equation 2.3-1.

$$E_{Cell} = E_0 + \eta_{\Omega} + \eta_{kin} + \eta_{MTL} \quad (2.3-1)$$

Figure 6 shows an exemplary polarization curve and its distribution of the cell voltage to the respective overpotentials.

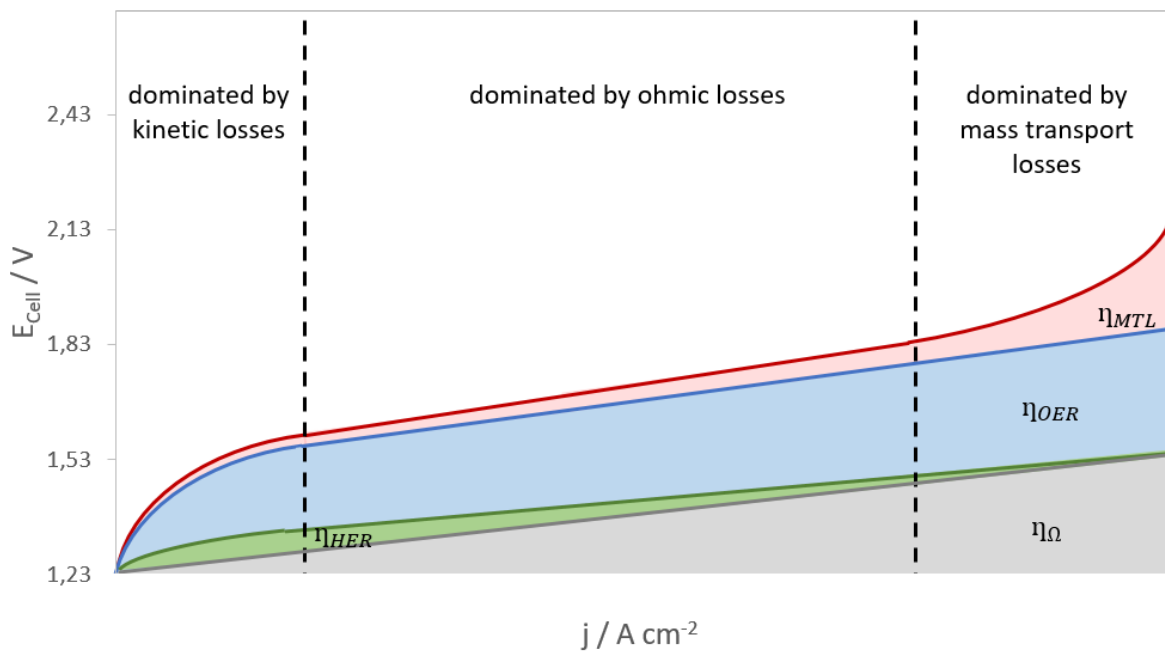


Figure 6. Schematic polarization curve splitted in its overpotentials associated with ohmic, kinetic and mass transport losses.

2.3.1 Ohmic Overpotential

The ohmic losses result from the electrical contacting of the BPP and PTL, interfacial contact resistances as well as from the ionic conduction through the layers comprising the electrolyzer. These can be calculated by the sum of all resistance R_i times the respective operating current I , as equation 2.3.1-1 indicates.

$$\eta_{\Omega} = I \sum_i R_i \quad (2.3.1-1)$$

2.3.2 Kinetic Overpotential

The kinetic overpotential can be explained as the energy needed to initiate the water splitting reaction and is related to the choice of catalyst as well as the membrane and their respective properties. Especially when using thin membranes, the kinetic losses become dominant. To describe the kinetic losses, the Butler-Volmer equation is used, which can be set up separately for both electrodes, anode and cathode, and relates the current density to the overpotential. The total current density j for a multi-step reaction is described by the apparent exchange current density j_0 and the transfer coefficient α_A and α_C for anode and cathode half-cell reaction, respectively, according to equation 2.3.2-1:^[32]

$$j = j_0 \left(e^{\frac{\alpha_A F}{RT} \eta_{kin}} - e^{-\frac{\alpha_C F}{RT} \eta_{kin}} \right) \quad 2.3.2-1$$

In the equilibrium state, the rates of charge transfer and thus the current densities of the anodic and cathodic reactions do not differ. The current density in equilibrium in the absence of an overpotential is called the exchange current density j_0 . This is a material-specific parameter and a measure for the catalytic activity.^[33] Indeed, while increasing the electrode potential accelerates a partial reaction, the other one is inhibited. This type of inhibition manifests itself in a transient overpotential. With the introduction of the transfer coefficient α , which evaluates the advantage of anode or cathode reaction, the different current densities are determined. In equilibrium, $\alpha=0.5$. With $0.5 < \alpha < 1$ the anodic and with $0 < \alpha < 0.5$ the cathodic reaction is accelerated. In the literature values of 2 and 0.5 can be found as typical values for the anodic and cathodic transfer coefficient, respectively.^[8] Thus, equation 2.3.2-1 can be expressed as:

$$i = i_0 e^{\frac{\alpha_A F}{RT} \eta_{kin}} \quad 2.3.2-2$$

$$i = -i_0 e^{-\frac{\alpha_C F}{RT} \eta_{kin}} \quad 2.3.2-3$$

Based on equations 2.3.2-2 and 2.3.2-3, the kinetic overpotential for the respective half-cell reaction can be calculated. This representation is known as the Tafel equation and is as follows:

$$\eta_{kin,A} = 2.303 \frac{RT}{\alpha_A F} \lg \frac{i}{i_0} \quad 2.3.2-4$$

$$\eta_{kin,C} = -2.303 \frac{RT}{\alpha_C F} \lg \frac{|i|}{i_0} \quad 2.3.2-5$$

2.3.3 Mass Transport Overpotential

The mass transport overpotential η_{MTL} is associated to the limitation in the supply of reactant water but also related to the blockage of active sites of the catalyst by excessing product gases and depends on the concentration in the case of gases. In electrolysis η_{MTL} can be described as logarithmic ratio of the concentration c of the product gases O_2 and H_2 at the catalyst layer CL compared to standard conditions 0. This was introduced by Marangio et al.^[34] as follows:

$$\eta_{MTL} = \eta_{MTL,A} + \eta_{MTL,C} = \frac{RT}{2F} \ln \frac{c_{O_2,CL}}{c_{O_2,CL,0}} + \frac{RT}{4F} \ln \frac{c_{H_2,CL}}{c_{H_2,CL,0}} \quad 2.3.3-1$$

However, this does not yet consider that at high current densities oxygen gas accumulates near the CL and thus inhibits the active centers for further reaction. This can be related to high flow rates of water required and a correspondingly large number of product gases produced at this operation condition. In the case of water electrolysis, this means that catalytically active centers are occupied by oxygen gas on the anode side and water cannot reach them quickly enough for the reaction to proceed again. Therefore, the gas generation rate but also the transport rate of the reactants relative to the active surfaces of the electrode affect the mass transport overpotential. To represent this, a term can be added to equation 2.3.3-1 that describes the ratio of the growing gas bubble in a PTL pore to the water displaced by it. When the gas bubble reaches the size of the pore, it is no longer available as a transport path for water to adjacent active centers or further pores of the PTL.^[35] According to this the mass transport losses can be expressed as:

$$\eta_{\text{MTL}} = \frac{RT}{2F} \ln \frac{c_{\text{O}_2, \text{CL}}}{c_{\text{O}_2, \text{CL}, 0}} + \frac{RT}{4F} \ln \left[\frac{c_{\text{H}_2, \text{CL}}}{c_{\text{H}_2, \text{CL}, 0}} + \left(\frac{\dot{V}_r}{\dot{V}_c} \right)^2 \right] \quad 2.3.3-2$$

Here \dot{V}_r describes the ratio of produced O_2 to the supplying water flow rate and \dot{V}_c stands for the required pore diameter to maintain a liquid transport path at the pore wall.

This makes it clear that the mass transport losses do not depend exclusively on the operating parameters, but also on the transport structure of the media itself. The porous materials can be characterized by their morphology resulting in properties such as porosity, pore and throat diameter, thickness or permeability. In order for the media to be transported in porous structures, the capillary pressure of the pores must be overcome. Capillary pressure can be described by the interaction of the surface tension of a fluid and the interfacial tension between fluid and solid material as follows:

$$P_c = \frac{2\gamma \cos\theta}{r_c} \quad 2.3.3-3$$

With γ is the surface tension, θ is the contact angle and r_c is the radius of the throat. This relationship shows that the capillary pressure to be overcome increases with decreasing throat size.

In principle, however, it can be summarized that mass transport losses correlate with the properties of the PTL morphology.^{[27],[36-40]} So far, however, no clear evidence for the decisive sub-resistance has been presented, nor have associated parameters or limiting processes have been identified. Therefore, the causes of mass transport losses in PEMWE are not well

understood, which is equally true for the contribution of transport and fluid dynamics in PEMWE catalyst layer.

2.4 Components

In the following section, the main components of a PEMWE cell, more specifically the catalyst coated membrane (CCM), bipolar plates (BPP) and porous transport layer (PTL), are introduced and their requirements for operation are highlighted.

2.4.1 Catalyst Coated Membrane (CCM)

In PEMWE, the so-called catalyst coated membranes (CCM) are usually used as the membrane electrode assembly (MEA), in which the catalysts for the anode and cathode are applied directly to a proton-conducting membrane. There are various methods for this, whereby a typical method is the spraying method. A mixture of catalyst, ionomer, isopropanol and deionized (DI) water is applied to a polytetrafluorethylene (PTFE) sheet using a spray gun, dried and finally hot-pressed onto a Nafion[®] membrane. This creates thin, porous catalyst layers that adhere well to the membrane and thus keep ohmic resistances low.

As electrocatalysts, catalytically highly active materials are required for the respective half-cell reaction. While iridium and ruthenium oxide (IrO_x , RuO_y) are used for the OER, Pt nanoparticles supported on carbon (Pt/C) are used for the HER. It should be added that Ir-based catalysts are state of art, as Ru is limited by its lower stability (due to corrosion) at higher activity than Ir. The loading of the catalysts ranges from $0.5 - 1 \text{ mg cm}^{-2}$ for the cathode and about 2 mg cm^{-2} for the anode catalyst. The reaction kinetics of the HER on Pt are very fast, so that only low overpotentials could be observed even at high reaction rates.^{[41],[42]} In contrast, the OER kinetics is much slower, which is reflected in overvoltages.^[43]

To promote proton conduction from the bulk of the catalyst layer to the membrane and thus also reduce ohmic losses, ion-conducting ionomer is added. In addition, it serves as a binder for embedding the catalyst so that the structure becomes stable and durable. The disadvantage, however, is that its electron resistivity reduces the electronic conductivity of the catalyst itself. By default, Nafion[®] solution is used as ionomer while the optimal loading is reported to be between 10-20 wt. %.^{[44],[45]}

Perfluorosulphonated polymers are used as membranes in PEMWE as solid electrolytes. The commercial Nafion[®] membranes are the most common, but Aquivion[®] or Flemion[®] are also used. Usually, Nafion 115 or Nafion 117 are used in the PEMWE, which show a thickness of 127 and 183 μm (5 and 7.2 mil), respectively. The membrane itself consists of a hydrophobic PTFE backbone for stability and a perfluoroalkyl ether side chain that ends hydrophilic with sulphonic acid (SA) groups.^[46] In the length of the side chains, the membranes mentioned

differ; while Nafion[®] is based on long side chains (LSC), Aquivion[®] uses short side chains (SSC).^[24] Microscopically, an interconnected pore structure is formed whose pore walls consist of the SA groups. If the water content of the membrane is sufficient, these form hydronium ions (H_3O^+), which creates the protonic conductivity.^[47] Thus, the protonic conductivity and the water content of the membrane depend strongly on the available SA groups, the so-called ion conducting units, and can be described as a function of the water content, which results from the ratio of the number of water molecules to the number of acid sites. An important parameter in the characterization of membranes is therefore the equivalent weight (EW), which describes the weight of the ionomer per sulfonic acid group and thus expresses the exchange capacity of the membrane. While typical Nafion[®] membranes have an EW of over 900 g mol^{-1} , Aquivion[®] membranes can offer the same stability at a lower EW due to higher ion exchange capacity.^[48] SSC membranes were first used in the field of fuel cells, but in recent years they have also gained importance in PEMWE.^{[49],[50]} In addition to proton conductivity and chemical-mechanical stability, it is important that the membrane remains impermeable to the gases. This remains a challenge especially with thin membranes (e.g. $50 \mu\text{m}$, Nafion[®] 212) and pressurized operation, which is why an application of a recombination catalyst (Pt) is proposed in the literature to prevent hydrogen in the oxygen gas stream at the anode for safety reason.^{[51],[52],[53]} Permeating H_2 is recombined at Pt interlayer with O_2 to water, which increases also the gas purity.

In summary, the requirements for the catalyst layer are high electrical and ionic conductivity as well as a high electrochemically active surface, while for the membrane/ionomer, high ionic conductivity, low permeability to gases as well as mechanical stability are indispensable criteria.

2.4.2 Bipolar Plate (BPP)

The BPP is the outer of two components, also known as interconnectors, and must enable uniform electrical connection to the adjacent porous transport layer (PTL), as well as effective transport of water to and removal of the reaction gases from the PTL. Furthermore, operation especially at high current densities result in heat production which need to be removed effectively by the liquid coolant to ensure durability but also high performances.^[54] In order to fulfil this demanding task, SoA BPP have more or less elaborate distribution structures that are formed or stamped into the plates. The different structures range from parallel, single and multiple serpentes^[55] as well as cascade design^[56] as shown in Figure 7. In addition, the BPP need mechanical stability to withstand the operating pressure and transfer a homogeneous contact pressure to both the sealings and $\sim 2.5 \text{ MPa}$ to the cell components to optimize cell performance.^[57] Besides to mechanical stability and high electrical conductivity to reduce interfacial contact resistance, the BPP must also be chemically stable in order to be resistant

to high potentials in an oxygen-saturated and acidic environment on the anode side. Titanium is suitable for this and is used as a standard material for the manufacture of the manifold structures. However, because titanium oxidizes under these conditions and forms an insulating passivation layer of TiO_2 , the BPPs are coated with precious metals to prevent this surface oxide formation and thus keep the contact resistances low.

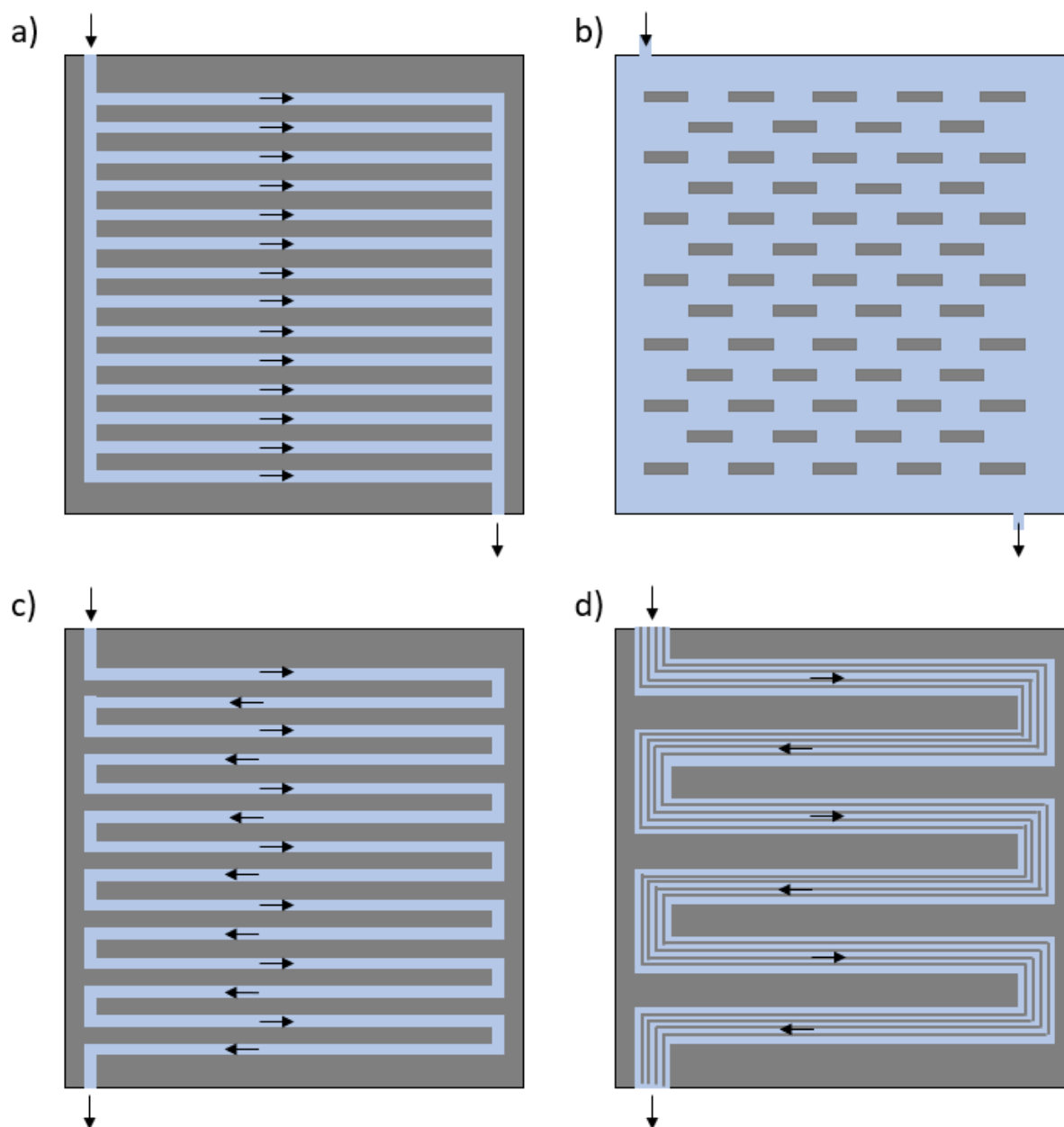


Figure 7. Schematic Overview about flow field structures in PEMWE a) parallel, b) cascade, c) single serpentine, d) multiple serpentine

The BPP account for more than 50 % of the stack cost^[58] which can be ascribed to titanium used as base material, sophisticated flow field structures and their machining as well as the protective coatings. Therefore, not only in research institutions but also in the industry, ways to save BPP costs were searched for. On the one hand, through material savings in the base

material Ti as well as in the coating materials, and on the other hand through optimized manufacturing processes, fewer manual work steps and economy of scale, the costs of the BPP could be reduced by more than 80 %.^{[18],[19]}

In order to reduce costs further, materials are being investigated for their suitability as substitutes for Ti. Stainless steel can be protected from corrosion by applying precious metal coatings like gold^[59] and Platinum,^[60] but also coatings with Ti,^[61] Nb or Nb/Ti^[62] and thus represents a cost-effective alternative. The stability of the latter was tested in a long-term test with 14,000 operating hours.^[63] Based on an end-of-life stack voltage of 2.2 V, a stack lifetime of 57,000 h could be assumed, which is in good agreement with previous work by Ayers et al. while this stack design used a total platinum group metals (PGM) loading of 10 mg cm⁻².^[64] Rojas et al. reported on Ti/TiN bi-layer coating on stainless steel 321 tested in a corrosion cell setup which can be considered as BPP material, although a test in a real PEMWE setup was not carried out.^[65] Another approach considers the treatment of Ti surface to increase the conductivity and performance using nitrided Ti BPPs.^[66] In addition, Shirvanian P. et al. see laser-treated 316L stainless steel, carbon-based and nitride coatings on stainless steel, as already investigated for PEMFC, as possible components for cathode-side use as BPP in PEMWE.^[24] Lastly, copper coated with Nb was demonstrated to be another real alternative for Ti as BPP material.^[67]

Ultimately, the BPP must ensure high electrical conductivity, mechanical stability and efficient media transport.

2.4.3 Porous Transport Layer (PTL)

The porous transport layer (PTL) is one of the PEMWE cell key components in between the BPP and the catalyst layer which allows effective transport of reactant water to the electrodes while facilitating gas removal towards the flow field of the BPP. These targets and the conditions during cell operation result in high requirements for the PTL.

On the cathode side, experience from PEM fuel cell can be used and steel- or carbon-based materials can be utilized.^[68] Since the operation conditions on the anode side are more aggressive due to highly concentrated O₂ environment and elevated cell potentials (> 2 V)^[8] carbon would oxidize and lead to formation of CO₂. This further leads to the reduction of electrical conductivity, decrease of active catalyst surface and successive decomposition of the anode, which causes a general degradation of the CCM.^[69] Nevertheless, some studies have used carbon paper as anode PTL since it seems to be sufficiently stable for short term experiments less than 20 hours.^{[70],[71]}

Titanium (or similar resistive materials) can withstand the prevailing harsh conditions on the anode and, as with the BPP, is also used as the standard material for the PTL. Nevertheless,

to avoid passivation, which leads to an increase in cell voltage over time,^{[72],[73]} titanium is coated with PGM.^{[72],[74]} Efficient gas/water management has a high impact on cell performance due to the reduction in mass transport losses,^{[75],[76],[77]} especially at high current density operation. Commercially available PTLs for the anode include sintered powders, felts, and meshes sold by companies such as GKN Sinter Metals, Bekaert and Melicon, respectively. Surface scanning electron microscope (SEM) images of some standard materials for PTLs are shown in Figure 8. Recent developments have included tunable PTLs with controlled porosities^{[78],[79]} and pore structures with a size gradient.^{[80],[81],[82]}

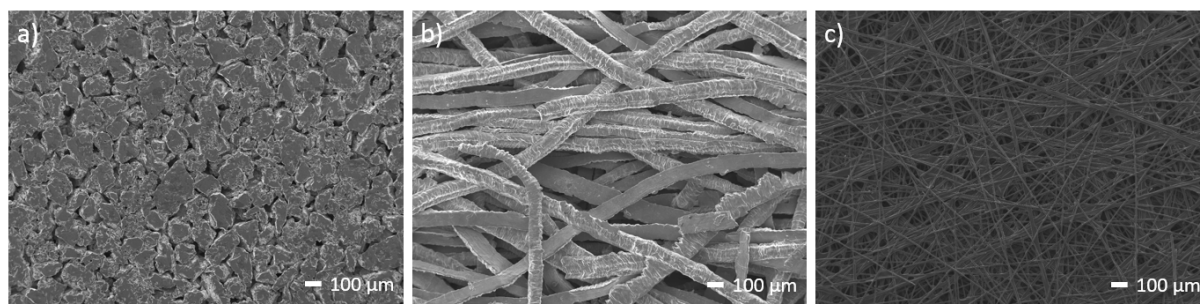


Figure 8. SEM images of PTL materials: a) sintered Ti, b) Ti felt and c) carbon paper

Recommendations regarding structural requirements such as optimal porosity of 30-50% and pore sizes between 10-13 μm in terms of electrical resistance to mass transport are given in the literature.^{[38],[82]} In this regard, Table 3 will provide an overview of both the materials used and their properties. In this context, Ti-felt is a cost-effective option for PTL, consisting of uniformly distributed fibers that are subsequently thermally sintered. Although the structure is finally roll-pressed, the material thickness is higher than other structures, resulting in increased fluidity and cell resistance. Further, sintered Ti materials are used, which were originally used in industry for filtration or medical applications, but have been intensively investigated for use in PEMWE in recent years.^[82] While pore sizes and porosity can be well controlled by the manufacturing process due to adaptation in powder fraction, sintering temperature and time, the energy needed for thermal sintering leading to high cost.^{[80],[83]} In order to reduce the cost, the structure thickness should be kept low, in addition, this also minimizes the electrical as well as diffusion resistance. In contrast, Ti mesh can be manufactured at very low cost i.e. by perforating or cutting slits (expanded) into metal sheets or weaving metal fibers.^{[80],[84]} However, these substrates usually have large pore diameters and an uneven surface, which can result in few contact points between PTL and the adjacent catalyst layer and consequently increased contact resistances as well as deformation of the CCM.^[83] Through the intensive studies of PTL and knowledge gained, multilayer structures were developed from different substrates and coatings. These pore gradient structures range from titanium-based to stainless steel structures on which a microporous layer (MPL) of titanium or niobium is deposited. Thanks to effective media transport within the optimized structures, increased performance can be

achieved. Further, Ti is oxidized to TiO_2 during PEMWE operation and forms non-conductive passivation layers, which increase the ohmic resistance and lead to performance degradation. Therefore, PGM-coated PTLs have been tested in various publications, resulting in stable and durable cell behavior with good performance, but have the major drawback of further increasing cost and technology reliance on PGM.

Table 3. Overview about used PTLs and their properties such as porosity, particle size, pore size, thickness or applied coatings found in the literature.

		base material	Porosity [μm]	pore size [μm]	particle/ fiber size [μm]	Thickness [μm]	coating	reference
titanium	homogeneous pores	felt	50 – 75	36-207	20-80	300 – 1000		[105], [106]
		sheet	29 – 71	100 – 790		25 – 200		[78],[107]
		sintered fibers	40 – 82	10 – 120	20 – 80	300 – 1000		[36], [77], [108], [109], [93]
		sintered particles (spherical)	8 – 40	11 - 100	40 – 520	250 - 1400		[38],[110]
		sintered particles (irregular)	30 - 54	52 – 96	30 – 1000	500 - 2000		[51], [91], [94], [87]
		mesh	27 – 77			170 – 534		[104], [111]
		pore-graded	20 – 50	6 – 70	7 – 125	120 – 1230		[27], [81], [82]
	surface modified	VPS	9-14.	1.6 – 3.7	< 45	13.4 – 62	Ti	[80]
coating		56 – 62	414	20	250	Ir, Pt, Au	[73], [74], [107]	
laser treated		56		20	200 – 1000		[112]	
other materials	metallic ceramics					10		[113]
	surface modified	sintered stainless steel	16 – 35		18 – 40	330 – 370	Nb	[114]
		mesh stainless steel	25	3 – 50	< 45		Nb/Ti	[40]

Unfortunately, high cost and limited stability of PTL material, particularly for the anode side, hinder the establishment and high efficiency of PEMWE in the market. The development of cost-effective PTLs applicable for PEMWE optimized regarding thickness, porosity and pore size which goes hand in hand with properties for the surface of the materials is still a topic that has not yet been fully addressed and needs to be further considered in future works.^[84] As approaches for cost reduction should be considered:^[5]

- 1) Coatings on Ti-PTLs to prevent passivation and reduce ohmic resistance

- 2) Morphology of PTLs should be optimized to improve catalyst utilization while stabilizing ultra-thin membranes
- 3) Use of stainless steel with cost-effective coatings by using non-PGM.

The use of stainless steel also for PTLs is preferable, but it is known from the literature that it corrodes severely when uncoated, thus poisoning the CCM with Fe and Ni.^{[85],[86]} Recently, by applying a non-precious metal coating of Nb/Ti, a stainless steel PTL could be tested for 1000 hours in a PEM electrolyzer under accelerated stress test (AST) conditions without showing signs of corrosion.^[40] In this work, the authors used both stainless steel-based PTL and BPP and showed that the fabrication of a complete PEMWE stack composed mainly of stainless steel is basically possible. Thus, stainless steel can provide a real alternative to titanium that saves costs.

Generally, for the manufacturing process it is important to ensure high control about porosity and pore size while area and thickness of the samples need to be scalable to plant sizes at least in the MW scale. In this context, it is essential to optimize the properties of the PTLs in terms of fulfilling their functions and tasks, which significantly influence cell performance. As the PTL is placed between the CCM and the BPP, it is the structure for ensuring the supply of water from the channel structure of the BPP to the active area, as well as the discharge of the generated gases away from the catalyst to the BPP. Additionally, this must establish electrical contact between the catalyst and the bipolar plate, and the heat generated at the reaction surfaces must be dissipated. The following are the tasks of the transport structure on both the anode and cathode sides:^{[87],[88]}

- i) Transport of reactant water
- ii) Removal of the generated gases
- iii) Ensures good electrical conductivity between BPP and catalyst layer and low interfacial contact resistance
- iv) Mechanical support of CCM
- v) Dissipation of process heat

Other demands on the PTL are that catalyst utilization is improved, as well as material stability against the acidic conditions and high potentials within the cell. These aspects and reconciling the properties of the PTL in terms of thickness, surface roughness, porosity, pore size, mechanical stability as well as electrical and thermal conductivity and the passivation of the material is a challenge.^[89] To fulfill all the demanding tasks the PTL need several attributes and properties which are listed in Table 4.

Table 4. Overview about PTL characteristics or features and their affection on PEMWE cell behavior

Characteristic/Feature	Property	Affect
Water/gas transport	Thickness: 0.2-1.3 mm ^{[90],[91],[92]}	Performance increase with thinner PTLs since ohmic and transport resistances decrease
	Porosity: 50-75 % ^{[92],[93]}	Wide range possible without affection of cell performance at porosities > 50 %
	Pore size: 12-13 μm Mean pore diameter: 16-90 μm	Pore size distribution affects capillarity and gas permeability
	Mass transport losses	Primarily responsible for reduced cell efficiency
Electrical conduction	High electrical conductivity of the bulk PTL and low interfacial contact resistance mandatory ^[89]	Uniform and sufficient contact PTL/CL reduces ICR resulting in improved performance and cell efficiency
	Through-plane: contact resistance dominant ^[74]	→ PGM coating or MPL can reduce ICR ^[80]
Mechanical support	Smooth surface to prevent CCM deformation ^[89]	High interfacial contact area reduce ohmic resistance resulting in increased performance
Heat transfer	Thermal conductivity: 21.9 W (mK) ^{-1[94]}	insufficient heat transfer can lead to CCM damage

In addition to efficient media transport, which is determined by overall PTL parameters such as thickness, porosity and pore size, cell performance is largely determined by the properties of the interface between PTL and catalyst. Therefore, this interface PTL/CL is found to be a key criterion for achieving high performance. Mo et al. found that OER occurs only at the interface between the PTL and CL, further emphasizing the importance of the PTL and the extent of its influence on cell performance.^[95] Considering the catalyst area in contact with the grains of the PTL surface, called the interfacial contact area, a relationship between this and its contact resistance to the ohmic resistance can be found. The contact resistance is the electrical resistance of an electrical contact surface and is composed proportionally of the constriction resistance and the film resistance.

The constriction resistance results from the microscopic unevenness of a contact surface, whereby the actual contact area is smaller, and the current flow is restricted. Depending on the resistivity of the material used, the surface unevenness and the number of effective contact areas, the constriction resistance is determined. Electrical contacts are assumed to be round

contact points but are formed by a large number of microcontacts. Considering the resistance values of several microcontacts, which can be grouped into a cluster, and a single conducting point covering the area of the cluster, they are comparable.^[96] However, the density of the micro-contacts has a significant influence, because the higher it is, the lower the constriction resistance. The application of pressure deforms the microcontacts, creating new contact points until sufficient points are reached to withstand the deformation.^[97] That is, the interfacial contact area includes not only the contact area between the PTL grains and the catalyst, but also from the total surface area of the microcontacts, which is a subarea of the former. Schuler et al.^[36] showed that this interfacial contact area significantly affects ohmic resistances, heat transfer and also mass transport limitations which result from inadequate catalyst utilization. If a higher catalyst utilization can be achieved by a larger fraction of active sites at the PTL/CL interface, this can be translated into a higher catalyst contribution to the reaction, which correlates with a higher achievable limiting current density. In summary, poor catalyst utilization, which is highly dependent on the interfacial structure of the PTL and the catalyst layer, significantly limits the efficiency of the cell.^{[36],[95],[98]} Interestingly, while the interfacial properties are affecting the cell performance a lot when having low catalyst loadings the impact does not seem to be that important when high PGM content is used for the catalyst layer.^[99] This shows how sensitive cell performance is to PTL properties, especially those at the interface with the catalyst layer. Thus, the PTL determines not only the ohmic but also the kinetic and mass transport losses. Therefore, the factors affecting the structural properties of the PTL must be identified and considered.

The film resistance describes the resistance resulting from the formation of a surface layer such as the oxide layer on titanium. This passivation layer forms spontaneously in air or water and protects the material from corrosion. Under PEMWE environment the thickness of the oxide layer grows about 2.2-2.5 nm V⁻¹^[100] and is therefore potential driven. This passivation layer is a semiconductor whose electrical conductivity depends mainly on point defects in the lattice structure. Here, the defects generated at the interface between metal and film are essential, which are vacant for oxygen. The oxygen vacancies migrate through the film toward the interface with the electrolyte and are eliminated there. If the formation or elimination of the film is in equilibrium, a stationary thickness is reached.^[101] In this process, the density of oxygen vacancies decreases exponentially with increasing growth rate. While it is constant throughout the film, it decreases exponentially at the film/solution interface.^[100] The oxygen vacancy concentration is up to 95% lower than that of the main film and is independent of the film formation potential. This region is thin enough (<0.5 nm) to allow charge transfer by quantum mechanical tunneling.^[101] Considering the results of Shibata et al.^[102], it is obvious that crystalline films form on titanium at the PTL/CL interface in PEMWE operation (>60 °C, > 1.5 V). Due to their lattice structure, a lower resistance is to be expected, and since they are

thicker, it can be assumed that they break at the metal/film interface due to mechanical stress. This in turn leads to increased contact resistance. Again, precious metal coatings offer a solution here, but the cost problem remains.

The brittleness of the layer formed shows that high compression pressures do not necessarily lead to better performance. Especially when using softer metals such as gold, higher contact pressures also achieve a larger contact area of the microcontacts, this is not true for hard metals such as titanium. The IrO₂ particles used as the anode catalyst are also very hard and additionally applied to the soft membrane. On the one hand, sufficiently high compression pressures are then required to achieve good electrical contacting and possibly a minimal increase in the contact area of the microcontacts. On the other hand, the compression pressures are distributed differently over the surface, since both the particle sizes and distribution on the PTL surface vary. Thus, locally very strong CCM deformations up to damage of the catalyst layer can occur, which results in an interruption of the conductive paths and thus in a deterioration of the conductivity and catalyst utilization. This makes it clear that the choice of compression pressure is a balancing act of sufficient contacting and low deformation of the CCM.

From this, it is clear that PTL properties have a significant impact on PEMWE performance and must be carefully selected to obtain an effective structure. The possible affection on cell performance, catalyst utilization or cell resistances are assigned to the corresponding properties of the PTL structures in Table 5. The needs and requirements of PTL structure have been intensively studied and summarized by Yuan et al.^[115] They found that due to the lack of data, it is not possible to properly correlate the interdependence of structural properties for all PTL types. Furthermore, the comparability of data is hampered by different operating parameters or CCMs used in the literature. Even if the aforementioned parameters are kept constant, a fair comparison of the different PTL types is difficult because, for example, they have different thicknesses with the same porosity. However, if similar PTLs of different materials with porosities between 50 - 60 % are compared, the average deviation in material thickness is $\pm 75 \mu\text{m}$ while the lowest cell voltage of 1.8 V at 2 A cm⁻², 80 °C could be achieved by Ti-mesh.^{[89],[105],[116]}

Lastly, the PTL has to ensure an adequate supply to the active sites at the CL with water while the produced gases need to be removed efficiently. High thermal conductivity as well as mechanical, chemical and electrochemical stability at high potentials and acidic environment is indispensable.

Table 5. PTL properties and their influence on cell parameters as cell potential, catalyst utilization or resistances correlating with cell performance

Property	Parameters	Affect	Comment
Powder/particle size	Small grain size result in small inter-particle distance and improve electron transfer Minimal CCM deformation	Cell potential	MPL application on PTL
Pore size	Vary between 10 – 32 μm dependent on PTL type	Cell potential	[38],[75],[79],[87],[92],[93],[103]
Porosity	Sintered: low impact Mesh: low porosity Thin/tunable PTL: high porosity	Cell potential	Influence due to porosity depends strongly on PTL type (dominant for thin/tunable PTLs)
Surface roughness	Relevant especially for sintered PTL type	Catalyst utilization	low deformation depth leads to high interfacial contact making the use of thin membranes feasible
Thickness	Sintered: powder-dependent Fiber-based: the thinner the better cell performance ^{[104],[105]}	Ohmic resistance	Irregular shaped powder used for PTL showed higher performance than for spherical shaped ^[89]
Permeability	Sintered: $0.29\text{-}3.4 \times 10^{-12} \text{ m}^2$ ^{[82],[94]} Fiber-based: design-dependent	Gas bubble detachment	Related to pore size, porosity, flow field design → larger permeability lead to reduced cell potential
Hydrophobicity	Mesh: hydrophobic Ti powder applied leading to increased ohmic and mass transport resistance ^[116]	Cell potential	
Conductivity	Conductive layer application: MPL ^[80] , Au ^{[105],[117]} , Ir ^[74] , nitride ^[105] , tungsten fibers ^[98]	ohmic resistance	Increase in in-plane conductivity of PTL lead to cell performance increase for all PTL types

2.4.4 Component Cost

By connecting individual cells in series, stacks and thus plants with a capacity of several hundred kW or even MW can be achieved. With the upscaling of PEMWE plants, the total costs decrease due to, among other things, the automation of the processes as well as the higher yield, so that the material costs become the dominant factor. These are directly dependent on the amount of material used. Assuming the compact cell design mentioned above, the stack mass fractions are only 5% of the entire system.^[21] This was based on a case

study for a 1 MW plant, the calculation of which showed that titanium accounts for the largest mass share of the PEMWE stack at more than 500 kg. Not only the costs for the high-purity base material, but also the difficulty of processing titanium itself contribute to the high cost shares. This clearly shows that costs will have to be significantly reduced in the future. Recent study already show potential for total savings of 55 % of the stack cost, while the BPP and PTL cost can be reduced by 74 %.^[18] The cost reduction can be realized on the one hand by saving or substituting materials, for example by using thinner BPP, lower catalyst loads or non-precious metal coatings, but also by optimized production processes and automation. Furthermore, efficiency increases through economies of scale also have a significant influence on the cost shares of the components.^{[19],[118]} In 2017, future costs for PEMWE were estimated at 397 – 955 € kW⁻¹.^[119]

2.5 Operating Conditions

The mode of operation of the PEMWE also has a major influence on the cost of the technology. The aim is to achieve high current densities, high pressures and intermittent modes of operation in order to reduce hydrogen production costs.^[118] The hydrogen production rate can be maximized by operating the plant at high current densities to reduce stack volume and therefore stack costs, at high temperatures to improve efficiency and high H₂ outlet pressures to save further pressure stages.^[27] In addition, the operating temperature can also be increased above 100 °C through pressure operation while maintaining the aggregate state of water, which requires less electrical effort for water splitting.^[20] However, the operating temperature is limited by the material stability of the membrane in particular. A compromise must be found between high performance through reduced ohmic and kinetic cell losses due to increased ionic conductivity of the membrane and also increased hydrogen permeability of the membrane under high temperatures. Therefore, the operating temperatures are limited with up to 90 °C and are chosen lower with 60 - 70 °C for current commercial systems due to stability.

Under thermodynamic equilibrium conditions, it can be assumed that only gas dissolved in water affects the active electrode area, which is negligible at pressures up to 100 bar due to the low solubility of both hydrogen and oxygen.^{[120],[121]} Therefore, the activity of the species can be equated with the partial pressures and, starting from the Nernst equation, the cell voltage increases with increasing pressure. However, this could not be observed in the literature when operating at balanced pressure operation^{[122],[123]} and can be attributed to an improved two-phase flow in the PTL due to smaller gas bubbles.^[20] However, the disadvantage in pressurised operation is the increased gas crossover, especially of hydrogen, and the associated contamination of the respective gas flows.

Currently, the standard operating range of commercial PEMWE systems is a nominal current density of 2 A cm⁻², stack temperatures between 60 – 80 °C at up to 30 bar.

3. Experimental Work and Methods

3.1 Experimental

3.1.1 Testbench

The cell components were measured in two different configurations. On the one hand, a conventional design was used in which water is supplied to the respective electrode sides and the product gases as well as water exit the cell flowing into the anode- and cathode-side water loops, respectively. Therefore, an in-house developed testbench was used, the relevant process instrumentation diagram (PID) of which is shown in Figure 9.

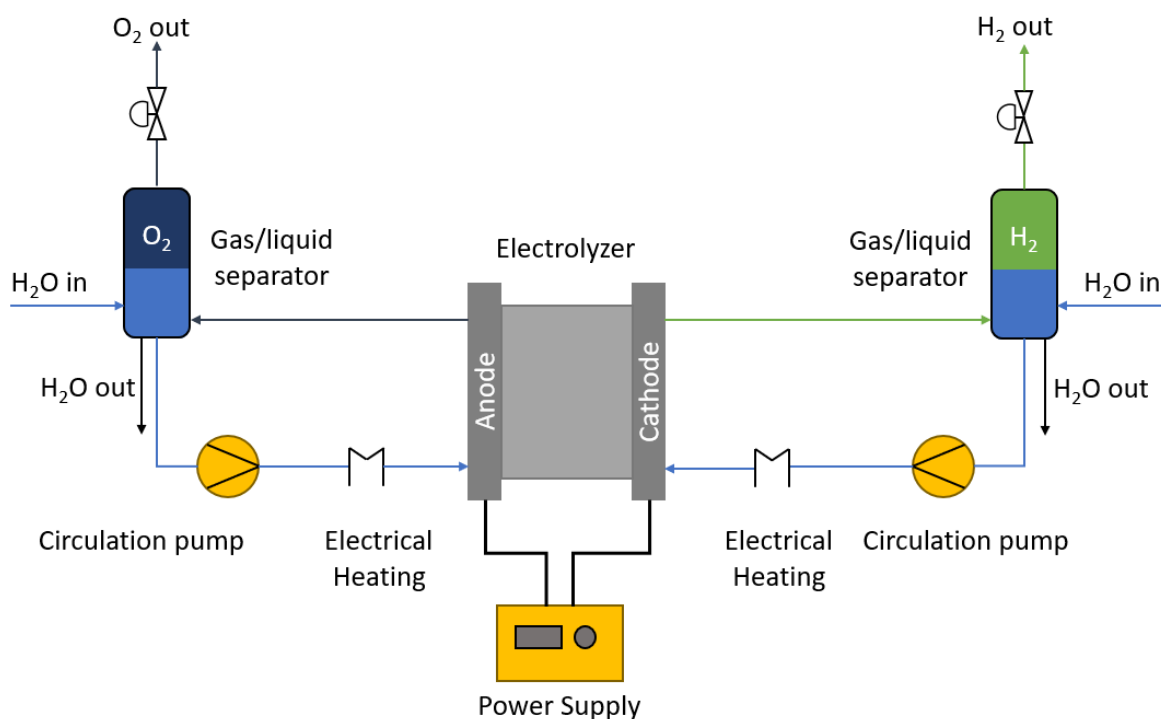


Figure 9. PID of the used in-house developed testbench

To the anode and cathode side the PEM electrolysis cell is supplied with DI water via a dosing pump (Finkct, Ritmo R033) with a flow rate of 1.7 l h^{-1} and 1.0 l h^{-1} , respectively. An ion exchange resin (Aldex Chemical Co LTD) was used to ensure high water quality with a conductivity of $> 0.1 \mu\text{S cm}^{-1}$ and prevent poisoning of the CCM with contaminants, which was placed in front of the anode side of the PEMWE cell. Fresh water is automatically supplied to the system on the anode side after triggering level sensors in the liquid/gas separators to compensate for the consumption by the cell. Temperature regulation takes place via electrical heating bands at the water inlet of the cell and, depending on the required operating temperature, by means of additional heat exchangers (LAUDA). For safety reasons, pressure sensors, normally open valves, mass flow controllers (Bronkhorst) as well as gas sensors for

measuring H₂ and O₂ content in the respective outlet streams of the cell's anode and cathode are installed to monitor operation.

This design has a balance of plant (BoP) with many components, such as the pumps, stainless steel piping, valves, gas separators as well as ion exchangers and is shown in Figure 10. Cell ageing due to dissolved metal poisoning of the CCM can take thousands of hours of operation. An AST is therefore urgently needed to test new materials and facilitate the introduction of them. For this purpose, a simplified configuration is designed in which the BoP has been made as simple as possible not using stainless steel pipes, pumps or other metal parts where ions could redeposit. Water is supplied separately from water reservoirs open to the ambient air on both the anode and cathode sides via a natural gradient. The water inlets are located at the bottom of the cell, while the gases produced can escape back into the water reservoirs via outlets at the top. The air space is constantly extracted via a ventilation system to prevent the formation of an explosive gas mixture controlled by gas sensors.

For automated operation, the control software of both testbenches was programmed in such a way that predefined measurement protocols with values for the corresponding operation can be read in from a table or that a safe shutdown of the cell experiment takes place when safety-relevant limit values are reached.



Figure 10. Testbench for standard PEM electrolysis cell operation with conventional BoP

3.1.2 PEM electrolysis cell

Different electrolysis cells were used to investigate the PTL materials, using both in-house designed and commercial cells.

Two different cell designs, developed in-house, differ in both active cell area and bipolar plate structure. While no flow field structure, i.e. flat BPP, was chosen for a cell with 4 cm² active area, the BPP of the 25 cm² cell have a parallel channel structure with a channel width of 2 mm, channel depth of 1 mm and a channel length of 20 mm. Furthermore, the BPPs for the small test cell were made of stainless steel and only coated with a dense protective Ti coating on the anode side. The 25 cm² electrolysis cell, on the other hand, was fully made of titanium. The modular design allowed for variance in contact pressure, as well as the use of different cell components. Only the cell seals had to be adapted to the respective components used in each case. The contact pressure was controlled by pressure measurement foil tests and adjusted by 4 and 8 screws for the 4 cm² and 25 cm² cell, respectively. A thermocouple was integrated into the BPP to monitor and control the cell temperature of the large test cell.

On the other hand, a commercial cell from Fraunhofer ISE was used whose Ti BPP does not have a flow field structure and is pressed together via a central mechanical screw connection.

The cell pressing can be monitored via the integrated pressure sensor and adjusted for the different material thicknesses. The active cell area of the cell was 4 cm².

In addition, a commercial stack from Nel Hydrogen consisting of four cells was used for the long-term test of 14,000 hours. These cells had all different component configurations and an active area of 86 cm². Details of the design are confidential and are the property of Nel Hydrogen.

The cells were operated at different temperatures at ambient pressure.

3.1.3 Porous Structure Layer Coating

The coatings on the respective substrates were realized using different methods. In addition to a cooperation with GKN Sinter Metals, in which a pure titanium PTL was produced by diffusion bonding,^[27] commercially available expanded metals were coated as PTL substrates, but also flat stainless steel BPPs. The coating was performed by vacuum plasma spraying (VPS) or physical vapor deposition (PVD), the processes of which are explained below.

3.1.3.1 Vacuum Plasma Spraying

Both the coatings for the PTLs and the BPPs were realized using vacuum plasma spraying (VPS) technique, which belongs to the family of thermal spraying techniques and is a coating technology for a wide range of applications. Layers with thicknesses of some tens of microns and different properties can be sprayed with VPS. The scheme shown in Figure 11 presents the plasma jet that is generated by applying a direct voltage and several hundred amperes to a gas mixture between a finger shaped cathode and a surrounding anode of the plasma torch. The flowing gas ionizes, becomes electrically conductive and heats up to several thousand degrees. Subsequently introduced particles in the size of a few hundred nm up to some 100 μm melt within the plasma and are accelerated to the substrate material to be coated. Different materials can be used as coating particles such as metals, ceramics but also polymers or mixtures of them. This coating technique makes use of the vacuum to prevent oxidation processes and thus be able to produce highly conductive coatings. By adjusting plasma enthalpy, speed, temperature and distance to the substrate, the parameters and properties such as coating density, roughness, porosity or thickness can be controlled.^[124] Depending on the spray parameters and the size of the particles, they are completely or partially melted in the plasma jet, impinge on the substrate where they cool out fast resulting in correspondingly dense or porous coatings.

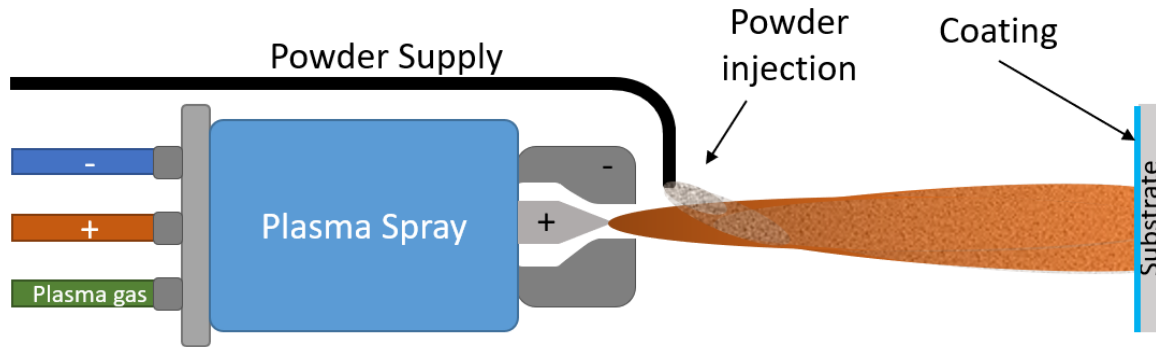


Figure 11: Vacuum Plasma Spraying Technique

Regardless of whether the coating was applied for a PTL or BPP, the substrates were heated to 250 °C before coating and Ti grade 1 (TLS Technik Spezialpulver, currently ECKART TLS GmbH) and Nb (H.C. Starck, currently FST Flame Spray Technologies) with a particle size < 45 µm was used as the coating powder, respectively. To protect the samples against deformation due to extreme heat input, the choice of nozzle speed and distance to the substrate were adjusted.

Coatings for PTLs:

Coatings of Nb/Ti were produced on 4-layer mesh-type stainless steel (GDL MeliDiff in 1.4404, Melicon GmbH) and 4-layer mesh-type Ti (GDL MeliDiff in Ti Grade 1, Melicon GmbH) PTLs. The chamber pressure was 40 mbar and the gas flow rates of Ar, N₂ and H₂ were carefully controlled to achieve the needed plasma enthalpy of 12.5 MJ kg⁻¹. First, six coating runs were carried out with Ti, more precisely, the plasma spray gun was swivelled over the substrates six times during the coating process. Subsequently, two further coating runs of Nb were sprayed on top. The torch sweep rates were 600 mm s⁻¹ for the samples. The produced PTL were labelled as Nb/Ti/ss-PTL and Nb/Ti/Ti-PTL, respectively.

Coatings for BPPs:

Ti and Nb coatings were deposited on stainless steel (1.4401, SS316) plates with circular shape delivered from Nel Hydrogen. As pre-treatment the substrates were sand-blasted with SiO₂ powder to increase surface roughness as well as adhesion of the coating powders. To achieve dense coatings for the BPPs, the plasma gas flow rates of Ar, N₂ and H₂ were carefully chosen to achieve a plasma enthalpy of 21.3 MJ kg⁻¹ for the respective coatings. A torch sweep rate of 350 mm s⁻¹ was used and to avoid the oxidation of both coatings a chamber pressure of 50 mbar was applied. 32 layers of Ti and Nb were applied to the respective BPPs. Finally, a full densification of the Nb coating was carried out using a capillary sealing process with an epoxy resin. To remove remaining air bubbles the resin was applied on top of the VPS-coating, a light vacuum of 150 mm Hg was applied for less than 5 min and the resin was fed into the

pores. As soon as the samples have dried at 65 °C, the surfaces were finally polished with sand paper of 240P and lastly 2400P grain size. With this step the Nb/ss-BPP was manufactured, while the Ti-coated plate needed further modification via physical vapour deposition (PVD).

3.1.3.2 Physical Vapour Deposition

Magnetron sputtering as a physical vapour deposition (PVD) process also belongs to the group of vacuum-based coating processes in which a plasma is generated and positively charged ions from the plasma are accelerated by an electric field superimposed on the negatively charged electrode. The positive ions are accelerated by potentials of a few hundred to a few thousand electron volts and strike the negative electrode with sufficient force to dislodge and eject atoms from it. These atoms are ejected from the surface of the negative electrode in a typical cosine line-of-sight distribution and condense on surfaces near this so-called magnetron sputter cathode or target. In general, almost all metals can be deposited by PVD and are mainly applied as thin layers in the range of a few nm to a few μm . The reason for this is primarily residual stresses within the coating, which can lead to delamination from the substrate. Magnetron sputtering is a special form of PVD in which permanent magnets are placed below the target plate to create a magnetic field near the target material. This concentrates the electrons and causes them to move in a spiral along the magnetic flux lines near the target. A schematic of the PVD magnetron sputtering coating method is visualized in Figure 12.

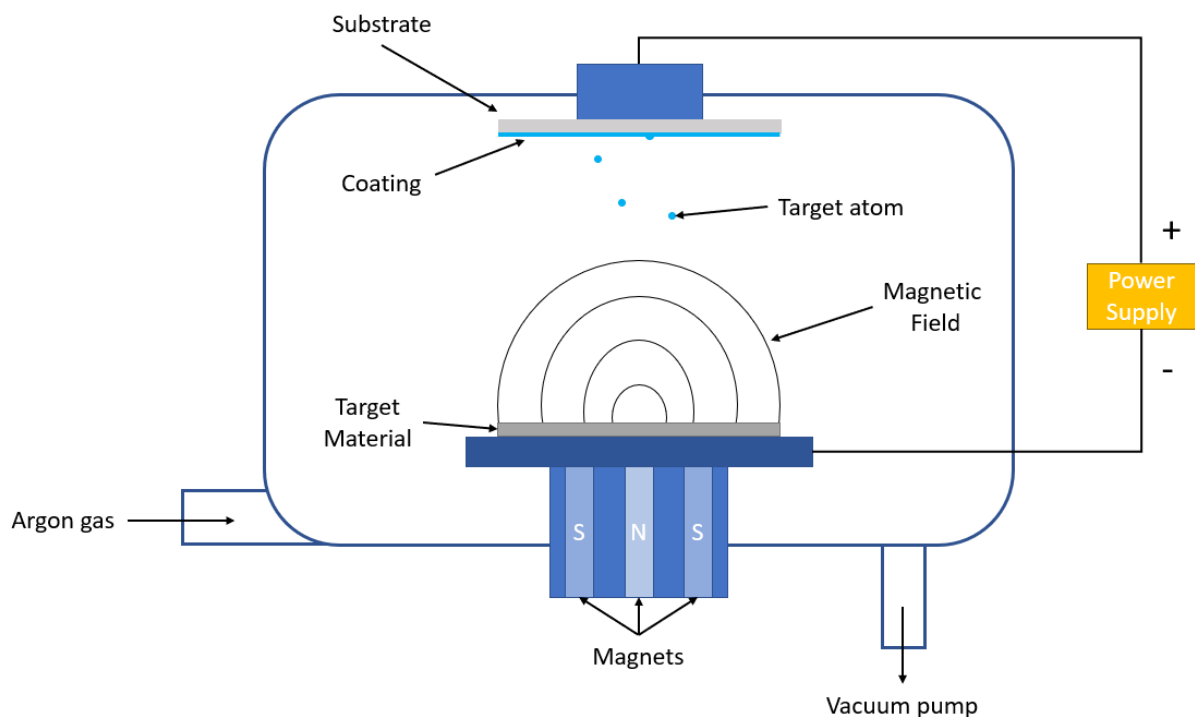


Figure 12. Scheme of PVD magnetron sputtering procedure adapted from [125]

Coatings for BPPs:

To modify the Ti coated BPP, Nb was applied using magnetron sputtering PVD technology. Before coating, the samples must be sanded with different grades of SiC without abrasives until a smooth surface was achieved with SC4000 abrasive paper. An industrial-sized gas-flow assisted coating machine (MEGA, SYSTEC of Co. SVS, Germany), which can accommodate four targets of 100×200 mm and enables the deposition of complex compounds, was used to apply the coating. Prior to this, the substrates were etched for 20 minutes by inverse sputter etching with argon plasma at 500 V pulse bias. To achieve a final layer thickness of 1.4 μm, the Nb layers were then deposited for 15 minutes at a power of 1.0 kW. This coating was also densified using the capillary sealing process described above in section 3.1.1.

3.1.4 Materials

To elucidate the influence of PTL on the performance of PEMWE under extreme operating conditions and the applicability of stainless steel-based materials for PEMWE without compromising performance or stability, both new developments and commercially available materials were investigated.

CCM: Commercial CCMs based on the available membrane materials Nafion 115, 117 and 212 were used for the tests in order to obtain a high reproducibility of the results and also to investigate the influence of the PTLs or BPP used. On the anode side, an Ir-based state of art catalyst was used, while on the cathode side a Pt-based material was chosen. The CCMs were not pre-treated and were used as received from the manufacturer.

PTLs: On the anode side, titanium-based components were investigated as reference material, on the one hand sintered titanium (SIKA-T 10, GKN Sinter Metals) but also 4-layer mesh-type Ti (GDL MeliDiff in Ti Grade 1, Melicon GmbH). Furthermore, a titanium-based PTL with a bilayer structure of titanium expanded metal bonded via diffusion bonding to a 0.7 mm thick porous titanium layer made of titanium powder was investigated. The resulting material porosity is between 40 – 60 %. Stainless steel-based (1.4404) PTLs made of 4-layer mesh-type structure from the company Melicon GmbH (GDL MeliDiff in 1.4404) were provided with a protective coating by means of VPS as described in 3.1.3 and measured.

On the cathode side, both an uncoated multilayer stainless steel mesh (Haver & Boecker OHG) and an untreated carbon paper (TGP-H-90, Toray) with a porosity of 78 % and a thickness of 280 μm were used.

BPP: Uncoated as well as coated stainless steel plates (1.4404) were used as BPP for the cathode and anode side, respectively. Details on the coatings can be found in section 3.1.3.

3.2 Methods

3.2.1 SEM - scanning electron microscope

Electrons emitted from an electron source are accelerated by an electric field. This electron beam (primary electrons) is focused on the surface of the object by means of magnetic coils and scanned line by line where it interacts with the atoms of the sample. Different detectors are used to evaluate the particular signals and their intensity.

So-called secondary electrons are produced due to such interaction of the electrons with the surface, which can be detected by an Inlens detector. They have a low energy of a few electron volts and therefore originate from the upper, few nm thick sample layers, whereby they map the sample topology.

Another imaging method is the detection of backscattered primary electrons (BSE), which are more energetic than the secondary electrons (SE) with a few keV. The signal intensity depends on the atomic number of the element, which is why heavier elements provide strong backscattering and thus appear brighter than lighter elements. Thus, the BSE image can provide information about the material composition of the sample and is also called a material contrast image.

Energy dispersive X-ray spectroscopy (EDX) is frequently used in SEM to analyse elemental composition. If an electron close to the nucleus of the atom is knocked out by an electron from the electron beam, the resulting gap is immediately filled by a higher-energy electron from a higher atomic shell. The difference in the respective energies is released as characteristic X-ray radiation and can be detected accordingly.

To avoid interactions with elements from the air, the examination takes place under vacuum and the samples must be introduced into the sample chamber for analysis. Furthermore, the charging of insulating materials must be prevented. On the one hand, the sample can become negatively charged locally if the energy of the electrons is low and only a few SE are emitted. On the other hand, the surface can be positively charged by a very energetic electron beam. This can be remedied either by applying a very thin layer of precious metal, for example gold or platinum, or by vapour deposition with carbon.

3.2.2 MIP - Mercury Intrusion Porosimetry

Edward Washburn proposed 1921 to measure pore size by intrusion of mercury with pressure into a porous sample. The so-called mercury intrusion porosimetry (MIP) is used as an analytical method to quantify various aspects of a porous material, such as pore size distribution, total pore volume, internal surface area, bulk density and absolute density. Therefore, the sample to be characterized is placed to a sample holder, called penetrometer,

which is made of glass. Samples in the size of typically smaller than 10 mm are placed into this cylindrical holder closed by a lid and connected to a capillary glass stem. This cell is evacuated within a pressure chamber and filled with mercury. This stem is surrounded by a metal tube which, together with the mercury column, forms a capacitor. This is arranged in an electrical measuring circuit and thus acts as an electronic burette. Using a known amount of mercury, the electrical response can be calibrated and consequently the amount of mercury that has penetrated the pores can be quantified. After each pressurization, the pressure is lowered and the system is returned to ambient pressure. This process of depressurization, which results in the withdrawal of the mercury, is called extrusion. Thanks to the non-wetting property of mercury, it is forced out of the pores, making a second liquid phase to displace it unnecessary.

Here, the pore size is determined as a function of the external pressure required to push the liquid into a pore against the surface tension of the liquid. Therefore, the so-called Washburn equation applies to cylindrical pores, which is as follows:

$$p_l - p_g = -\frac{4\gamma\cos\theta}{d_p} \quad (3.2.2-1)$$

With pressure of the liquid phase p_l , pressure of the gas p_g , surface tension of the liquid γ , contact angle of the liquid θ and the pore diameter d_p . For most solids, the contact angle of mercury is between 135° and 142° while the surface tension at 20 °C under vacuum is 480 mN m⁻¹. The pore diameter is then obtained by substituting as follows:

$$d_p = \frac{1470 \text{ kPa } \mu\text{m}}{p_l} \quad (3.2.2-2)$$

In general, it can be said that pores in the range of a few nm to approx. 1100 μm can be analyzed using MIP. The material properties to be determined with this method also have a great influence on the physical properties of materials and their behaviour in certain environments. For example, the porosity influences the adsorption behaviour, permeability, strength or density of a material and is therefore one of the most important material parameters for the porous transport structures in PEMWE.

3.2.3 ICR - Interfacial Contact Resistance

The method for measuring the interfacial contact resistance (ICR) was adapted from PEM fuel cell (PEMFC) to PEMWE. The ohmic resistance of an electrolysis cell is one contributor to the overall cell performance as described in section 2.3. Accordingly, the aim is to keep the ICR of the respective materials as low as possible. In the case of new material developments, this

method is used to have comparative values to standard materials before the materials are tested in the cell. On the one hand, this could already give a first indication of the cell performance, but also a comparative value of the materials to be tested among each other.

For this purpose, the samples are placed between two pieces of carbon paper, as this has a very high electrical conductivity and is intended to simulate the interfacial contact with the catalyst materials used in the cell and adjacent to the samples. The structure can be seen in Figure 13. In general, the actual cell structure and the corresponding application area of the sample are simulated to measure the resistance, so that the result can be compared as accurately as possible with the conditions in the test cell. This sandwich is placed between two copper cylinders coated with gold, a constant current is applied while the compaction force on the measurement setup is gradually increased. By measuring the potential difference between the plate samples, the interfacial resistance, which depends on the compaction force, could be calculated according to the following equation:

$$R_C = R_{measured} - \sum R_{layer} \tag{3.2.3-1}$$

The ICR can be considerably reduced using precious metal coatings such as platinum.^{[126],[127]}

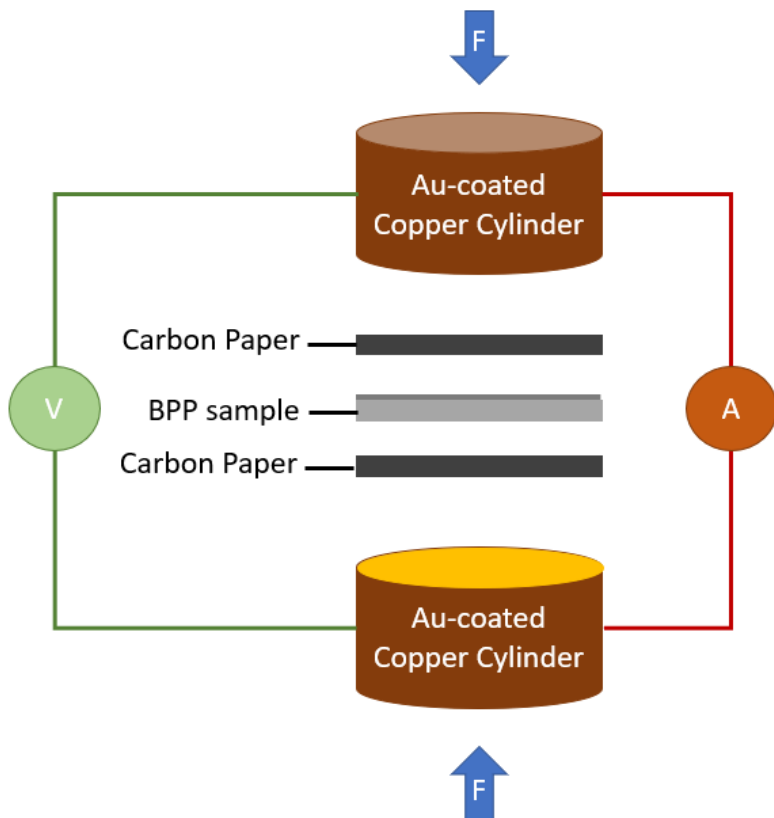


Figure 13: Interfacial Contact Resistance of a BPP sample

3.2.4 Electrochemical Characterization

For the electrochemical characterization of the PEMWE cells, polarization curves on the one hand and electrochemical impedance spectroscopy on the other hand were used. These enable the comparison of the cells with regard to their performance as well as the allocation of cell processes to ohmic losses, reaction kinetics and mass transport losses and their changes depending on stressors such as operating modes, water quality, current density, temperature or pressure.

3.2.4.1 Polarization Curve

A current- or voltage-controlled excitation of an electrochemical system leads to a reaction which is recorded in the form of a polarization curve, which is also known as j/E -characteristic. Either the voltage E [V] or the power density P_d [$W\ cm^{-2}$] is plotted against the current I [A] or the current density j [$A\ cm^{-2}$] of the cell or stack. If a constant current is used to excite the system, it is referred to galvanostatic mode, whereas a constant voltage is called potentiostatic mode. The performance of the tested cell or stack is measured from the lowest to the highest current density (ascending curve), followed by the measurement of the performance from the highest to the lowest current density (descending curve). Test protocols should start and end with a polarization curve to compare the performance at the beginning of the test (BoT) and at the end of the test (EoT) to assess degradation.

For characterization, the cells were saturated with water after assembly and brought to the appropriate operating temperature (65 – 90 °C). The test protocols harmonized by the JRC^[128] served as the basis for measuring the polarization curves. Polarization curves were recorded accordingly until the maximum operating current density was reached, i.e. galvanostatically conducted and up to $6\ A\ cm^{-2}$.

3.2.4.2 EIS - Electrochemical Impedance Spectroscopy

Electrochemical impedance spectroscopy (EIS) is based on transfer function and used to characterize electrical properties of materials, material interfaces for example with electronically conducting electrodes or electrode processes. At an interface, physical properties such as mechanical, compositional, and especially electrical properties change drastically, and polarizations (heterogeneous charge distributions) reduce the overall electrical conductivity of a system.^[129] As a non-destructive measurement, EIS provides e.g. information on both performance and cell degradation related to the individual cell components during operation by comparing the behaviour of the real system with an idealized model circuit which consists of electrical components. In this measurement method, a sinusoidal input signal in the form of an interfering AC signal is used as excitation for an electrochemical system over a frequency spectrum from high values in the kHz range to low mHz values. The electrochemical

system is operated under constant conditions. To obtain a linear behaviour of the system, the amplitude of the excitation must be sufficiently small. The characterization of the output signal of the linear system is then performed by changing the phase and amplitude.

Here, a distinction can be made between the galvanostatic and potentiostatic measurement method. In current-controlled (galvanostatic) measurement, the frequency dependence of the impedance Z of a cell is measured by applying an alternating current (AC) as a disturbance signal to the electrochemical system and measuring the response as an AC voltage. Conversely, in potentiostatic measurement, the frequency dependence of the impedance Z of a cell is measured by applying an AC voltage and simultaneously measuring the AC voltage response.

Such a system can be expressed with the following equations:

$$E(t) = E_A \cos(\omega t) \quad (3.2.4-1)$$

$$I(t) = I_A \cos(\omega t + \varphi) \quad (3.2.4-2)$$

With $E(t)$ as the potential at time t , $I(t)$ is the current at time t , E_A and I_A representing the amplitudes of the respective signals while ω and φ are given as the angular frequency and phase shift between the measured and the input signal, respectively. In the case where the excitation signal is the current and the response signal is the system voltage, the transfer function is the system impedance and can be represented as follows:

$$Z(\omega) = \frac{E(\omega)}{I(\omega)} = Z' - iZ'' = |Z| (\cos(\varphi) - i \sin(\varphi)) = \text{Re}(Z) - i \text{Im}(Z) \quad (3.2.4-1)$$

To represent the resistive contribution of an electrochemical system, a Nyquist plot is usually used in which the negative imaginary part $-Im(Z)$ is plotted as a function of the real part $Re(Z)$ as shown in Figure 14 a). Since ohmic resistors do not cause phase shift and voltage and current increase linearly, they are plotted on the x-axis, the real part. In contrast, capacitive and inductive components that cause a phase shift between the current and voltage curves are displayed on the y-axis, the imaginary part.

Therefore, the ohmic resistance is represented by the intersection of the first semi-circle in the high-frequency range with the x-axis. The high frequency arc represents the resistance induced by HER,^[130] charge transfer resistance coupled with double layer effects^[131] or the first charge transfer of the two-electron process of the OER.^[132] The charge transfer of the rate-determining step for the OER and mass transport losses are then assigned to the medium and low-frequency arc, respectively.^[133]

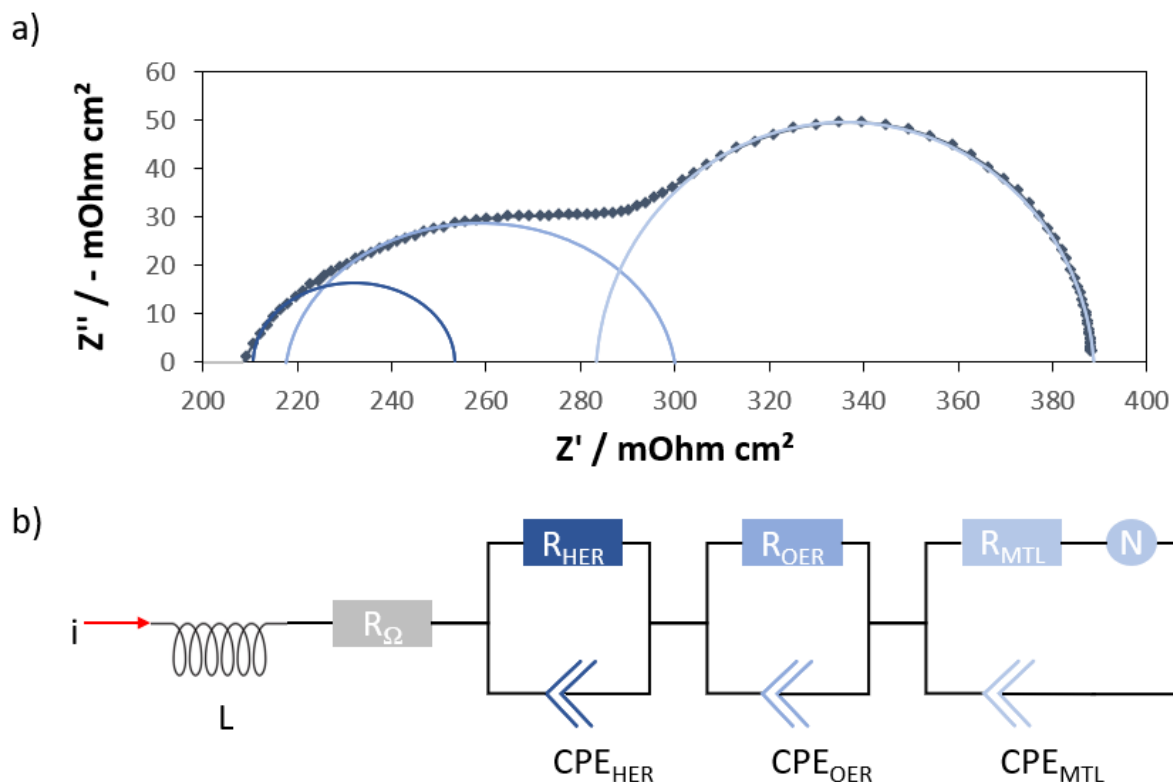


Figure 14: a) Nyquist plot of the EIS and the frequency-dependent assignment of the equivalent circuit diagram b) Electrical equivalent circuit diagram of the individual processes

A Randles circuit is often used as a basis, consisting of an electrolyte resistor R_S in series with the parallel combination of the double layer capacitance C_{dl} and charge transfer process with diffusion of the reactants. Since the Randles equivalent circuit is one of the simplest models to describe the processes at an electrochemical interface and in real electrochemical systems the impedance spectra are usually more complicated, the Randles equivalent circuit often has to be adapted. In Figure 14 b) a possible electrical equivalent circuit diagram is suggested. This equivalent circuit consists of a serial connection of the following elements: (i) an inductivity L for the cables in the setup, (ii) an ohmic resistance R_Ω mainly dominated by the electrolyte resistance (membrane), (iii) RC element (parallel element of an ohmic resistance R_{HER} and a capacitor CPE_{HER}) and (iv) RC element (parallel element of an ohmic resistance R_{OER} and a capacitor CPE_{OER}) for the polarization reaction, and (v) an RNC element for mass transport. Instead of ideal capacitors, a constant phase element (CPE) is used, which flattens the perfect semicircle, as the capacitance is often not ideal and the surface roughness influences the capacitive behavior.^[134]

3.2.5 Capital cost estimation for upscaling the developed materials

The future price development of CAPEX for PEM electrolysis is strongly related to the upscaling of the technology, which needs to be realized in a timely manner to implement the strategies to meet climate targets. This as well as the continuous development of the technology lead to the expectation of decreasing costs. This development could be observed in the past for PV technology, for example. Corresponding price development predictions were made here by determining so-called learning curves depending on the learning rate.^[135] This approach is also well known from other areas and has been applied to fuel cell systems.^{[136],[137],[138]} In this process, the price for a product is determined from the historical price development, which experience has shown to fall by a certain percentage with increasing installed capacity. This approach is due to Wright's Law^[139] and can be represented as follows:

$$C_P = C_R(1 - LR)^{\left(\frac{\ln X - \ln X_R}{\ln 2}\right)} \quad (4.1-1)$$

With the product price C_P at a given time with a cumulative production X , the initial product price C_R at a cumulative production X_R and the learning rate LR .

Furthermore, this approach was also investigated for electrolysis, where the manufacturing process is classified as both modular and standardizable. For simple repeatable processes, learning curves are classified in the range of 18 – 22 %^[140] where published empirical values for PEM electrolysis fit well with 13 – 18 %.^{[5],[118],[119],[141],[142],[143]} In determining these experience curves, the underlying assumptions such as reference prices for electrolysis or assumed growth in the market are important.^{[142],[144]} Looking at the CAPEX development of PEMWE over the last years shown in Figure 15, there is a 50 % cost reduction, which is in line with BloombergNEF's assessment.^[23]

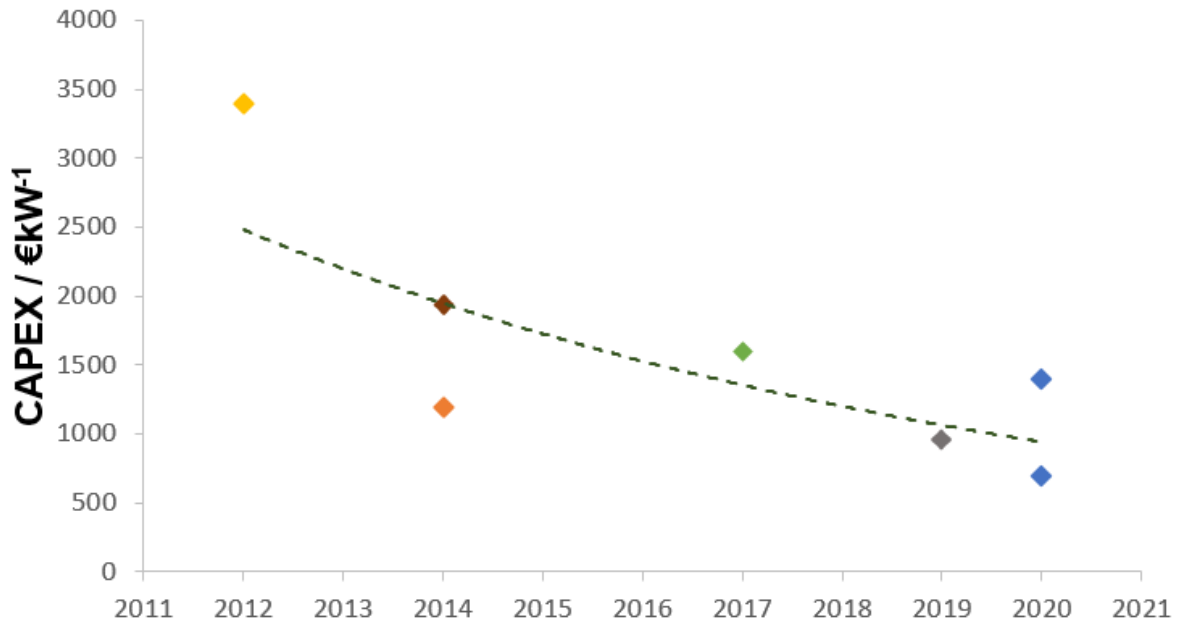


Figure 15. PEMWE cost development within the last ten years based on literature values [5],[9],[17],[145],[146]

In addition, there are several studies on the cost distribution of the PEMWE system and stack. Thereby, the stack costs are in the range of about 30 – 60 % proportionally to the system. [5],[141],[144],[147] The starting value for the cost calculation is the averaged values of the International Renewable Energy Agency study in terms of CAPEX with 1050 € kW⁻¹. According to the stack specifications for a 1 MW electrolyzer by Smolinka et al. the number of cells per stack as well as the active cell area were assumed to be 265 and 1000 cm², respectively. [145]

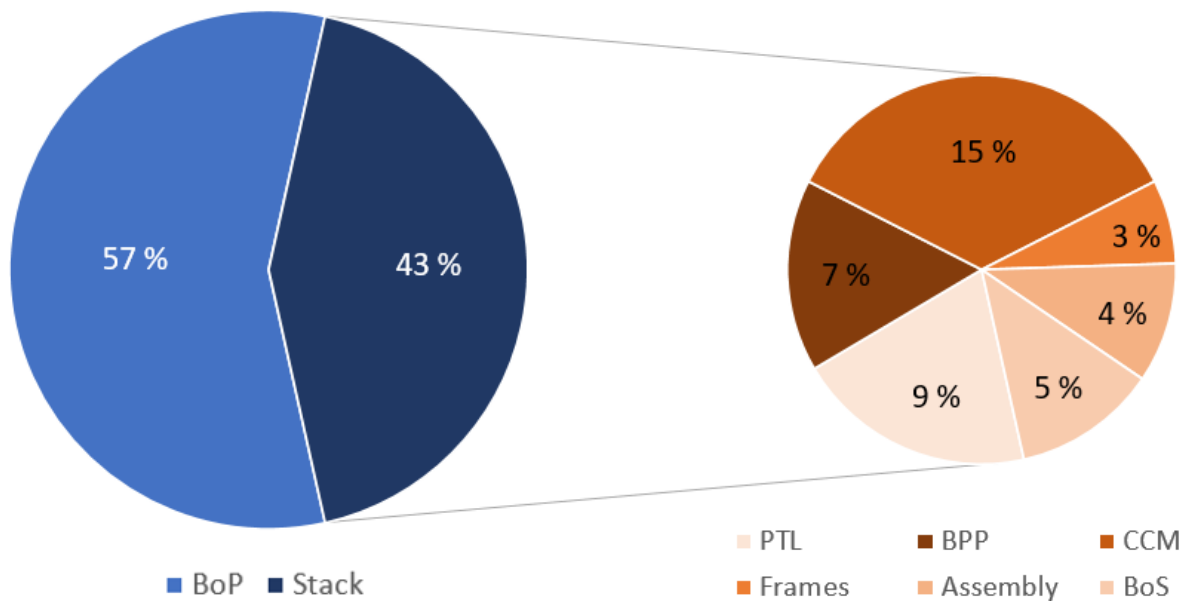


Figure 16. Cost breakdown of PEM electrolyzer based on Mayyas et al. [19].

Economies of scale in terms of plant size and in production have a significant impact on electrolyzer costs. Materials, but also energy, can be used more efficiently, for example

through material development or automation. Finally, design optimization also plays a role in reducing the cost of the technology. Since this approach of upscaling PEM electrolysis technology is an important part of achieving the planned electrolyzer capacity in Europe, the system or stack cost distribution from the study by Mayyas et al. is used.^[19] The authors have performed a bottom-up cost analysis for PEM electrolysis, focusing on manufacturing costs under the influence of increasing production rates. The determined cost distribution of the stack, shown in Figure 16 for a MW-scale plant, served as further baseline values for the cost estimation. Component costs were determined for the stack configurations studied in Articles I, II, and III, which are summarized in Table 6.

Table 6. Cell components developed within the scope of the present work that contribute to cost reduction in the respective stack configurations.

Parameter	Article I	Article II	Article III
BPP	Nb-coated stainless steel	Ti-coated stainless steel	Ti-coated stainless steel
PTL		Nb/Ti-coated stainless steel	Porous sintered layer on Ti-mesh

Coating costs were calculated by Gago et al. in a previous publication for BPPs of 1000 cm².^[60] For the calculation of PEMWE costs by scaling to 1 GW, the learning rates for the respective components according to Böhm et al. were used.^[141] For the CCM, this was further specified in the study and the learning rates for membrane and catalysts were broken down to 18 % and 8 %, respectively, which were assumed to be 11 % on average for this work, since the costs for the CCM are considered as a holistic component here. For the BoP, a value for the learning rate of 10 % was applied; all other components were assumed to have an average learning rate of 15 %.^[148]

To determine the annual OPEX depending on operating hours as well as specific electricity costs, the hydrogen production rate for a reference stack and the stacks corresponding to the articles on which this work is based were calculated as follows:

$$f_{H_2} = \eta_F \frac{n_{cell} a_{cell} i}{zF} \frac{22.41}{1000} 3600 \quad (4.1-2)$$

where η_F is the Faraday efficiency, n_{cell} the number of cells assembled to the stack, j the current density and a_{cell} the active cell area.

Since the reduction of green hydrogen production costs is considered a key factor for further commercialization and upscaling of the technology, these were calculated as a function of

operating hours for the respective stack configurations and plant sizes. The hydrogen production costs C_{H_2} could be presented as follows:

$$C_{H_2} = \frac{LHV}{\eta_{ges}} \left(\left(\frac{i(1+i/100)^n}{(1+i/100)^n - 1} + C_{M/O} \right) \frac{CAPEX}{t_o} + P_E \right) \quad (4.1-3)$$

with the lower heating value of hydrogen LHV , nominal system efficiency η_{ges} , rate of interest i , depreciation period n , maintenance and operating cost $C_{M/O}$, specific investment costs $CAPEX$, annual full load hours t_o and specific electricity price P_E .

Table 7 summarizes the assumptions made for the calculations, while the blue CAPEX values represent the calculated costs for a 1 MW electrolyzer with an Article II or III stack configuration. Since a coated stainless steel bipolar plate is also the basis for Articles II and III, no separate costing was done for Article I, which would only look at BPP. Nevertheless, to determine the cost savings of using stainless steel for the bipolar plates, the component costs were determined using titanium as the base material.

Table 7. Assumptions for estimating CAPEX as well as hydrogen production costs.

Parameter	2020	Article II		Article III	
Rated stack power / MW ^[145]		1			
Cell area / cm ² ^[145]		1000			
Cells per stack ^[145]		265			
Current density / A cm ⁻²	2	2	4	2	4
Cell voltage / V	1.90	1.70	1.90	1.85	2.20
Faraday efficiency / %		99			
CAPEX / € kW ⁻¹ ^[5]	1050	1001		1012	
Coating Costs VPS (PTL, BPP) / € kW ⁻¹ based on ^[60]		0.83		0.83	
LR for BoP / %		10			
LR for PTL / %		18			
LR for BPP / %		18			
LR for CCM / %		(avg.) 11			
LR for Frames / %		15			
LR for Assembly / %		8			
LR for BoS / %		15			
Rate of interest / % ^[149]		5			
Depreciation period / a		20			
Maintenance and operating cost / % CAPEX a ⁻¹ ^[149]		3.3			
Specific electricity price / € kWh ⁻¹		0.06			

In order to have a comparable starting point for all new developments, titanium-based components are taken as the basis. For Article I, the BPP can be optimized in terms of cost in that the flow-field structure is no longer required and one processing step, namely the embossing of this channel structure, is eliminated and the coating itself consists of less expensive non-precious metals Ti or Nb. In Article II, the costs optimized by Article I are further reduced by the use of stainless steel as the base material for the PTL as well as the non-precious metal coating and the scaling effect. Article III also uses the low-cost stainless steel BPP already described for Article I and II. The titanium based PTL developed here does not require further coating, eliminating this step in the fabrication process.

The stack configurations from Articles II and III were used to calculate the hydrogen production costs. Comparing the performance of the cells at the same operating conditions and the same membrane (Nafion115), the PTL from Article III confirms a performance advantage of 3 % when operating at high current density of 4 A cm^{-2} compared to the PTL from Article II. As a further development step towards the next generation of PEM electrolyzers, the stainless steel based PTL from Article II was characterized at $80 \text{ }^\circ\text{C}$ and with a CCM based on a thin Nafion212 membrane. This shows a further 9 % increase in efficiency at 4 A cm^{-2} , which was investigated as the future nominal operating point. Accordingly, the performances of these two stack configurations served as the basis of the overall efficiency analysis of the PEMWE system used in the calculation of the hydrogen production costs. The data were compared at a standard operating current density of 2 A cm^{-2} or operation at high current densities of 4 A cm^{-2} as shown in Figure 17 and presented as data η and j , respectively.

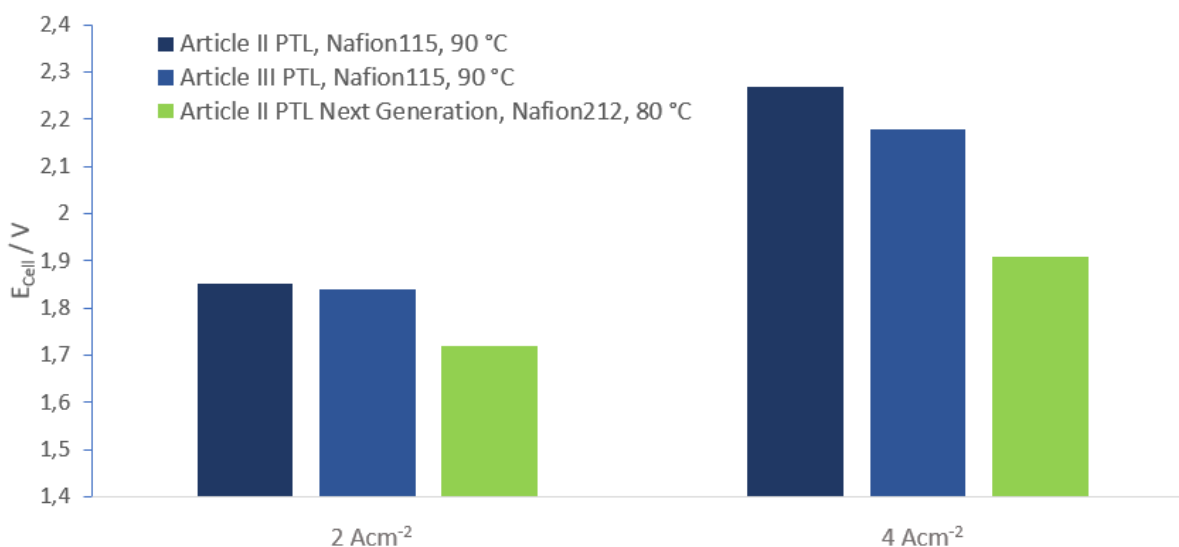


Figure 17. Performance comparison of PTLs developed in Articles II and III. For comparability of the PTL developments, both components were tested at $90 \text{ }^\circ\text{C}$ and a Nafion115-based CCM was used.

In conclusion, the scaling of the PEM electrolysis system as well as the operation of the component at extreme conditions influences the cost.

4. Discussion

4.1 Discussion of the Results

In its 2020 cost analysis, the International Renewable Energy Agency highlights the savings potential for green hydrogen production and identifies medium potential for coating materials (Ir, Pt) and BPP and the highest potential for BoP components (power supply, pumps, H₂ processing, cooling), manufacturing, membrane and PTLs.^[5] They saw a major challenge in the production of Ti-free PTLs as well as precious metal-free protective coatings for these structures. Furthermore, their realization was rated with a very large benefit in terms of cost reduction and thus for the competitiveness of green hydrogen compared to fossil fuels.

Nevertheless, the aforementioned measures only have an influence on the investment costs of a plant; the operating costs are not considered. In principle, both CAPEX and OPEX are cost drivers for PEMWE, but their impact varies depending on region, country, electrolysis technology or mode of operation.^[148]

Therefore, in this cumulative dissertation, two main approaches to cost reduction were investigated. Articles I and II deal with the replacement of Ti with low-cost materials such as stainless steel protected from corrosion by non-precious metal coatings for the BPPs and PTLs. The previous developments by Gago et al.^[60] and Lettenmeier et al.^{[61],[62]} have shown so far that it is possible to use stainless steel as the base material for BPP fabrication. To prove the material durability a 14,000 h PEMWE test was performed in this work. Besides the flat stainless steel anode BPPs with dense Nb and Nb/Ti coatings applied by VPS and PVD, a baseline material from Nel Hydrogen was tested comparatively while on the cathode side uncoated stainless steel BPPs also without flow-field structure were used. All cells showed comparable performance at 1.9 V at 1 A cm⁻², which can also be expressed as a cell efficiency of nearly 78 % while the cell degradation rate was only 5.5 μV h⁻¹ over the entire operating period. The post-test analysis demonstrated that the applied non-precious metal coatings provided complete protection against corrosion in the aggressive PEMWE environment over such a long period. If a value of 2.2 V is assumed as the end-of-life cell voltage, the stack could be operated for approx. 57,000 h and thus represent a stack lifetime relevant for industry and market requirements. However, from a cost perspective, the pure Nb coating would be preferable, as it can be produced in only one process step. This long-term test showed that a coating of the stainless steel BPP is not necessary on the cathode side and that this also contributes to cost reduction. These investigations are described in detail in Article I.

A far more difficult challenge is to manufacture PTLs from stainless steel for use in PEMWE. There have been attempts in the literature, but so far no one has been able to achieve comparable performance to the state of art titanium PTL. Article II describes the approach of

applying a developed coating of titanium and niobium to commercially available stainless steel multi-layered meshes. Preliminary physical testing of the material with regard to its quality and suitability for PEMWE use was promising, so that the samples were also electrochemically characterized and investigated. Furthermore, an AST of more than 1000 h was conducted with the PEMWE cell for durability test. Post-test physical analyses revealed full protection of the stainless steel PTL against corrosion by Nb/Ti coating. The results showed that the Nb/Ti coating on stainless steel PTL reduced the cell overpotential by more than 300 mV at 2 A cm^{-2} , resulting in an efficiency increase of 12 %. As the EIS measurements confirmed, these positive effects were more evident at current densities above 0.25 A cm^{-2} due to the following:

- (i) a reduction in the ohmic resistance, which is caused by gas formation at the interface with the anode
- (ii) an improved utilization of the anode catalyst resulting in enhanced OER kinetics
- (iii) a reduction in mass transport losses.

To further understand the observed phenomena, pore network modelling showed that the advantage of the Nb/Ti coating was explicitly due to the preferred transport of water and gas to and from the active surfaces of the anode. Moreover, to reduce the cost of green hydrogen, future PEMWE will have to operate at much higher current densities than 2 A cm^{-2} , e.g. 4 A cm^{-2} as nominal load and 6 A cm^{-2} as overload, with efficiency above 70 %. Accordingly, the PEMWE cell was tested with coated stainless steel PTL and was able to achieve an unprecedented 77 % efficiency at 4 A cm^{-2} and $80 \text{ }^\circ\text{C}$. This performance of the PEMWE cell with stainless steel components is comparable to the highest performances reported so far by renowned research and development institutes in the field of electrolysis.

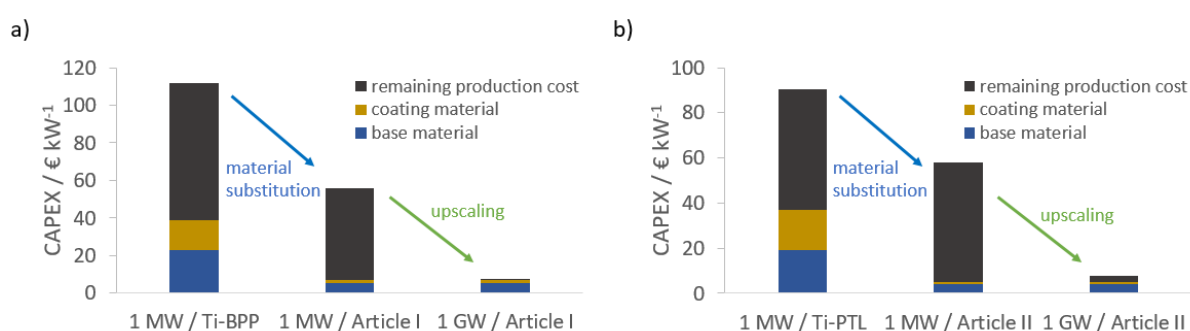


Figure 18. Potential cost savings compared to titanium based components with Au or Pt coating of a) stainless steel based Article I component (BPP) with respect to system upscaling and b) stainless steel based Article II component (PTL) with respect to system upscaling.

If the cost reduction potential from the component developments of Article I and II, i.e. the substitution of titanium by stainless steel for the BPP and PTL, is also considered like an upscaling from MW- to GW-scale, there are overall savings of more than 80 %. For comparability of the reduction potentials, coated titanium components were assumed as the

basis in each case. For the comparison of the stainless steel based BPP from Article I, the cost distribution of the component according to Mayyas et al.^[19] was calculated back to titanium as the base material. Figure 18 a) and b) show that around 40 % of the BPP and PTL costs are attributable to the material, while the remainder is accounted for by energy, manufacturing, waste and equipment costs. Although material substitution reduces material costs, the remaining costs for manufacturing remain the same and thus increase proportionally to the component to almost 90 % for the MW range. Economies of scale, depreciation of equipment for manufacturing, and more efficient processes can reduce these costs by more than 90 % and 60 % for the manufacture of BPP and PTL, respectively, when increasing annual production rates to the GW range, resulting in a price of 7.64 and 7.94 € kW⁻¹, respectively. It becomes clear that in the GW-scale, material costs are the predominant factor on total component costs, which is in line with the findings of Mayyas et al.^[19] Accordingly, the relevance of the lower material costs of stainless steel compared with titanium is particularly evident from the GW scale upward.

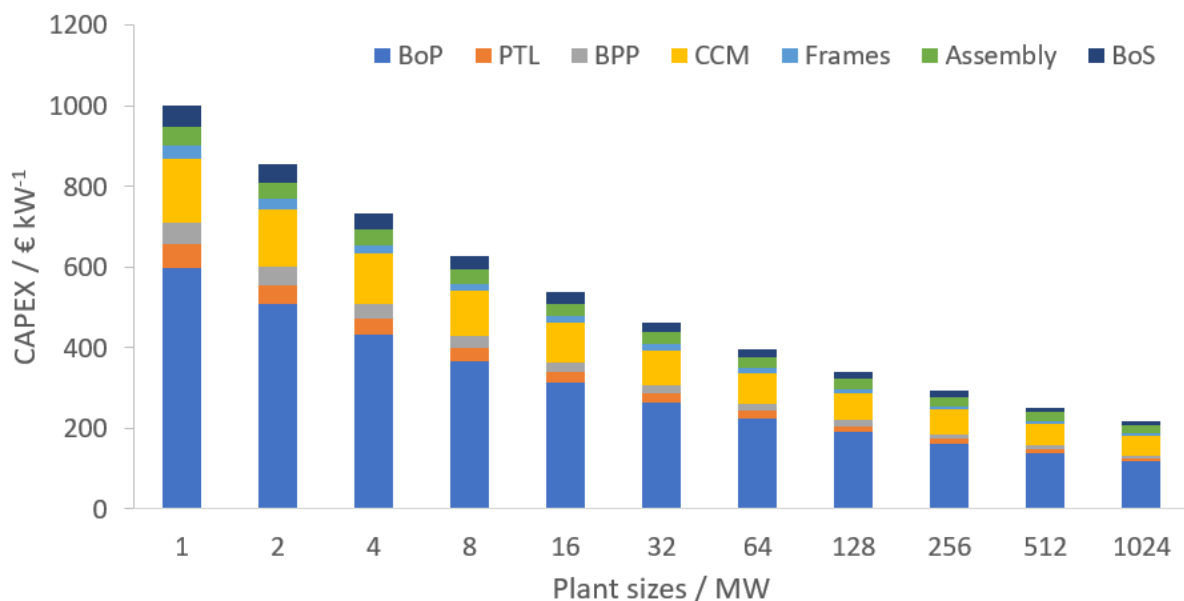


Figure 19. CAPEX development of Article II stack configuration depending on plant size

Using the example of the stack configuration examined in Article II based on a stack made almost entirely of stainless steel, Figure 19 shows the cost development of the stack components as a function of the annual production rate. The assumed learning rates allow costs to be saved in all areas, but of course considering the material developments carried out in this work, especially in the area of BPP and PTL. As shown in Figure 20, their shares in the stack can thus be reduced to 2 and 3 %, respectively. The CCM continues to account for the largest share of costs in the stack, at 15 %. Since this was not the focus of the work, this component was considered with a relatively conservative learning rate, since otherwise a further subdivision into membrane and the respective catalyst layers would have been

necessary. Predictions regarding future development progress are difficult, but currently there are already catalysts with reduced PGM loadings, especially on the cathode side. In the future, the aim will be to reduce these further, especially on the anode side, or even to develop PGM-free catalysts and thus further reduce the costs of PEM electrolysis technology. Summarizing the developments in material substitution and considering the stack cost distribution of a stack based on stainless steel components, the cost shares of the system shift further to the detriment of the BoP at almost 70 % due to the cost reduction in the stack components as shown in Figure 20.

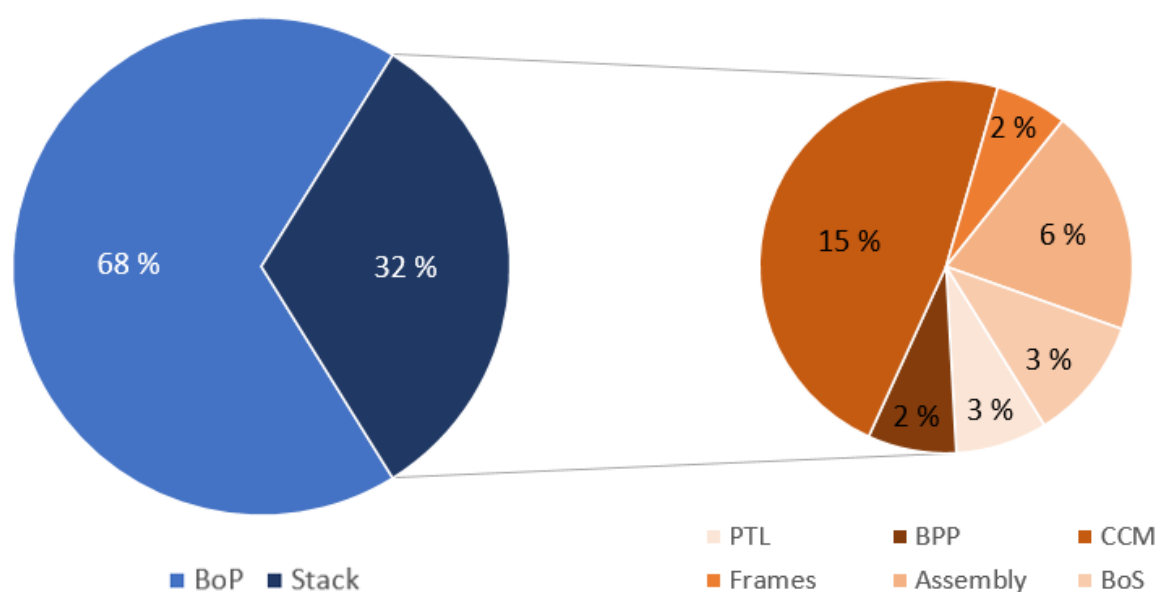


Figure 20. Updated Cost breakdown of PEM electrolyzer made almost entirely from stainless steel components

Article III addresses the second approach to reduce cost by optimized Ti-based PTLs with which higher cell efficiency can be achieved by operating them under extreme conditions (current density, temperature, pressure) and thus increasing the H₂ production rate. Therefore, a macro-porous sintered structure of Ti was deposited on a Ti expanded metal by diffusion bonding. This Ti-based PTL exhibits improved properties and is optimized in terms of its pore characteristics, allowing operation up to 6 A cm⁻², 90 °C and 90 bar H₂ outlet pressure. Investigations via pore network modeling have shown that the cell performance achieved could be attributed to the high permeability for both liquid and gas phases, allowing effective two-phase transport to be realized at these high current densities. Thus, a performance of 2.53 V at a maximum current density of 6 A cm⁻² and 2.19 V at a current density of 4 A cm⁻² could be achieved, respectively. Thinking about new standard operating conditions, the nominal current density can be set at 4 A cm⁻², at which an efficiency increase of almost 25 % could be achieved compared to the reference material in the tests performed. This has a direct impact on the operating costs, which can be reduced accordingly. Conversely, if the measured cell performance is compared with the current standard of approx. 2 V at 2 A cm⁻² twice as much

hydrogen can be produced at almost the same voltage. The operating temperatures of the SoA, however, are in the range of 60 – 80 °C. For illustration, the hydrogen production costs were calculated as a function of the operating hours and shown in Figure 21.

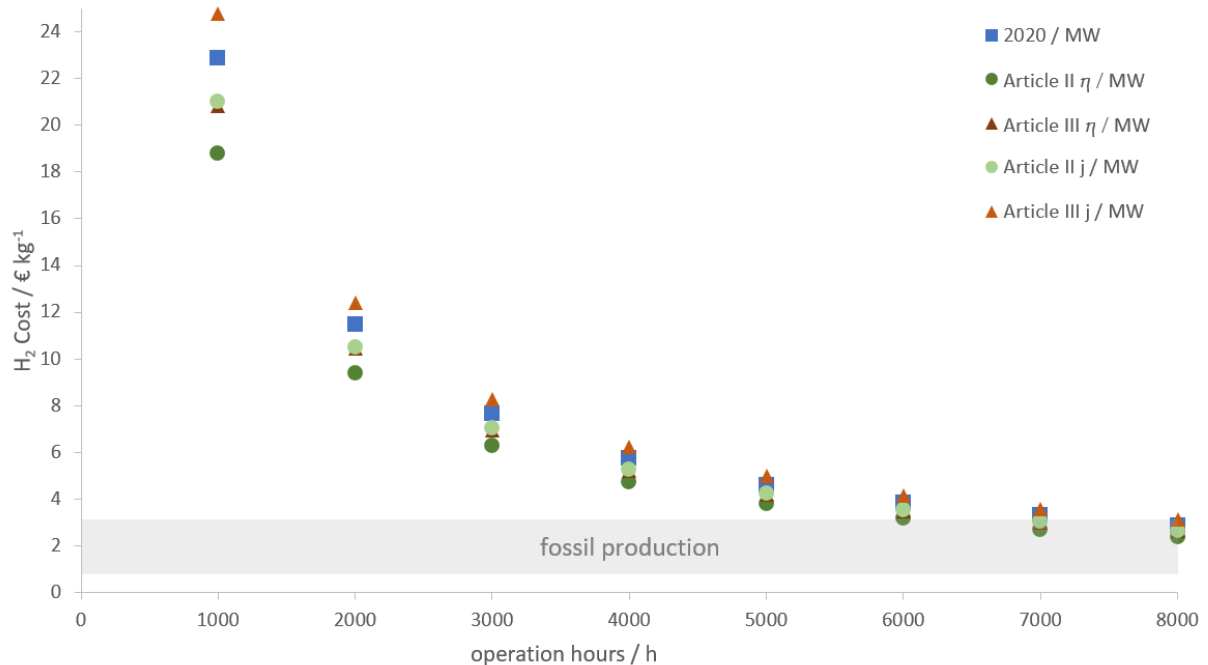


Figure 21. Hydrogen production cost of PEM electrolyzer stacks using the PTLs developed within Articles II and III compared to a SoA reference stack in 2020 based on an electricity price of 0.06 € kWh⁻¹.

As the number of operating hours increases, the differences between the scenarios considered diminish. Electrolysers are currently operated at 2 A cm⁻² by default, which will be considered comparatively for the components developed in Articles II and III. Since this implies an operating point with voltage efficiencies higher than 80 % for the new components, this is defined as an efficiency-oriented operating point. Operation at high current densities of 4 A cm⁻² is therefore defined as a current density oriented operating point. Compared to the 2020 reference scenario, the studied stacks from Articles II and III seem to differ only marginally in their CAPEX in component costs and, accordingly, in total plant costs, with about 5 and 4 %, respectively. Nevertheless, this has an impact on the hydrogen production costs at low operating hours. This 1 % CAPEX difference can be calculated in 2 € per kg hydrogen difference at 1000 h operation. The more operating hours, the more the hydrogen production costs become OPEX dominated.^[145] Already from 6000 operating hours one comes close to the costs of fossil produced hydrogen or from 7000 h hydrogen can be produced competitively. Assuming a maximum operating time of 8000 h, the costs for hydrogen are 2.63 and 2.37 € kg⁻¹ for the stack configurations with titanium- and stainless steel-based PTL, respectively. Calculating the price difference to SoA, 0.26 and 0.52 € kg⁻¹ can be saved by using the PTLs developed in Article III and II, respectively. For a hydrogen demand of 90 TWh in 2030,^[150] the

example of the stack configuration with titanium based PTL from Article III can already save around 700 million Euro.

In summary, there is an urgent need to reduce the cost of large PEMWE cells. By developing a non-precious metal coating of Nb/Ti and applying it to the lowest cost structure that can be used as a PTL in PEMWE, namely a stainless steel mesh, in combination with a stainless steel based BPP, an unprecedented cost reduction can be achieved. The presented results suggest that a promising option has been presented here to replace Ti as the base material for fabricating expensive porous structures for PTLs; low-cost stainless steel mesh can be used instead. In addition, stainless steel meshes with different aperture sizes allow the use of flat plates as BPPs, which can also be fabricated from stainless steel, without a flow field. Thus, the cost of a PEMWE cell could be drastically reduced as it is almost entirely made of stainless steel, which can potentially establish this technology as a competitive solution for renewable green hydrogen production. While the PTL cost can be reduced by 88 % to about 8 € kW⁻¹ for the coated stainless steel component, the BPP cost also decreased by about 90 %. Compared to the literature^[19], this corresponds to a reduction of PTL costs in the GW range by another 68 % and is below the medium-term estimated reduction potential for the component.

4.2 Overall Context

Thanks to intensive research and development work to optimize electrolyzer technology, the share of production costs that limits the introduction of green hydrogen is decreasing. In addition to these, however, the electricity costs for operating the electrolyzers represent a significant cost factor. Although these have decreased in the past, mainly due to declining electricity costs for renewable energy, green hydrogen at medium operating hours is currently still about twice as expensive as hydrogen produced from fossil fuels. This makes it clear that electricity costs must also be developed at lower prices to make green hydrogen competitive. For various reasons, however, there is currently no relief in sight on the electricity market. On the one hand, the constantly growing demand for energy and also the demand from the various sectors, such as individual households, but also from industry for green electricity is immense and growing. The energy transition itself brings costs - among others, the expansion of new renewable energy plants, the infrastructure development for the distribution of generated electricity and also the development of storage facilities. Renewable energy technologies must compete with the high efficiencies of highly controllable coal-fired power plants. Although the Ukraine conflict seems to provide further arguments for the energy transition and to give a boost to research and development topics in this regard, their expansion is inhibited due to rising prices for materials and energy. This makes it clearer that market deployment requires incentive systems, which can be in the form of subsidies or credits.

From the cost calculation carried out, it became apparent that a significant cost factor lies in the production and manufacturing costs of the components, which are strongly dependent on the installed electrolysis capacity. Therefore, manufacturers must specialize as suppliers for the production of electrolyser components in order to ensure cost-effective production and thus keep component costs low.

In this respect, the optimizations achieved in Articles I and II are an essential key to realizing the introduction of cost-efficient components even faster. This is due to the use of more readily available, machinable material, stainless steel, which is already common and well-known in the industry. This can sometimes increase the pool of suppliers and involve companies specializing not only in the machining and processing of titanium in this restructuring.

It is known that the longer electrolysis systems are operated, the more total costs are dominated by their operation, i.e. OPEX.^[145] If materials can be produced at low cost, the efficiency improvement approach remains to reduce the hydrogen production cost. The efficiencies achieved in Article III can reduce the second significant variable in hydrogen production costs, which is electricity consumption or cost.

5. Conclusion

5.1 General Conclusion

This cumulative PhD thesis addresses one of the most important topics in electrolysis technology, namely, cost savings in both CAPEX and OPEX for an electrolyzer and its operation based on performance increase due to component development. The suitability of stainless steel components for both the bipolar plates (BPP) and porous transport layers (PTL) to replace titanium was investigated in cell tests. Another approach focused on the operation of the electrolyzer under extreme conditions such as high current densities, temperature and pressure to increase efficiency.

Article I on the long-term testing of coated stainless steel bipolar plates is the starting point of this work. With a total operating time of 14,000 h, the test is the longest tests carried out to date by academia in which stainless steel-based components were measured together with standard materials from an electrolyzer manufacturer and examined afterwards. It was interesting to note that the cells with the respective components showed comparable performance. Losses were also acceptable and similar for all cells, including those found in the literature for equivalent long-term tests but with standard materials. The predicted lifetime of the components is promising and suggests applicability in commercial systems.

A much greater challenge is posed by material substitution in PTL, which, as far as is known from the literature, has not been able to achieve comparable performance to that of the state of art material titanium in the past. Article II describes a solution by developing a coating of titanium and niobium and applying it to commercially available multi-layered stainless steel meshes. The material stability could be confirmed and it is interesting how clearly the optimized structure of the PTL affects the cell performance. Improved transport properties, increased catalyst utilization or reduced ohmic resistance can be mentioned as reasons and thus also enable operation at high current densities, while unprecedented efficiencies could be achieved. This represents a significant development step and provides the basis for further testing.

Finally, Article III presents a PTL for operation under extreme conditions such as high current densities, temperature, and pressure. This is based on a porous sintered titanium structure on a single-layer titanium mesh which, thanks to its effective two-phase transport, does not experience mass transport limitation even at high current densities and thus exhibits high performance. These, as well as the development towards high temperatures and pressures, will be standard operating parameters in the future from an economic point of view. The material thus offers the best prerequisites for use here and contributes to cost reduction.

In summary, there is a serious demand to reduce the cost of large PEMWE cells. By developing a non-precious metal coating and applying it to the most cost-effective structure that can be

used as a PTL in PEMWE, namely a stainless steel mesh, in combination with a stainless steel based BPP, a remarkable cost reduction has been achieved here. The presented results suggest that titanium can be replaced as a base material for fabricating expensive porous structures for PTLs; instead, low-cost stainless steel meshes can be used. In addition, stainless steel meshes with different aperture sizes enable utilization of BPP without flow field structure, which can also be fabricated in stainless steel. Thus, the cost of a PEMWE cell has, in principle, been reduced drastically by being made almost completely of stainless steel, thus establishing this technology as the most promising solution for green hydrogen production. In addition, this thesis can serve as a basis for establishing new standard operating conditions that require a smaller active area for hydrogen production by increasing efficiency, thus conserving materials and resources.

6. General Outlook

Although research in the field of PEMWE has increased significantly in recent years, the field still offers many open questions that need to be answered. This dissertation was able to clarify some important questions, but also opens new tasks.

The durability of the stainless steel based BPPs was clarified with the 14,000 h test. A comparable test of the stainless steel based PTLs using a stack size relevant for the industry is the next step on the way to commercialization of the component and a stainless steel based stack. Likewise, the components must be able to withstand the new standard operating conditions proposed in this work, which means operating the electrolyzer at high current densities up to 6 A cm^{-2} , temperatures up to $90 \text{ }^\circ\text{C}$ and pressures up to 100 bar.

On the part of PTL material optimization from a cost perspective, stainless steel expanded metals could be considered as substrate materials for porous sintered structures. As seen in Article III, these ensure sufficient distribution and transport of the media even at high current densities and can also be made of stainless steel. The construction of multilayer mesh structures does not appear to be necessarily required. For the manufacturer, this involves a great deal of effort to maintain the specified tolerances of the respective layers, as well as the accuracy of the spot welding of the grids, and thus makes the component more expensive.

Spherical particles were used for the coatings. They are produced by melting and injecting the material in question into a chamber filled with argon, in which a slight vacuum is maintained. As it falls, the material cools in the form of spherical balls. Non-spherical coating powders could be used instead, which are potentially not only cheaper to produce but also have a higher particle surface area. If these are then not completely melted in the VPS process as described, the surface area of the coatings produced also remains increased. This would mean a larger contact area with the adjacent cell component, the CCM, reducing ohmic resistances and allowing more active area to be used for the actual reaction. This approach would need to be evaluated in continuing work.

The coating method is another point of potential optimization. Instead of a VPS coating, the coating can also be carried out at ambient pressure using ambient pressure spraying (APS). Unchanged, of course, are the labor costs, while compared to VPS, both machining and other operating costs are reduced. Likewise, the investment costs of the APS are only 17 % of those of VPS, which means that a cost reduction from VPS to APS can be estimated at over 50 %. Instead of a thermal process for material bonding between the substrate and the porous layer, a batching process could also be considered.

In addition, the results suggested that thanks to the properties of the applied porous coating and closure of the grid holes, the deformation of the membrane is lower, but also the catalyst utilization seems to be increased. This would suggest that either high hydrogen production rates can be achieved from the high cell performance shown, or a reduction in the Ir content of the anode catalyst can be considered. Both would lead to further cost reduction. The reduction of Ir will be of particular interest here, as it may be the "bottleneck" for the technology due to the materials low market availability, few suppliers, and low occurrence in the Earth's crust. In fact, further tests would have to validate to what extent the precious metal content can be reduced without degrading the cell performance too much and to be able to produce competitive hydrogen accordingly.

Furthermore, the production of cost estimates for electrolyzers is limited. There are several challenges here, because in addition to the limited availability of data, its confidentiality often poses a problem in determining parameters and costs. In addition, cost analyses often vary in scope, i.e., cell, stack, or even system level is considered. Electrolyzers, their technology and production have only recently started to boom, which could be another reason why there are often no suppliers who have already specialized in this area. Standard dimensions do not exist and therefore the desired high material yield is not achieved yet. However, due to the great interest, also from the political side, suppliers will soon open up to the market and be able to offer more specific products.

Possibly the research results obtained could not only mark a turning point for future electrolysis research, where stack components based on stainless steel are considered as the new standard, but also lay the foundation for massive cost reduction in PEMWE and thus an essential factor for the production of competitive green hydrogen. Manufacturers of electrolyzers or stack components may consider stainless steel and reengineer their commercial products with a view to using it for PEMWE. This successful development is expected to be one of the most important breakthroughs in PEMWE technology in years.

Nevertheless, it is far from solving all the challenges that need to be overcome on the way to competitive green hydrogen production by PEMWE. A PEM electrolyzer, which consists almost entirely of stainless steel components, must be tested for durability in a long-term test and under extreme operating conditions. An analytical method originating from the PEM fuel cell, electrochemical noise, an in-situ analysis for monitoring various electrochemical processes, could be transferred to PEMWE and used to monitor cell corrosion. This may remove any final doubts about the applicability of stainless steel for PEMWE in the community. Further material alternatives to non-precious PTL coatings such as molybdenum, vanadium or tantalum should be sought and investigated for their suitability for the technology.

The operating parameters achieved and investigated are extreme from the current point of view, but these will certainly represent the standard in the future. Based on the cell performance achieved, the materials presented have not yet reached the end of their capabilities and could still be exhausted in this respect. However, the ever higher current densities and stack sizes have disadvantages in terms of analysis. The equipment for analysis, for example EIS, must be adapted so that the limitations of the cells can be investigated further.

Ultimately, the research results have made it possible to take a significant step towards establishing green hydrogen by electrolysis and, in all probability, to accelerate its economic viability. There is still a lot of potential to reduce CO₂ emissions by using environmentally friendly technologies and to still achieve the Paris Agreement of a temperature target of 1.5 °C. In addition, it is becoming increasingly important to conserve limited resources and to use materials that are less limited in their availability - such as stainless steel - and to minimize plant losses through high efficiencies.

7. Bibliography

- [1] IEA, Global Energy Review: CO₂ Emissions in 2021, IEA, Paris, <https://iea.blob.core.windows.net/assets/c3086240-732b-4f6a-89d7-db01be018f5e/GlobalEnergyReviewCO2Emissionsin2021.pdf>, accessed: May 2022.
- [2] D. R. Baker, S. Stapczynski, D. Murtaugh and R. Morison, Bloomberg, Global Energy Crisis is the First of Many in the Clean-Power Era, <https://www.bloomberg.com/news/articles/2021-10-05/global-energy-crisis-is-the-first-of-many-in-the-clean-power-era>, accessed: May 2022.
- [3] EEA, EEA greenhouse gases – data viewer, EEA, Copenhagen, <https://www.eea.europa.eu/data-and-maps/data/data-viewers/greenhouse-gases-viewer>, accessed: January 2022.
- [4] IRENA, Green Hydrogen for Industry – A guide to policy making, International Renewable Energy Agency (IRENA), Abu Dhabi, <https://irena.org/publications/2022/Mar/Green-Hydrogen-for-Industry>, accessed: May 2022.
- [5] IRENA, Green Hydrogen Cost Reduction – Scaling up electrolyzers to meet the 1.5 °C climate goal, International Renewable Energy Agency (IRENA), Abu Dhabi, <https://irena.org/publications/2020/Dec/Green-hydrogen-cost-reduction>, accessed: February 2021.
- [6] Hydrogen Europe, Hydrogen Production, <https://hydrogeneurope.eu/hydrogen-production-0>, accessed: February 2021.
- [7] D. Bessarabov, P. Millet, PEM Water Electrolysis (Volume 1), Hydrogen and Fuel Cells Primer Series, Academic Press 2018.
- [8] M. Carmo, D. L. Fritz, J. Mergel, D. Stolten, A comprehensive review on PEM water electrolysis. *Int. J. Hydrogen Energy*, **38**, 4901 – 4934 (2013). <https://doi.org/10.1016/j.ijhydene.2013.01.151>.
- [9] A. Buttler, H. Spliethoff, Current status of water electrolysis for energy storage, grid balancing and sector coupling via power-to-gas and power-to-liquids: A review. *Renew. Sust. Energy Rev.*, **82**, 2440 – 2454 (2018). <https://doi.org/10.1016/j.rser.2017.09.003>.

- [10] S. S. Kumar, V. Himabindu, Hydrogen production by PEM water electrolysis – A review. *Materials Science Ener. Techn.*, **2**, 442 – 454 (2019). <https://doi.org/10.1016/j.mset.2019.03.002>.
- [11] A. Nechache, S. Hody, Alternative and innovative solid oxide electrolysis cell materials: A short review. *Renew. Sust. Energy Rev.*, **149**, 111322 (2021).
- [12] European Commission (2021), Communication from the commission to the European Parliament, the Council, the European Economic and Social Committee and the Committee of the Regions – ‘Fit for 55’: delivering the EU’s 2030 Climate Target on the way to climate neutrality, Brussels, <https://eur-lex.europa.eu/legal-content/EN/TXT/PDF/?uri=CELEX:52021DC0550&from=EN>, accessed: August 2021.
- [13] Energy Factsheet, https://ec.europa.eu/commission/presscorner/detail/en/fs_21_3672, accessed: August 2021.
- [14] Hydrogen Factsheet, https://ec.europa.eu/commission/presscorner/detail/en/fs_21_3676, accessed: August 2021.
- [15] A. Van Wijk, J. Chatzimarkakis, Green Hydrogen for a European Green Deal – A 2x40 GW Initiative. *Hydrogen Europe*, (2020), https://hydrogeneurope.eu/sites/default/files/Hydrogen%20Europe_2x40%20GW%20Green%20H2%20Initiative%20Paper.pdf, accessed: July 2020.
- [16] FCH-JU, Addendum to the Multi-Annual Work Plan 2014-2020, Fuel Cells and Hydrogen 2 Joint Undertaking 2018.
- [17] L. Bertuccioli, A. Chan, D. Hart, F. Lehner, B. Madden, E. Standen, Development of Water Electrolysis in the European Union. *Fuel Cells and Hydrogen Joint Undertaking* (2014).
- [18] K. E. Ayers, N. Danilovic, R. Ouimet, M. Carmo, B. Pivovar, M. Bornstein, Perspectives on Low-Temperature Electrolysis and Potential for Renewable Hydrogen at Scale. *Annual Review Chem. Biomol. Eng.*, **10**, 219 – 239 (2019).

- [19] A. Mayyas, M. Ruth, B. Pivovar, G. Bender, K. Wipke, Manufacturing Cost Analysis for Proton Exchange Membrane Water Electrolyzers. National Renewable Energy Laboratory, Golden (CO). NREL/TP-6A20-72740, (2018). <https://doi.org/10.2172/1557965>.
- [20] U. Babic, M. Suermann, F. N. Büchi, L. Gubler, T. J. Schmidt, Review – Identifying Critical Gaps for Polymer Electrolyte Water Electrolysis Development. *J. Electrochem. Soc.*, **164** (4), F387 - F399 (2017). <https://doi.org/10.1149/2.1441704jes>.
- [21] K. Bareiß, C. de la Rua, M. Möckl, T. Hamacher, Life cycle assessment of hydrogen from proton exchange membrane water electrolysis in future energy systems. *Appl. Ener.*, **237**, 862 – 872 (2019). <https://doi.org/10.1016/j.apenergy.2019.01.001>.
- [22] H2NEW, Hydrogen (H₂) from Next-generation Electrolyzers of Water Overview – Annual Merit Review and Peer Evaluation Meeting 2021, https://www.hydrogen.energy.gov/pdfs/review21/p196_pivovar_boardman_2021_o.pdf, accessed: January 2022.
- [23] BNEF (2020), Hydrogen Economy Outlook – Key messages, BloombergNEF <https://data.bloomberglp.com/professional/sites/24/BNEF-Hydrogen-Economy-Outlook-Key-Messages-30-Mar-2020.pdf>, accessed: January 2021.
- [24] P. Shirvanian, F. Van Berkel, Novel components in Proton Exchange Membrane (PEM) Water Electrolyzers (PEMWE): Status, challenges and future needs. A mini review. *Electrochem. Communic.*, **114**, 106704 (2020). <https://doi.org/10.1016/j.elecom.2020.106704>.
- [25] H. Becker, L. Castanheira, G. Hinds, Local measurement of current collector potential in a polymer electrolyte membrane water electrolyser. *J. Power Sources*, **448**, 227563 (2020). <https://doi.org/10.1016/j.jpowsour.2019.227563>.
- [26] M. Sartory, E. Wallnöfer-Ogris, P. Salman, T. Fellingner, M. Justl, A. Trattner, M. Klell, Theoretical and experimental analysis of an asymmetric high pressure PEM water electrolyser up to 155 bar. *Int. J. Hydrogen Energy*, **42**, 30493 – 30508 (2017). <https://doi.org/10.1016/j.ijhydene.2017.10.112>.

- [27] S. Stiber, H. Balzer, A. Wierhake, F. J. Wirkert, J. Roth, U. Rost, M. Brodmann, J. K. Lee, A. Bazylak, W. Waiblinger, A. S. Gago, K. A. Friedrich, Porous Transport Layers for Proton Exchange Membrane Electrolysis under Extreme Conditions of Current Density, Temperature and Pressure. *Adv. Energy Mater.*, **33** (11), 2100630 (2021). <https://doi.org/10.1002/aenm.202100630>.
- [28] J. H. Russel, L. J. Nuttall, A. P. Fickett, Hydrogen generation by solid polymer electrolyte water electrolysis. *American Chemical Society Division of Fuel Chemistry Preprints*, **18** (3), 24-40 (1973).
- [29] P. K. Shen, C.-Y. Wang, S. P. Jiang, X. Sun, J. Zhang, *Electrochemical Energy – Advanced Materials and Technologies*, CRC Press, Boca Raton, FL 2017.
- [30] M. Bernt, J. Schröter, M. Möckl, H. A. Gasteiger, Analysis of Gas Permeation Phenomena in a PEM Water Electrolyzer Operated at High Pressure and High Current Density. *J. Electrochem. Soc.*, **167**, 124502 (2020). <https://doi.org/10.1149/1945-7111/abaa68>.
- [31] M. Suermann, A. Patru, T. J. Schmidt, F. N. Büchi, High pressure polymer electrolyte water electrolysis: Test bench development and electrochemical analysis. *Int. J. Hydrogen Energy*, **42** (17), 12076 – 12086 (2017). <https://doi.org/10.1016/j.ijhydene.2017.01.224>.
- [32] S. Fletcher, Tafel slopes from first principles. *J Solid State Electrochem.*, **13**, 537 – 549 (2009). <https://doi.org/10.1007/s10008-008-0670-8>.
- [33] J. N. M. Unruh, *Lehrbuch der Elektrochemie*, 1. Auflage, Bad Saulgau: Eugen G. Leuze Verlag KG, 2013.
- [34] F. Marangio, M. Santarelli, M. Calì, Theoretical model and experimental analysis of a high pressure PEM water electrolyser for hydrogen production. *Int. J. Hydrogen Energy*, **34**, 1143 – 1158 (2009). <https://doi.org/10.1016/j.ijhydene.2008.11.083>.
- [35] D. L. Fritz, J. Mergel, D. Stolten, PEM Electrolysis Simulation and Validation. *ECS Trans.*, **58** (19), 1 – 9 (2014).
- [36] T. Schuler, T. J. Schmidt, F. N. Büchi, Polymer Electrolyte Water Electrolysis: Correlating Performance and Porous Transport Layer Structure: Part II.

- Electrochemical Performance Analysis. *J. The Electrochem. Soc.*, **166** (10), F555 - F565 (2019).
- [37] M. Suermann, T. J. Schmidt, F. N. Büchi, Investigation of Mass Transport Losses in Polymer Electrolyte Electrolysis Cells. *ECS Trans.*, **69** (17), 1141 – 1148 (2015). <https://doi.org/10.1149/06917.1141ecst>.
- [38] S. A. Grigoriev, P. Millet, S. A. Volobuev, V. N. Fateev, Optimization of porous current collectors for PEM water electrolyzers. *Int. J. Hydrogen Energy*, **34** (11), 4968 – 4973 (2009). <https://doi.org/10.1016/j.ijhydene.2008.11.056>.
- [39] H. Ito, T. Maeda, A. Nakano, A. Kato, T. Yoshida, Influence of pore structural properties of current collectors on the performance of proton exchange membrane electrolyzer. *Electrochim Acta*, **100**, 242 - 248 (2013). <https://doi.org/10.1016/j.electacta.2012.05.068>.
- [40] S. Stiber, N. Sata, T. Morawietz, A. S. Ansar, T. Jahnke, J. K. Lee, A. Bazylak, A., Fallisch, A. S. Gago, K. A. Friedrich, High-performance, Durable and Low-Cost Proton Exchange Membrane Electrolyser with Stainless Steel Components. *Energy Environ. Sci.*, **15**, 109 – 122 (2021). <https://doi.org/10.1039/D1EE02112E>.
- [41] J. Durst, C. Simon, F. Hasché, H. A. Gasteiger, Hydrogen Oxidation and Evolution Reaction Kinetics on Carbon supported Pt, Ir, Rh, and Pd Electrocatalysts in Acidic Media. *J. Electrochem. Soc.*, **162** (1), F190 - F203 (2015). <https://doi.org/10.1149/2.0981501jes>.
- [42] W. Sheng, H. A. Gasteiger, Y. Shao-Horn, Hydrogen Oxidation and Evolution Reaction Kinetics on Platinum: Acid vs. Alkaline Electrolytes. *J. Electrochem. Soc.*, **157** (11), B1529 - B1536 (2010). <https://doi.org/10.1149/1.3483106>.
- [43] E. Fabbri, A. Habereder, K. Waltar, R. Kötz, T. J. Schmidt, Developments and perspectives of oxide-based catalysts for the oxygen evolution reaction. *Catal. Sci. Technol.*, **4**, 3800 – 3821 (2014). <https://doi.org/10.1039/C4CY00669K>
- [44] P. Trinke, G. P. Keeley, M. Carmo, B. Bensmann, R. Hanke-Rauschenbach, Elucidating the Effect of Mass Transport Resistance on Hydrogen Crossover and Cell Performance in PEM Water Electrolyzers by Varying the Cathode Ionomer

- Content. *J. Electrochem. Soc.*, **166** (8), F465 - F471 (2019).
<https://doi.org/10.1149/2.0171908jes>.
- [45] M. Bernt, H. A. Gasteiger, Influence of Ionomer Content in IrO₂/TiO₂ Electrodes on PEM Water Electrolyzer Performance. *J. Electrochem. Soc.*, **163** (11), F3179 - F3189 (2016). <https://doi.org/10.1149/2.0231611jes>.
- [46] J. E. Park, J. Kim, J. Han, K. Kim, S. Park, S. Kim, H. S. Park, Y.-H. Cho, J.-C. Lee, Y.-E. Sung, High-performance proton-exchange membrane water electrolysis using a sulfonated poly(arylene ether sulfone) membrane and ionomer. *J. Membr. Sci.*, **620**, 118871 (2021). <https://doi.org/10.1016/j.memsci.2020.118871>.
- [47] K. A. Mauritz, R. B. Moore, State of Understanding of Nafion. *Chem. Rev.*, **104** (10), 4535-4585 (2004). <https://doi.org/10.1021/cr0207123>.
- [48] K. Talukdar, P. Gazdzicki, K. A. Friedrich, Comparative investigation into the performance and durability of long and short side chain ionomers in Polymer Electrolyte Membrane Fuel Cells. *J. Power Sources*, **439**, 227078 (2019). <https://doi.org/10.1016/j.jpowsour.2019.227078>.
- [49] S. Siracusano, C. Oldani, M. A. Navarra, S. Tonella, L. Mazzapioda, N. Briguglio, A. S. Aricò, Chemically stabilised extruded and recast short side chain Aquivion® proton exchange membranes for high current density operation in water electrolysis. *J. Membr. Sci.*, **578**, 136 – 148 (2019). <https://doi.org/10.1016/j.memsci.2019.02.021>.
- [50] S. Siracusano, V. Baglio, A. Stassi, L. Merlo, E. Moukheiber, A. S. Aricò, Performance analysis of short-side-chain Aquivion perfluorosulfonic acid polymer for proton exchange membrane water electrolysis. *J. Membr. Sci.*, **466**, 1 – 7 (2014). <https://doi.org/10.1016/j.memsci.2014.04.030>.
- [51] S. Garbe, U. Babic, E. Nilsson, T. J. Schmidt, L. Gubler, Communication – Pt-doped Thin Membranes for Gas Crossover Suppression in Polymer Electrolyte Water Electrolysis. *J. Electrochem. Soc.*, **166** (13), F873 - F875 (2019). <https://doi.org/10.1149/2.0111913jes>.
- [52] S. A. Grigoriev, P. Millet, S. V. Korobtsev, V. I. Porembskiy, M. Pepic, C. Etievant, C. Puyenchet, V. N. Fateev, Hydrogen safety aspects related to high-pressure

- polymer electrolyte membrane water electrolysis. *Int. J. Hydrogen Energy*, **34**, 5986 – 5991 (2009). <https://doi.org/10.1016/j.ijhydene.2009.01.047>.
- [53] C. Klose, P. Trinke, T. Böhm, B. Bensmann, S. Vierrath, R. Hanke-Rauschenbach, S. Thiele, Membrane Interlayer with Pt Recombination Particles for Reduction of the Anodic Hydrogen Content in PEM Water Electrolysis. *J. Electrochem. Soc.*, **165** (16), F1271 - F1277 (2018). <https://doi.org/10.1149/2.1241814jes>.
- [54] H. Teuku, I. Alshami, J. Goh, M. S. Masdar, K. S. Loh, Review on bipolar plates for low-temperature polymer electrolyte membrane water electrolyzer. *Int. J. Energy Res.*, **45**, 20583 – 20600 (2021). <https://doi.org/10.1002/er.7182>.
- [55] S. Toghyani, E. Afshari, E. Baniasadi, S. A. Atyabi, Thermal and electrochemical analysis of different flow field patterns in a PEM electrolyzer. *Electrochim. Acta*, **267**, 234 – 245 (2018). <https://doi.org/10.1016/j.electacta.2018.02.078>.
- [56] H. Li, H. Nakajima, A. Inada, K. Ito, Effect of flow-field pattern and flow configuration on the performance of a polymer-electrolyte-membrane water electrolyzer at high temperature. *Int. J. Hydrogen Energy*, **43** (18), 8600 – 8610 (2018). <https://doi.org/10.1016/j.ijhydene.2018.02.171>.
- [57] E. Borgardt, L. Giesenberg, M. Reska, M. Müller, K. Wippermann, M. Langemann, W. Lehnert, D. Stolten, Impact of clamping pressure and stress relaxation on the performance of different polymer electrolyte membrane water electrolysis cell designs. *Int. J. Hydrogen Energy*, **44** (42), 23556 – 23567 (2019). <https://doi.org/10.1016/j.ijhydene.2019.07.075>.
- [58] L. Bertuccioli, A. Chan, D. Hart, F. Lehner, B. Madden, E. Standen, Study on Development of Water Electrolysis in the EU by E4tech Sarl with Element Energy Ltd for the Fuel Cells and Hydrogen Joint Undertaking 2014.
- [59] A.S. Gago, S. A. Ansar, P. Gazdzicki, N. Wagner, J. Arnold, K. A. Friedrich, Low Cost Bipolar Plates for Large Scale PEM Electrolyzers. *ECS Trans.*, **64** (3) 1039 – 1048 (2014). <https://doi.org/10.1149/06403.1039ecst>.
- [60] A. S. Gago, S. A. Ansar, B. Saruhan, U. Schulz, P. Lettenmeier, N. A. Cañas, P. Gazdzicki, T. Morawietz, R. Hiesgen, J. Arnold, K. A. Friedrich, Protective coatings on stainless steel bipolar plates for proton exchange membrane (PEM) electrolyzers.

- J. Power Sources*, **307**, 815 – 825 (2016).
<https://doi.org/10.1016/j.jpowsour.2015.12.071>.
- [61] P. Lettenmeier, R. Wang, R. Abouatallah, F. Burggraf, A. S. Gago, K. A. Friedrich, Coated Stainless Steel Bipolar Plates for Proton Exchange Membrane Electrolyzers. *J. Electrochem. Soc.*, **163**, F3119 – F3124 (2016).
<https://doi.org/10.1149/2.0141611jes>.
- [62] P. Lettenmeier, R. Wang, R. Abouatallah, B. Saruhan, O. Freitag, P. Gazdzicki, T. Morawietz, R. Hiesgen, A. S. Gago, K. A. Friedrich, *Sci. Rep.*, **7**, 44035 (2017).
<https://doi.org/10.1038/srep44035>.
- [63] S. Stiber, M. Carmo, M. Müller, K. E. Ayers, C. Capuano, T. Morawietz, I. Biswas, P. Gazdzicki, J. F. Heger, A. S. Gago, K. A. Friedrich, Long-term Operation of Coated Stainless Steel Bipolar Plates for Proton Exchange Membrane Water Electrolyzers. *Adv. Ener. Sustain. Research*. 2022. <https://doi.org/10.1002/aesr.202200024>.
- [64] K. E. Ayers, J. N. Renner, N. Danilovic, J. X. Wang, Y. Zhang, R. Maric, H. Yu, Pathways to ultra-low platinum group metal catalyst loading in proton exchange membrane electrolyzers. *Cat. Today*, **262**, 121 – 132 (2016).
<http://dx.doi.org/10.1016/j.cattod.2015.10.019>.
- [65] N. Rojas, M. Sánchez-Molina, G. Sevilla, E. Amores, E. Almandoz, J. Esparaza, M. R. Cruz Vivas, C. Colominas, Coated stainless steels evaluation for bipolar plates in PEM water electrolysis conditions. *Int. J. Hydrogen Energy*, **46** (51), 25929 – 25943 (2021). <https://doi.org/10.1016/j.ijhydene.2021.03.100>.
- [66] J. T. Toops, M. P. Brady, F.-Y. Zhang, H. M. Meyer III, K. Ayers, A. Roemer, L. Dalton, Evaluation of nitrated titanium separator plates for proton exchange membrane electrolyzer cells. *J. Power Sources*, **272**, 954 – 960 (2014).
<http://dx.doi.org/10.1016/j.jpowsour.2014.09.016>.
- [67] A. Kellenberger, N. Vaszilcsin, D. Duca, M. L. Dan, N. Duteanu, S. Stiber, T. Morawietz, I. Biswas, S. A. Ansar, P. Gazdzicki, F. J. Wirkert, J. Roth, U. Rost, M. Brodmann, A. S. Gago, K. A. Friedrich, Towards Replacing Titanium with Copper in the Bipolar Plates for Proton Exchange Membrane Water Electrolysis. *Materials*, **15** (5), 1628 (2022). <https://doi.org/10.3390/ma15051628>.

- [68] S. Park, J.-W. Lee, B. N. Popov, A review of gas diffusion layer in PEM fuel cells: Materials and designs. *Int. J. Hydrogen Energy*, **37** (7), 5850 – 5865 (2012). <https://doi.org/10.1016/j.ijhydene.2011.12.148>.
- [69] G. Borisov, A. Stoyanova, E. Lefterova, E. Slavcheva, A novel non-carbon gas diffusion layer for PEM water electrolysis anodes. *Izvestiya po Khimiya Bulgarska Akademiya na Naukite*. 45 (2015).
- [70] G. Bender, M. Carmo, T. Smolinka, A. Gago, N. Danilovic, M. Mueller, F. Ganci, A. Fallisch, P. Lettenmeier, K. A. Friedrich, K. Ayers, B. Pivovar, J. Mergel, D. Stolten, Initial approaches in benchmarking and round robin testing for proton exchange membrane water electrolyzers. *Int. J. Hydrogen Energy*, **44**, 9174 – 9187 (2019). <https://doi.org/10.1016/j.ijhydene.2019.02.074>.
- [71] S. Song, H. Zhang, X. Ma, Z. Shao, R. T. Baker, B. Yi, Electrochemical investigation of electrocatalysts for the oxygen evolution reaction in PEM water electrolyzers. *Int. J. Hydrogen Energy*, **33**, 4955 – 4961 (2008). <https://doi.org/10.1016/j.ijhydene.2008.06.039>.
- [72] C. Rakousky, U. Reimer, K. Wippermann, M. Carmo, W. Lueke, D. Stolten, An analysis of degradation phenomena in polymer electrolyte membrane water electrolysis. *J. Power Sources*, **326**, 120 – 128 (2016). <https://doi.org/10.1016/j.jpowsour.2016.06.082>.
- [73] C. Liu, M. Shviro, A. S. Gago, S. F. Zaccarine, G. Bender, P. Gazdzicki, T. Morawietz, I. Biswas, M. Rasinski, A. Everwand, R. Schierholz, J. Pfeilsticker, M. Müller, P. P. Lopes, R.-A. Eichel, B. Pivovar, S. Pylypenko, K. A. Friedrich, W. Lehnert, M. Carmo, Exploring the Interface of Skin-Layered Titanium Fibers for Electrochemical Water Splitting. *Adv. Energy Mater.*, **11** (8), 2002926 (2021). <https://doi.org/10.1002/aenm.202002926>.
- [74] C. Liu, M. Carmo, G. Bender, A. Everwand, T. Lickert, J. Young, T. Smolinka, D. Stolten, W. Lehnert, Performance enhancement of PEM electrolyzers through iridium-coated titanium porous transport layers. *Electrochem. Commun.*, **97**, 96 – 99 (2018). <https://doi.org/10.1016/j.elecom.2018.10.021>.
- [75] J. O. Majasan, F. Iacoviello, P. R. Shearing, D. J. L. Brett, Effect of Microstructure of Porous Transport Layer on Performance in Polymer Electrolyte Membrane Water

- Electrolyser. *Energy Procedia*, **151**, 111 – 119 (2018).
<https://doi.org/10.1016/j.egypro.2018.09.035>.
- [76] K. Bromberger, G. Jagdishkumar, T. Lickert, A. Fallisch, T. Smolinka, Hydraulic ex situ through-plane characterization of porous transport layers in PEM water electrolysis cells. *Int. J. Hydrogen Energy*, **43**, 2556–2569 (2018).
<https://doi.org/10.1016/j.ijhydene.2017.12.042>.
- [77] T. Lickert, M. L. Kiermaier, K. Bromberger, G. Jagdishkumar, S. Metz, A. Fallisch, T. Smolinka, On the influence of the anodic porous transport layer on PEM electrolysis performance at high current densities. *Int. J. Hydrogen Energy*, **45**, 6047 – 6058 (2020). <https://doi.org/10.1016/j.ijhydene.2019.12.204>.
- [78] Z. Kang, J. Mo, G. Yang, S. T. Retterer, D. A. Cullen, T. J. Toops, J. B. Green Jr, M. M. Mench, F.-Y. Zhang, Investigation of thin/well-tunable liquid/gas diffusion layers exhibiting superior multifunctional performance in low-temperature electrolytic water splitting. *Energy Environ. Sci.*, **10**, 166 – 175 (2017).
<https://doi.org/10.1039/C6EE02368A>.
- [79] T. Schuler, R. De Bruycker, T. J. Schmidt, F. N. Büchi, Polymer Electrolyte Water Electrolysis: Correlating Porous Transport Layer Structural Properties and Performance: Part I. Tomographic Analysis of Morphology and Topology. *J. Electrochem. Society*, **166** (4), F270 - F281 (2019).
<https://doi.org/10.1149/2.0561904jes>.
- [80] P. Lettenmeier, S. Kolb, F. Burggraf, A. S. Gago, K. A. Friedrich, Towards developing a backing layer for proton exchange membrane electrolyzers. *J. Power Sources*, **311**, 153 – 158 (2016). <http://dx.doi.org/10.1016/j.jpowsour.2016.01.100>.
- [81] P. Lettenmeier, S. Kolb, N. Sata, A. Fallisch, L. Zielke, S. Thiele, A. S. Gago, K. A. Friedrich, Comprehensive investigation of novel pore-graded gas diffusion layers for high-performance and cost-effective proton exchange membrane electrolyzers. *Energy Environ. Sci.*, **10**, 2521 – 2533 (2017). <https://doi.org/10.1039/c7ee01240c>.
- [82] T. Schuler, J. M. Ciccone, B. Krentscher, F. Marone, C. Peter, T. J. Schmidt, F. N. Büchi, Hierarchically Structured Porous Transport Layers for Polymer Electrolyte Water Electrolysis. *Adv. Ener. Mat.*, **10** (2), 1903216 (2020).
<https://doi.org/10.1002/aenm.201903216>.

- [83] E. T. Ojong, Characterization of the performance of PEM water electrolysis cells operating with and without flow channels, based on experimentally validated semiempirical coupled-physics models, *PhD thesis*, Brandenburg University of Technology, 2018, <https://dnb.info/1172718202/34>.
- [84] F. Arbabi, A. Kalantarian, R. Abouatallah, R. Wang, J. S. Wallace, A. Bazylak, Feasibility study of using microfluidic platforms for visualizing bubble flows in electrolyzer gas diffusion layers. *J. Power Sources*, **258**, 142 – 149 (2014). <https://doi.org/10.1016/j.jpowsour.2014.02.042>.
- [85] J. Mo, S. M. Steen, F. Y. Zhang, T. J. Toops, M. P. Brady, J. B. Green, Electrochemical investigation of stainless steel corrosion in a proton exchange membrane electrolyzer cell. *Int. J. Hydrogen Energy*, **40** (36), 12506 – 12511 (2015). <https://doi.org/10.1016/j.ijhydene.2015.07.061>.
- [86] J. Mo, S. Steen, Z. Kang, G. Yang, D. A. Taylor, Y. Li, T. J. Toops, M. P. Brady, S. T. Retterer, D. A. Cullen, J. B. Green, F.-Y. Zhang, Study on corrosion migrations within catalyst-coated membranes of proton exchange membrane electrolyzer cells. *Int. J. Hydrogen Energy*, **42** (44), 27343 – 27349 (2017). <https://doi.org/10.1016/j.ijhydene.2017.09.020>.
- [87] J. O. Majasan, F. Iacoviello, J. I. S. Cho, M. Maier, X. Lu, T. P. Neville, I. Dedigama, P. R. Shearing, D. J. L. Brett, Correlative study of microstructure and performance for porous transport layers in polymer electrolyte membrane water electrolyzers by X-ray computed tomography and electrochemical characterization. *Int. J. Hydrogen Energy*, **44** (36), 19519 – 19532 (2019). <https://doi.org/10.1016/j.ijhydene.2019.05.222>.
- [88] X.-Z. Yuan, E. Gu, R. Bredin, M. Baker, S. Lee, T. Biggs, A. Bock, V. Banhardt, J. Russell, F. Girard, Development of a 3-in-1 device to simultaneously measure properties of gas diffusion layer for the quality control of proton exchange membrane fuel cell components. *J. Power Sources*, **477**, 229009 (2020). <https://doi.org/10.1016/j.jpowsour.2020.229009>.
- [89] F. J. Hackemüller, E. Borgardt, O. Panchenko, M. Müller, M. Bram, Manufacturing of Large-Scale Titanium-Based Porous Transport Layers for Polymer Electrolyte

- Membrane Electrolysis by Tape Casting. *Adv. Energy Mater.*, **21** (6), 1801201 (2019). <https://doi.org/10.1002/adem.201801201>.
- [90] H. Becker, L. Castanheira, G. Hinds, Local measurement of current collector potential in a polymer electrolyte membrane water electrolyser. *J. Power Sources*, **448**, 227563 (2020). <https://doi.org/10.1016/j.jpowsour.2019.227563>.
- [91] O. Panchenko, E. Borgardt, W. Zwaygardt, F. J. Hackemüller, M. Bram, N. Kardjilov, T. Arlt, I. Manke, M. Müller, D. Stolten, W. Lehnert, In-situ two-phase flow investigation of different porous transport layer for a polymer electrolyte membrane (PEM) electrolyzer with neutron spectroscopy. *J. Power Sources*, **390**, 108 – 115 (2018). <https://doi.org/10.1016/j.jpowsour.2018.04.044>.
- [92] H. Ito, T. Maeda, A. Nakano, A. Kato, T. Yoshida, Influence of pore structural properties of current collectors on the performance of proton exchange membrane electrolyzer. *Electrochim. Acta*, **100**, 242 – 248 (2013). <https://doi.org/10.1016/j.electacta.2012.05.068>.
- [93] H. Ito, T. Maeda, A. Nakano, C. M. Hwang, M. Ishida, A. Kato, T. Yoshida, Experimental study on porous current collectors of PEM electrolyzers. *Int. J. Hydrogen Energy*, **37**, 7418 – 7428 (2012). <https://doi.org/10.1016/j.ijhydene.2012.01.095>.
- [94] M. Suermann, K. Takanohashi, A. Lamibrac, T. J. Schmidt, F. N. Büchi, Influence of Operating Conditions and Material Properties on the Mass Transport Losses of Polymer Electrolyte Water Electrolysis. *J. Electrochem. Soc.*, **164** (9), F973 - F980 (2017). <https://doi.org/10.1149/2.13517109jes>.
- [95] J. Mo, Z. Kang, S. T. Retterer, D. A. Cullen, T. J. Toops, J. B. Green Jr., M. M. Mench, F.-Y. Zhang, Discovery of true electrochemical reactions for ultrahigh catalyst mass activity in water splitting. *Sci. Adv.*, **2** (11), e1600690 (2016). <https://doi.org/10.1126/sciadv.1600690>.
- [96] J. A. Greenwood, Constriction resistance and the real area of contact. *Br. J. Appl. Phys.*, **17** (12), 1621 (1966). <https://doi.org/10.1088/0508-3443/17/12/310>.
- [97] M. Braunovic, N. K. Myshkin, V. V. Konchits, Electrical Contacts: Fundamentals, Applications and Technology, CRC Press, Boca Raton, FL, 2017.

- [98] J. Mo, Z. Kang, G. Yang, Y. Li, S. T. Retterer, D. A. Cullen, T. J. Toops, G. Bender, B. S. Pivovar, J. B. Green Jr., F.-Y. Zhang, In-situ investigation on ultrafast oxygen evolution reactions of water splitting in proton exchange membrane electrolyzer cells. *J. Mater. Chem. A*, **5**, 18469 – 18475 (2017). <https://doi.org/10.1039/C7TA05681H>.
- [99] J. Lopata, Z. Kang, J. Young, G. Bender, J. W. Weidner, S. Shimpalee, Effects of the Transport/Catalyst Layer Interface and Catalyst Loading on Mass and Charge Transport Phenomena in Polymer Electrolyte Membrane Water Electrolysis Devices. *J. Electrochem. Soc.*, **167**, 064507 (2020). <https://doi.org/10.1149/1945-7111/ab7f87>.
- [100] B. Roh, D. D. Macdonald, Effect of oxygen vacancies in anodic titanium oxide films on the kinetics of the oxygen electrode reaction. *Russ. J. Electrochem.*, **43**, 125 – 135 (2007). <https://doi.org/10.1134/S1023193507020012>.
- [101] B. Roh, D. D. Macdonald, Passivity of titanium, part IV: reversible oxygen vacancy generation/annihilation. *J Solid State Electrochem.*, **23**, 2863–2879 (2019). <https://doi.org/10.1007/s10008-019-04363-w>.
- [102] T. Shibata, Y.-C. Zhu, The effect of film formation conditions on the structure and composition of anodic oxide films on titanium. *Corros. Sci.*, **37** (2), 253 – 270 (1995). [https://doi.org/10.1016/0010-938X\(94\)00133-Q](https://doi.org/10.1016/0010-938X(94)00133-Q).
- [103] T. Schuler, T. J. Schmidt, F. N. Büchi, Polymer Electrolyte Water Electrolysis: Correlating Performance and Porous Transport Layer Structure: Part II. Electrochemical Performance Analysis. *J. Electrochem. Soc.*, **166** (10), F555 – F565 (2019). <https://doi.org/10.1149/2.1241908jes>.
- [104] S. M. Steen III, J. Mo, Z. Kang, G. Yang, F.-Y. Zhang, Investigation of Titanium Liquid/Gas Diffusion Layers in Proton Exchange Membrane Electrolyzer Cells. *Int. J. Green Energy*, **14** (2), 162 – 170 (2017). <http://dx.doi.org/10.1080/15435075.2016.1253582>.
- [105] J. Mo, S. M. Stehen III, B. Han, Z. Kang, A. Terekhov, F.-Y. Zhang, S. T. Retterer, D. A. Cullen, Investigation of Titanium Felt Transport Parameters for Energy Storage and Hydrogen/Oxygen Production. *13th Int. Energy Conv. Engineer. Conference*,

- Propulsion and Energy Forum, AIAA 2015-3914, Session: Fuel Cells, Energy Storage, and Combustion (2015). <https://doi.org/10.2514/6.2015-3914>.
- [106] C. M. Hwang, M. Ishida, H. Ito, T. Maeda, A. Nakano, Y. Hasegawa, N. Yokoi, A. Kato, T. Yoshida, Influence of properties of gas diffusion layers on the performance of polymer electrolyte-based unitized reversible fuel cells. *Int. J. Hydrogen Energy*, **36**, 1740 – 1753 (2011). <https://doi.org/10.1016/j.ijhydene.2010.10.091>.
- [107] J. Mo, Z. Kang, G. Yang, S. T. Retterer, D. A. Cullen, T. J. Toops, J. B. Green Jr. II, F.-Y. Zhang, Thin liquid/gas diffusion layers for high-efficiency hydrogen production from water splitting. *Appl. Energy*, **177**, 817 – 822 (2016). <http://dx.doi.org/10.1016/j.apenergy.2016.05.154>.
- [108] L. Zielke, A. Fallisch, N. Paust, R. Zengerle, S. Thiele, Tomography based screening of flow field / current collector combinations for PEM water electrolysis. *RSC Adv.*, **4**, 58888 – 58894 (2014). <https://doi.org/10.1039/C4RA12402B>.
- [109] M. Bühler, F. Hegge, P. Holzapfel, M. Bierling, M. Suermann, S. Vierrath, S. Thiele, Optimization of anodic porous transport electrodes for proton exchange membrane water electrolyzers. *J. Mater. Chem. A*, **7**, 26984 (2019). <https://doi.org/10.1039/c9ta08396k>.
- [110] E. Borgardt, O. Panchenko, F. J. Hackemüller, J. Giffin, M. Bram, M. Müller, W. Lehnert, D. Stolten, Mechanical characterization and durability of sintered porous transport layers for polymer electrolyte membrane electrolysis. *J. Power Sources*, **374**, 84 – 91 (2018). <https://doi.org/10.1016/j.jpowsour.2017.11.027>.
- [111] S. Siracusano, V. Baglio, A. Di Blasi, N. Briguglio, A. Stassi, R. Ornelas, E. Trifoni, V. Antonucci, A. S. Aricò, Electrochemical characterization of single cell and short stack PEM electrolyzers based on a nanosized IrO₂ anode electrocatalyst. *Int. J. Hydrogen Energy*, **35**, 5558 – 5568 (2010). <https://doi.org/10.1016/j.ijhydene.2010.03.102>.
- [112] M. Suermann, T. Gimpel, L. V. Böhre, W. Schade, B. Bensmann, R. Hanke-Rauschenbach, Femtosecond laser-induced surface structuring of the porous transport layers in proton exchange membrane water electrolysis. *J. Mater. Chem. A*, **8**, 4898 (2020). <https://doi.org/10.1039/c9ta12127g>.

- [113] G. Chen, H. Zhang, H. Zhon, H. Ma, Gas diffusion layer with titanium carbide for a unitized regenerative fuel cell. *Electrochim. Acta*, **55**, 8801 – 8807 (2010). <https://doi.org/10.1016/j.electacta.2010.07.103>.
- [114] N. F. Daudt, F. J. Hackemüller, J. Bram, Powder metallurgical production of 316L stainless steel/niobium composites for Proton Exchange membrane electrolysis cells. *Powder Metallurgy*, **62** (3), 176 – 185 (2019). <https://doi.org/10.1080/00325899.2019.1607461>.
- [115] X.-Z. Yuan, N. Shaigan, C. Song, M. Aujla, V. Neburchilov, J. T. H. Kwan, D. P. Wilkinson, A. Bazylak, K. Fatih, The porous transport layer in proton exchange membrane water electrolysis: perspectives on a complex component. *Sust. Ener. Fuels*, **6**, 1824 – 1853 (2022). <https://doi.org/10.1039/D2SE00260D>.
- [116] H. Li, T. Fujigaya, H. Nakajima, A. Inada, K. Ito, Optimum structural properties for an anode current collector used in a polymer electrolyte membrane water electrolyzer operated at the boiling point of water. *J. Power Sources*, **332**, 16 – 23 (2016). <https://doi.org/10.1016/j.jpowsour.2016.09.086>.
- [117] Z. Kang, J. Mo, G. Yang, Y. Li, D. A. Talley, S. T. Retterer, D. A. Cullen, T. J. Toops, M. P. Brady, G. Bender, B. S. Pivovar, J. B. Green Jr., F.-Y. Zhang, Thin film surface modifications of thin/tunable liquid/gas diffusion layers for high-efficiency proton exchange membrane electrolyzer cells. *Appl. Energy*, **206**, 983 – 990 (2017). <http://dx.doi.org/10.1016/j.apenergy.2017.09.004>.
- [118] O. Schmidt, A. Gambhir, I. Staffell, A. Hawkes, J. Nelson, S. Few, Future cost and performance of water electrolysis: An expert elicitation study. *Int. J. Hydrogen Energy*, **42**, 30470 – 30492 (2017). <https://doi.org/10.1016/j.ijhydene.2017.10.045>.
- [119] S. M. Saba, M. Müller, M. Robinius, D. Stolten, The investment costs of electrolysis – A comparison of cost studies from the past 30 years. *Int. J. Hydrogen Energy*, **43** (3), 1209 – 1223 (2018). <https://doi.org/10.1016/j.ijhydene.2017.11.115>.
- [120] R. Wiebe, V. L. Gaddy, The Solubility of Hydrogen in Water at 0, 50, 75 and 100 ° from 25 to 1000 Atmospheres. *J. Am. Chem. Soc.*, **56** (1), 76 – 79 (1934). <https://doi.org/10.1021/ja01316a022>.

- [121] H. Ito, T. Maeda, A. Nakano, H. Takenaka, Properties of Nafion membranes under PEM water electrolysis conditions. *Int. J. Hydrogen Energy*, **36** (17), 10527 – 10540 (2011). <https://doi.org/10.1016/j.ijhydene.2011.05.127>.
- [122] S. A. Grigoriev, V. I. Porembskiy, S. V. Korobtsev, V. N. Fateev, F. Auprêtre, P. Millet, High-pressure PEM water electrolysis and corresponding safety issues. *Int. J. Hydrogen Energy*, **36** (3), 2721 – 2728 (2011). <https://doi.org/10.1016/j.ijhydene.2010.03.058>.
- [123] S. A. Grigoriev, V. N. Fateev, D. G. Bessarabov, P. Millet, Current status, research trends, and challenges in water electrolysis science and technology. *Int. J. Hydrogen Energy*, **45** (49), 26036 – 26058 (2020). <https://doi.org/10.1016/j.ijhydene.2020.03.109>.
- [124] P. Fauchais, M. Vardelle, A. Vardelle, Reliability of plasma-sprayed coatings: monitoring the plasma spray process and improving the quality of coatings. *J. Phys. D: Appl. Phys.*, **46**, 224016 (2013). <https://doi.org/10.1088/0022-3727/46/22/224016>.
- [125] N. K. Jain, M. S. Sawant, S. H. Nikam, S. Jhavar, Encyclopedia of Plasma Technology, Metal Deposition: Plasma-Based Processes, CRC Press, Boca Raton, FL 2016, 10.1081/E-EPLT-120053919.
- [126] H.-Y. Jung, S.-Y. Huang, B. N. Popov, High-durability titanium bipolar plate modified by electrochemical deposition of platinum for unitized regenerative fuel cell (URFC). *J. Power Sources*, **195**, 1950 – 1956 (2010). <https://doi.org/10.1016/j.jpowsour.2009.10.002>.
- [127] C. Rakousky, U. Reimer, K. Wippermann, M. Carmo, W. Lueke, D. Stolten, An analysis of degradation phenomena in polymer electrolyte membrane water electrolysis. *J. Power Sources*, **326**, 120 – 128 (2016). <http://dx.doi.org/10.1016/j.jpowsour.2016.06.082>.
- [128] G. Tsotridis, JRC validated methods, reference methods and measurements report – EU Harmonised Polarisation Curve Test Method for Low Temperature Water Electrolysis, Joint Research Center (JRC), Brussels 2018.

- [129] E. Barsoukov, J. R. Macdonald, Impedance Spectroscopy: Theory, Experiment, and Applications. Wiley, Ed., 2005, 10.1002/0471716243.
- [130] S. Siracusano, S. Trocino, N. Briguglio, V. Baglio and A. S. Arico', Electrochemical Impedance Spectroscopy as a Diagnostic Tool in Polymer Electrolyte Membrane Electrolysis. *Materials*, **11** (8), 1368 (2018). <https://doi.org/10.3390/ma11081368>.
- [131] P. Lettenmeier, R. Wang, R. Abouatallah, S. Helmly, T. Morawietz, R. Hiesgen, S. Kolb, F. Burggraf, J. Kallo, A. S. Gago, K. A. Friedrich, Durable Membrane Electrode Assemblies for Proton Exchange Membrane Electrolyzer Systems Operating at High Current Densities. *Electrochim. Acta*, **210**, 502 – 511 (2016). <https://doi.org/10.1016/j.electacta.2016.04.164>.
- [132] C. Rozain, E. Mayousse, N. Guilleta, P. Millet, Influence of iridium oxide loadings on the performance of PEM water electrolysis cells: Part II – Advanced oxygen electrodes. *Appl. Catal. B*, **182**, 123 – 131 (2016). <http://dx.doi.org/doi:10.1016/j.apcatb.2015.09.011>.
- [133] M. Eikerling, A. A. Kornyshev, Electrochemical impedance of the cathode catalyst layer in polymer electrolyte fuel cells. *J. Electroanal. Chem.*, **475**, 107 – 123 (1999). [https://doi.org/10.1016/S0022-0728\(99\)00335-6](https://doi.org/10.1016/S0022-0728(99)00335-6).
- [134] U. Rammelt, G. Reinhard, On the applicability of a constant phase element (CPE) to the estimation of roughness of solid metal electrodes. *Electrochim. Acta*, **35** (6), 1045 – 1049 (1990). [https://doi.org/10.1016/0013-4686\(90\)90040-7](https://doi.org/10.1016/0013-4686(90)90040-7).
- [135] I. Mauleón, Photovoltaic learning rate estimation: Issues and implications. *Renew. Sust. Energy Rev.*, **65**, 507 – 524 (2016). <https://doi.org/10.1016/j.rser.2016.06.070>.
- [136] I. Staffell, R. Green, The cost of domestic fuel cell micro-CHP systems. *Int. J. Hydrogen Energy*, **38** (2), 1088 – 1102 (2013). <https://doi.org/10.1016/j.ijhydene.2012.10.090>.
- [137] I. Staffell, R. J. Green, Estimating future prices for stationary fuel cells with empirically derived experience curves. *Int. J. Hydrogen Energy*, **34** (14), 5617 – 5628 (2009). <https://doi.org/10.1016/j.ijhydene.2009.05.075>.
- [138] G. Anandarajah, W. McDowall, P. Ekins, Decarbonising road transport with hydrogen and electricity: Long term global technology learning scenarios. *Int. J. Hydrogen Energy*, **38** (8), 3419 – 3432 (2013). <https://doi.org/10.1016/j.ijhydene.2012.12.110>.

- [139] T. P. Wright, Factors Affecting the Cost of Airplanes. *J. The Aeronautical Sci.*, **3**, 1936. <https://doi.org/10.2514/8.155>.
- [140] A. Malhotra, T. S. Schmidt, Accelerating Low-Carbon Innovation. *Joule*, **4** (11), 2259 – 2267 (2020). <https://doi.org/10.1016/j.joule.2020.09.004>.
- [141] H. Böhm, S. Goers, A. Zauner, Estimating future costs of power-to-gas – a component-based approach for technological learning. *Int. J. Hydrogen Energy*, **44** (14), 30789 – 30805 (2019). <https://doi.org/10.1016/j.ijhydene.2019.09.230>.
- [142] O. Schmidt, A. Hawkes, A. Gambhir, I. Staffell, The future cost of electrical energy storage based on experience rates. *Nat. Energy*, **2**, 17110 (2017). <https://doi.org/10.1038/nenergy.2017.110>.
- [143] Hydrogen Council, Path to hydrogen competitiveness – A cost perspective (2020), Brussels, https://hydrogencouncil.com/wp-content/uploads/2020/01/Path-to-Hydrogen-Competitiveness_Full-Study-1.pdf, accessed: September 2022.
- [144] Energy Transitions Commission, Making the Hydrogen Economy Possible: Accelerating Clean Hydrogen in an Electrified Economy (2021), <https://www.energy-transitions.org/wp-content/uploads/2021/04/ETC-Global-Hydrogen-Executive-Summary-Short.pdf>, accessed: September 2022.
- [145] Fraunhofer ISE, Cost forecast for Low Temperature Electrolysis – Technology driven bottom-up prognosis for PEM and Alkaline Water Electrolysis Systems, (2021), Freiburg, <https://www.ise.fraunhofer.de/content/dam/ise/de/documents/publications/studies/cost-forecast-for-low-temperature-electrolysis.pdf>, accessed: September 2022.
- [146] Fuel Cells and Hydrogen Joint Undertaking (FCH JU). Multi - Annual Work Plan 2014 - 2020. https://www.fch.europa.eu/sites/default/files/MAWP%20final%20version_endorsed%20GB%2015062018%20%28ID%203712421%29.pdf
- [147] A. Mayyas, M. Mann, Emerging Manufacturing Technologies for Fuel Cells and Electrolyzers. *Procedia Manufact.*, **33**, 508 – 515 (2019). <https://doi.org/10.1016/j.promfg.2019.04.063>.
- [148] M. Chatenat, B. G. Pollet, D. R. Dekel, F. Dionigi, J. Deseure, P. Millet, R. D. Braatz, M. Z. Bazant, M. Eikerling, I. Staffell, P. Balcombe, Y. Shao-Horn, H. Schäfer, Water electrolysis: from textbook knowledge to the latest scientific strategies and industrial developments. *Chem. Soc. Rev.*, **51**, 4583 (2022). <https://doi.org/10.1039/d0cs01079k>.

- [149] M. Roeb, S. Brendelberger, A. Rosenstiel, C. Agrafiotis, N. Monnerie, V. Budama, N. Jacobs, Wasserstoff als ein Fundament der Energiewende – Teil 1: Technologien und Perspektiven für eine nachhaltige und ökonomische Wasserstoffversorgung. Deutsches Zentrum für Luft- und Raumfahrt (DLR), (2020), Köln, https://www.dlr.de/content/en/downloads/2020/hydrogen-research-study-part-1.pdf;jsessionid=4C754FBF2F136800D66CF6F58129B1A3.delivery-replication2?__blob=publicationFile&v=2, accessed: September 2022.
- [150] Deutscher Bundestag, Wissenschaftliche Dienste, Ausarbeitung – Wasserstoffbedarf, WD 5 – 3000 – 024/22 (2022), Berlin, <https://www.bundestag.de/resource/blob/894040/0adb222a2cbc86a20d989627a15f4bd8/WD-5-024-22-pdf-data.pdf>, accessed: September 2022.

8. List of Figures

Figure 1. Potential sector coupling by green hydrogen adapted from [4]	2
Figure 2. The present work in brief with the three areas of investigation belonging to the two categories with potential cost savings.....	6
Figure 3. Summarized methodology of the thesis showing the individual steps for conducting the experiments and achieving the results	7
Figure 4. Sketch of electrolysis cell design a) State of Art, b) New Cell Design	10
Figure 5. Schematic illustration of PEM electrolysis cell components showing their electrochemical and mechanical interactions. The demonstrated components are represented by SEM images. However, the scale is different for the respective components and serves only to schematic representation.....	11
Figure 6. Schematic polarization curve splitted in its overpotentials associated with ohmic, kinetic and mass transport losses.....	15
Figure 7. Schematic Overview about flow field structures in PEMWE a) parallel, b) cascade, c) single serpentine, d) multiple serpentine	20
Figure 8. SEM images of PTL materials: a) sintered Ti, b) Ti felt and c) carbon paper	22
Figure 9. PID of the used in-house developed testbench	31
Figure 10. Testbench for standard PEM electrolysis cell operation with conventional BoP ..	33
Figure 11: Vacuum Plasma Spraying Technique	35
Figure 12. Scheme of PVD magnetron sputtering procedure adapted from [125].....	36
Figure 13: Interfacial Contact Resistance of a BPP sample	40
Figure 14: a) Nyquist plot of the EIS and the frequency-dependent assignment of the equivalent circuit diagram b) Electrical equivalent circuit diagram of the individual processes	43
Figure 15. PEMWE cost development within the last ten years based on literature values [5],[9],[17],[145],[146]	45
Figure 16. Cost breakdown of PEM electrolyzer based on Mayyas et al. ^[19]	45
Figure 17. Performance comparison of PTLs developed in Articles II and III. For comparability of the PTL developments, both components were tested at 90 °C and a Nafion115-based CCM was used.....	48

Figure 18. Potential cost savings compared to titanium based components with Au or Pt coating of a) stainless steel based Article I component (BPP) with respect to system upscaling and b) stainless steel based Article II component (PTL) with respect to system upscaling...	51
Figure 19. CAPEX development of Article II stack configuration depending on plant size	52
Figure 20. Updated Cost breakdown of PEM electrolyzer made almost entirely from stainless steel components.....	53
Figure 21. Hydrogen production cost of PEM electrolyzer stacks using the PTLs developed within Articles II and III compared to a SoA reference stack in 2020 based on an electricity price of 0.06 € kWh ⁻¹	54

9. List of Tables

Table 1. Classification and parameters of state of art of the respective electrolysis technologies [5],[8-11]	3
Table 2. Reaction equations and the particular potentials of electrochemical water splitting for PEMWE at standard conditions.	11
Table 3. Overview about used PTLs and their properties such as porosity, particle size, pore size, thickness or applied coatings found in the literature.	23
Table 4. Overview about PTL characteristics or features and their affection on PEMWE cell behavior	25
Table 5. PTL properties and their influence on cell parameters as cell potential, catalyst utilization or resistances correlating with cell performance.....	28
Table 6. Cell components developed within the scope of the present work that contribute to cost reduction in the respective stack configurations.	46
Table 7. Assumptions for estimating CAPEX as well as hydrogen production costs.	47

10. Scientific Articles

10.1 Article I

RESEARCH ARTICLE

ADVANCED
ENERGY & SUSTAINABILITY
RESEARCH

www.advenergysustres.com

Long-Term Operation of Nb-Coated Stainless Steel Bipolar Plates for Proton Exchange Membrane Water Electrolyzers

Svenja Stiber, Michael Hehemann, Marcelo Carmo, Martin Müller, Katherine E. Ayers, Christopher Capuano, Nemanja Danilovic, Tobias Morawietz, Indro Biswas, Pawel Gazdzicki, Jan-Frederik Heger, Aldo Saul Gago,* and Kaspar Andreas Friedrich

Proton exchange membrane water electrolysis (PEMWE) is the most promising technology for green hydrogen production using renewable electricity, but it is expensive due to the Ti bipolar plates (BPPs). Herein, a PEMWE stack with coated stainless steel (ss) BPPs (Nb/Ti/ss-BPP and Nb/ss-BPP) is reported, which operates for about 14 000 h at $1.63 \pm 0.12 \text{ A cm}^{-2}$ and 65°C . The average degradation rate is as low as 1.2% or $5.5 \mu\text{V h}^{-1}$. Scanning electrode microscopy reveals no signs of corrosion of the ss beneath the coatings. The interfacial contact resistance increases due to the formation of poorly conductive amorphous Nb oxides, as shown by atomic force microscopy and X-Ray photoelectron spectroscopy, although it does not affect the cell performance. The results prove that Ti is not needed anymore as base material for manufacturing the BPPs, thus the cost of PEMWE can be significantly reduced.

Hydrogen production by water electrolysis can decouple energy production from actual demand by storing electricity from renewable energies as hydrogen and using it when needed. In July 2021, the EU emphasized the importance of action and resolved the ambitious targets to reduce net emissions by at least 55% by 2030 compared to 1990 and to be the first climate-neutral continent by 2050.^[1] To this purpose, the share of renewable energies must be increased to 40%^[2] and hydrogen is to be used particularly in sectors such as industry or transport, where emissions are difficult to reduce.^[3] Therefore, large-scale electrolysis implementation is necessary for the conversion of surplus electricity from renewable energies sources like wind

or sun to green hydrogen which significantly promotes the reduction in global CO₂ emissions.^[4] In recent years, various companies are currently involved in the large-scale installation of electrolysis plants, for example, a recently installed 10 MW electrolysis plant at a Shell refinery which started operation in July 2021.^[5] However, with the scaling of electrolysis plants, the cost aspect is becoming increasingly important in order to be able to offer green hydrogen at competitive prices. The urgently needed cost reduction of electrolysis technologies can

1. Introduction

The current energy crisis, which is leading to an increasing demand for oil due to the shortage of coal and gas, makes it clear that the society must finally switch to renewable energies to become independent of fossil fuels. It is therefore necessary to tighten up the already ambitious targets of the political agreements and to push ahead with the expansion of renewable energies, with hydrogen playing a key role as an energy carrier.

S. Stiber, T. Morawietz, I. Biswas, P. Gazdzicki, A. S. Gago, K. A. Friedrich
Institute of Technical Thermodynamics/Electrochemical Energy
Technology
German Aerospace Center (DLR)
Pfaffenwaldring 38-40, 70569 Stuttgart, Germany
E-mail: aldo.gago@dlr.de

M. Hehemann, M. Carmo, M. Müller
Institute of Energy and Climate Research (IEK-14): Electrochemical
Process Engineering
Forschungszentrum Jülich GmbH
52425 Jülich, Germany

M. Carmo
Mechanical and Materials Engineering
Queen's University
Kingston, ON K7L 3N6, Canada

M. Carmo, K. E. Ayers, C. Capuano, N. Danilovic
Corporate Technology
Nel Hydrogen
10 Technology Drive, Wallingford, CT 06492, USA

N. Danilovic
Electric Hydrogen
835 East San Carlos Avenue, San Carlos, CA 94070, USA

T. Morawietz, J.-F. Heger
Faculty of Science, Energy and Building Services
University of Applied Sciences Esslingen
Kanalstrasse 33, 73728 Esslingen, Germany

K. A. Friedrich
Institute of Building Energetics
Thermal Engineering and Energy Storage (IGTE)
University of Stuttgart
Pfaffenwaldring 31, D-70569 Stuttgart, Germany

 The ORCID identification number(s) for the author(s) of this article can be found under <https://doi.org/10.1002/aesr.202200024>.

© 2022 The Authors. Advanced Energy and Sustainability Research published by Wiley-VCH GmbH. This is an open access article under the terms of the Creative Commons Attribution License, which permits use, distribution and reproduction in any medium, provided the original work is properly cited.

DOI: 10.1002/aesr.202200024

be realized by new operating standards with the objective to increase the hydrogen production rate^[6,7] and by the replacement of cost intensive materials.^[8,9]

Two different types of commercial electrolyzer technologies are available for low-temperature operation, namely, proton exchange membrane water electrolysis (PEMWE) and alkaline water electrolysis (AWE).^[10,11] Basically, the technologies in the field of electrolysis can be distinguished with regard to their electrolyte or separator, which significantly influences the applicability of the operating parameters. Considering the main factors for the widespread use of water electrolysis for hydrogen production such as performance, durability, cost, operating range, current density, and pressure level,^[12] PEMWE^[13–15] with solid electrolyte offers some advantages over AWE,^[16] especially for the use with intermittent renewables like wind and solar. Nevertheless, PEMWEs currently use costly materials, such as titanium and platinum group metals (PGM), due to the harsh oxidative conditions within the cells.

The component separating the two electrodes, namely, the polymer electrolyte membrane, consists of a proton conducting perfluorosulfonic acid (PFSA) proton exchange membrane ionomer. Iridium oxide is used as anode catalyst and platinum on the cathode. The other two important components are the porous transport layers (PTLs) and bipolar plates (BPPs). The PTL is responsible to provide effective transport of reactants and products between the electrodes and the BPP. Similarly, the BPP must enable uniform electrical connection to the PTL, as well as effective transport of water to and removal of the reaction gases from the PTL. In order to fulfill this demanding task, state of art (SoA) BPPs have more or less elaborate distribution structures that are formed into the plates. While steel-based BPP and—as well known from PEM fuel cell—carbon-based PTLs^[17] can be applied on the cathode side, Ti-based or similar corrosion resistive materials must be used for the two components on the anode side. Ti is sufficiently stable at the highly oxidative conditions caused by the oxygen concentrations and elevated cell potentials due to the formation of a dense oxide scale.^[16] Moreover, the manufacturing costs for inserting the manifold structure drive up the component costs. The BPPs can account for up to 60 % of the stack costs.^[18] Consequently, there are development approaches of the scientific community as well of the industry to reduce costs. A study from Ayers et al.^[19] showed a cost improvement by more than 50 % due to, among other things, reduction in titanium use, yield in manufacturing processes as well as lowering manual processes. Others range from surface treatments of the standard material Ti to its substitution. Toops et al. showed that nitrided Ti BPPs achieve higher conductivities and performance, although their long-term stability has not been investigated.^[20] In our previous work, it was already suggested that conventional BPPs for PEMWE can be basically made of stainless steel (ss) and protected from degradation by applying coatings made of Au,^[21] Pt, Ti, and Nb or combinations of them.^[22–24] However, these coatings were only evaluated in corrosion cells and short-term PEMWE tests. Therefore, the question about their long-term durability and thus their commercial applicability remained unanswered. Recently, Rojas et al. reported on Ti coatings on different ss-BPPs which were tested in a three-electrode corrosion cell revealing ss 321 with a Ti/TiN bilayer coating can be considered as BPP material for PEMWE.^[25] A measurement of

the component in a real PEMWE environment was not carried out. Niobium has been used and cited as an interesting candidate in the 1980s.^[26]

In this work, a long-term PEMWE test of about 14 000 h with standby and shutdown periods was performed, making it one of the longest PEMWE tests carried out by any R&D institute. The PEMWE stack with cost-effective coatings of Nb/Ti and Nb on ss-BPP substrates at the anode and uncoated ss-BPP at the cathode was operated at 65 °C, under a current range between 130 and 150 A and ambient pressure. Intensive posttest surface analysis on the BPPs was performed by interfacial contact resistance (ICR), scanning electron microscopy/energy dispersive X-Ray spectroscopy (SEM/EDS), atomic force microscopy (AFM), and X-Ray photoelectron spectroscopy (XPS) measurements. The novel plasma-sprayed Nb coating produced using a single-step method was successfully tested and compared to our previously reported Nb/Ti coating produced using a two-step coating technique. The results demonstrated a manageable degradation rate of 5.5 $\mu\text{V h}^{-1}$. Furthermore, the test showed that ss can indeed be used as a BPP material for PEMWE and can replace Ti as a commercial base material.

2. Experimental Section

2.1. Coating of ss-BPPs

2.1.1. Vacuum Plasma Spraying

Ti and Nb coatings were deposited via vacuum plasma spraying (VPS) on the ss (1.4401, SS316) plates with circular shape and an active area of 86 cm² from Nel Hydrogen. The coating procedure was already described in previous work for the titanium deposition process.^[22] In brief, the description including the details for Nb deposition via VPS is as follows. Before starting the spraying procedure, the substrates were sand-blasted with SiO₂ powder to increase surface roughness as well as adhesion of the coating powders and preheated to 250 °C in the vacuum chamber. Considerable parameters like the plasma gas flow rates of Ar, N₂, and H₂ were carefully chosen to achieve a plasma enthalpy of 21.3 MJ kg⁻¹ for Ti and Nb coating. A torch sweep rate of 350 mm s⁻¹ was used for both coatings. Ti powder (grade 1, grain size <45 μm , TLS Technik Spezialpulver) and Nb powder (grain size <45 μm , TLS Technik Spezialpulver) were sprayed in the VPS system at a chamber pressure of 50 mbar to avoid the oxidation of Ti and Nb. The coatings were thermally sprayed onto the ss substrates by varying the number of coating runs and thus applying 32 layers of Ti and Nb to the respective BPP. Finally, a full densification of the Nb coating was carried out using a capillary sealing process with an epoxy resin. To remove remaining air bubbles, a light vacuum was applied and the resin was fed into the pores. As soon as the samples have dried at 65 °C, the surfaces were polished. With this step the Nb/ss-BPP is manufactured, while the Ti-coated plate needs further modification described in the following section.

2.1.2. Physical Vapor Deposition

According to previous results of our group, to produce Nb/Ti/ss-BPP, the surface of Ti-coated BPP (Section 2.1.1) was modified

with Nb by magnetron sputtering physical vapor deposition (PVD).^[22] In short, after the thermally sprayed Ti surface was polished stepwise with SiC abrasive paper (Struers, SiC sand paper, SC 4000, diameter 200 mm) until an even surface was created, the Nb coating was applied. The metallic Nb coatings were deposited using an industry sized gas-flow assisted coater (MEGA, SYSTEC of Co. SVS, Germany). The substrate must be pretreated for 20 min by inverse sputter etching with argon plasma at 500 V pulse bias before coating with Nb. Finally, the Nb layers were deposited by applying a power of 1.0 kW for 15 min, so that a layer thickness of 1.4 μm was achieved, which was sealed using the aforementioned capillary sealing process.

2.2. Physical–Chemical Characterization

2.2.1. SEM and EDS

SEM was used for analyzing the coating quality, the morphology of the produced coated samples as well as analyzing the samples for possible changes after operation. The working distance and accelerating voltage were 9.2–9.5 mm and 15 kV, respectively. SEM analysis was performed using a JEOL 7200F FE SEM equipped with Bruker Quantax EDX spectrometer with XFlash detector. EDS mappings were performed with 1024 Pixels for each line and 10 measurements averaged. The EDS spectra were extracted from the mappings. Evaluation of the EDS measurements was done using Bruker Esprit Software.

2.2.2. Ion Cutting for Sample Preparation

In addition to the analysis of the surface, cross sections were prepared using a JEOL IB-1953° CP Cross Section Polisher. The samples were cut to approximately 0.5 × 1 cm² and then clamped into the sample holder of the ion cutting device. The BPP samples were cut using up to 8 kV accelerating voltage with subsequently enabled fine mode with 2 kV. Stage swing was used while keeping the argon ion beam on for 10 s and off for 5 s.

2.2.3. ICR

ICR versus compaction force measurements were performed on pristine and operated samples of a size of 30 × 30 mm² to evaluate the conductivity of the coatings. For the measurement, the BPPs were placed between two pieces of untreated carbon paper (Sigratherm CP) and two gold-coated copper cylinders. This sandwich-like assembly was placed into a hydraulic press to apply a pressure of 0.49–4.9 kPa in steps of 0.49 kPa. A potentiostat/galvanostat (Zahner Elektrik IM6) with a booster (Module PP240) was connected to the cylinders applying a constant current of 5 A while the response voltage was monitored. The ICR of the particular coatings was calculated by the following equation

$$R_{C/Coating} = R_{measured} - 2R_{C/Au} - R_{C/ss} \quad (1)$$

where $R_{C/Au}$ can be assigned to the ICR of the interface gold-coated cylinder and carbon paper, while $R_{C/ss}$ refers to the ICR of the interface of uncoated ss substrate to the carbon paper.

To investigate the ICR of the pristine coatings, the oxide layers on the surfaces of the samples were stepwise removed and

measured iteratively as described. As the Nb coating made by PVD is very thin, polishing with sanding paper would possibly remove the layers. Therefore, all coated surfaces were treated by Ar⁺ ion etching as described in Section 2.2.5 to partially remove the oxide layers. The uncoated sides of the BPPs were polished with sanding paper.

All samples were measured at least 3 times in order to give accurate error bars.

2.2.4. AFM

After the durability test, AFM measurements were performed on the samples surface. Nanomechanical properties as well as the electrical conductivity were recorded along with the height information. The samples were attached to a 12 mm steel disc with conductive double-sided carbon tape. AFM measurements were performed with a Bruker Multimode 8 AFM in PF-TUNA conductive tapping mode. A conductive doped diamond tip was used (Bruker DDESP) and a bias of 3 V was applied between the AFM tip and the sample.

2.2.5. XPS

The elemental and chemical compositions of the Nb coatings after the 14 000 h long-term test were investigated with X-Ray photoemission spectroscopy. In addition, the coatings were etched with a scanned Ar⁺ ion beam to stepwise etch the surface and to lay open the layer composition. The Nb 3d signals were analyzed in detail and deconvoluted to quantify the oxidation states of the compounds.

The analysis was carried out with a hemispherical electron analyzer (Thermo Scientific ESCALAB 250) in a vacuum chamber of a base pressure of 2 × 10⁻¹⁰ mbar. Samples were excited with a conventional Al Kα source (14 866 eV, 300 W). Spectra were energy calibrated with reference to the Ag 3d_{3/2} signal of a clean etched silver surface. Depth profiling by Ar⁺ ion bombardment was carried out with a scanning off-axis ion source (Thermo Scientific EX05) at Ar pressure of ≈2.5 × 10⁻⁸ mbar and with an average sample current density of 0.2 μA mm⁻². Numerical peak fitting of the recorded spectra was carried out using convoluted Gaussian/Lorentzian peak shapes (Unifit 2016).^[27]

2.3. PEM Water Electrolysis Long-Term Test

A Nel Hydrogen commercial stack was utilized for the long-term testing; the cell assembly consisted of Nb-coated ss-BPPs as well as one baseline BPP, the IEK-14 MEA from the Forschungszentrum Jülich (FZJ) and balance of cell components from Nel Hydrogen. The cells had an active area of 86 cm². To the best of our knowledge, it is the first time a short stack test platform is assembled using uncoated ss as cathode BPP with a flat flow field pattern. The stack was assembled in a four-cell configuration, having different anode BPP while only the following three were evaluated and operated for 14 000 h: 1) the commercial baseline material from Nel Hydrogen; 2) DLR Ti coating applied via VPS on ss, followed by a Nb coating via PVD on top as described in Sections 2.1.1 and 2.1.2 (Nb/Ti/ss-BPP);

and 3) DLR Nb coating applied via VPS on ss substrate plate (Nb/ss-BPP).

Furthermore, for the cell with the baseline material BPP a commercial catalyst-coated membrane (CCM) was used while for all other cells the CCMs were produced in-house using a Nafion 117 membrane with an Ir-based anode and Pt-based cathode electrode at loadings of 2.6 and 0.8 mg cm⁻², respectively. Figure 1a shows a magnified drawing of the evaluated stack with all components, while in b) the operated stack can be seen. For operation, the stack was implemented in a test stand that corresponds to the commonly used standard design for PEMWE.

Before starting the long-term test, a pressure test was performed at 1, 2, and 3 bars in order to detect possible leakage of the stack or the balance of plant (BoP). This initial pressure test is shown in Figure S1, Supporting Information. The stack was operated for 14 000 h between 130 and 150 A, while the anode temperature was kept constant at 65 °C. The 14 000 h test protocol did not include any previously planned shutdown

periods, yet these events occurred triggered by common test stations issues and common challenges found when operating test-rigs for such a long time. Figure S2a,b, Supporting Information, demonstrates the average cell voltage and the stack current over the whole period of operation, respectively. Our recently published test method for water electrolyzers was used.^[28] Polarization curves of the particular cells before and after stack operation for 14 000 h are plotted in Figure S3, Supporting Information.

3. Results and Discussion

3.1. Electrochemical Performance and Durability

Figure 2 shows the E_{Cell} over time measured at 1 A cm⁻², 1 bar, and at an average outlet temperature of 65 °C including shutdown/standby periods. Over 14 000 h one can observe that the cells with coated ss-BPP show a performance of $1.9 \text{ V} \pm 50 \text{ mV}$ at 1 A cm⁻² which is similar to the performance of the commercial baseline cell.

During the first 500 h of operation, initial issues with the test bench related to malfunction of the pumps and cooling system occurred and affected the stability of the measurement within this period. Furthermore, the resistivity of the water ($0.3 \mu\text{S cm}^{-1}$) fed into the anode increased tenfold during this time. The cell components had to be conditioned to the operating parameters, which means that particularly high ion release rates which decreased over time can be seen in the first 100 h with a commercial electrolyzer system.^[24] These impurities can be ascribed from different sources such as the feed water, BoP, membrane, or the catalysts.^[29] For example, Ca²⁺, Na⁺, Ni²⁺, Fe³⁺, F⁻, or Ir²⁺ can be released to the water loop^[30–32] and need to be removed to keep the feed water quality at acceptable levels. Moreover, the use of highly purified feed water and ion exchange resins slow down potential poisoning of the CCM which can cause an increase in cell potential.^[33] For the first 500 h of operation, an increase in E_{Cell} of 3.8% relative to E_{Cell} at the beginning of test (BoT) was observed. Therefore, an additional ion exchanger was installed to the feeding water circle to consequently bring down the water resistivity again to a constant value of $0.3 \mu\text{S cm}^{-1}$ due to the absorption of released ions. Consequently, stable cell operation was ensured for the remaining testing period. Between 5000 and 10 000 h of operation, the deviation between the particular cells increase on average to $\pm 25 \text{ mV}$ and afterward decrease again to $\pm 12 \text{ mV}$. During this period, the ion exchange resin was renewed two more times, which can explain the temporary increase and subsequent decrease in E_{Cell} . Calculating the degradation rate by dividing the difference in cell potential at BoT and end of test (EoT) by the operation time a value of $5.5 \mu\text{V h}^{-1}$ is determined. If the end of life of the stack is set at an average voltage of 2.2 V, this would mean a further 43 500 h of operation at this degradation rate, i.e., a total running time of the stack of approximately 57 000 h. This is in good agreement with an earlier long-term test reported by Ayers et al. reaching a degradation rate of $4 \mu\text{V h}^{-1}$ with the 2003 stack design using a total PGM loading of 10 mg cm^{-2} .^[34]

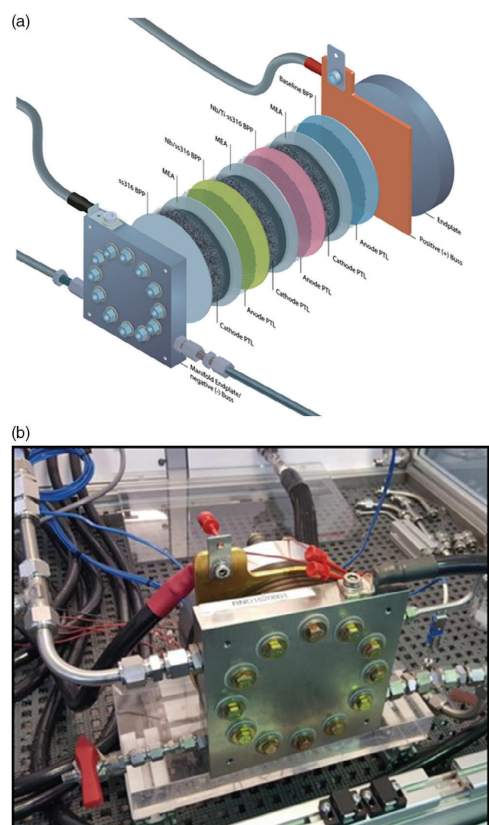


Figure 1. a) 3D explosion scheme of cell arrangement in the stack and b) photograph of the 14 000 h operated stack.

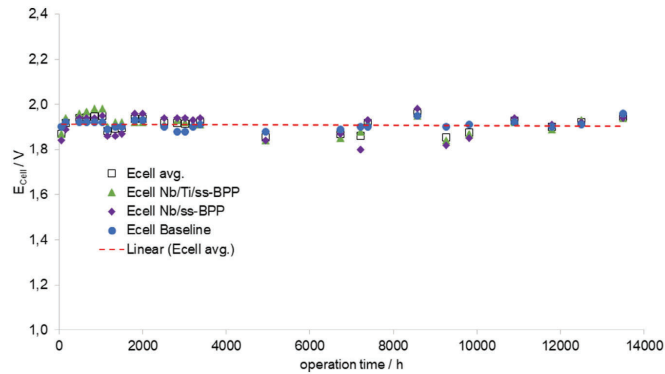


Figure 2. E_{Cell} over time of the 14 000 h long-term test measured at 1 A cm^{-2} , 1 bar, average outlet temperature of 65°C including shutdown/standby periods. The stack was operated under a current range between 130 and 150 A corresponding to an averaged current density of 1.63 A cm^{-2} .

When monitoring the degradation of each single cell, it turned out that the cell with Nb/Ti/ss-BPP did not show any increase of E_{Cell} , while E_{Cell} of the cell with Nb/ss revealed an increase of 2.7% over the first 2520 h. The cell having the baseline material resulted in a slight increase of cell potential by 0.53% in comparison to BoT. Consistently, it can be observed that at 59 h the cell performance decreases, but after 1155 h an increase in cell performance can be documented again, resulting at 2520 h in similar performances deviating by 1.1% as after 59 h. A slight difference in deviation of E_{Cell} among the cells can be due to intrinsic variations of catalyst loading, membrane thickness, and passivation of PTLs among the CCMs used. Nevertheless, it should be mentioned that the deviation of the cell voltages of all cells at 1 A cm^{-2} was only $\pm 1.2\%$ over the entire operation of 14 000 h.

3.2. Morphology of the Pristine and Operated BPPs

After the test was finalized, the morphology as well as possible impacts of PEMWE operation on the various coated anode BPPs, Nb/Ti/ss-BPP and Nb/ss-BPP, as well as one uncoated cathode plate were characterized physically. First, ICR measurements were carried out at different compression forces. The results are shown in Figure 3.

The results of the pristine samples are shown as dashed lines. The ICR values of the pristine Nb/Ti/ss-BPPs are in good agreement with the measurements of previous work.^[22] The ICRs of the operated samples were compared at 150 N cm^{-2} which lies within the pressure range for clamping of commercial stacks as reported by Lettenmeier et al.^[22] Compared to the pristine

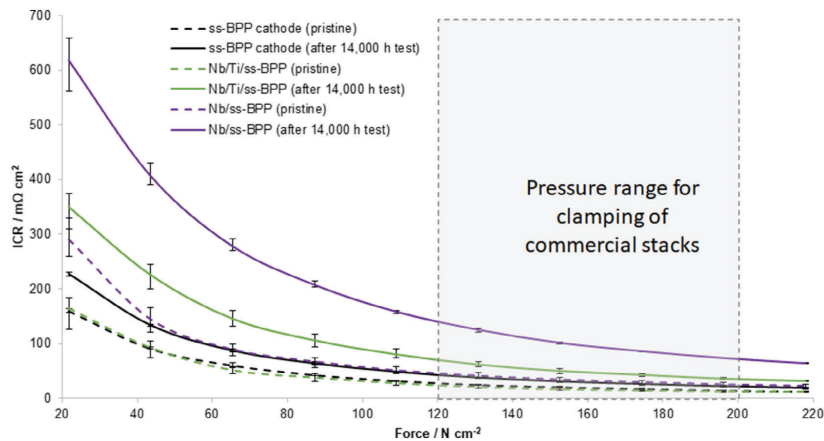


Figure 3. Interfacial contact resistance before and after 14 000 h operation at different compaction forces for uncoated ss, Nb/Ti/ss-BPP, and Nb/ss-BPP, respectively.

samples, the ICR increased by a factor of 1.5–30.6 $\text{m}\Omega \text{cm}^2$ for ss and by a factor of 3.0–49.8 and 101.4 $\text{m}\Omega \text{cm}^2$ for Nb/Ti-BPP as well as Nb/ss-BPP, respectively. One possible reason for the observed increase in contact resistance of the ss-BPP used on the cathode is due to hydrogen embrittlement. The resulting cracks and fractures lead to surface changes^[35,36] that can justify the results obtained. Similar to titanium,^[37–39] niobium forms a passive semiconductive oxide layer on its surface during electrolysis according to the following equation^[40]



Based on the operating temperature of the cell of 65 °C and assuming a $\text{pH} = 3$ ^[30] during operation, a standard potential of $E_0 = 0.284 \text{ V}$ results for Equation (2).

It is reported in the literature that the formed oxide layer on Ti during PEMWE operation leads to an increase in the ICR.^[24,25,41] Therefore, it is not surprising that the formed Nb pentoxide layer also leads to the observed increase in the contact resistance measurements.^[42,43] Furthermore, Nb/ss-BPP shows generally higher values what could be explained by a lower surface adherence of the Nb coating on ss substrate compared to the adherence on Ti substrate.^[22] Another reason can be given as the particles are not completely melted during VPS coating and larger grains are remained in the coating. These lead to a rougher surface whose remaining pores are filled with epoxy resin and consequently achieve a smaller contact area with the adjacent component than the Nb coating by PVD, which increases the contact resistance.

To verify these results, the surface and cross-sectional areas of the samples were further analyzed via SEM and EDS. Figure 4a,b

shows surface images of ss-BPP for the pristine and aged samples, respectively, while Figure 4c presents a cross-sectional image of ss-BPP after long-term test. Similarly, the figures for sample Nb/Ti/ss-BPP and Nb/ss-BPP can be found in Figure 4d–f,g–i, respectively. For the cathode ss-BPP images of pristine and for operated samples, degradation of the surface structure was observed and ascribed to hydrogen embrittlement as reported in the literature,^[35,44,45] explaining also the findings for ICR measurements. Further surface SEM images of ss-BPP showing the pristine and operated sample can be found in Figure S4, Supporting Information.

Clearly, the different surface structure of Nb of the two coated BPPs can be observed. While single Nb flakes can be seen for the pristine sample of Nb/Ti/ss-BPP, a homogeneous surface with a few fine scratches caused by polishing the sample was observed for Nb/ss-BPP. Comparing pristine Nb/Ti/ss-BPP with the operated sample, the particles on the surface become smaller and sharper by forming the oxide layer on top of the niobium flakes. Looking at the operated sample Nb/ss-BPP, the small scratches in the surface layer appear slightly deeper in some places. Likewise, the edges of the remaining pores on the surface look rougher than at BoT. Particularly in these areas, one can imagine that the water supplied for cell operation abrades these regions over an operating time. Lower magnifications of the surface of Nb/ss-BPP before and after operation show this more clearly and are shown in Figure S5, Supporting Information. Additionally, high-magnification images with 30 000× and 50 000× were performed and added in Figure S6 and S7, Supporting Information, for Nb/Ti/ss-BPP and Nb/ss-BPP, respectively, to show the grown surface oxide layer.

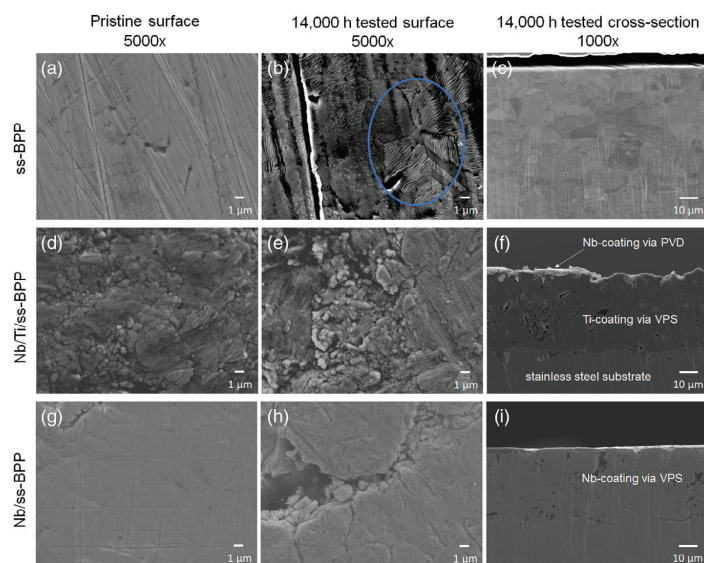


Figure 4. SEM images for ss-BPP, Nb/Ti/ss-BPP, and Nb/Ti-BPP are shown in a–c), d–f), and g–i). The first and second columns demonstrate surface images of the pristine and 14 000 h tested samples, respectively, while the third column display cross sectional images of the respective samples.

Additionally, cross-sectional images of the operated Nb/Ti/ss-BPP and Nb/ss-BPP are recorded and shown in Figure 4f,i, demonstrating both the morphology of the respective layers on the ss substrate and their functionality. The respective dense plasma sprayed Ti and Nb coatings in dark gray on the ss substrate are clearly visible and demonstrate the conventional splat structure due to their high enthalpy during the plasma coating deposition.^[23] The Nb coating applied on top of the Ti coating via PVD of Nb/Ti/ss is shown in a light gray and partially detached. While it is only visible on the left half of the specimen, on the right part of the image the underlying Ti coating shows through. EDS analysis of the surface was performed for Nb/Ti/ss-BPP and shown in Figure S8a, Supporting Information. Clearly, Ti from below the Nb coating can be detected distributed over the entire sample corroborating the findings from cross-sectional image. Furthermore, the analysis showed that some areas of the Nb coating delaminated on the surface for the operated Nb/Ti/ss-BPP compared to the pristine sample that is in good agreement with the observations of the surface SEM images. In contrast, the cross section of Nb/ss-BPP in Figure 4i shows a homogeneous and dense coating. Supplementary EDS mapping of ion-cut cross sections is shown in Figure S9, Supporting Information. A light gray line can be seen at the upper edge, which can be classified as an artifact due to radiation from the surface and thus an increased volume for secondary electron emission under the microscope. Based on the sample section, no deeper cracks extending to the subjacent substrate could be found. Therefore, the sample surface was examined via EDS (see Figure S8b,

Supporting Information). The analysis showed that the surface of this sample is basically intact. Likewise, single pores remaining from plasma spraying which are still closed with the epoxy resin for the operated sample. Generally, the EDS analysis demonstrated the high purity of all coatings that is necessary to protect the substrate materials from corrosion, although delamination of Nb was partially observed for Nb/Ti/ss-BPP. Furthermore, the increase in ICR for the metallic BPPs due to operation in the PEMWE does not seem to play a role, as it is not reflected in the cell performance or the material composition of the component. This is suggested by the fluctuation of all cells by 50 mV over the entire operating time, which value alone should come into play due to the ICR difference of $50 \text{ m}\Omega \text{ cm}^2$ at 150 N cm^{-2} . Considering the long operation time with the minor changes in the elemental composition and no signs of corrosion of the ss there is every indication that both coatings fully protect the substrate during operation and are satisfactory suitable for PEMWE.

3.3. Posttest Physical–Chemical Analysis of Operated BPPs

AFM measurements were carried out to investigate the structure and conductivity of the samples before and after operation. The results of pristine and aged samples are shown in Figure 5. After investigating the surface of the ss substrate, scratches and cracks were observed which can be correlated with structural changes in the surface layer of ss due to hydrogen uptake, as previously also found by Barrera et al.^[46] The hydrogen can easily

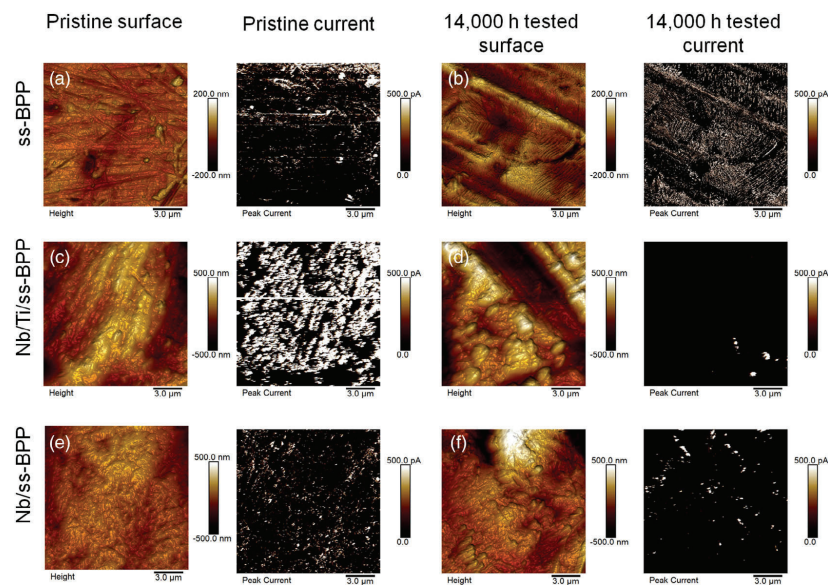


Figure 5. AFM images for uncoated ss BPP in a) pristine, b) operated; for Nb/Ti/ss-BPP in c) pristine, d) operated; and for Nb/ss-BPP in e) pristine and f) operated. The first and third columns present height profiles of the sample surfaces before and after 14 000 h operation, while columns 2 and 4 show the particular peak current measured on the sample surface of the pristine and operated samples, respectively.

diffuse in the ss structure even at room temperature. Hydrogen accumulates at microstructural defects such as voids, dislocations, grain boundaries, and precipitates.^[47] In addition to the cracks, protruding structures were observed. These structures show a possible high hydrogen concentration due to the metal displacement and are the starting point for the cracks. Together with the observations from the ICR measurements as well as the SEM images, a combined process of hydrogen uptake and corrosion is concluded as the cause for the present material change. As the investigations of Brightman et al. have shown,^[48] the cathodic potential increases significantly up to +0.9 V by a shutdown process and thus causes corrosion not only of the carbon support of the Pt/C catalyst but can thereby also lead to corrosion of the cathodic cell components such as the ss-BPP. It is assumed that due to this corrosion process, and the associated structural changes in the ss of the cathodic BPP, which in turn can serve as starting points for hydrogen uptake as previously described.

For anode samples, namely, Nb/Ti/ss-BPP and Nb/ss-BPP, it turned out that the conductivity decreased significantly after operation. To this purpose, substrate areas of $50 \times 50 \mu\text{m}^2$ were measured using in conductive tapping AFM mode and compared to each other. The conductive area at a bias of 3 V of the Nb/Ti/ss-BPP decreased from 44% to 3% after operation. The Nb/ss-BPP remained 12% conductive. For evaluation of the conductive area, all pixels with positive current values were considered. In addition, numerous $V(i)$ curves were recorded on the surface of the BPP and averaged to give a hint for the bandgap change after operation (Figure S10, Supporting Information). Here, one can see that the surface or interlayer oxide changed to a less conductive species. Alternatively, the thickness/surface coverage increased significantly. Both factors may result in a larger bandgap and less conductivity and was found for all evaluated cells. The lower conductivity of the sample surfaces confirms the results of the ICR measurement by structural change of the surface of ss or by formation of non- or less conductive oxide layers on the surface of Nb/Ti/ss-BPP and Nb/ss-BPP.

Furthermore, the height profile of Nb/Ti/ss-BPP surface demonstrated large deviations in the μm range. The valleys and heights can be conformed with the used PTL; the net was already visibly by the naked eye on the surface of the plate. The elemental mapping demonstrated that the oxide grows in between the contact points of the net.

Finally, XPS was carried out not only to prove elemental composition but also to evaluate the oxidation states formed on the surfaces. In Figure 6a,b, the XPS analysis for Nb/Ti/ss-BPP and Nb/ss-BPP is displayed. Impurities of Ca^{2+} , F^- , and Zn^{2+} were found on top of both plates which increased due to operation and most likely originated by feed water. To investigate the different oxide layer thicknesses, the samples were sputtered for 24 000 s while the oxide layers were removed stepwise. It can be seen that for the Nb/Ti/ss-BPP the overall oxygen content is higher than for the Nb/ss-BPP. This is unsurprising, given the observed smoothness of the Nb/ss-BPP (see Figure 4i), which leads to a smaller effective surface that can be oxidized and etched less effectively, and given the partially exposed titanium (see Figure S8a, Supporting Information) on the Nb/Ti/ss-BPP surface. Generally, the same oxidation states were found, namely, Nb^{+2} (NbO), Nb^{+4} (NbO_2), and Nb^{+5} (Nb_2O_5), while it needs

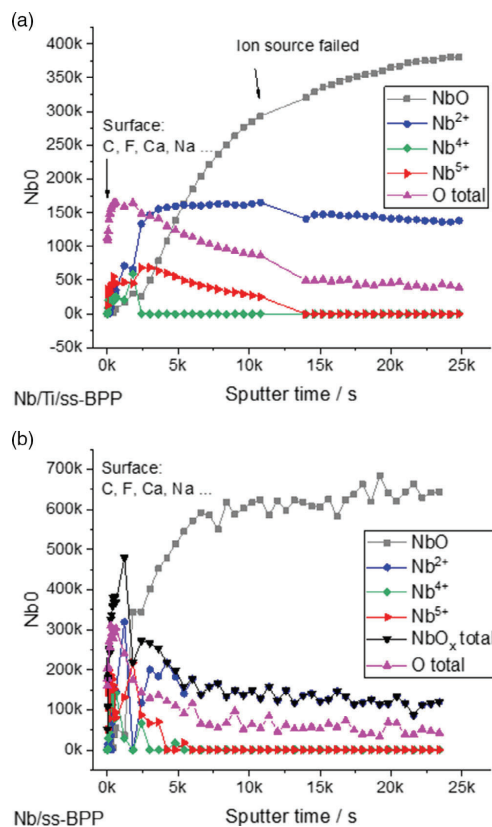


Figure 6. XPS analysis of the Nb oxides found for a) Nb/Ti/ss-BPP and b) Nb/ss-BPP.

to be stated that the surfaces probably were modified by the sputtering process itself. After sputtering of 24 000 s, Nb/Ti/ss-BPP showed still a residual oxide layer (NbO), while Nb/ss-BPP was completely reduced to metallic Nb. This difference can be caused either both by intermixing of NbO with TiO_2 at the interface of the Nb/Ti coatings,^[41] which is supported by partially layered open Ti interface (visible in Figure S8a, Supporting Information), or and by its higher surface roughness, which provides a shadow to averted faces of the coating particles in the given off-axis geometry of the Ar^+ beam, or both effects combined. Further results of the XPS analysis at different sputtering times are shown in Figure S11 and S12, Supporting Information, for Nb/Ti/ss-BPP and Nb/ss-BPP, respectively.

These findings can be translated into a thickness of oxide layer with about 400 nm for Nb/Ti/ss-BPP and 170 nm for Nb/ss-BPP. With this and the higher oxygen content for Nb/Ti/ss-BPP, it is very likely that an oxygen layer is formed in between Ti and Nb. Furthermore, they confirm the results from the AFM measurements, which showed a stronger formation of the surface

nonconducting oxide layer for Nb/Ti/ss-BPP compared to Nb/ss-BPP.

4. Conclusions

In summary, to date one of the longest PEMWE tests in the academy with a total operating time of 14 000 h was conducted with a stack having ss-BPPs, without precious metal coatings and no flow field is required. Here, we showed the results of a novel plasma-sprayed Nb-coated BPP in comparison to our previously evaluated Nb/Ti coating^[22] and the baseline material from Nel Hydrogen. Such BPPs were produced using a single manufacturing step, its performance tested, and evaluated in the long-term test. Both the cell with the Nb/Ti and the one with the Nb coating performed comparably to the baseline material from Nel Hydrogen. All cells delivered a cell voltage of about 1.9 V at 1 A cm⁻² over the entire operating time, which can be translated to a cell efficiency of nearly 78%. It should be emphasized that the degradation rate of the evaluated cells was only 1.2% or 5.5 μV h⁻¹, which is acceptable for commercial PEMWE stacks.

The posttest investigations of the two coated BPPs showed that, in general, both protect the ss substrate against corrosion and are suitable for use in PEMWE. However, from a cost perspective, the Nb coating offers a clear advantage over Nb/Ti, as it requires two processing steps to apply and form a thick and stable oxide layer. Moreover, the long-term test also demonstrated that the opportunity to use uncoated ss on the cathode side (hydrogen) of PEM electrolyzers, contributing to further cost reductions of these devices.

In conclusion, Ti as a base material for the manufacture of BPP can be replaced by ss, thus reducing the cost for a PEMWE cell even further. Herein, the results achieved can mark a turning point for future electrolysis research, in which steel-based stack components are seen as the new standard, laying the foundation for the massive cost reduction in PEMWE and thus an essential factor for the production of competitive green hydrogen. With this, the widespread use of PEM water electrolyzers for the large-scale integration of renewable energies is advanced.

Supporting Information

Supporting Information is available from the Wiley Online Library or from the author.

Acknowledgements

The research leading to these results has received funding from the Helmholtz-Gemeinschaft Deutscher Forschungszentren e.V. (HGF). The authors thank to Jörg Bürkle and Vincent Wilke for performing technical support. Finally, the authors thank Noriko Sata for providing measurements for the preparation of the revised version.

Conflict of Interest

The authors declare no conflict of interest.

Author Contributions

S.S.: carried out the interfacial contact resistance measurements. T.M.: performed SEM/EDS and AFM measurements. J.F.H.: was responsible for sample preparation and ion cutting. I.B.: carried out XPS measurements and ion beam etching. M.H., M.M., and M.C.: as well as C.C. and K.A. carried out the PEMWE measurements. A.S.G.: led the posttest analysis and characterization of the BPPs. K.A.F.: supervised the overall work in regular discussions. All the authors contributed to writing and proofing the manuscript.

Data Availability Statement

The data that support the findings of this study are available from the corresponding author upon reasonable request.

Keywords

bipolar plates, long-term stability, PEM electrolyzers, PEM electrolysis, stainless steels

Received: February 11, 2022

Revised: April 30, 2022

Published online:

- [1] European Commission, Communication from the commission to the European Parliament, the Council, the European Economic and Social Committee and the Committee of the Regions – 'Fit for 55': delivering the EU's 2030 Climate Target on the way to climate neutrality, 2021, <https://eur-lex.europa.eu/legal-content/EN/TXT/PDF/?uri=CELEX:52021DC0550&from=EN>.
- [2] European Commission, Energy Factsheet, 2021, https://ec.europa.eu/commission/presscorner/detail/en/fs_21_3672.
- [3] European Commission, Hydrogen Factsheet, 2021, https://ec.europa.eu/commission/presscorner/detail/en/fs_21_3676.
- [4] A. Van Wijk, J. Chatzimarkakis, Green Hydrogen for a European Green Deal – A 2x40 GW Initiative, Hydrogen Europe, 2020, https://hydrogeneurope.eu/sites/default/files/Hydrogen%20Europe_2x40%20GW%20Green%20H2%20Initiative%20Paper.pdf.
- [5] REFHYNE, Clean Refinery Hydrogen for Future, 2020, <https://refhyne.eu/>.
- [6] M. Sartory, E. Wallnöfer-Ogris, P. Salman, T. Fellingner, M. Justl, A. Trattner, M. Klell, *Int. J. Hydrogen Energy* 2017, 42, 30493.
- [7] S. Stiber, H. Balzer, A. Wierhake, F. J. Wirkert, J. Roth, U. Rost, M. Brodmann, J. K. Lee, A. Bazylak, W. Waiblinger, A. S. Gago, K. A. Friedrich, *Adv. Energy Mater.* 2021, 11, 2100630.
- [8] P. Shirvanian, F. Van Berkel, *Mini Rev. Electrochem. Commun.* 2020, 114, 106704.
- [9] S. Stiber, N. Sata, T. Morawietz, A. S. Ansar, T. Jahnke, J. K. Lee, A. Bazylak, A. Fallisch, A. S. Gago, K. A. Friedrich, *Energy Environ. Sci.* 2021, 15, 109.
- [10] FCH-JU, Addendum to the Multi-Annual Work Plan 2014-2020, Fuel Cells and Hydrogen 2 Joint Undertaking, 2018.
- [11] International Energy Agency (IEA). The Future of Hydrogen – Seizing today's opportunities, 2019, <https://webstore.iea.org/download/direct/2803>.
- [12] P. K. Shen, C.-Y. Wang, S. P. Jiang, X. Sun, J. Zhang, *Electrochemical Energy – Advanced Materials And Technologies*, CRC Press 2017.
- [13] A. Buttler, H. Spliethoff, *Renewable Sustainable Energy Rev.* 2018, 82, 2440.

- [14] M. Bernt, J. Schröter, M. Möckl, H. A. Gasteiger, *J. Electrochem. Soc.* **2020**, *167*, 124502.
- [15] M. Suermann, A. Patru, T. J. Schmidt, F. N. Büchi, *Int. J. Hydrogen Energy* **2017**, *42* 12076.
- [16] M. Carmo, D. L. Fritz, J. Mergel, D. Stolten, *Int. J. Hydrogen Energy* **2013**, *38*, 4901.
- [17] S. Park, J.-W. Lee, B. N. Popov, *Int. J. Hydrogen Energy* **2012**, *37*, 5850.
- [18] L. Bertuccioli, A. Chan, D. Hart, F. Lehner, B. Madden, E. Standen, Study on Development of Water Electrolysis in the EU by E4tech Sarl with Element Energy Ltd for the Fuel Cells and Hydrogen Joint Undertaking, **2014**.
- [19] K. Ayers, N. Danilovic, R. Ouimet, M. Carmo, B. Pivovar, M. Bornstein, *Annu. Rev. Chem. Biomol. Eng.* **2019**, *10*, 219.
- [20] T. J. Toops, M. P. Brady, F.-Y. Zhang, H. M. Meyer, K. Ayers, A. Roemer, L. Dalton, *J. Power Sources* **2014**, *272*, 954.
- [21] A. S. Gago, A. S. Ansar, P. Gazdzicki, N. Wagner, J. Arnold, K. A. Friedrich, *ECS Transaction* **2014**, *64* 1039.
- [22] P. Lettenmeier, R. Wang, R. Abouatallah, B. Saruhan, O. Freitag, P. Gazdzicki, T. Morawietz, R. Hiesgen, A. S. Gago, K. A. Friedrich, *Sci. Rep.* **2017**, *7*, 44035.
- [23] A. S. Gago, S. A. Ansar, B. Saruhan, U. Schulz, P. Lettenmeier, N. A. Cañas, P. Gazdzicki, T. Morawietz, R. Hiesgen, J. Arnold, K. A. Friedrich, *J. Power Sources* **2016**, *307*, 815.
- [24] P. Lettenmeier, R. Wang, R. Abouatallah, F. Burggraf, A. S. Gago, K. A. Friedrich, *J. Electrochem. Soc.* **2016**, *163*, F3119.
- [25] N. Rojas, M. Sánchez-Molina, G. Sevilla, E. Amores, E. Almandoz, J. Esparza, M. R. Cruz Vivas, C. Colominas, *Int. J. Hydrogen Energy* **2021**, *46*, 25929.
- [26] J. H. Russell, Solid Polymer Electrolyte Water Electrolysis Technology Development for Large-Scale Hydrogen Production. General Electric Co., Wilmington, MA, US, DOE/ET/26 202-1, US Department of Energy, **1981**.
- [27] R. Hesse, T. Chassé, R. Szargan, *Fresenius J. Anal. Chem.* **1999**, *365*, 48.
- [28] G. Bender, M. Carmo, T. Smolinka, A. Gago, N. Danilovic, M. Mueller, F. Ganci, A. Fallisch, P. Lettenmeier, K. A. Friedrich, K. Ayers, B. Pivovar, J. Mergel, D. Stolten, *Int. J. Hydrogen Energy* **2019**, *44*, 9174.
- [29] X. Wang, L. Zhang, G. Li, G. Zhang, Z.-G. Shao, B. Yi, *Electrochim. Acta* **2015**, *158*, 253.
- [30] Q. Feng, X. Z. Yuan, G. Liu, B. Wei, Z. Zhang, H. Li, H. Wang, *J. Power Sources* **2017**, *366*, 33.
- [31] M. Langemann, D. L. Fritz, M. Müller, D. Stolten, *Int. J. Hydrogen Energy* **2015**, *40* 11385.
- [32] N. Li, S. S. Araya, S. K. Kær, *J. Power Sources* **2019**, *434*, 226755.
- [33] S. Sun, Z. Shao, H. Yu, G. Li, B. Yi, *J. Power Sources* **2014**, *267*, 515.
- [34] K. E. Ayers, J. N. Renner, N. Danilovic, J. X. Wang, Y. Zhang, R. Maric, H. Yu, *Catal. Today* **2016**, *262*, 121.
- [35] E. Herms, J. M. Olive, M. Puiggali, *Mater. Sci. Eng.* **1999**, *A272*, 279.
- [36] S. K. Dwivedi, M. Vishwakarma, *Int. J. Hydrogen Energy* **2018**, *43* 21603.
- [37] N. K. Kuromoto, R. A. Simão, G. A. Soares, *Mater. Charact.* **2007**, *58* 114.
- [38] D. Bessarabov, H. Wang, H. Li, N. Zhao, *PEM Electrolysis For Hydrogen Production: Principles And Applications*, CRC Press, Boca Raton FL **2015**.
- [39] J.-T. Wang, W.-W. Wang, C. Wang, Z.-Q. Mao, *Int. J. Hydrogen Energy* **2012**, *37*, 12069.
- [40] E. Asselin, T. M. Ahmed, A. Alfantazi, *Corros. Sc.* **2007**, *49*, 694.
- [41] C. Liu, M. Shviro, A. S. Gago, S. F. Zaccarine, G. Bender, P. Gazdzicki, T. Morawietz, I. Biswas, M. Rasinski, A. Everwand, R. Schierholz, J. Pfeilsticker, M. Müller, P. P. Lopes, R.-A. Eichel, P. Bryan, S. Pilypenko, K. A. Friedrich, W. Lehnert, M. Carmo, *Adv. Energy Mat.* **2021**, *11*, 2002926.
- [42] S. Lædre, O. E. Kongstein, A. Oedegaard, H. Karoliussen, F. Seland, *Int. J. Hydrogen Energy* **2017**, *42*, 2713.
- [43] A. Kellenberger, D. Duca, N. Vaszilcsin, C. M. Craciunescu, *Int. J. Electrochem. Sci.* **2020**, *15*, 10664.
- [44] H. G. Nelson, *Treatise Mater. Sci. Technol.* **1983**, *25*, 275.
- [45] D. Eliezer, *J. Mater. Sci.* **1984**, *18*, 1540.
- [46] O. Barrera, D. Bombac, Y. Chen, T. D. Daff, E. Galindo-Nava, P. Gong, D. Haley, R. Horton, I. Katzarov, J. R. Kermode, C. Liverani, M. Stopher, F. Sweeney, *J. Mater. Sci.* **2018**, *53*, 6251.
- [47] A. Pundt, R. Kirchheim, *Annu. Rev. Mater. Res.* **2006**, *36*, 555.
- [48] E. Brightman, J. Dodwell, N. van Dijk, G. Hinds, *Electrochem. Commun.* **2015**, *52*, 1.



Cite this: DOI: 10.1039/d1ee02112e

A high-performance, durable and low-cost proton exchange membrane electrolyser with stainless steel components†

S. Stiber,^a N. Sata,^b T. Morawietz,^a S. A. Ansar,^a T. Jahnke,^b J. K. Lee,^c
A. Bazylak,^d A. Fallisch,^d A. S. Gago^{id}*^{ae} and K. A. Friedrich^{id}^{ae}

Proton exchange membrane water electrolysis (PEMWE) is the most promising technology for sustainable hydrogen production. However, it has been too expensive to compete with current state-of-the-art technologies due to the high cost of titanium bipolar plates (BPPs) and porous transport layers (PTLs). Here, we report a high-performance, durable and low-cost PEMWE cell with coated stainless steel (ss) BPPs and PTLs. When using uncoated ss components in the PEMWE cell, the cell depolarizes rapidly, reaching 2 V at only 0.15 A cm⁻². After the application of non-precious metal coatings of Ti and Nb/Ti on the ss-BPP and ss-PTL, respectively, the current density can be increased by a factor of 13 while maintaining the same performance. Extensive physical and electrochemical characterization supported by pore network modelling shows that the Nb/Ti coating on the ss-PTL leads to efficient water and gas transport at the interface with the anode. The PEMWE cell with coated ss components was evaluated in an accelerated stress test (AST) for more than 1000 h. No sign of Fe contamination in either the membrane or the electrodes is observed at the end of the test. With our results, we demonstrate that PEMWE cells can be manufactured almost entirely in ss, facilitating an unprecedented cost reduction in this technology and advancing the widespread use of green H₂.

Received 8th July 2021,
Accepted 22nd September 2021

DOI: 10.1039/d1ee02112e

rsc.li/ees

Broader context

Global warming due to high CO₂ emissions worldwide is one of the greatest challenges of the 20th century. In the last few years, it has become clear that the current political agreements and efforts will probably not contribute to a sufficient reduction of CO₂ emissions. Besides energy and heat generation, the chemical industry and the mobility sector are some of the largest emitters of CO₂. Alternatives to the use of fossil fuels must be found for the respective sectors and integrated into the processes in order to stop the steady upward trend. It is therefore essential to tighten up the already ambitious targets set out in the Paris Agreement and to push ahead the expansion of renewable energies. However, energy supply based on renewable energies entails dependence on weather conditions and geographical locations. Both, wind and sun, are not necessarily available when and where energy is needed. Here, hydrogen production *via* water electrolysis using renewable electricity (green hydrogen) can decouple energy production from actual demand in terms of time, and energy can thus be stored. Proton exchange membrane water electrolysis (PEMWE) is the most suitable technology for this purpose but is still expensive and mainly due to the use of titanium for manufacturing stack components such as bipolar plates (BPP) and porous transport layers (PTLs). Herein, we report a PEMWE cell that is almost fully made of stainless steel, exhibiting high performance and durability. As BPPs and PTLs are made of titanium, the most expensive components of the electrolyzer stack, a significant cost reduction in this technology has been achieved by showing that they can be manufactured in stainless steel. This PEMWE cell with stainless steel components will contribute to the widespread production of green hydrogen.

^a Institute of Engineering Thermodynamics/Electrochemical Energy Technology, German Aerospace Center (DLR), Pfaffenwaldring 38-40, 70569 Stuttgart, Germany. E-mail: aldo.gago@dlr.de; Fax: +49 711 6862-747; Tel: +49 711 6862-8090

^b Institute of Engineering Thermodynamics/Computational Electrochemistry, German Aerospace Center (DLR), Pfaffenwaldring 38-40, 70569 Stuttgart, Germany

^c Department of Mechanical and Industrial Engineering, Faculty of Applied Science and Engineering, University of Toronto Institute for Sustainable Energy, University of Toronto, Toronto, Ontario, M5S 3G8, Canada

^d Fraunhofer-Institut für Solare Energiesysteme ISE, Heidenhofstraße 2, 79110 Freiburg, Germany

^e Institute of Building Energetics, Thermal Engineering and Energy Storage (IGTE), University of Stuttgart, Pfaffenwaldring 31, 70569 Stuttgart, Germany

† Electronic supplementary information (ESI) available. See DOI: 10.1039/d1ee02112e

1. Introduction

Currently, the main commercial electrolytic technologies for the large-scale production of hydrogen are alkaline water electrolysis (AWE) and proton exchange membrane water electrolysis (PEMWE).¹ AWE is already a well-developed technology, but issues in terms of gas purity, safety and response time remain.² PEMWE, on the other hand, is a promising candidate that exhibits high efficiency, a rapid response and a wide dynamic operation range within an easy-to-maintain compact design and a simple auxiliary system.³ The main drawback of



View Article Online

Paper

Energy & Environmental Science

PEMWE compared with that of alkaline water electrolysis is the high capital cost: €600 kW⁻¹ alkaline vs. €900 kW⁻¹ PEMWE.⁴

The main components of a PEMWE cell are the catalyst coated membrane (CCM), porous transport layers (PTLs) and bipolar plates (BPPs). The CCM consists of iridium and ruthenium oxides (IrO₂-RuO₂) as the anode and platinum nanoparticles supported on carbon (Pt/C) as the cathode. Besides the BPPs, the PTL is one of the key components of a PEMWE cell that allows effective transport of reactant water to the electrodes while facilitating gas removal towards the flow field of the BPP. Efficient gas/water management has a high impact on the cell performance due to the reduction in mass transport losses.⁵⁻⁷ On the cathode side, carbon paper is a state-of-the-art PTL material, which is often used in PEM fuel cells (FC).⁸ On the anode side, titanium is widely used for PTLs since titanium can withstand the harsh conditions of a highly concentrated O₂ environment and elevated cell potentials (>2 V).³ Commercially available PTLs for the anode include sintered powders, felts, and meshes sold by companies such as GKN Sinter Metals, Bekaert and Melicon, respectively. Recent developments have included tunable PTLs with controlled porosities,^{9,10} and pore structures with a size gradient.^{11,12}

Manufacturing sophisticated porous structures such as sintered powders or felts in titanium is cost prohibitive. Moreover, to avoid passivation, which leads to an increase in cell voltage over time,^{13,14} titanium must be coated with platinum group metals (PGMs). A stainless steel PTL (ss-PTL) would be preferable, but it severely corrodes, thus poisoning the CCM with Fe and Ni.^{15,16} Our previous developments have demonstrated that it is possible to use ss as a base material for manufacturing the BPP. A dense coating applied by plasma spraying provides full protection against corrosion in the aggressive PEMWE environment.¹⁷ These coatings have been integrated into commercial electrolyser stacks and tested for more than 1000 h without the ss substrate showing any signs of corrosion.^{18,19} Likewise, physical vapor deposition (PVD) applied Ti/TiN coatings on steel components could be considered for anode-side application in PEMWE cells, which have already been evaluated for their suitability by N. Rojas *et al.*²⁰ However, a test in a real PEMWE cell was not carried out here. Complementing the anode-side use of the Nb/Ti coated steel BPP, Shirvanian P. *et al.* see laser-treated 316L stainless steel, carbon-based and nitride coatings on stainless steel, as already investigated for the PEMFC cell, as possible components for cathode-side use as the BPP in PEMWE cells.²¹

Depending on the cell configuration, *e.g.*, with or without a flow field in the BPP, the PTL and the BPP together approximately represent between 70%²² and 60%²³ of the PEMWE stack cost. The cost of Ir catalyst is the other key cost driver in PEMWE systems and it will become increasingly important as the large-scale manufacturing cost of PTLs and BPPs is reduced. There have been some attempts to use ss-PTLs in PEMWE cells. J. Mo *et al.* tested an uncoated mesh type ss-PTL in a PEMWE cell.¹⁶ The ss-PTL corroded rapidly and the realised Fe poisoned heavily the CCM. Another attempt was made by N. F. Daut *et al.* in which they sintered a Nb coating on a ss-PTL.²⁴ From their PEMWE tests,

one can notice that the slopes of their polarization curves with the coated ss-PTL bend sharply upwards at *ca.* 1 A cm⁻², which is an indication of either mass transport losses or severe degradation. The authors do not report any stability test though.

A complete PEMWE stack manufactured mainly in ss, that is, PTLs and BPPs, remains an important challenge. Such a stack could drastically reduce the PEMWE cost for large-scale applications, making green hydrogen more competitive. In this work, we report the first efficient, stable and high performance PTL made of ss coated with non-precious Nb/Ti metal by plasma spraying. The coating not only protects the PTL against corrosion but also significantly improves the cell performance. Through extensive characterization and numeric simulation, we provide a comprehensive explanation of this improved performance. The coated ss-PTLs in combination with our previous development of coated ss-BPPs allow the production of a PEMWE cell with all metallic components made of ss, thus marking an unprecedented cost reduction in this technology.

2. Methods

2.1. Plasma-sprayed coatings

Coatings of Nb/Ti were produced by vacuum plasma spraying (VPS) on 4-layer mesh-type ss PTLs (GDL MeliDiff in 1.4404, Melicon GmbH). The chamber pressure was 40 mbar. The coating powders were grade 1 Ti (TLS Technik Spezialpulver) and Nb (H.C. Starck, currently FST Flame Spray Technologies) with a particle size of <45 μm. The gas flow rates of Ar, N₂ and H₂ were carefully controlled to achieve the needed plasma enthalpy of 12.5 MJ kg⁻¹ for the Ti and Nb layers. Six coating runs with Ti were first applied; specifically, the plasma spray gun was oscillated over the substrates six times during the coating process. Subsequently, two additional coating runs of Nb were sprayed on top of the finest mesh of the multi-layer mesh-type PTL. The torch sweep rates were 600 mm s⁻¹ for all the samples. Before deposition, the PTL substrates were heated to 250 °C. The produced PTL is labelled Nb/Ti/ss-PTL. In Fig. 1 the ss-PTL sample with the Nb/Ti coating is shown schematically. For comparison purposes, similar coatings were applied on 4-layer mesh-type Ti-PTLs (GDL MeliDiff in Ti Grade 1, Melicon GmbH). The resulting sample is labelled Nb/Ti/Ti-PTL.

2.2. Physical characterization

2.2.1. Scanning electron microscopy (SEM). SEM was used to analyse the morphology of the produced coated samples. For all samples, cross-sectional images were recorded with an FE-SEM Zeiss ULTRA plus in secondary electron mode with charge compensation. The working distance and accelerating potential were between 8.0 and 8.3 mm and 20 kV, respectively. The purity of the Nb/Ti coatings was determined by energy-dispersive X-ray spectroscopy (EDS) using an annular backscatter detector (AsB) for high material contrast. For the elemental mapping on post-tested CCMs, a JEOL JSM7200F equipped with a Bruker Quantax energy-dispersive X-ray system was used. The working distance was between 10.2 and



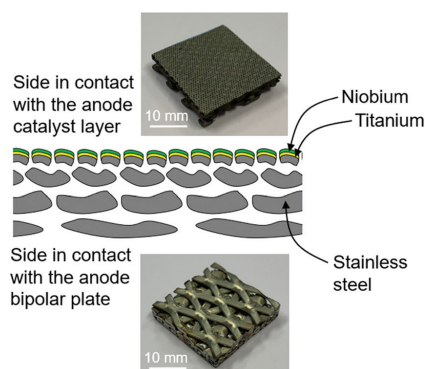


Fig. 1 Scheme of the ss-mesh PTL with a plasma-sprayed Nb/Ti coating at the interface with the anode catalyst layer.

12.5 mm, while the accelerating potential was reduced to 15 kV. The mapping was performed with 2 μm per pixel and a pixel time of 128 μs for 10 cycles. The images were averaged with Esprit 2 software for noise reduction.

2.2.2. Mercury intrusion porosimetry (MIP) and X-ray computed tomography (CT). The porosities of the Nb/Ti coatings on ss-PTL and Ti-PTL were determined by MIP up to a pressure of 200 MPa (Pascal 140/240, Thermo Scientific). Prior to the measurements, the samples ($\sim 1 \times 2 \text{ cm}^2$) were dried in an oven at 60 $^\circ\text{C}$ overnight. Since the MIP of the coated samples was performed on the top mesh of the PTL substrates, the obtained pore volume was the overall sum in both the finest mesh of the substrate and the coating. The geometrical parameters of the samples were taken into consideration, and their mathematical formulation is provided in eqn (1), with which the coating porosity can be estimated:

$$p_{\text{coat}} = \frac{1}{\left(1 + \frac{m_{\text{coat}} \times 1000}{\delta_{\text{theoretical}} \times V_{\text{coat}}^{\text{p}} \times m_{\text{sample}}}\right)} \quad (1)$$

here, p_{coats} , $V_{\text{coat}}^{\text{p}}$ [$\text{mm}^3 \text{ g}^{-1}$], m_{sample} [g], m_{coat} [g] and $\delta_{\text{theoretical}}$ [g cm^{-3}] are the coating porosity, pore volume of the coating per total sample weight, total sample weight, weight of the coating and theoretical density of the coating, respectively. Classically, the quotient of the pore volume of the sample given by the MIP and the sample volume is used. However, for samples made of a relatively thick substrate and thin coating, this calculation becomes inaccurate. Therefore, $V_{\text{coat}}^{\text{p}}$ is calculated based on data from two measurements by subtracting the pore volume of the uncoated mesh, which was determined by MIP, from the total pore volume of the sample, *i.e.*, the substrate and coating. m_{coat} is calculated using the weight ratios of the mesh before and after coating.

X-ray CT analysis was performed with a multi-scale X-ray nanotomograph (Skyscan 2211, Bruker). The reconstructed sample volume was $484.4 \times 1386 \times 1649.9 \mu\text{m}^3$, achieving a

resolution of 0.7 μm . An acceleration potential of 70 kV was used.

2.2.3. Interfacial contact resistance. The effect of the Nb/Ti coating on the interfacial contact resistance (ICR) of the ss-PTLs with respect to the compaction force was measured based on the method previously reported for measuring the coated BPP.¹⁹ First, all PTL samples were cleaned before being measured by immersing them in deionized (DI) water and isopropanol baths and applying ultrasonication for 10 minutes after each step. The last cleaning cycle was carried out with DI water for 5 minutes, and thereafter, the PTL samples were placed in an oven for 20 minutes at 60 $^\circ\text{C}$. Second, ICR measurements were performed by sandwiching the cleaned PTLs with a titanium plate (3.7025) and a TGP-H-90 between two gold-coated copper cylinders (inset of Fig. 5). The experimental setup was set in a hydraulic press, and a weight of 20 to 200 kg was applied in steps of 20 kg. The cylinders were connected to a potentiostat/galvanostat (Zahner Elektrik IM6) with a booster (Module PP240). A constant current of 1.25 A cm^{-2} was applied, and the response voltage was monitored. The ICR between the carbon paper and the Nb/Ti coating was determined by $R_{\text{C/Coating}} = R_{\text{measured}} - R_{\text{C/Au}}$, where $R_{\text{C/Au}}$ is the ICR of the carbon paper with the Au-coated cylinder. The Nb/Ti/Ti-PTL, uncoated Ti-PTL and ss-PTL were also measured for comparison purposes.

2.3. Pore network modelling

Pore network modelling (PNM) was conducted to elucidate the microscale mass transport behaviour on the Nb/Ti coating. Due to the vastly different length scales in the mesh pores, only the finest mesh layer and the Nb/Ti coating were considered as the simulation domain. Based on the CT images, a binarized 3D reconstruction was created using GeoDict[®].²⁵ The resolution was 0.7 microns per pixel, and the domain was cropped to $1250 \times 1250 \times 230$ pixels. The pore network was extracted from the binarized CT images using the marker-based watershed segmentation algorithm developed by Gostick *et al.*²⁶ In the pore network simulations, the pores of the network were represented with spheres connected by cylindrical throats, while the spatial distribution of the pores and the total void space were kept intact. The simulation was performed using an open source PNM package, OpenPNM.²⁷ The drainage of a wetting phase (liquid water) due to the invasion of a non-wetting phase (oxygen gas) was simulated on the coating network. In this drainage process, all throats connected to the inlet surface satisfying the entry (threshold) capillary pressure were invaded. The entry threshold capillary pressure of the cylindrical throats was approximated using the Young-Laplace equation:

$$P_c = \frac{2\gamma \cos \theta}{r} \quad (2)$$

where γ is the surface tension [N m^{-1}], θ is the contact angle [radians], and r is the radius of the throat [m].

2.4. PEMWE tests

Conventionally, PEMWE cell components are tested in a setup such as that shown in Fig. 2a. In this system, fresh DI water is



continuously pumped through the PEMWE cell, entering separately on each electrode side through the inlets. It flows through the PTLs to the active site of the catalyst layers and then exits the cell through the outlets. Subsequently, the water and the product gases are driven to the anode and cathode water loops that make up the balance of the plant and include many components, such as ss pipes, pumps, gas separators, water conductivity sensors, ion exchange resins, and electro-mechanical valves. In this setup, cell degradation due to the poisoning of the CCM by the transport of metal ions can require thousands of hours of operation.^{28,29} Most of the corrosion products from the cell will redeposit on the metallic parts that comprise the balance of plant (BoP), and only after long-term periods will they appear on the electrodes and membrane. Therefore, an accelerated stress test (AST) is required to evaluate the potential of a novel high-risk component, such as a coated ss-PTL, for implementation in commercial PEMWE.³⁰

In contrast, such as the setup in Fig. 2b, the anode and cathode water loops of the BoP are kept as simple as possible. There are no ss pipes, pumps or any other metal parts in which ions could redeposit. The inlets and outlets of the cell are connected to small volume water reservoirs that are opened to the air. The water is fed to the cell *via* natural flow and the water level is kept constant by filling periodically with fresh water. This setup does not contain an ion exchange resin. Therefore, in this setup, any Fe^{2+} released due to the corrosion of Nb/Ti/ss-PTLs will rapidly poison the CCM as the water volume is kept small and constant. Any other impurities in the DI water, such as Ca^{2+} , Cu^{2+} , Na^{+} , organics and metal ions in the ppm range, also continuously increase with each refill. Consequently, the cells with either Ti-PTL or coated ss-PTL will rapidly degrade,

but the degradation rates will be different if the ss PTL substrate corrodes. Therefore, this setup can be well used for an AST in which water purity is the main stressor.

The AST setup was employed for evaluating the Nb/Ti/ss-PTL in PEMWEs with an active area of 4 cm^2 . On the anode side, the following interconnecting components were used: a ss-BPP with a dense coating of Ti,¹⁹ and a Nb/Ti/ss-PTL, and for the cathode side: an uncoated multi-layer mesh-type ss-PTL (Haver & Boecker OHG) and a ss-BPP. All stainless steel components were of 1.4404 grade. An untreated carbon paper (TGP-H-90) was placed between the cathode electrode and the ss-PTL. CCMs with an Ir-based anode, Pt-based cathode and chemically stabilized Nafion 115 membrane were used for all electrochemical tests, except for the test of Fig. 10. The loading of the catalyst is 2.5 mg cm^{-2} for iridium and 0.95 mg cm^{-2} for platinum. Polarization curves up to 2 A cm^{-2} with a scan rate of $4 \text{ mA cm}^{-2} \text{ s}^{-1}$ and electrochemical impedance spectroscopy (EIS) spectra were obtained at 0.25 and 1 A cm^{-2} and an amplitude of 50 mA and 200 mA , respectively, from 50 kHz to 100 mHz . A potentiostat/galvanostat (Zahner Elektrik IM6) with a booster (Module PP240) was used for these measurements, which were carried out at $65 \text{ }^\circ\text{C}$ and ambient pressure. The Nb/Ti/Ti-PTL, uncoated Ti-PTL and ss-PTL were also measured for comparison purposes. Once the polarization curves and the EIS were completed, a constant current of 2 A cm^{-2} was applied for an AST for more than 1000 h .

3. Results

3.1. Morphology of the coatings

The morphology and micro-structure of the Nb/Ti coatings were analysed by SEM. Fig. 3a presents a cross-sectional image of the

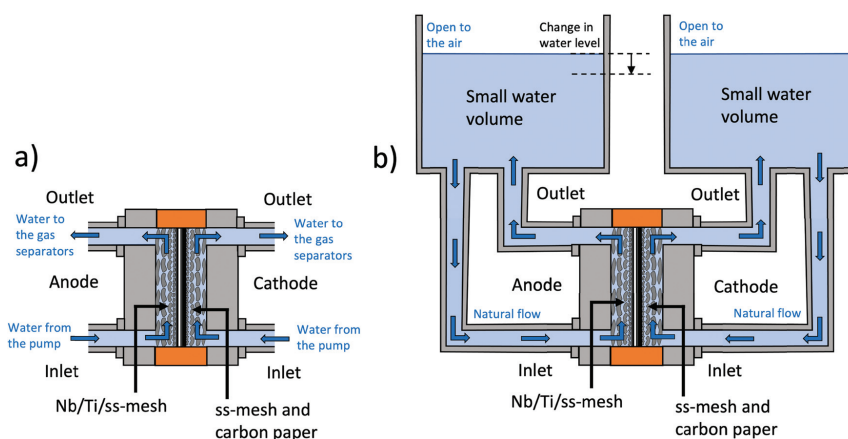


Fig. 2 (a) Conventional cell configuration for long-term tests in which DI water is flown through the anode and cathode inlets and the component corrosion products are taken away to the water loop in the BoP of the test station. (b) Cell configuration for an accelerated stress test (AST) in which the cell operates with a low volume of water under natural flow, allowing an increase in the component corrosion products and accelerating the degradation due to CCM poisoning.



Ti-PTL, showing the various layers of Ti meshes with different aperture sizes. The mesh with the lowest aperture size contacts the anode catalyst layer of the CCM, while the rest of the meshes distribute the electrical current, manage the water supply and release the formed O₂ bubbles. Ultimately, the mesh with the largest aperture size contacts the bipolar plate and acts as a flow field. The Nb/Ti coatings are applied only on the finest Ti-mesh, as shown in Fig. 3b (low magnification) and Fig. 3c (high magnification). The corresponding cross-sectional SEM images of the Nb/Ti coating deposited on the ss-PTL are displayed in Fig. 3d–f. Additional SEM images from the surface of the ss-PTL and Ti/Nb/ss-PTL are shown in Fig. S1 (ESI†).

First, the Ti layer covers almost the entire surface of the fine-mesh ss substrates, which is particularly important for protecting the PTL against the corrosive environment in the vicinity of the anode catalyst layer. Subsequent layers of Ti are porous to allow the transport of reactants and products from the water splitting process. The Ti particles of the porous layer do not form the conventional sput structure that one can observe in the dense Ti coatings¹⁷ due to their low enthalpy during the plasma coating deposition. However, the Ti particles have a certain degree of inter-particle diffusion among each other, ensuring the mechanical stability of the coating. On top of the Ti porous layer, Nb uniformly follows the rugosity of the coating composed of Ti particles. Nb functions as an anti-passivation coating for Ti,¹⁹ which is an alternative to costly precious metals that are normally used for extending the lifetime of PEMWE cells. It is worthwhile noting that the Nb/Ti coating slightly reduces the gaps of the punched holes in the ss fine mesh, which can improve the catalyst utilization of the electrode.^{9,31}

One important aspect regarding the corrosion resistance of the Nb/Ti coatings is the purity of Ti and Nb. EDS was carried out on different cross-sectional areas of the coated PTLs.

Table 1 EDS of the specific areas (MW) in Fig. 3

Area designation	O [wt%]	Si [wt%]	Ti [wt%]	Cr [wt%]	Fe [wt%]	Ni [wt%]	Nb [wt%]	Mo [wt%]
MW 1	2.36	—	0.91	—	—	—	96.73	—
MW 2	2.37	—	0.79	—	—	—	96.85	—
MW 3, 4, 5, 6	—	—	100.00	—	—	—	—	—
MW 7	3.10	—	0.35	—	—	—	96.55	—
MW 8	3.32	—	0.57	—	—	—	96.12	—
MW 9, 10	—	—	100.00	—	—	—	—	—
MW 11	0.71	0.39	0.54	16.99	68.93	10.03	—	2.40
MW 12	0.69	0.31	0.21	17.50	69.57	9.44	—	2.28

These areas are indicated as red rectangles and labeled MW in Fig. 3c and f for Nb/Ti-Ti-PTL and Nb/Ti/ss-PTL, respectively. The results of the EDS analysis are summarized in Table 1. The SEM image of Fig. 3c shows almost no colour contrast between the Ti particles (MW 3) and the Ti-mesh substrate (MW 5), suggesting that they both have the same elemental composition. The EDS results confirm that Ti-mesh substrates are pure Ti and can be considered Ti Gd1, which is the standard material for the PTL in PEMWE. Conversely, the MW 10 and 11 areas in Fig. 3f show deep contrast since these areas correspond to two very different materials, ss and Ti. The brightest material in the image corresponds to Nb. The anti-passivation layer of Nb also has a high degree of purity, and the presence of less than 1 wt% Ti is most likely attributed to the fluorescence of Ti since the measured area is quite close to the Nb/Ti interface. While EDS is not a suitable technique for measuring elements with low atomic mass, the presence of oxygen can be disregarded because during the plasma deposition process oxygen combines with the feed-stock H₂ gas to form H₂O.

3.2. Pore properties and contact resistance

The pore size distribution profiles and porosities of the Nb/Ti and Ti coatings as well as uncoated PTLs are shown in Fig. 4.

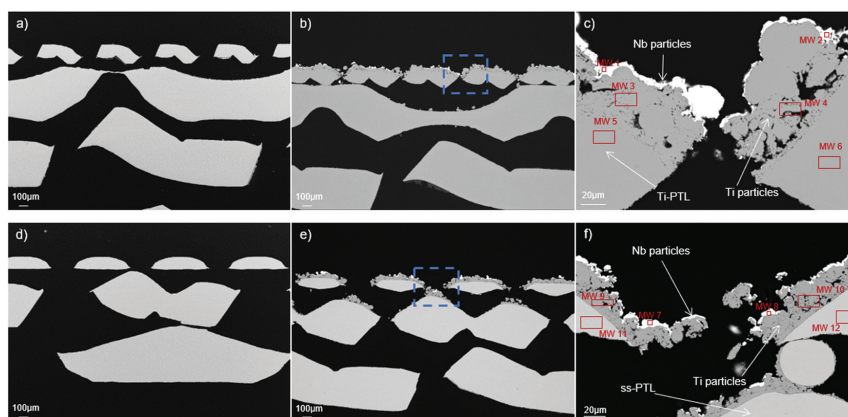


Fig. 3 Scanning electron microscopy (SEM) images of Ti-PTL (a) without and (b) with plasma-sprayed Nb/Ti coatings and ss-PTL (d) without and (e) with plasma-sprayed Nb/Ti coatings. Cutaway images of Nb/Ti on (c) Ti-PTL and (f) ss-PTL, which correspond to the blue dashed squares in (b) and (e). The solid-line squares in (c) and (f) indicate the areas where EDS was carried out, and the results are summarized in Table 1.



Paper

View Article Online

Energy & Environmental Science

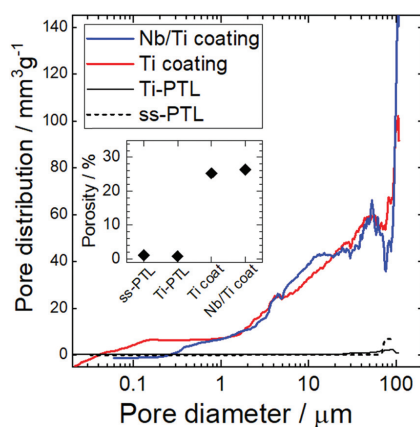


Fig. 4 Pore size distribution from mercury intrusion porosimetry (MIP) for Ti and Nb/Ti coatings on Ti-PTL or ss-mesh PTLs as well as uncoated PTLs for comparison. The inset shows the porosities of the coatings and the mesh substrates.

The pore distribution curve, $dV/d(\log D)$, derived by the differentiation of cumulative pore volume, is plotted per weight for each coating and uncoated Ti- and ss-PTLs for comparison. Here, variables V and D are the cumulative pore volume and the pore diameter, respectively. Both mesh PTLs are apparently dense; their pore size (or namely the gaps of the mesh) ranges above several tens of μm which is too large to be detected as pores in MIP measurements. MIP can detect the pores between a few nm and $\sim 100 \mu\text{m}$, and therefore, the PTL mesh is not porous and the estimated porosities are approximately 1%. In the case of the Nb/Ti and Ti coatings, the estimated porosities using eqn (1) are approximately 25% (inset of Fig. 4), and most of the pores are below several tens of μm down to $3 \mu\text{m}$, at which diameter the distribution curve increases sharply. It should be noted here that the achievable total pore volume in MIP is limited due to the small volume of the coating compared to the dense substrate; therefore, the pore distribution profiles of the Nb/Ti and Ti coatings are nearly identical within the error considering the experimental limit. Thus, the pore size distribution of the coatings is in good agreement with the observed morphology by SEM in Fig. 3.

In addition to the optimized pore properties of Nb/Ti/ss-PTL, a good electrical connection between the plasma-sprayed coating and the catalyst layers ensures high performance due to low ICR. The ICR measurements of the Nb/Ti/ss-PTL, Nb/Ti/Ti-PTL, and uncoated PTL substrates with respect to the compaction force are presented in Fig. 5. The method for estimating the ICRs of the plasma-sprayed coatings has been previously reported,^{11,19} and the experimental setup is schematized in the inset of Fig. 5. A thin sheet of carbon paper is placed between the PTLs and one of the Au-coated Cu cylinders. The ICR between the Nb/Ti coating and the anode catalyst layer can be approximated by using a carbon paper sheet instead of the Ir-based layer, as both have high

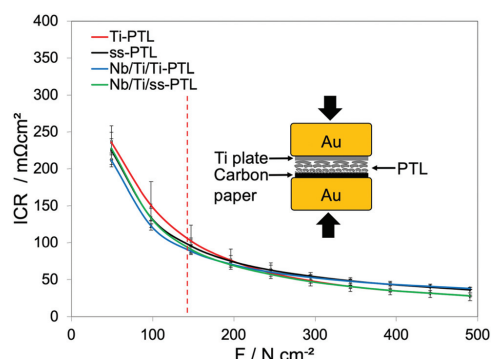


Fig. 5 Interfacial contact resistance (ICR) with respect to the compaction force of Ti-PTL, ss-PTL, Nb/Ti/Ti-PTL and Nb/Ti/ss-PTL. The inset shows a scheme of the experimental setup.

in-plane electrical conductivity. Furthermore, carbon paper acts as a material that can be compressed in the applied range of compaction forces.

First, Fig. 5 reveals that all PTLs have relatively the same ICR, which is approximately $100 \text{ m}\Omega \text{ cm}^2$ at a compaction force of 150 N cm^{-2} , corresponding to the compression of the PEMWE cell during the assembly. This result is quite remarkable, although it might be characteristic of only multi-layer mesh-type PTLs. In contrast, Bernt *et al.*³² and Kang *et al.*³³ report different resistance values between different PTLs, with and without MPL coating. For this kind of PTL, the Nb/Ti coatings have essentially no influence at all in the ICR of the PTL, and this effect should be reflected in the PEMWE tests. However, we will demonstrate in the next section that the Nb/Ti coating has a strong influence on the performance of the PEMWE in which the coating reduces ohmic losses at high current densities.

3.3. Electrochemical performance and simulation

From the ICR results with the ss-PTL and Nb/Ti/ss-PTL, which showed practically no differences in ohmic resistance, one could infer that the Nb/Ti coating will only serve to protect the ss-PTL against corrosion. Compared with the use of the uncoated Ti-PTL, any additional advantages when using the Nb/Ti/ss-PTL would be expected in the PEMWE performance, as the ohmic resistance is the same for both PTLs.

Fig. 6a shows the $E_{\text{Cell}}-j$ characteristics of a PEMWE cell with the ss-PTL, Nb/Ti/ss-PTL, and Nb/Ti/Ti-PTL and the E_{Cell} values at a constant 2 A cm^{-2} . We observe that the use of an uncoated ss-PTL causes rapid cell depolarization, reaching up to 2.28 V at only 0.4 A cm^{-2} . The cell is only operated up to this current density, and therefore, the E_{Cell} at a constant 2 A cm^{-2} is not plotted. The PEMWE cell becomes inoperable afterwards, turning the feedstock water into a yellowish solution, similar to the colour of the electrolyte used for evaluating ss-BPPs under simulated conditions of a PEMWE cell. These results provide clear evidence for the magnitude of the challenge when using ss as a base material for the manufacture of a low-cost PTL.



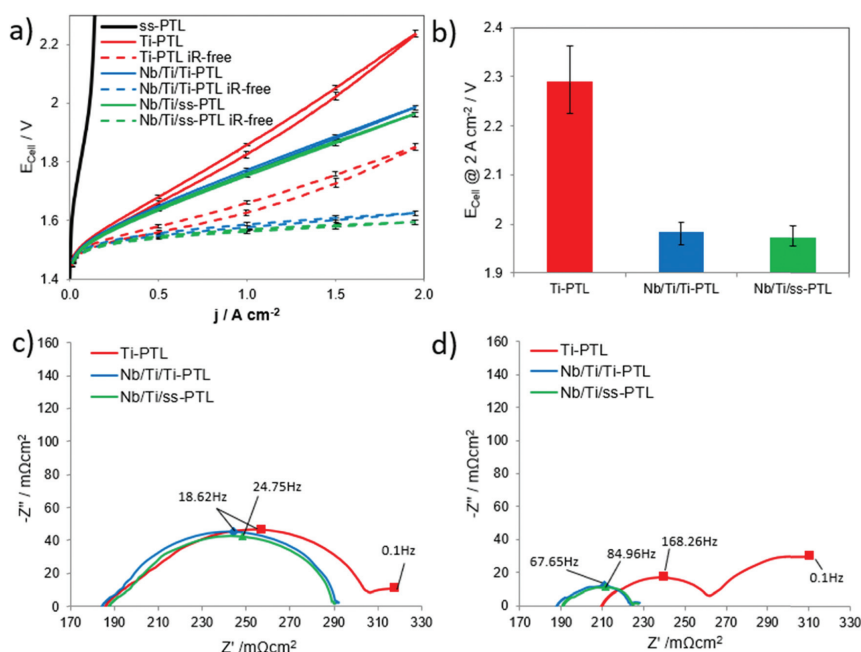


Fig. 6 (a) Polarization curves of PEMWE cells with the Ti-PTL, ss-PTL, Nb/Ti/Ti-PTL and Nb/Ti/ss-PTL. The scan rate was $4 \text{ mA cm}^{-2} \text{ s}^{-1}$. The dashed curves show the iR-correction of the curves. (b) The cell potential values of the different PTLs at 2 A cm^{-2} . Nyquist plots at (c) 0.25 and (d) 1 A cm^{-2} from 100 mHz to 50 kHz . All measurements were carried out at 65°C and ambient pressure.

In stark contrast, by coating the ss-PTL with Nb/Ti in PEMWE cells, it is possible to achieve performances comparable to those of commercial electrolyzers, such as those from Hydrogenics,³⁴ Siemens³⁵ and Proton Onsite.³⁶ Clearly, the Nb/Ti coating not only protects the ss-PTL against corrosion but also has a staggering influence on the cell performance. To understand this effect, a PEMWE cell with a mesh-type Ti-PTL similar to the ss-mesh was also tested. The mesh-type Ti-PTL is the lowest cost PTL in the market, but it leads to low performances, as shown in Fig. 6a and b. Consequently, most PEMWEs use Ti felts and sinter powder plates as PTLs, although these are much more expensive than a Ti punched mesh due to the manufacturing process. First, an interesting observation is that there are large differences in the slope of the polarization curve of Ti-PTL and those of Nb/Ti/ss-PTL and Nb/Ti/Ti-PTL. At first glance, this result contradicts the observations from the ICR measurements, which show no difference in ohmic resistance among all the PTLs. Second, the polarization curve of the cell with the Ti-PTL shows a hysteric behaviour, while for the others, the forward curve overlaps with the one measured backwards. Finally, the Nb/Ti coating reduces the E_{Cell} by more than 300 mV at 2 A cm^{-2} compared with that of the uncoated Ti-PTL. This decrease in the overpotential represents an efficiency increase of approximately 12%, which has an important impact on the cost of hydrogen production. EIS will provide comprehensive

explanations for all these phenomena. It is important to remark that the mesh Ti-PTL cannot be considered a baseline as the cell performance is too low compared to other well-known baselines such as the Ti felt and sintered Ti plates. However, the Ti mesh is considerably cheaper than the felt or the sintered structures and even more so is a stainless steel mesh. As a consequence, there is lot of interest from the industry to use this kind of PTL and it has potential to become the new PTL baseline in PEMWE cells. In this work we aim to use the lowest cost materials available, that is stainless steel meshes and plates to construct the PEMWE cells, and the achieved performances are comparable to other reports that use baseline sintered Ti-PTLs.^{31,37} In Fig. S2 (ESI[†]) we show a comparison between the polarization curve of Nb/Ti/ss-PTLs in Fig. 6a and the one from a baseline Ti-PTL from GKN Sinter Metals,³⁸ which is commercial, and having a Pt coating applied *via* magnetron sputtering PVD.¹⁹ The resulting curves show that the performances of the PEMWE cells with the Nb/Ti/ss-PTL and the baseline Pt/Ti-PTL (GKN Sinter Metals) are quite comparable.

The Nyquist plots of the PEMWE cell with the Ti-PTL, Nb/Ti/Ti-PTL and Nb/Ti/ss-PTL at 0.25 and 1 A cm^{-2} are shown in Fig. 6c and d, respectively. The spectra were analysed based on the equivalent circuit introduced in previous work and are shown in Fig. S3 (ESI[†]).¹² The ohmic resistance is given by the interception of the first semi-circle in the high-frequency



View Article Online

Paper

Energy & Environmental Science

region with the x -axis. The resistances induced by the hydrogen evolution reaction (HER),³⁹ charge transfer resistance coupled with double layer effects³⁴ or the first charge transfer of the two-electron process of the oxygen evolution reaction (OER)⁴⁰ are represented by the high-frequency arc. The medium- and low-frequency arcs thereby describe the charge transfer of the OER rate-determining step and the mass transport losses.⁴¹

At 0.25 A cm^{-2} , all three cells show comparable ohmic resistance of approximately $188 \pm 1 \text{ m}\Omega \text{ cm}^2$, which is in good agreement with the ICR results of Fig. 5. However, the discrepancy between the ICR and EIS could be due to the additional resistance in the catalyst layer depending on its components, such as ionomer and binder, and therefore ICR measurements cannot be directly linked to the measurements from EIS. In general, the curves for the Nb/Ti/Ti-PTL and Nb/Ti/ss-PTL are comparable to each other in their behaviour, while Ti-PTL presents a slightly larger high-frequency arc. For all samples, the second semi-circle that is associated with the OER kinetics is equivalent in size, and only for Ti-PTL there is an appearance of a small third arc with an apex at 0.1 Hz , indicating mass transport losses. In contrast, at 1 A cm^{-2} , the differences in the EIS between the cells with the coated and uncoated PTLs are very noticeable. The first most noticeable change at 1 A cm^{-2} is the increase in the ohmic resistance for Ti-PTL, while for the Nb/Ti/Ti-PTL and Nb/Ti/ss-PTL, the ohmic resistance remains almost the same at both 0.25 and 1 A cm^{-2} . Another important change in the EIS is the increase in the radius of the medium-frequency semi-circle for Ti-PTL compared to Nb/Ti/Ti-PTL and Nb/Ti/ss-PTL. Finally, the low-frequency arc of Ti-PTL increases drastically, indicating higher mass transport losses, which is in good agreement with the hysteresis shape of the polarization curve in Fig. 6a. Conversely, the mass transport effects for the coated PTLs are barely visible.¹²

The Nb/Ti coatings have a significant influence on the ohmic resistance, anode performance and mass transport behaviour during PEMWE. The ohmic resistance refers to the transitions of all cell components (PTLs, BPPs, membranes, and catalyst layers); these components should have the lowest possible resistance due to their high contact with each other. On the one hand, this contact can be worsened by the formation of non-conductive passivation layers on the Ti-PTL;^{42,43} however, on the other hand, insufficient compression and thus insufficient utilization of the possible contact area can also worsen the ohmic resistance. The optimum compression of the components can be reduced by either different material expansion coefficients depending on the temperature or the conceivable formation of a gas cushion between the catalyst layer and PTL. Due to inefficient gas-water management, which can be observed in simple PTLs,⁴⁴ the produced gas accumulates at the boundary layer and reduces the contact. While no mass transport loss is observed for the coated PTLs, the Ti-PTL is the only sample that shows ohmic loss shifts to higher values; thus, mass transport limitations seem to have a decisive effect on the Ti-PTL.

Nevertheless, it should be noted that the increase in performance due to the application of the Nb/Ti coating is not only caused by the reduction in mass transport losses.

The highly developed surfaces of the coated PTLs with their small porous particle layers provide a high interfacial contact area, resulting in low membrane deformation. In contrast, the region of the catalyst layer not in contact with the uncoated PTL surfaces intrudes into the large pore space, becomes degraded and thus loses conductivity. The surface of the anode at the interface between the catalyst layer and Nb/Ti/Ti-PTL or Nb/Ti/ss-PTL is highly active, whereas large areas of the interface between the catalyst layer and Ti-PTL are electrochemically inactive. This is consistent with the EIS results in Fig. 6d, which show improved kinetics of both the HER and OER, for Nb/Ti/Ti-PTL and Nb/Ti/ss-PTL. Furthermore, this finding agrees very well with the results of Schuler *et al.*,³¹ who revealed that the advantage of the MPL lies in the local microscopic compression of the catalyst layer, which preserves the electrical catalyst percolation network. In addition to an increase in the catalyst utilization, this can also be understood as a reduction in membrane deformation, resulting in a significant increase in performance. Lopata *et al.*⁴⁵ came to the same conclusion and confirmed the dominance of the interface between the PTL and catalyst layer with regard to the cell performance influencing the high-frequency resistance, catalyst utilization, coverage of PTL grains due to gas bubble formation and ionomer conductivity.

PNM was employed to understand the improved mass transport phenomena in PEMWE cells with the addition of the Nb/Ti coatings. The mass transport characteristics of the coated PTLs are described by the simulated drainage curve and the capillary entry pressure of the pores. The drainage curve shown in Fig. 7 exhibits a wide range of entry capillary pressures, from approximately 780 Pa to 100 kPa . During the process of drainage, the non-wetting phase first preferentially invades pores with lower entry (threshold) capillary pressures (*i.e.*, first invades larger pores in the fine mesh substrate). Although a wide range of capillary pressures is required to fully drain the wetting phase, the wetting phase saturation dramatically decreases at the lower end of the capillary pressure curve (shown as a plateau from 1 to 0.1 in Fig. 7).

The wetting phase saturation decreases to below 10% at a capillary pressure of 3.6 kPa , indicating that most of the pore space in the coated PTL is composed of pores from the fine mesh substrate. At this capillary pressure, the larger pores (mostly from the fine mesh) are invaded by the non-wetting phase (left inset of Fig. 7), while the smaller pores (at the Nb/Ti coatings) remain uninvaded. The smaller pores become invaded after all the larger pores have been penetrated, as shown in the right inset of Fig. 7, where the small pores from the Nb/Ti coating are invaded with gas at a capillary pressure of 25 kPa . At approximately 100 kPa , the full domain of the coated PTLs becomes saturated with the non-wetting phase. To fully invade the PTL, the gas generated from the OER requires a capillary pressure build-up over an order of magnitude higher than the value to attain a 10% wetting phase saturation, which is unlikely to occur during electrolysis. Instead, the gas will break through to the larger pores in the coarser mesh by establishing a preferential transport pathway, thus leaving



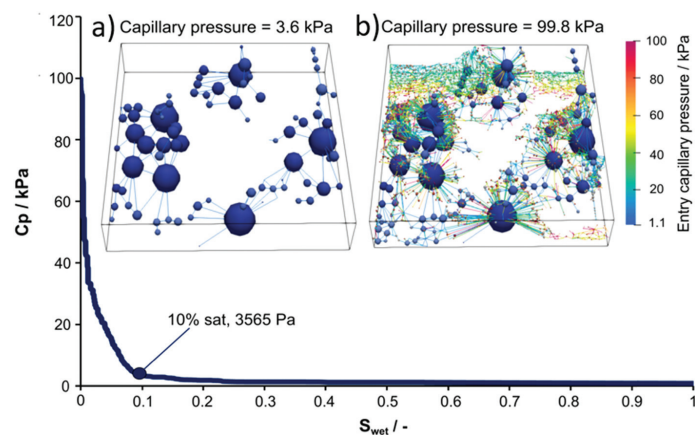


Fig. 7 Drainage characteristics generated from the pore network simulation results on the coated PTLs, (a) invaded pores and throats at capillary pressures of 3.6 kPa and (b) 99.8 kPa.

small pores in the Nb/Ti coatings uninvaded. Similar observations are reported in the previous literature.^{46,47} First, Lee *et al.* revealed *via* modelling and *in operando* neutron imaging experiments that having a porosity gradient from low to high porosity facilitates mass transport during electrolysis. Moreover, they further⁴⁷ demonstrated that when a custom pore structure was applied to the PTL (*i.e.*, pores with diameters excessively larger than the average pores in the PTL), the gas saturation at the catalyst layer-PTL interface was significantly reduced and mass transport behaviour was enhanced particularly at higher current density operation. Therefore, the Nb/Ti coatings in our PTL lead to improved mass transport behaviour – the smaller pore structure (from the Nb/Ti coating) provides additional reactant transport pathways while the larger pore structure (pores from the mesh) provides effective gas removal pathways.

In contrast, during imbibition of liquid water into the PTL, the liquid water will preferentially invade pores with a higher capillary pressure (*i.e.*, smaller pores in the Nb/Ti coating). Therefore, additional transport pathways for reactant water are supplied by the small pores of the Nb/Ti coating. It is anticipated that even at high current densities, gas removal is facilitated through the large pores, and water is transported through the smaller pores in the Nb/Ti coating. In the absence of the small pores inherent in the Nb/Ti coating, reactant transport would be impeded by the gas removal process and lead to mass transport losses.

3.4. Durability under AST and post-test analysis

Fig. 6a demonstrates that the Nb/Ti coating protects the ss-PTL against corrosion for the duration of polarization. However, industry requires testing for more than 50 000 h to validate the implementation of novel components in their commercial systems.⁴⁸ Such long-term tests are impractical, and hence, the Nb/Ti/ss-PTL was evaluated under the AST described in Section 2.4. Fig. 8 shows the E_{Cell} measured at a constant

2 A cm⁻² of PEMWE cells with the Nb/Ti/ss-PTL, Nb/Ti/Ti-PTL and Ti-PTL. The PEMWE cell with the ss-PTL is not measured since it is highly unstable and cannot withstand the applied load. Additionally, there are intermittent periods in which the cells are not operated. These intermittent interruptions are applied intentionally to resemble shut-downs and induce further degradation.

All three PEMWE cells degrade rapidly, but the cells with the Ti-PTL in particular reach E_{Cell} values close to 2.5 V, which we define as the end of test (EoT), in less than 100 h. Basically, two irreversible degradations that lead to an increase in E_{Cell} are identified in the literature: (i) an increase in ohmic resistance due to the formation of oxides at the interface of Ti-PTL^{13,49} at the anode and (ii) CCM poisoning due to impurities in the water.^{28,50} A third irreversible degradation mechanism is also known, which is the loss of polymeric material in the CCM, but in this case, the E_{Cell} decreases over time.^{34,51} For the short time of the AST, the passivation of titanium is clearly not the dominant degradation mechanism, see Fig. S4 (ESI[†]), but the CCM poisoning caused by the impurities in the water that increase over time. The test with the cell with the Ti-PTL was stopped at approximately 720 h as the E_{Cell} was no longer below the EoT. A different behaviour is observed with the PEMWE cells containing the Nb/Ti/ss-PTL and Nb/Ti/Ti-PTL. The E_{Cell} values for both electrolyzers have almost identical trends over time, which is a preliminary indication that the ss substrate of the Nb/Ti/ss-PTL is not corroding. Otherwise, the cell with Nb/Ti/ss-PTL should degrade faster than the cell with Nb/Ti/Ti-PTL. The ASTs for PEMWE cells with the Nb/Ti/Ti-PTL and Nb/Ti/ss-PTL were stopped at approximately 1450 h.

At the EoT, a re-assembly procedure was implemented to quantitatively determine how much the ageing of the Nb/Ti/ss-PTL contributed to the overall cell degradation and is shown in Fig. S5 (ESI[†]). By cleaning all metal cell components and replacing the CCM, the initial cell voltage at constant 2 A cm⁻²



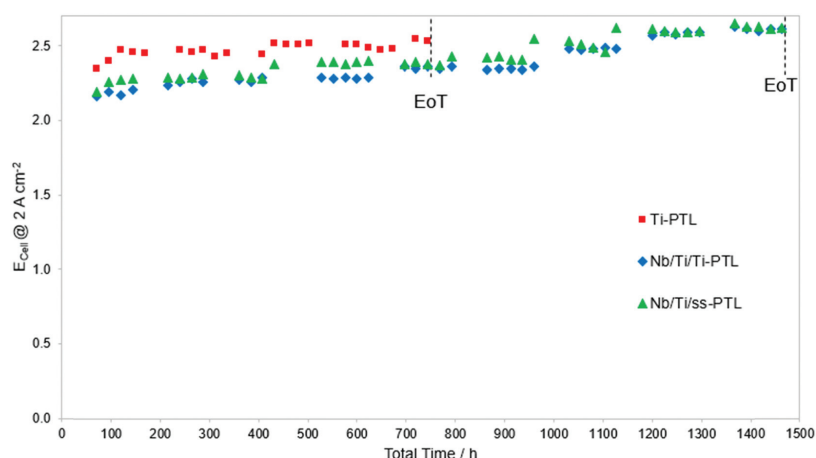


Fig. 8 Accelerated stress test (AST) of cells with the Ti-PTL, Nb/Ti/Ti-PTL and Nb/Ti/ss-PTL.

was almost completely recovered with 99%. Based on these findings, which were also observed by Sun *et al.*,²⁸ we conclude that the CCM is mainly responsible for the degradation of the cell. Fig. S6 (ESI[†]) shows the E_{Cell} vs. time of a PEMWE cell with Nb/Ti/ss-PTL in a conventional test station with ss pipes, pumps, gas separators, sensors, valves and other BoP components. As expected, the test in this setup does not show any increase in the E_{Cell} values due to degradation mechanisms (i) and (ii); rather, the E_{Cell} values decrease slightly over time, as is the case of an electrolyser with very stable BPPs and PTLs,³⁴ thus corresponding to degradation mechanism (iii).

An AST alone is still not sufficient to prove that Nb/Ti protects the ss-PTL against corrosion. If there is indeed any release of Fe^{2+} ions from the ss-PTL, it should be present in the post-tested CCM. Elemental mapping with EDS was carried out on the CCMs of PEMWE cells with Nb/Ti/ss-PTL and Nb/Ti/Ti-PTL that were subjected to the AST in Fig. 8. The results are presented in Fig. 9. The first column of images corresponds to the uncoated ss-PTL just after the first polarization curve shown in Fig. 6a. Fe (coloured in blue) is substantially present in the Ir-based anode, Pt-based cathode and Nafion membrane. In this latter component, the formed Fe crystals are most likely Fe_3O_4 ¹⁵ (see Fig. S7a, ESI[†]). In stark contrast, the Nb/Ti/ss-PTL (second column in Fig. 9) does not show any apparent traces of Fe in the anode, cathode or membrane, which is the same as the case of the cell with Nb/Ti/Ti-PTL (third column of images in Fig. 9). This characterization of the post-tested CCMs in the PEMWE cells with the coated ss-PTL and ss-BPP for the anode and the uncoated ss-PTL and ss-BPP for the cathode clearly demonstrates that ss can be used as a base material for manufacturing the metal components of the entire electrolyser. Additionally, the SEM images of the uncoated ss-PTL and Nb/Ti/ss-PTL after the AST are shown in Fig. S8 (ESI[†]). The surface of the ss-PTL was clearly eroded due to the corrosion in the PEMWE cell while for the Nb/Ti/ss-PTL, no sign of degradation

can be observed in either the Nb/Ti coating or the ss-PTL substrate. Lastly, X-ray photoelectron emission spectrometry (XPS) measurements, Fig. S9 (ESI[†]), did not reveal any Fe on the cathode of the CCM of the cell with the Nb/Ti/Ti-PTL that pass from the anode to the cathode across the PEM and inductive coupled plasma mass spectrometry (ICP-MS) of a water sample taken at the end of the test shown in Fig. 8 did not detect any increase of Fe.

3.5. Next generation PEMWE

To reduce the cost of green hydrogen further, the PEMWE cells will have to operate at much higher current densities than 2 A cm^{-2} , e.g. 4 A cm^{-2} as nominal load and 6 A cm^{-2} as overload,⁵² while keeping efficiencies above 70%. This will only be possible if the temperature is increased to 80°C or above and the stack uses thin membranes such as Nafion 212, and not Nafion 115, which is the state of art. Hence, one can wonder if the coated stainless-steel PEMWE components reported herein will be suitable for the next generation of PEMWE cells that will have thinner membranes than current ones and will operate up to 6 A cm^{-2} at 80°C . Fig. 10 shows the polarization curve of a PEMWE cell with Nafion 212, Nb/Ti/ss-PTL and the other stainless steel components described in Section 2.4. As shown in the figure, the PEMWE cell can achieve an unprecedented efficiency of 77% at 4 A cm^{-2} and 80°C . Furthermore, the slope of the polarization curve is kept straight up to 6 A cm^{-2} , in the forward and backward direction. If the curve would present hysteresis it would be an indication of mass transport losses¹² caused by Nb/Ti coating on the ss-PTL or degradation, as shown in Fig. 6a. The performance of the PEMWE cell with stainless steel components is comparable to the highest performances reported up to now by renowned R&D institutes in electrolysis.^{31,37,53,54} However, thin membranes such as Nafion 115 are not yet suitable for industrial PEMWE since they degrade much faster than Nafion 212 leading to an increased H_2 crossover into the O_2 stream and



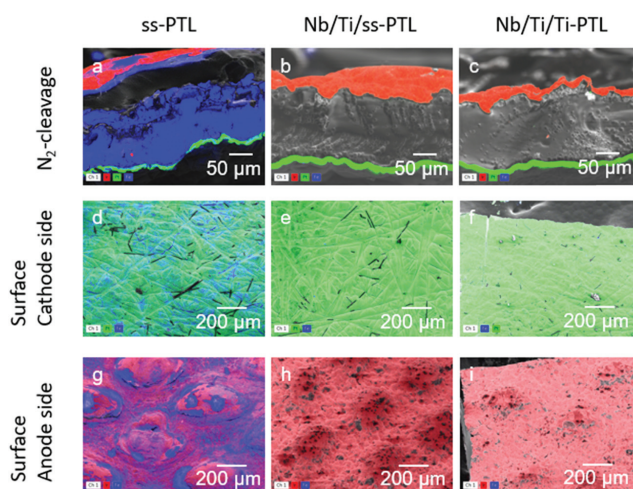


Fig. 9 EDX mapping of the (a–c) cross-section of the CCM, (d–f) cathode and (g–i) anode surfaces of the PEMWE cell with the uncoated ss-PTL, Nb/Ti/Ti-PTL, and Nb/Ti/ss-PTL.

thus compromising the safety of the electrolyser. However, it is expected that R&D institutes as well as companies like Chemours and Solvay will solve this issue in the upcoming years.

Regarding the cost/scalability of the vacuum plasma spraying technique for the deposition of Nb/Ti on the ss-PTL we have previously estimated a cost for the coating (without Nb) of about 20–100 USD m^{-2} .¹⁷ The cost of coating production is significantly low, but it could be decrease further if the coatings are applied in a line of production, where the torch is sweeping and spraying the materials continuously on the substrate, which is either a mesh-type PTL or a flat BPP. The substrates can be produced in

large area metal rolls that can be un-folded during the coating process. Industrial plasma spraying processes are scalable but one challenge may be the use of vacuum that contributes to cost that is more sensitive for the electrolysis application than for traditional uses of VPS (e.g. coating of turbine blades or implants). In this regard, further investigations in the future are needed to produce Nb/Ti coatings *via* atmospheric plasma spraying (APS), without affecting the structure, mechanical integrity and purity of the coatings.

4. Conclusion

There is an urgent need for reducing the cost of large PEMWE cells, and here, we have presented a solution that addresses the most expensive stack components, which are the BPPs and PTLs. Previously, we demonstrated that BPPs can be manufactured with ss,¹⁷ but in this study, we solved a far more difficult challenge, which is the use of ss for PTLs. We developed a non-precious metal coating of Nb/Ti and applied it on the most inexpensive structure that can be used as a PTL in PEMWE, which is a ss mesh. The Nb/Ti fully protected the ss-PTL against corrosion, as the physical analyses revealed after a more than 1000 h AST for durability. Furthermore, the Nb/Ti coating on the ss-PTL reduced the cell overpotential by more than 300 mV at 2 A cm^{-2} , resulting in an efficiency increase of 12%. As the EIS measurements confirmed, these positive effects were more evident at current densities above 0.25 A cm^{-2} due to the following factors:

- A reduction in the ohmic resistance, which is caused by gas formation at the interface with the anode.
- An improved utilization of the anode catalyst resulting in enhanced OER kinetics.
- A reduction in mass transport losses.

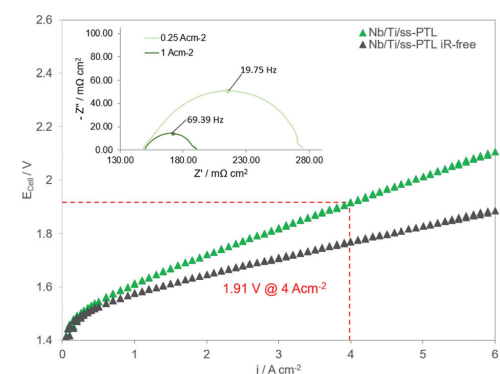


Fig. 10 Polarization curve and the iR-free curve up to 6 A cm^{-2} of a PEMWE cell with Nb/Ti/ss-PTL. The cell was operated at 80 °C and using a CCM with Nafion 212. The inset shows Nyquist plots of the cell at 0.25 and 1 A cm^{-2} from 100 mHz to 50 kHz.



View Article Online

Paper

Energy & Environmental Science

To further understand the observed phenomena, PNM showed that the advantage of the Nb/Ti coating was explicitly due to the preferred transport of water and gas to and from the active surfaces of the anode. With the results presented herein, it can be concluded that Ti can be ruled out as a base material for the manufacture of expensive porous structures for PTLs; instead, low-cost ss meshes can be used. Moreover, ss meshes with different aperture sizes allow the use of flat plates as BPPs, which can also be manufactured in ss, without a flow field. Thus, the cost of a PEMWE cell has been reduced drastically by being almost entirely made of ss, establishing this technology as the most promising solution for the production of green hydrogen from renewable sources.

Author contributions

S. Stiber carried out the ICR and PEMWE measurements. N. Sata performed the MIP on the coatings. T. Morawietz analysed the samples by SEM. A. Fallisch carried out the micro-CT measurements. S. A. Ansar produced the Nb/Ti coatings by plasma spraying. J. K. Lee, A. Bazylak, and T. Jahnke developed the PNM. A. S. Gago led the development, tests and characterization of the PTLs. K. A. Friedrich supervised the overall work with regular discussions. All the authors contributed to writing and proofing the manuscript.

Conflicts of interest

The authors declare no competing interests.

Acknowledgements

The research leading to these results has received funding from the European Union's Horizon 2020 research and innovation programme under grant agreement No. 779478 (PRETZEL project), which is supported by FCH JU. Furthermore, funding from the European Union's Horizon 2020 research and innovation programme under grant agreement No. 862253 (PROMET-H2) was received. The authors thank Ina Plock, Günther Roth and Jörg Bürkle for performing the SEM measurements, the production of the coatings on the PTLs by VPS and the technical support, respectively. The authors also acknowledge the support from G. Moutinho and A. Martínez Séptimo in carrying out the PEMWE measurements as part of their master theses. The authors acknowledge Lukas Mues and Nina Bengen for ICP-MS measurements as well as Dr. Indro Biswas, Prof. Thomas Chassé and Dustin O'Neill Quinones for providing XPS analysis. Finally, the authors thank Vincent Wilke for supporting the preparation of the revised version since the first author Svenja Stiber was in maternity leave.

References

- 1 A. Buttler and H. Spliethoff, Current status of water electrolysis for energy storage, grid balancing and sector coupling via power-to-gas and power-to-liquids: A review, *Renewable Sustainable Energy Rev.*, 2018, **82**, 2440–2454, DOI: 10.1016/j.rser.2017.09.003.
- 2 J. Eichman, K. Harrison and M. Peters, *Novel Electrolyzer Applications: Providing More Than Just Hydrogen*, National Renewable Energy Laboratory, 2014.
- 3 M. Carmo, D. L. Fritz, J. Mergel and D. Stolten, A comprehensive review on PEM water electrolysis, *Int. J. Hydrogen Energy*, 2013, **38**, 4901–4934, DOI: 10.1016/j.ijhydene.2013.01.151.
- 4 FCH-JU, Addendum to the Multi-Annual Work Plan 2014–2020, Fuel Cells and Hydrogen 2 Joint Undertaking (2018).
- 5 J. O. Majasan, F. Iacoviello, P. R. Shearing and D. J. L. Brett, Effect of Microstructure of Porous Transport Layer on Performance in Polymer Electrolyte Membrane Water Electrolyser, *Energy Procedia*, 2018, **151**, 111–119.
- 6 K. Bromberger, G. Jagdishkumar, T. Lickert, A. Fallisch and T. Smolinka, Hydraulic ex situ through-plane characterization of porous transport layers in PEM water electrolysis cells, *Int. J. Hydrogen Energy*, 2018, **43**, 2556–2569.
- 7 T. Lickert, M. L. Kiermaier, K. Bromberger, G. Jagdishkumar, S. Metz, A. Fallisch and T. Smolinka, On the influence of the anodic porous transport layer on PEM electrolysis performance at high current densities, *Int. J. Hydrogen Energy*, 2020, **45**, 6047–6058.
- 8 S. Park, J.-W. Lee and B. N. Popov, A review of gas diffusion layer in PEM fuel cells: Materials and designs, *Int. J. Hydrogen Energy*, 2012, **37**, 5850–5865.
- 9 Z. Kang, J. Mo, G. Yang, S. T. Retterer, D. A. Cullen, T. J. Toops, J. B. Green Jr, M. M. Mench and F.-Y. Zhang, Investigation of thin/well-tunable liquid/gas diffusion layers exhibiting superior multifunctional performance in low-temperature electrolytic water splitting, *Energy Environ. Sci.*, 2017, **10**, 166–175.
- 10 T. Schuler, R. De Bruycker, T. J. Schmidt and F. N. Büchi, Polymer Electrolyte Water Electrolysis: Correlating Porous Transport Layer Structural Properties and Performance: Part I. Tomographic Analysis of Morphology and Topology, *J. Electrochem. Soc.*, 2019, **166**(4), F270–F281.
- 11 P. Lettenmeier, S. Kolb, F. Burggraf, A. S. Gago and K. A. Friedrich, Towards developing a backing layer for proton exchange membrane electrolyzers, *J. Power Sources*, 2016, **311**, 153–158.
- 12 P. Lettenmeier, S. Kolb, N. Sata, A. Fallisch, L. Zielke, S. Thiele, A. S. Gago and K. A. Friedrich, Comprehensive investigation of novel pore-graded gas diffusion layers for high-performance and cost-effective proton exchange membrane electrolyzers, *Energy Environ. Sci.*, 2017, **10**, 2521–2533.
- 13 C. Rakousky, U. Reimer, K. Wippermann, M. Carmo, W. Lueke and D. Stolten, An analysis of degradation phenomena in polymer electrolyte membrane water electrolysis, *J. Power Sources*, 2016, **326**, 120–128.
- 14 C. Liu, M. Shviro, A. S. Gago, S. F. Zaccarine, G. Bender, P. Gazdzicki, T. Morawietz, I. Biswas, M. Rasinski, A. Everwand, R. Schierholz, J. Pfeilsticker, M. Müller, P. P. Lopes, R.-A. Eichel, B. Pivovar, S. Pylypenko,



View Article Online

Energy & Environmental Science

Paper

- K. A. Friedrich, W. Lehnert and M. Carmo, Exploring the Interface of Skin-Layered Titanium Fibers for Electrochemical Water Splitting, *Adv. Energy Mater.*, 2021, **11**, 2002926.
- 15 J. Mo, S. M. Steen, F. Y. Zhang, T. J. Toops, M. P. Brady and J. B. Green, Electrochemical investigation of stainless steel corrosion in a proton exchange membrane electrolyzer cell, *Int. J. Hydrogen Energy*, 2015, **40**, 12506–12511.
- 16 J. Mo, S. Steen, Z. Kang, G. Yang, D. A. Taylor, Y. Li, T. J. Toops, M. P. Brady, S. T. Retterer, D. A. Cullen, J. B. Green and F. Y. Zhang, Study on corrosion migrations within catalyst-coated membranes of proton exchange membrane electrolyzer cells, *Int. J. Hydrogen Energy*, 2017, **42**, 27343–27349.
- 17 A. S. Gago, S. A. Ansar, B. Saruhan, U. Schulz, P. Lettenmeier, N. A. Cañas, P. Gazdzicki, T. Morawietz, R. Hiesgen, J. Arnold and K. A. Friedrich, Protective coatings on stainless steel bipolar plates for proton exchange membrane (PEM) electrolyzers, *J. Power Sources*, 2016, **307**, 815–825.
- 18 P. Lettenmeier, R. Wang, R. Abouatallah, F. Burggraf, A. S. Gago and K. A. Friedrich, Coated Stainless Steel Bipolar Plates for Proton Exchange Membrane Electrolyzers, *J. Electrochem. Soc.*, 2016, **163**, F3119–F3124.
- 19 P. Lettenmeier, R. Wang, R. Abouatallah, B. Saruhan, O. Freitag, P. Gazdzicki, T. Morawietz, R. Hiesgen, A. S. Gago and K. A. Friedrich, Low-Cost and Durable Bipolar Plates for Proton Exchange Membrane Electrolyzers, *Sci. Rep.*, 2017, **7**, 44035.
- 20 N. Rojas, M. Sánchez-Molina, G. Sevilla, E. Amores, E. Almandoz, J. Esparza, M. R. Cruz Vivas and C. Colominas, Coated stainless steels evaluation for bipolar plates in PEM water electrolysis conditions, *Int. J. Hydrogen Energy*, 2021, **46**(51), 25929–25943.
- 21 P. Shirvanian and F. Van Bekel, Novel components in Proton Exchange Membrane (PEM) Water Electrolyzers (PEMWE): Status, challenges and future needs. A mini review, *Electrochem. Commun.*, 2020, **114**, 106704.
- 22 L. Bertuccioli, A. Chan, D. Hart, F. Lehner, B. Madden and E. Standen, *Development of Water Electrolysis in the European Union*, Fuel Cells and Hydrogen Joint Undertaking, 2014.
- 23 K. Ayers, N. Danilovic, R. Ouimet, M. Carmo, B. Pivovar and M. Bornstein, Perspectives on Low-Temperature Electrolysis and Potential for Renewable Hydrogen at Scale, *Annu. Rev. Chem. Biomol. Eng.*, 2019, **10**, 219–239.
- 24 N. F. Daudt, F. J. Hackemüller and M. Bram, Powder metallurgical production of 316L stainless steel/niobium composites for Proton Exchange membrane electrolysis cells, *Powder Metall.*, 2019, **62**, 176–185, DOI: 10.1080/00325899.2019.1607461.
- 25 GeoDict, www.geodict.com. 11/30/2018.
- 26 J. Gostick, Versatile and efficient pore network extraction method using marker-based watershed segmentation, *Phys. Rev. E*, 2017, **96**(2), 023307.
- 27 J. Gostick, M. Aghighi, J. Hinebaugh, T. Tranter, M. Hoeh, H. Day, B. Spellacy, M. Sharqawy, A. Bazylak, A. Burns, W. Lehnert and A. Putz, OpenPNM: A Pore Network Modeling Package, *Comput. Sci. Eng.*, 2016, **18**(4), 60–74.
- 28 S. Sun, Z. Shao, H. Yu, G. Li and B. Yi, Investigations on degradation of the long-term proton exchange membrane water electrolysis stack, *J. Power Sources*, 2014, **267**, 515–520, DOI: 10.1016/j.jpowsour.2014.05.117.
- 29 Q. Feng, X. Z. Yuan, G. Liu, B. Wei, Z. Zhang, H. Li and H. Wang, A review of proton exchange membrane water electrolysis on degradation mechanisms and mitigation strategies, *J. Power Sources*, 2017, **366**, 33–55, DOI: 10.1016/j.jpowsour.2017.09.006.
- 30 P. Afsmann, A. S. Gago, P. Gazdzicki, K. A. Friedrich and M. Wark, Toward developing accelerated stress tests for proton exchange membrane electrolyzers, *Curr. Opin. Electrochem.*, 2020, **21**, 225–233, DOI: 10.1016/j.coelec.2020.02.024.
- 31 T. Schuler, J. M. Ciccone, B. Krentscher, F. Marone, C. Peter, T. J. Schmidt and F. N. Büchi, Hierarchically Structured Porous Transport Layers for Polymer Electrolyte Water Electrolysis, *Adv. Energy Mater.*, 2020, **10**, 1903216, DOI: 10.1002/aenm.201903216.
- 32 M. Bernt and H. A. Gasteiger, Influence of Ionomer Content in IrO₂/TiO₂ Electrodes on PEM Water Electrolyzer Performance, *J. Electrochem. Soc.*, 2016, **163**, F3179–F3189, DOI: 10.1149/2.0231611jes.
- 33 Z. Kang, S. M. Alia, M. Carmo and G. Bender, In-situ and in-operando analysis of voltage losses using sense wires for proton exchange membrane water electrolyzers, *J. Power Sources*, 2021, **481**, 229012, DOI: 10.1016/j.jpowsour.2020.229012.
- 34 P. Lettenmeier, R. Wang, R. Abouatallah, S. Helmlly, T. Morawietz, R. Hiesgen, S. Kolb, F. Burggraf, J. Kallo, A. S. Gago and K. A. Friedrich, Durable Membrane Electrode Assemblies for Proton Exchange Membrane Electrolyzer Systems Operating at High Current Densities, *Electrochim. Acta*, 2016, **210**, 502–511, DOI: 10.1016/j.electacta.2016.04.164.
- 35 F. J. Hackemüller, E. Borgardt, O. Panchenko, M. Müller and M. Bram, Manufacturing of Large-Scale Titanium-Based Porous Transport Layers for Polymer Electrolyte Membrane Electrolysis by Tape Casting, *Adv. Eng. Mater.*, 2019, **21**, 1801201, DOI: 10.1002/adem.201801201.
- 36 K. E. Ayers, J. N. Renner, N. Danilovic, J. X. Wang, Y. Zhang, R. Maric and H. Yu, Pathways to ultra-low platinum group metal catalyst loading in proton exchange membrane electrolyzers, *Catal. Today*, 2016, **262**, 121–132, DOI: 10.1016/j.cattod.2015.10.019.
- 37 M. Bernt, J. Schröter, M. Möckl and H. A. Gasteiger, Analysis of Gas Permeation Phenomena in a PEM Water Electrolyzer Operated at High Pressure and High Current Density, *J. Electrochem. Soc.*, 2020, **167**, 124502, DOI: 10.1149/1945-7111/ABAA68.
- 38 S. Stiber, H. Balzer, A. Wierhake, F. J. Wirkert, J. Roth, U. Rost, M. Brodmann, J. K. Lee, A. Bazylak, W. Waiblinger, A. S. Gago and K. A. Friedrich, Porous Transport Layers for Proton Exchange Membrane Electrolysis under Extreme Conditions of Current Density, Temperature and Pressure, *Adv. Energy Mater.*, 2021, **11**, 2100630, DOI: 10.1002/aenm.202100630.
- 39 S. Siracusano, S. Trocino, N. Briguglio, V. Baglio and A. S. Aricó, Electrochemical Impedance Spectroscopy as a



View Article Online

Paper

Energy & Environmental Science

- Diagnostic Tool in Polymer Electrolyte Membrane Electrolysis, *Materials*, 2018, **11**, 1368.
- 40 C. Rozain, E. Mayousse, N. Guilleta and P. Millet, Influence of iridium oxide loadings on the performance of PEM water electrolysis cells: Part II – Advanced oxygen electrodes, *Appl. Catal., B*, 2016, **182**, 123–131.
- 41 M. Eikerling and A. A. Kornyshev, Electrochemical impedance of the cathode catalyst layer in polymer electrolyte fuel cells, *J. Electroanal. Chem.*, 1999, **475**, 107–123.
- 42 M. Metikos-Hukovic and M. Ceraj-Ceric, Anodic oxidation of Titanium: Mechanism of non-stoichiometric oxide formation, *Surf. Technol.*, 1985, **24**, 273–283, DOI: 10.1016/0376-4583(85)90077-9.
- 43 P. Millet, N. Mbemba, S. A. Grigoriev, V. N. Fateev, A. Aukauloo and C. Étévant, Electrochemical performance of PEM water electrolysis cells and perspectives, *Int. J. Hydrogen Energy*, 2011, **36**, 4134–4142.
- 44 J. Van der Merwe, K. Uren, G. Van Schoor and D. Bessarabov, Characterization tools development for PEM electrolyzers, *Int. J. Hydrogen Energy*, 2014, **39**(26), 14212–14221.
- 45 J. Lopata, Z. Kang, J. Young, G. Bender, J. W. Weidner and S. Shimpalee, Effects of the Transport/Catalyst Layer Interface and Catalyst Loading on Mass and Charge Transport Phenomena in Polymer Electrolyte Membrane Water Electrolysis Devices, *J. Electrochem. Soc.*, 2020, **167**, 064507, DOI: 10.1149/1945-7111/ab7f87.
- 46 J. K. Lee, C. H. Lee, K. F. Fahy, P. J. Kim, J. M. LaManna, E. Baltic, D. L. Jacobson, D. S. Hussey, S. Stiber, A. S. Gago, K. A. Friedrich and A. Bazylak, Spatially Graded Porous Transport Layers for Gas Evolving Electrochemical Energy Conversion: High Performance Polymer Electrolyte Membrane Electrolyzers, *Energy Convers. Manage.*, 2020, **226**, 113545.
- 47 J. K. Lee, C. H. Lee, K. F. Fahy, P. J. Kim, K. Krause, J. M. LaManna, E. Baltic, D. L. Jacobson, D. S. Hussey and A. Bazylak, Accelerating bubble detachment in porous transport layers with patterned through pores, *ACS Appl. Energy Mater.*, 2020, **3**, 9676–9684.
- 48 C. Chardonnet, L. De Vos, F. Genoese, G. Roig, F. Bart, J.-C. Lanoix, T. Ha and B. Van Genabet Study on early business cases for H2 in energy storage and more broadly power to H2 applications, (2017), https://www.fch.europa.eu/sites/default/files/P2H_Full_Study_FCHJU.pdf, 02/19/2020.
- 49 C. Liu, M. Carmo, G. Bender, A. Everwand, T. Lickert, J. L. Young, T. Smolinka, D. Stolten and W. Lehnert, Performance enhancement of PEM electrolyzers through iridium-coated titanium porous transport layers, *Electrochem. Commun.*, 2018, **97**, 96–99, DOI: 10.1016/j.elecom.2018.10.021.
- 50 X. Wang, L. Zhang, G. Li, G. Zhang, Z.-G. Shao and B. Yi, The influence of Ferric ion contamination on the solid polymer electrolyte water electrolysis performance, *Electrochim. Acta*, 2015, **158**, 253–257.
- 51 S. Siracusano, N. Hodnik, P. Jovanovic, F. Ruiz-Zepeda, M. Šala, V. Baglio and A. S. Aricò, New insights into the stability of a high performance nanostructured catalyst for sustainable water electrolysis, *Nano Energy*, 2017, **40**, 618–632, DOI: 10.1016/j.nanoen.2017.09.014.
- 52 PRETZEL – Novel modular stack design for high pressure PEM water electrolyzer technology with wide operation range and reduced cost. <http://pretzel-electrolyzer.eu>, 12/11/2020 07:01.
- 53 F. Scheepers, M. Stähler, A. Stähler, E. Rauls, M. Müller, M. Carmo and W. Lehnert, Improving the Efficiency of PEM Electrolyzers through Membrane-Specific Pressure Optimization, *Energies*, 2020, **13**, 612, DOI: 10.3390/en13030612.
- 54 S. Siracusano, C. Oldani, M. A. Navarra, S. Tonella, L. Mazzapioda, N. Briguglio and A. S. Aricò, Chemically stabilised extruded and recast short side chain Aquivion proton exchange membranes for high current density operation in water electrolysis, *J. Membr. Sci.*, 2020, **578**, 136–148, DOI: 10.1016/j.memsci.2019.02.021.

Open Access Article. Published on 07 October 2021. Downloaded on 10/26/2021 9:18:01 PM.
This article is licensed under a Creative Commons Attribution 3.0 Unported Licence.




RESEARCH ARTICLE

Porous Transport Layers for Proton Exchange Membrane Electrolysis Under Extreme Conditions of Current Density, Temperature, and Pressure

Svenja Stiber, Harald Balzer, Astrid Wierhake, Florian Josef Wirkert, Jeffrey Roth, Ulrich Rost, Michael Brodmann, Jason Keonhag Lee, Aimy Bazylak, Wendelin Waiblinger, Aldo Sau Gago,* and Kaspar Andreas Friedrich

Hydrogen produced via water electrolysis powered by renewable electricity or green H₂ offers new decarbonization pathways. Proton exchange membrane water electrolysis (PEMWE) is a promising technology although the current density, temperature, and H₂ pressure of the PEMWE will have to be increased substantially to curtail the cost of green H₂. Here, a porous transport layer for PEMWE is reported, that enables operation at up to 6 A cm⁻², 90 °C, and 90 bar H₂ output pressure. It consists of a Ti porous sintered layer (PSL) on a low-cost Ti mesh (PSL/mesh-PTL) by diffusion bonding. This novel approach does not require a flow field in the bipolar plate. When using the mesh-PTL without PSL, the cell potential increases significantly due to mass transport losses reaching ca. 2.5 V at 2 A cm⁻² and 90 °C. On the other hand, the PEMWE with the PSL/mesh-PTL has the same cell potential but at 6 A cm⁻², thus increasing substantially the operation range of the electrolyzer. Extensive physical characterization and pore network simulation demonstrate that the PSL/mesh-PTL leads to efficient gas/water management in the PEMWE. Finally, the PSL/mesh-PTL is validated in an industrial size PEMWE in a container operating at 90 bar H₂ output pressure.

1. Introduction

In recent years, carbon dioxide (CO₂) emissions have been increasing worldwide by more than 60% from 1990 to 2019.^[1] In April 2020, the “Mission 2020” was launched to strengthen the efforts and implementation of CO₂ reduction approaches in the key sectors,^[2] because even if CO₂ emissions remain constant in 2020, the goals of the Paris Agreement of 2015 can no longer be achieved.^[3] Currently, about 48% of today’s hydrogen demand is produced from steam methane reformation, 30% from crude oil cracking and 18% from coal gasification, 3% as chlor-alkali byproduct while only 1% is produced by water electrolysis.^[4] If electricity from renewable energies is used for hydrogen production by electrolysis,

this is also referred to as green hydrogen.^[5,6] Recently, the European Union stressed the need for green H₂ to achieve carbon neutrality by 2050^[7] and plans to install 2x40 GW electrolyzer capacity by 2030.^[8] In Europe, the overall investments in renewable hydrogen are to be increased to € 180–470 billion by 2050.^[7] This unprecedented integration of large-scale electrolysis for the production of green H₂ can lead to a significant reduction in CO₂ emissions.

Two electrolysis technologies are particularly suitable for the implementation of green hydrogen production on the aforementioned scale. These include the already well matured, widely used alkaline water electrolysis (AWE) and the proton exchange membrane water electrolyzer (PEMWE).^[9] The main difference between the two technologies is the electrolyte. While AWE uses an alkaline solution as the electrolyte, PEMWE uses a solid membrane. This difference is directly coupled with the advantages and disadvantages of the respective technology. Although AWE is a mature technology, it has the disadvantage that can only operate at low current densities and operating pressure. Most commercial AWE can operate up to 0.5 A cm⁻²^[10] while PEMWE has a nominal load of about 2 A cm⁻².^[11] However, the cost of PEMWE systems is lagging behind AWE, which is 33% higher (900 € kW⁻¹).^[12]

The widespread installation of PEMWE around the world for generating green H₂ has been increasing rapidly. For example, Hydrogenics installed an operational 1 MW PEMWE in 2016.^[13] Already in 2018, Shell has started the installation of a 10 MW

S. Stiber, W. Waiblinger, Dr. A. S. Gago, Prof. K. A. Friedrich
Institute of Technical Thermodynamics / Electrochemical Energy Technology
German Aerospace Center (DLR)
Pfaffenwaldring 38–40, 70569 Stuttgart, Germany
E-mail: aldo.gago@dlr.de
Dr. H. Balzer, A. Wierhake
GKN Sinter Metals Filters GmbH
Dahlienstraße 43, 42477 Radevormwald, Germany
Dr. F. J. Wirkert, J. Roth, Dr. U. Rost,^[1] Prof. M. Brodmann
Westfälisches Energieinstitut
Westfälische Hochschule University of Applied Sciences
Neidenburger Str. 43, 45897 Gelsenkirchen, Germany
Dr. J. K. Lee, Prof. A. Bazylak
Department of Mechanical and Industrial Engineering
Faculty of Applied Science and Engineering
University of Toronto
Toronto, Ontario M5S 3G8, Canada
Prof. K. A. Friedrich
Institute for Building Energetics
Thermotechnology and Energy Storage
University of Stuttgart
70550 Stuttgart, Germany

The ORCID identification number(s) for the author(s) of this article can be found under <https://doi.org/10.1002/aenm.202100630>.

© 2021 The Authors. Advanced Energy Materials published by Wiley-VCH GmbH. This is an open access article under the terms of the Creative Commons Attribution-NonCommercial-NoDerivs License, which permits use and distribution in any medium, provided the original work is properly cited, the use is non-commercial and no modifications or adaptations are made.

^[1]Present address: ProPuls GmbH, Neidenburger Str. 10, 45897 Gelsenkirchen, Germany

DOI: 10.1002/aenm.202100630

PEMWE from ITM Power in its refinery as part of the EU project REFHYNE,^[14] which covers only up to 1% of the hydrogen consumption of the plant. Within the project “Westküste 100” the small refinery Heide, located near Hamburg, started the integration of a 30 MW electrolysis plant in the beginning of 2020, which will produce green hydrogen by using surplus offshore wind power and will be one of the first large scale demonstration plants of the energy transition or “Energiewende” in Germany.^[15] BP, Nouryon, and the Port Authority of Rotterdam are also working on a feasibility study for the installation of a 250 MW electrolysis plant to produce 45 kt H₂ per year. Nouryon, Orsted, ITM Power, and their partners are also investigating the implementation and installation of a 1 GW electrolysis plant.^[16,17] These extraordinary efforts contribute fundamentally to making green hydrogen competitive and thus potentially reducing CO₂ emissions significantly. Nevertheless, the IEA estimates that the cost of green H₂ should be 3.5–5 € kg⁻¹ compared to 1.5 € kg⁻¹ for grey hydrogen in order to be competitive.^[18]

Basically, two approaches can be considered for cost reduction of PEMWE. On the one hand, costs can be reduced by replacing expensive stack materials such as Pt, Ir, or Ti. However, this approach will compromise the performance or durability. Another and more realistic approach would be to operate the electrolyzer at conditions that will allow achieving high H₂ production rates. Thus, the highest demands of H₂ production from renewable energies for refueling vehicles, grid stabilization, and reserve energy market as well as various industrial applications can be met. The following operation aspects are fundamental for performance enhancement:

- i) High H₂ production rates by increasing the current density to reduce stack investment cost as well as stack volume
- ii) High operating temperature to enhance cell efficiency
- iii) High H₂ output pressure to avoid mechanical compression thus reducing costs and increasing efficiency on system level

Current standard operation range for commercial PEMWE is about 60 to 80 °C, 30 bar, and a nominal current density of 2 A cm⁻².^[11,19] Optimized PEMWE cell components have already been developed for these operating parameters. A scheme of a state-of-art (SoA) PEMWE single cell is shown in Figure 1a. Core components are the membrane electrode assembly (MEA), porous transport layers (PTL), and bipolar plates (BPP). The MEA consists of a proton exchange membrane (PEM) on which the anodic and cathodic catalyst layers are applied. The electrode catalysts consist of iridium or ruthenium oxides (IrO_x-RuO_x) on the anode side and platinum nanoparticles on carbon nanostructures (Pt/C) on the cathode side. The PTL on the anode, which is made of Ti, is an important key component, which needs to ensure effective media transport, specifically water transport from the flow field of the BPP to the electrodes and gas removal. It is well known that gas/water management strongly influences cell performance^[20–22] and mass transport losses (MTL) must be kept low. Therefore, this phenomenon becomes more relevant with increasing the applied electrical current,

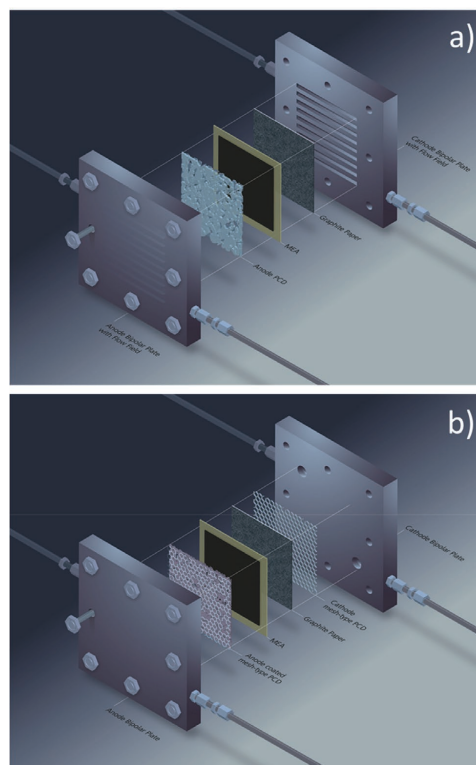


Figure 1. Schemes of PEMWE cell configurations: a) State-of-art (SoA) cell with Ti porous PTL which still requires a flow field in the BPP and b) cell with Ti PSL/mesh-PTL and BPP without flow field.

as the production rates of the gases increase. Anode PTLs that are commercially available vary from sintered powder structures, felts, and meshes, but there are also new developments like tuneable PTLs with controlled parameters like porosity^[23,24] and pore structure with size gradients.^[25,26] Carbon paper is commonly used for the cathode PTL in PEMWE.^[27]

However, sophisticated PTLs for the anode need to be redesigned to minimize high overpotentials due to MTLs which reduce the cell efficiency. In this study we developed a novel PTL produced by diffusion bonding of a Ti porous sintered layer (PSL) on a Ti expanded metal sheet or mesh, allowing to dispense with the flow field in the BPP. The PTL was tested in a PEMWE under extreme conditions of current density, temperature, and pressure, that is up to 6 A cm⁻², 90 °C, and 90 bar. The PTL ensures efficient gas/water management at high current densities. Finally, the functionality of the PTL at 90 bar H₂ output pressure was successfully validated in an industrial size PEMWE in a container with a stack-based on the hydraulic cell compression concept.^[28–30]

2. Discussion of Results

2.1. Morphology of the Coatings

Photos of the PSL/mesh-PTL produced by diffusion bonding are presented in Figure S1a,b, Supporting Information, which corresponds to the side in contact with the BPP and MEA, respectively. The difference between the two surfaces is clearly visible in Figure 2: the hills and valleys of the expanded mesh in Figure 2a,b that play a similar function as the flow field in the BPP and the dense surface of the PSL in cross-sectional images of Figure 2c,d which contacts uniformly the catalyst layer (CL). The morphology and the microstructural properties of the PSL/mesh-PTL were investigated by SEM.

A homogeneous porous structure of the coated powder can be observed, which is diffusion bonded to the expanded mesh

substrate. This detail is shown by a high-magnification image in Figure 2e. While the PSL structure contacts the electrode, the mesh substrate is correspondingly oriented towards the BPP distributing the applied current and managing gas/water transport. The fine porous structure closes completely the holes of the substrate mesh, avoiding that the MEA is pressed into the valleys of the expanded mesh during cell compression and is therefore protected from mechanical stress.^[31] Cross-sectional images of the MEAs with and PSL/mesh-PTL are shown in Figure S2, Supporting Information. Moreover, closing the holes of the mesh-PTL with the PSL is also advantageous as it increases the catalyst utilization.^[32,33] Figure S3, Supporting Information, presents PSL/mesh-PTL under polarized light. The polarized light provides particularly good contrast and visualization of the structure and grains of the Ti particles. Due to the heat treatment a classical α , β structure forms the

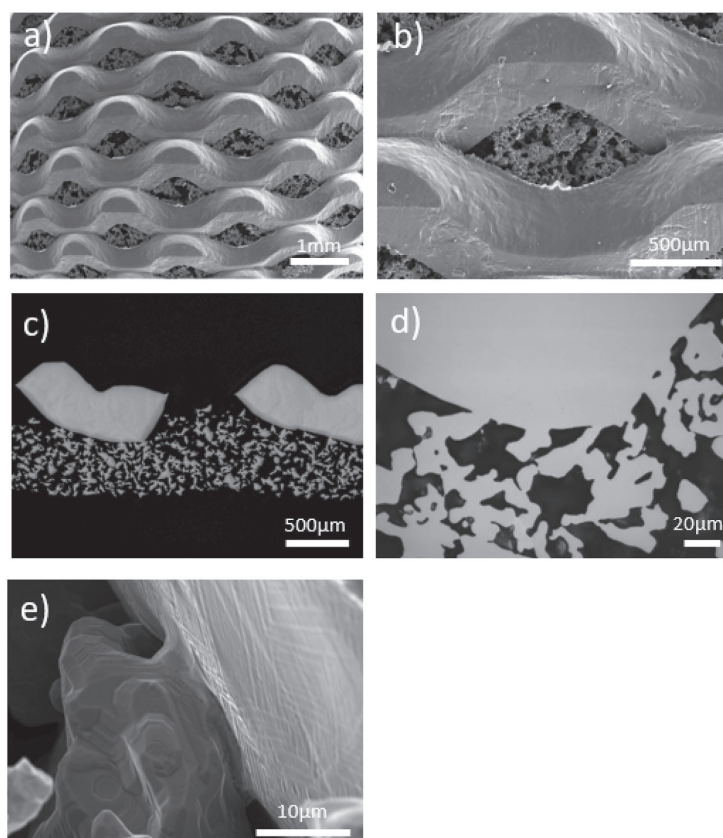


Figure 2. Images of PSL/mesh-PTL a) substrate side with low magnification, b) substrate side with high magnification as well as cross-sectional images of c) PSL/mesh-PTL with low magnification, d) PSL/mesh-PTL with high magnification, and e) high magnification image of the interface of the mesh substrate and the macro-porous structure coating of PSL/mesh-PTL.

Table 1. Pore properties from filter specific tests for PSL/mesh-PTL measured at the PSL.

Property	PSL/mesh-PTL
Thickness/mm	0.7 ± 0.1
Pore size/ μm (calculated from Bubble Point)	52,3
Density/%	50–60
Porosity/%	40–50
SP ^{a)} / μm	18
MFP ^{a)} / μm	36
LP ^{a)} / μm	70
Bubble Point/mbar (isopropanol)	18
Flow/ $\text{m}^3 \text{h}^{-1} \text{m}^{-2}$ (air, 1 mbar)	365
Permeability	
$\alpha/10^{-12} \text{m}^2$	13,5
β/m	8,5

^{a)}measured at PSL.

composition of the PSL which can be observed under the polarized light. A uniform structure is the basis for the high stability of the sample under the corrosive conditions in the PEMWE, which Ti is known to withstand.^[11]

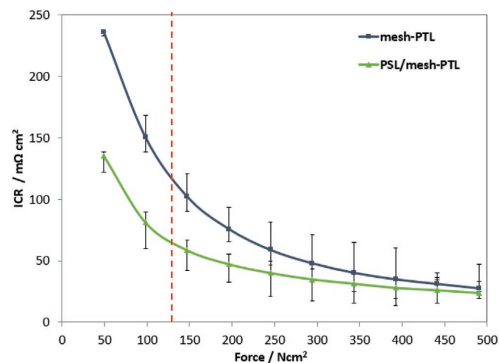
2.2. Pore Properties and Interfacial Contact Resistance (ICR)

The pore properties of PSL/mesh-PTL found by the bubble point, pore size distribution, and permeability tests described in section 2.2.2 are presented in Table 1 summarizing sample thickness, pore size, density, porosity, bubble point, and permeability. Real porous structures usually have more than just a certain pore size as in a supposedly ideal porous structure, which is why values are given for small pores (SP), mean flow pore (MFP), and large pores (LP). The pore size variation within the porous layer of the PSL/mesh-PTL ranges from 18 to 70 μm for the SP and LP, respectively, and a porosity of about 40 to 50 % can be determined.

In addition to optimal pore properties, the electrical contacting of the samples within a cell plays an important role in achieving high performance. This can be evaluated by determining the ICR and was measured comparatively for PSL/mesh-PTL as well as for mesh-PTL. For the measurement, a setup was chosen that comes as close as possible to the conditions for the PTL in an electrolysis cell. Due to its high in-plane electrical conductivity, the carbon paper acts as a substitute for the precious metal-based electrode with which the PTL is contacted in the cell. Considering the ICR at a compaction force of 150 N cm^{-2} , which is typically used in commercial electrolyzer stacks,^[34] the PSL reduces the contact resistance by 43% to about 58 $\text{m}\Omega \text{cm}^2$ compared to the uncoated mesh. The results are presented in Figure 3.

2.3. Electrochemical Performance and Simulation

Figure 4a presents the E_{Cell}/j -characteristics of the PEMWEs using mesh-PTL and PSL/mesh-PTL up to 6 A cm^{-2} . For a

**Figure 3.** Interfacial contact resistance (ICR) with respect to compaction force of mesh-PTL and PSL/mesh-PTL. The slashed line indicates the typical compaction force of a commercial PEMWE stack.

PEMWE operated under extreme conditions, a current density of 4 A cm^{-2} can be considered as a nominal load while 6 A cm^{-2} would correspond to overload. The cell with mesh-PTL is operable to a current density of only up to 4 A cm^{-2} already reaching an E_{Cell} of 2.89 V while not exceeding 3.0 V. Operation at this high potential is economically not attractive and oxides are formed on the surfaces of Ti components leading to higher ohmic resistance. Furthermore, a deviation between ascending and descending curves occurs which can be evaluated as a first indicator for MTLs according to earlier publications.^[26] The upward bend of the curve corresponds to a limitation due to inefficient gas/water management. Expanded Ti meshes as tested comparatively in this study have a clear price advantage over other expensive PTLs such as Ti felts but as demonstrated in Figure 4a they are far less efficient. In contrast, the cell with the PSL/mesh-PTL achieves a cell voltage of 2.54 V at 6 A cm^{-2} (overload) showing a polarization curve with a totally linear slope, and ca. 2.2 V at 4 A cm^{-2} . For comparison PEMWE commercial electrolyzers, such as those from Hydrogenics,^[35] Siemens,^[36] and Proton Onsite^[37] achieve about 2.2 V at 2 A cm^{-2} while the PEMWE with the PSL/mesh-PTL allows operation at twice the current density at the same cell potential. However, currently, these PEMWE operate in the temperature range of 60–80 °C. The PSL/mesh-PTL combines low-cost Ti expanded mesh with a porous layer that allows reducing the cell overpotential by 693 mV at 4 A cm^{-2} compared to the mesh-PTL. Thus, an efficiency increase of 24 % can be achieved which has a significant impact on the operational cost of the electrolyzer.

Further, a deep explanation of the observed phenomena is given by electrochemical impedance spectroscopy (EIS). The Nyquist plots of the PEMWE with mesh-PTL and PSL/mesh-PTL at 0.25, 1, and 4 A cm^{-2} are given in Figure 4b–d, respectively. In earlier work, an equivalent circuit was introduced as a basis for the analysis of Nyquist spectra,^[26] which was further adapted and is described in Figure S4, Supporting Information. The ohmic resistance can be determined from the intersection of the first semicircle in the high-frequency range with the x-axis. Literature references assign the high-frequency arc to the hydrogen evolution reaction (HER),^[38] charge transfer

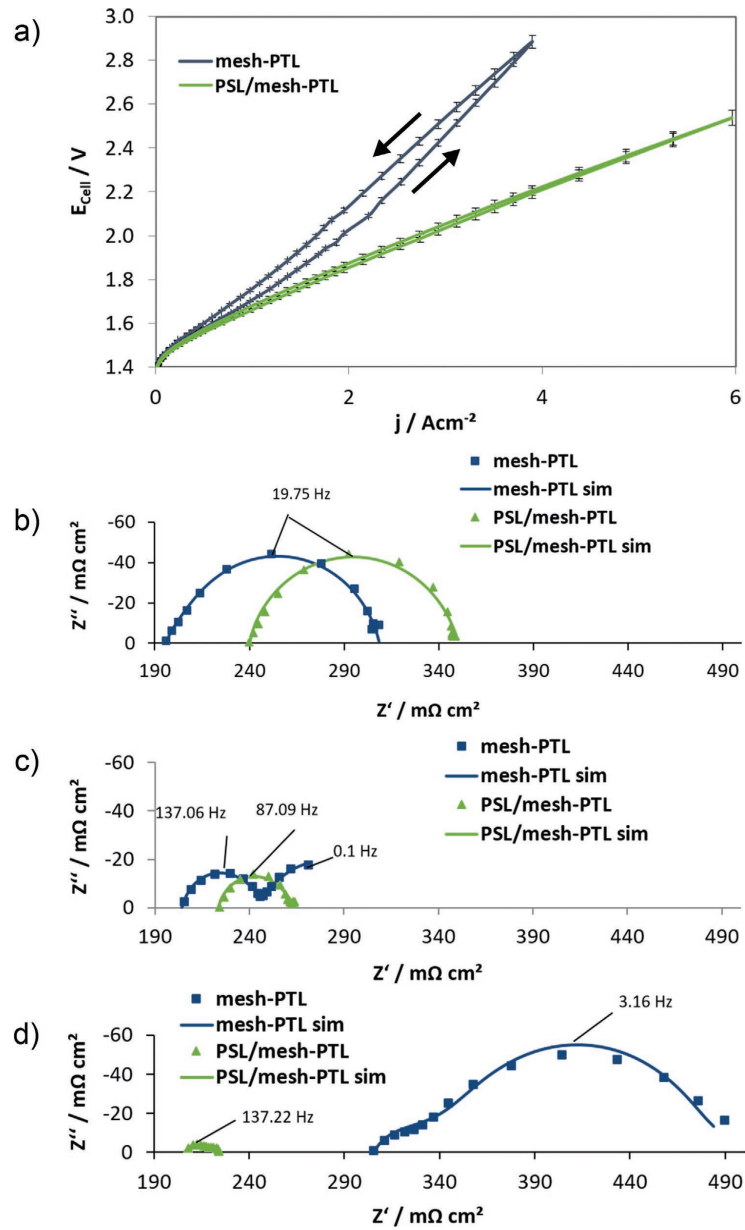


Figure 4. a) Polarization curves of PEMWE cells with mesh-PTL and PSL/mesh-PTL up to 6 A cm^{-2} . Nyquist plots at b) 0.25 , c) 1 , and d) 4 A cm^{-2} from 100 mHz to 50 kHz . All measurements were carried out at $90 \text{ }^\circ\text{C}$ and ambient pressure.

resistance coupled with double layer effects,^[35] or the first charge transfer of the 4-electron process of the oxygen evolution reaction (OER). The OER in the electrochemical splitting of water into O₂ is a 4-electron process (independent of the reaction mechanism and the catalyst used, i.e., Pt or IrO₂). The Krasil'shchikov mechanism formulated in C. Rozain et al. is only for 1/2 O₂, thus requiring only two electrons.^[39] However, to generate O₂ it will require 4 electrons. The medium and low-frequency semicircle can be attributed to the charge transfer of the OER rate determination step and the MTLs.^[40]

At 0.25 A cm⁻² for both samples, one semicircle occurs with a peak at a frequency of 19.75 Hz and is thus mainly caused by charge transfer resistances with respect to OER. The difference between the mesh-PTL and PSL/mesh-PTL can be seen in the intersections with the real part axis, which results from the different ohmic resistance of the PTLs. The EIS at 0.25 A cm⁻² reveals an ohmic resistance of 190 and 239 mΩ cm² for mesh-PTL and PSL/mesh-PTL. When increasing current density to 1 A cm⁻² the semi-circles start to change in their behavior. The ohmic resistance changes for both cells and the values approach each other. For mesh-PTL, the resistance increases by 9 mΩ cm², while PSL/mesh-PTL decreases by 16 mΩ cm². For the cell with the mesh-PTL, the semicircle, which is associated to the OER kinetics, is insignificantly larger in size than for PSL/mesh-PTL with a maximum at 13706 Hz. Only for mesh-PTL, a second arc with an apex at 0.1 Hz appears, indicating MTLs. This is in good agreement with the polarization curves of the cell with mesh-PTL in which the slope starts bending upwards at about 1 A cm⁻² while for the cell with the PSL/mesh-PTL the slope keeps a linear behavior.

While at low currents, the slow kinetics of the OER results in performance loss, for the cell with mesh-PTL the MTL becomes the determining factor at high current densities. At 4 A cm⁻², the ohmic resistance of the cell with the mesh-PTL increases to 306 mΩ cm² and the second semicircle related to MTL with a peak at 3.16 Hz enlarges considerably. Conversely, the arc associated with the OER in the cell with the PSL/mesh-PTL decreases in size as expected and shifts gradually to the left with the applied current density. The latter effect can be due to heat generation at the interface between the PSL and the electrode. Most notably, the arc associated with the MTLs is almost not visible even at 6 A cm⁻².

In order to explain the phenomenon of oppositely developing ohmic resistances for mesh-PTL as well as PSL/mesh-PTL at 1 as well as 4 A cm⁻², simulation data are interpreted. From these, the resistance caused by the MTL can be determined and accounts for 96 mΩ cm² (see Figure S5b, Supporting Information). The high resistance associated with the MTL is caused by the absence of SPs at the contact surface of the uncoated mesh, which means that gas bubbles can only be discharged to a limited extent by capillary forces, as the pore gradient is too small.^[43] The gas blocks the active centers until a certain bubble size is reached. In addition, Ito et al. show that the bubble size depends on the pore size of the PTLs.^[42] The larger gas bubbles increase the gas coverage of the transport channels and obstruct the water supply. This accumulation of gas at the interface of PTL/CL can also explain the increase in ohmic resistance due to the formed gas cushion which reduces the electrical contact between the components.

For the PSL/mesh PTL, the ohmic resistance is 203 mΩ cm² and a second semicircle can barely be seen. With a modal pore diameter of 44 μm and increased porosity, the PSL/mesh-PTL ensures improved mass transport at high current densities. By simulating the Nyquist plots the resistance related to MTL can be determined and corresponds to 5.07 mΩ cm² (see Figure S5b, Supporting Information) and therefore MTL can be neglected. Since MTL has been practically eliminated for the PSL/mesh PTL, the gas/water management is optimized, particularly at high current densities. As a result, the electrical contact, which is directly coupled to the ohmic resistance of the cell, is maintained. Due to the optimal electron and mass transport for the PSL/mesh-PTL, the loss processes for high current densities are minimal compared to the mesh-PTL.

The improved mass transport properties of the PSL/mesh-PTL can be explained by pore network modeling. The drainage curve acquired with the PSL/mesh-PTL, Figure 5a, exhibited similar trends as reported in the literature with other PTLs.^[43] Due to the larger pore openings at the mesh interface, the required capillary pressure to remove gas was lower (7143.55 Pa required to achieve 86 % gas saturation). In fact, the permeability of liquid water with gas saturated pores (also known as the two-phase permeability)^[44-46] in the PSL/mesh-PTL was orders of magnitude higher than the predicted permeabilities of the liquid water in PTLs in previous work,^[44,45] which implies that reactant delivery was more effective with the PSL/mesh-PTL. With both phases present, the permeability of liquid water and the permeability of gas have significant impacts on electrolyzer performance. The permeability of liquid water determines how effectively liquid water reactant reaches the reaction sites, and the permeability of gas determines how effectively product gas is removed from the reaction sites. We previously reported that the flow of liquid water exerts a shear stress (proportional to its kinetic energy) on the counter-flowing gas traveling through the PTL. Increasing the permeability of the gas phase facilitates more gas removal in the PTL of an operating electrolyzer.^[47] For conventional PEMWEs, permeability can be considered a less energy-demanding flow mechanism as compared to two-phase flows in microscopic pores. However, the PEMWE used for this work have BPPs without a flow field and water is not flowing. Therefore, there is practically no friction between the gas exiting and the water entering the electrolyzer and thus a two-phase mass transport mechanism was used for the calculation of permeabilities.

Based on invasion percolation simulations with various inlet conditions, the gas saturation in the PTL remained significantly low (12%) even at the high surface coverage of gases at the interface with the CL, 750 inlet clusters, a subset of Figure 5a. The low gas saturation of the PSL/mesh-PTL is due to the porosity gradient resulting from a bilayer structure of the PSL and mesh-PTL. Previous modeling results in the literature^[42] reported a significant reduction in gas saturation (up to 70% reduction of gas saturation) when lower porosity was positioned next to the CL. The low gas saturation in the PSL/mesh-PTL suggested that even at high current density operation, the generated gases would be effectively removed via larger pores in the PTL. Therefore, the PSL/mesh-PTL exhibited high permeability of both liquid water and gas as shown in the grey regions of Figure 5b,c, providing effective two-phase transport for higher current density operations.

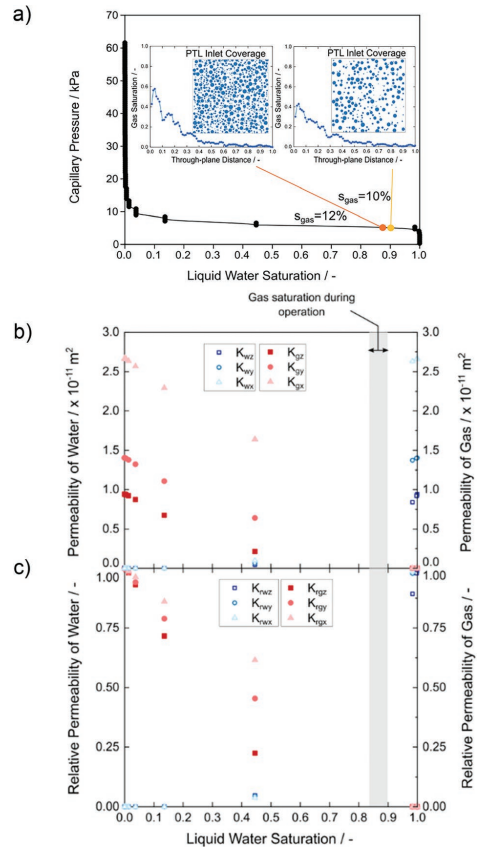


Figure 5. Pore network simulations that account for the mass transport mechanisms in the PSL/mesh-PTL. a) drainage curve acquired for PSL/mesh-PTL. The subset figures indicate the gas surface coverage at the CL-PSL interface, simulating scenarios of high and low current densities (750 and 250 inlet clusters) and their resultant gas saturation profiles. Although the number of inlet clusters increases significantly from 250 to 750 clusters (at the CL-PSL interface), the overall gas saturation only increases by 2% due to the effect of the porous structure of the PSL/mesh-PTL. b) Permeability of liquid water and gas in the presence of both phases in the pore structure and c) relative permeability (ratio of the permeability of liquid water with and without the presence of gas saturated pores) of the PSL/mesh-PTL. The grey shaded region (gas saturation during operation) was obtained by performing invasion percolation with varying inlet coverage as shown in (a).

2.4. Validation in High H₂ Pressure System

Due to safety reasons, the evaluation of the PSL/mesh-PTL in a PEMWE that produces high H₂ pressure requires an industrial system in a container such as the one shown in Figure 6a. For these tests, only the PSL/mesh-PTL was tested in the stack as

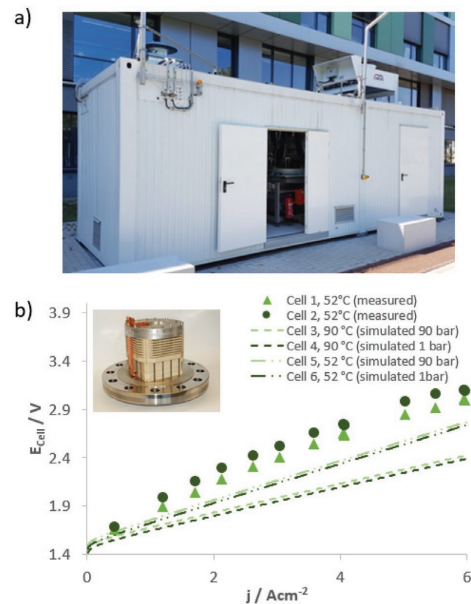


Figure 6. a) Photo of the PEMWE system for a maximum production of 5 Nm³ h⁻¹ integrating the stack showed b) Polarization curve with PSL/mesh-PTL at a pressure of 1 and 90 bar at 52 and 90 °C up to 6 A cm⁻². The dashed lines represent the simulated polarization curve of PSL/mesh-PTL at 1 and 90 bar as well as 90 °C up to 6 A cm⁻². A photograph of the utilized stack based on hydraulic cell compression is shown in the inset. Following the polarization curve from Figure 6b, a durability test was carried out for 600 h. The stack was operated at 65 °C and constant 2 A cm⁻². The results show a negligible degradation rate of 4.43 μV h⁻¹ and can be seen in Figure S7, Supporting Information.

the cells with the mesh-PTL cannot keep the E_{Cell} low at high current densities. In Figure 6b an exemplary E_{Cell}/j-characteristic of this test cell is recorded at ca. 52 °C, 95 bar oxygen pressure, and up to 6 A cm⁻² resulting in a voltage at a peak current density of 2.98 V. Currently, it is not possible to reach 90 °C. In a conventional stack design, the temperature increases sharply along with current density causing the bending of the polarization curve.^[35] However, a stack-based on hydraulic compression technology is designed to dissipate heat in a very efficient way through the hydraulic media ensuring a homogeneous temperature over the cell area. In this regard, to reach 90 °C the balance of plant (BoP) of the PEMWE requires a retrofitting system, which is currently under development. Therefore, at present, it is not possible to evaluate the PSL/mesh-PTL under the three extreme conditions of operation all at the same time due to the PEMWE system limitations. That is, the PEMWE can operate either under 6 A cm⁻², 90 °C, and 1 bar or 6 A cm⁻², 52 °C, and up to 90 bar. In any case, it is clearly proven that the PSL/mesh-PTL can withstand the three extreme conditions of operation. By using a simple numerical model based on the

Nernst equation one can simulate the polarization curve at 1 and 90 bar which are shown as dashed lines in Figure 6b at 52 and 90 °C. The calculated E_{Cell} of the stack at 6 A cm⁻², 90 °C, and 90 bar is comparable to the one achieved with single-cell measurements. The details for the calculation of the cell voltage can be taken from the SI.

Translating the results presented in this work to the current market needs, the cost of green hydrogen can be significantly reduced. The integration of intermittent renewable energy into the power grid, including the provision of balancing power, raises new requirements in terms of efficiency, flexibility, partial load and stand-by operation, PEMWE capacity (GW scale plants), and investment cost (Capital expenditure(CAPEX)) depending on the specific application/operation strategies. By operating the PEMWE at a high current density and maintaining SoA cell efficiency, an increased H₂ production rate can be achieved, which reduces costs further. Higher specific H₂ production rates reduce the stack volume, lower the system costs, decrease the footprint of the electrolyzer, and ultimately bring closer the widespread utilization of green H₂ in the industry and mobile sectors.

One remaining question is about the long-term stability of the PSL/mesh-PTL. Certainly, PEMWE cell components may degrade faster under operation at extreme conditions. However, the PSL/mesh-PTL is made of Ti and at nominal operation, which we defined now at 4 A cm⁻², the E_{Cell} is still kept low, thus no excessive formation of TiO₂ is expected. Moreover, operating at 90 °C instead of 65 °C will not increase significantly the rate of Ti oxidation. Last, thanks to hydraulic cell compression technology, the mechanical stress on the PSL/mesh-PTL is lower than what it would be in the traditional PEMWE designs. Operation at highly stressing conditions will most likely have an impact on the PEM and ionomer of the MEA as well as on the BoP components. Therefore, more R&D is needed on these topics to bring to the market a PEMWE that can operate at extreme conditions of current, density, and pressure.

3. Conclusion

We have developed a novel PTL for PEMWE by sintering a macro-porous structure of Ti on an expanded Ti mesh, PSL/mesh-PTL, thus producing a fully functional cell component with enhanced properties. The PSL has uniform pore size distribution and porosity and is fully bonded via diffusion to the mesh-PTL, which eliminates any interfaces that cause ohmic losses. From the PEMWE tests, the PSL/mesh-PTL allows achieving up to 6 A cm⁻², 90 °C, and 90 bar H₂ output operation. The PEMWE with the PSL/mesh-PTL reached 31% higher efficiency than the mesh-PTL at a nominal load of 4 A cm⁻². Pore network modeling showed that the large increase in performance is attributed to the high permeability for both liquid and gas for the PSL/mesh-PTL, providing effective two-phase transport at high current densities. The PSL/mesh-PTL design addresses all tasks in the cell regarding water distribution and gas transport, thereby eliminating the need for a bipolar plate with a complex flow field. Operating PEMWE at high current density, temperature, and pressure makes it more economically attractive. In the near future, these challenging operating conditions can be established

as the new SoA in electrolysis for the large-scale integration of renewable energies, thus reductions in CO₂ emissions can continue at a more aggressive pace. The PSL/mesh-PTL presented in this work will be now a commercial product and possible interested laboratories can order it from GKN Sinter Metals.

4. Experimental Section

PSL on Ti-Mesh by Diffusion Bonding: Fine Ti powder and a supporting expanded mesh were used to produce porous, asymmetrically structured current distributors. Both deployed raw materials were composed of grade 1 titanium. These expanded metal sheets were produced by cutting slits into a plate and stretching this plate afterward. This process created a specific pattern with open gaps resulting in an open porosity of 55 %. Subsequently, Ti powder was deposited on the expanded mesh to produce the PSL.

The deposition technique has been optimized so that a homogeneous layer on the structural supporting material is generated. Next step was diffusion bonding via a sintering process to generate a firmly bonded asymmetric compound structure. The heat treatment was performed under a vacuum of 2×10⁻⁵ mbar to prevent oxide formation. Typically, the sinter temperature is 70 % of the absolute melting temperature. The optimal sinter temperature varied also within the particle size distribution of the metal powder: the finer the powder the higher the diffusion activity. The batch furnace used for heat treatment was build up with metal heating elements and metal shielding without any graphite elements to prevent carbide formation. The produced PTL was labeled as PSL/mesh-PTL. In order to obtain a better understanding of the PSL properties, a similarly produced porous film (without expanded metal sheet) was prepared and examined so that the specific pore properties could be determined without any loss in accuracy due to the larger pores of the mesh compared to those of the PSL which would affect the measurements.

Polarized Light Microscopy: A microscope system for materials research was used for analyzing the coating quality as well as the morphology of the produced coated samples. Cross-section images were recorded with a Zeiss AXIO Imager.A2m using a Jenoptik ProgRes Speed XT core 5 camera. Furthermore, polarized light was used to determine the structure and grains of the material by interference, depending on the sample thickness, birefringence, and the resulting light path difference.

Filter Specific Tests and X-Ray Computer Tomography (CT): Filter-specific tests like bubble point, pore size distribution, permeability as well as μ CT measurements were carried out to characterize the morphology and sample properties.

Bubble point measurements were performed according to ISO 4003: "Permeable sintered metal materials; Determination of bubble test pore size" for filter, bearings, and porous electrodes, which have an inner connected pore structure. The measured pressure value gives information of the (theoretical) apparent maximum pore size which could be determined by the formula (Equation (1)):

$$d = \frac{4\delta \cos \varphi}{\Delta p} \quad (1)$$

Here, d , δ , φ , and Δp are the apparent pore size, surface tension, contact angle, and differential pressure, respectively. This pore size merely relates to idealized cylindrical pore structures, and a determination was performed by infiltrating a test specimen with an appropriate liquid with known surface tension via sample immersion. An increasing gas pressure was charged to one side of the specimen until one first bubble could be detected. The minimum gas pressure that was required to force liquid out of the capillary is called the bubble point pressure.

According to ASTM E 1294, pore size distribution measurement was conducted. This standard test enabled calculation of the pore size distribution according to largest pore (LP), MFP size, and smallest pore (SP) within a filter medium and was based on the bubble point test. Therefore, an automated liquid PMI porometer was used. The specimen

to be examined was infiltrated with Topor (16.0 mN m⁻¹, Topas GmbH). Gradually gas pressure was increased to charge the porous specimen until the test liquid was removed and all pores were free from test liquid. During the test, the flow rate was accurately recorded by the porometer. Afterward, a second test run without test liquid was executed. From the measured gas pressure and flow rates the pore diameters, the pore size distribution and the gas permeability could be calculated.

The third physical characterization was the determination of permeability following ISO 4022 "Permeable sintered metal materials – determination of fluid permeability" giving information on how well a medium, gas, or liquid, flowed through a porous filter. For the calculation of permeability, the applied pressure, the pressure-drop across the filter, and the flow rate were needed. Usually, air was used for flow rate measurement. The viscosity of the flowing medium was an important parameter for the flow rate as a function of pressure drop. The fluid permeability can be expressed in terms of viscous and inertia permeability coefficients as follows:

$$\Delta p = \frac{V s}{A} \left[\frac{\eta}{\alpha} + \frac{\rho \dot{V}}{\beta A} \right] \quad (2)$$

α , β , s , \dot{V} , ρ , Δp , A , and η express here viscosity coefficient, inertia coefficient, filter thickness, flow rate, fluid density, pressure drop at the filter, filter area, and dynamic viscosity.

X-ray CT analysis was performed with a multi-scale X-ray microtomograph (Skyscan1172, Bruker). The reconstructed sample volume was 1760.3×4239.6×3599.6 μm³, achieving a resolution of 1.43 812 μm. An acceleration potential of 80 kV was used.

Interfacial Contact Resistance (ICR): The influence of the PSL on interfacial contact resistance (ICR) of the PSL/mesh-PTL with respect to the compaction force was measured according to previously published methodology.^[34] After all PTL samples were cleaned by immersing in deionized (DI) water and isopropanol baths while applying ultrasonication for 10 min for each step, a final cleaning cycle was carried out with DI water for 5 min. The PTL samples were placed in an oven for 20 min at 60 °C for drying. To measure ICR the cleaned PTLs were placed in between a titanium plate (3.7025) and a TGP-H-90 and sandwiched by two gold-coated copper cylinders. A hydraulic press, in which this setup was placed, was used to apply a weight of 20 to 200 kg in steps of 20 kg. A potentiostat/galvanostat (Zahner Elektrik IM6) with a booster (Module PP240) was connected to the cylinders applying a constant current of 1.25 A cm⁻². The response voltage was monitored. Determination of the ICR between the carbon paper and the PSL was calculated by the following equation:

$$R_{C/Coating} = R_{measured} - R_{C/Au} \quad (3)$$

where $R_{C/Au}$ can be assigned to the ICR of the gold-coated cylinder. An uncoated mesh-PTL made of Ti was also measured for comparison purposes.

PEMWE Tests: The samples to be tested were investigated using cells having different cell sizes and ranging from laboratory to system scale. First electrochemical characterization was performed using a laboratory cell with an active area of 4 cm². On the anode side Ti-BPP grade 1 and PSL/mesh-PTL were used while on the cathode side an uncoated carbon paper (TGP-H-90), as well as multilayer stainless steel mesh-PTL (Haver & Boecker OHG) and stainless steel BPP with 1.4404 grade, were used. An Ir-based anode, Pt-based cathode, and chemically stabilized Nafion 115 membrane were used as MEA for all electrochemical tests. The catalyst loading was 2.5 mg cm⁻² for iridium and 0.95 mg cm⁻² for platinum. Based on the results from a torque study of the described cell arrangement and considering mechanical stress at high compaction force, the cells were tensioned with 1 N m. Polarization curves up to 6 A cm⁻² were recorded and EIS was performed at 0.25, 1, and 4 A cm⁻² and an amplitude of 100, 200, and 500 mA, respectively, from 100 mHz to 50 kHz. Both electrochemical

characterizations were performed according to JRC protocols.^[48,49] A potentiostat/galvanostat (Zahner Elektrik IM6) with a booster (Module PP240) was used for these measurements, which were carried out at 90 °C and ambient pressure. For comparison reasons, the mesh-PTL was measured.

For the tests at high H₂ output pressure, the PSL/mesh-PTL was evaluated in a 5 Nm³ h⁻¹ PEMWE system in a container using a stack design based on hydraulic cell compression. For the study described in this work, a stack was developed based on R&D results which were described elsewhere. It has been shown that for earlier PEMWE prototypes, homogeneous cell compression was achieved over the active cell area due to a hydraulic cell clamping.^[50] The principles and benefits of hydraulic cell compression were adapted to develop an advanced PEMWE prototypic stack for high operation temperatures, high current density, and high operation pressure up to 90 °C, 6 A cm⁻², and 100 bar.

Single electrolyzer cells were also completely surrounded by a hydraulic medium, while the pole plates (PP) were utilized as a part of the flexible pockets, in which the active material was integrated.^[51] By increasing the pressure level of the hydraulic medium, compression forces were applied to the PEMWE cell's PP through their intrinsic flexibility. As a result, the pressure level was equal in each point of the active cell area and, therefore, cell compression was as well homogeneous as adjustable to increasing hydrogen production pressures. Furthermore, circulation of the hydraulic medium was established with an integrated heat exchanger for waste heat removal facilitating even temperature conditions for investigated cells. Controlling the temperature and pressure of the hydraulic medium resulted in reproducible test conditions, which can be precisely adjusted.

The utilized PEMWE test stack comprised two cells with PSL/mesh-PTLs. Similar MEAs as in the single-cell measurements were used. The active cell area for the cells investigated in this study was 210 cm². Polyetheretherketone (PEEK) was chosen as frame material to integrate the active components, due to its inertness, especially against the process water as well as evolving hydrogen and oxygen. For the analysis reported in this study, it has been integrated into a specially developed 5 Nm³ h⁻¹ containerized test system shown in Figure 6a for high-pressure operation.

Polarization curves were recorded up to 6 A cm⁻² at 52 °C with oxygen and hydrogen output pressure of 95 and 90 bar, respectively. Later, it will be justified why the stack could only reach 52 °C and not 90 °C. In contrast to conventional stack designs with mechanical compression, the innovative design^[28–30] allowed homogeneous temperature distribution and cell compression. Therefore, hotspots due to inhomogeneous current density distribution or mechanical stress can be avoided enabling the ambitious operating parameters.

Numerical Modeling: Two-phase transport properties of the PSL/mesh-PTL were simulated using pore network modeling via an open-source pore network model (OpenPNM).^[52] For a more detailed description of the pore network modeling on PTLs for PEMWE, the readers were directed to the following studies.^[44–46] For the pore network model implemented in this work, while the pores were represented as spheres connected by cylindrical throats, the total volume of the pore space itself was unaltered. The drainage of liquid water (wetting phase in a hydrophilic PTL) via the quasi-static invasion of oxygen gas (non-wetting phase) was used to simulate two-phase flow inside the anode compartment of the PEMWE. The nature of gas invasion into a water-filled PTL was dominated by the entry capillary pressures of the throats. Specifically, during drainage, the gaseous phase preferentially invaded pores connected to throats with the lowest capillary pressure. In this work, the capillary pressure of all pores and throats were calculated using the Young-Laplace equation:

$$P_c = \frac{-2\gamma \cos \theta}{r} \quad (4)$$

where P_c is the capillary pressure (Pa), γ is the surface tension (N m⁻¹), r is the radius of a pore throat (m), and θ is the contact angle (radians).

The drainage curve of the PSL/mesh-PTL was obtained by incrementing capillary pressure until the PTL became fully void of liquid water from an initially fully wet condition.

The permeability was used as an indicator to predict mass transport in the PTL. The single-phase permeability (permeability of one phase in a porous structure) was solely the property of the porous structure. However, permeability values change in the presence of the second phase. Specifically, when the second phase occupies pore spaces, the permeability of the first phase was reduced. Herein, this permeability was referred to as the permeability of liquid water, which illustrates the effectiveness of the PTL to facilitate the delivery of reactants to the reaction sites in the presence of oxygen gas. Permeability of gas also illustrated the effectiveness of the PTL to facilitate the removal of the by-product gases from the reaction sites in the presence of liquid water. To calculate the permeability of the PTL, the net flow into each pore was first determined by applying the conservation of mass to each pore:

$$q_i = \sum_{j=1}^n g_{h,ij} (P_j - P_i) = 0 \quad (5)$$

where i and j are the current and neighboring pores, respectively. q_i is the net flow in pore i ($\text{m}^3 \text{s}^{-1}$), P is the pressure at each pore ($\text{kg m}^{-1} \text{s}^{-2}$), and $g_{h,ij}$ is the hydraulic conductivity for flow between each neighboring pore ($\text{m}^4 \text{s kg}^{-1}$), which was calculated with the Hagen–Poiseuille model^[53]

$$g_h = \frac{\pi r^4}{8L\mu} \quad (6)$$

where r is the radius of a pore or throat (m), L is a length of a pore or throat (m), and μ is the dynamic viscosity ($\text{kg m}^{-1} \text{s}^{-1}$). The net hydraulic conductivity was then calculated with linear resistor theory using values of hydraulic conductivities for half of pore i , the connecting throat, and half of pore j :

$$\frac{1}{g_{h,ij}} = \frac{1}{g_{h,pi}} + \frac{1}{g_{ht}} + \frac{1}{g_{h,qj}} \quad (7)$$

The total flow, Q ($\text{m}^3 \text{s}^{-1}$), across the PTL was solved from a set of linear equations (Equation (5)) in conjunction with the prescribed pressure boundary conditions at the inlet and outlet of the PTL. Using Darcy's law, the permeability of the PTL was calculated as follows:

$$Q = \frac{KA}{\mu l} (P_{\text{in}} - P_{\text{out}}) \quad (8)$$

where K is the permeability (m^2), A is the cross-sectional area of the PTL (m^2), and l is the length of the PTL in the flow direction (m).

The invasion percolation simulation with varying inlet conditions was implemented to predict gas saturation in an operating PEM water electrolyzer. A number of gaseous droplets (with diameters randomly selected between 7.5 to 60 μm) were stochastically placed at the CL-PTL interface to mimic realistic operating conditions. A set of 250 inlet droplets was used to represent low current density operation, and 750 inlet droplets were used to represent high current density operation. Only the pores connected to the inlet droplets (or clusters connected to the inlet droplet) were considered for invasion at each step; therefore, gas filling occurred sequentially from the CL interface, and the invasion percolation simulation was considered completed when the pore at the outlet was invaded. It was assumed that after the point of breakthrough, subsequent gas removal takes place via these deterministically established gas pathways, as has been shown in previous studies.^[54,55]

Supporting Information

Supporting Information is available from the Wiley Online Library or from the author.

Acknowledgements

The research leading to these results has received funding from European Union's Horizon 2020 research and innovation program under grant agreement No 779478 (PRETZEL project) supported by FCH JU. The authors thank Ina Plock, Jörg Bürkle, and Henrike Schmies for performing SEM measurements, technical support, and μCT measurements, respectively. The authors also acknowledge the support from A. Üstün in carrying out the PEMWE measurements as part of her master thesis. J.K.L. is grateful for graduate scholarships awarded from the Natural Sciences and Engineering Research Council of Canada (NSERC) Alexander Graham Bell Canada Graduate Scholarships–Doctoral Program, Queen Elizabeth II/Edward Rygiel Graduate Scholarship in Science and Technology, Ontario Graduate Scholarship, and Glynn Williams Fellowships. Finally, the authors acknowledge Vincent Wilke for supporting the preparation of the revised version of the manuscript as the first author S.S. was in maternity leave during the revision process.

Open access funding enabled and organized by Projekt DEAL.

Conflict of Interest

The authors declare no conflict of interest.

Data Availability Statement

The data that support the findings of this study are available from the corresponding author upon reasonable request.

Keywords

high current density, high pressure, high temperature, PEM electrolysis, porous transport layers

Received: February 22, 2021

Revised: May 22, 2021

Published online: July 3, 2021

- [1] IEA, Global CO₂ emissions in 2019, International Energy Agency (IEA), Paris, <https://www.iea.org/articles/global-co2-emissions-in-2019> (accessed: July 2020).
- [2] Mission 2020, <https://mission2020.global/> (accessed: July 2020).
- [3] C. Figueres, H. J. Schellnhuber, G. Whiteman, J. Rockström, A. Hobley, S. Rahmstorf, *Nature* **2017**, 546, 593.
- [4] D. Bessarabov, P. Millet, P. *PEM Water Electrolysis*, Vol. 1, Academic Press, Cambridge, MA **2018**.
- [5] IRENA, Green Hydrogen Cost Reduction – Scaling up electrolyzers to meet the 1.5 °C climate goal, International Renewable Energy Agency (IRENA), Abu Dhabi, <https://irena.org/publications/2020/Dec/Green-hydrogen-cost-reduction> (accessed: February 2021).
- [6] Hydrogen Europe, Hydrogen Production, <https://hydrogeneurope.eu/hydrogen-production-0> (accessed: February 2021).
- [7] European Commission, Communication from the commission to the European Parliament, the Council, the European Economic and Social Committee and the Committee of the Regions – A hydrogen

- strategy for a climate-neutral Europe, Brussels, https://ec.europa.eu/energy/sites/ener/files/hydrogen_strategy.pdf, (accessed: July 2020).
- [8] A. Van Wijk, J. Chatzimakakis, Green Hydrogen for a European Green Deal – A 2x40 GW Initiative, Hydrogen Europe, https://hydrogeneurope.eu/sites/default/files/Hydrogen%20Europe_2x40%20GW%20Green%20H2%20Initiative%20Paper.pdf, (accessed: July 2020).
- [9] D. Bessarabov, H. Wang, H. Li, N. Zhao, *PEM Electrolysis for Hydrogen Production: Principles and Applications*, CRC Press, Boca Raton, FL 2015.
- [10] S. A. Grigoriev, V. N. Fateev, D. G. Bessarabov, P. Millet, *Int. J. Hydrogen Energy* **2020**, *45*, 26036.
- [11] M. Carmo, D. L. Fritz, J. Mergel, D. Stolten, *Int. J. Hydrogen Energy* **2013**, *38*, 4901.
- [12] FCH-JU, *Addendum to the Multi-Annual Work Plan 2014-2020*, Fuel Cells and Hydrogen 2 Joint Undertaking, Brussels 2018.
- [13] Dena (Deutsche Energie-Agentur), WindGas Hamburg, <https://www.powertogas.info/fr/projektarte/windgas-hamburg/> (accessed: February 2020).
- [14] REFHYNE, Clean Refinery Hydrogen for Future, <https://refhyne.eu/> (accessed: February 2020).
- [15] WESTKÜSTE 100, <https://www.westkueste100.de/en/> (accessed: July 2020).
- [16] ITM-Power, Gigastack Feasibility Study with Orsted, <https://www.itm-power.com/item/58-project-to-demonstrate-delivery-of-bulk-low-cost-and-zero-carbon-hydrogen-through-gigawatt-scale-pem-electrolysis-manufactured-in-the-uk> (accessed: July 2020).
- [17] Y. Van Delft, Starting signal for design of gigawatt electrolysis plant, TNO, <https://www.tno.nl/en/about-tno/news/2019/3/starting-signal-for-design-of-gigawatt-electrolysis-plant/> (accessed: July 2020).
- [18] IEA, The Future of Hydrogen – Seizing Today's Opportunities, International Energy Agency (IEA), Paris, <https://webstore.iea.org/download/direct/2803> (accessed: July 2020).
- [19] A. Buttler, H. Spliethoff, *Renewable Sustainable Energy Rev.* **2018**, *82*, 2440.
- [20] M. Suermann, K. Takanohashi, A. Lamibrac, T. J. Schmidt, F. Büchi, *J. Electrochem. Soc.* **2017**, *164*, F973.
- [21] K. Bromberger, G. Jagdishkumar, T. Lickert, A. Fallisch, T. Smolinka, *Int. J. Hydrogen Energy* **2018**, *43*, 2556.
- [22] T. Lickert, M. L. Kiermaier, K. Bromberger, G. Jagdishkumar, S. Metz, A. Fallisch, T. Smolinka, *Int. J. Hydrogen Energy* **2020**, *45*, 6047.
- [23] Z. Kang, J. Mo, G. Yang, S. T. Retterer, D. A. Cullen, T. J. Toops, J. B. Green Jr., M. M. Mench, F.-Y. Zhang, *Energy Environ. Sci.* **2017**, *10*, 166.
- [24] T. Schuler, R. De Bruycker, T. J. Schmidt, F. Büchi, *J. Electrochem. Soc.* **2019**, *166*, F270.
- [25] P. Lettenmeier, S. Kolb, F. Burggraf, A. S. Gago, K. A. Friedrich, *J. Power Sources* **2016**, *311*, 153.
- [26] P. Lettenmeier, S. Kolb, N. Sata, A. Fallisch, L. Zielke, S. Thiele, A. S. Gago, K. A. Friedrich, *Energy Environ. Sci.* **2017**, *10*, 2521.
- [27] S. Park, J.-W. Lee, B. N. Popov, *Int. J. Hydrogen Energy* **2012**, *37*, 5850.
- [28] M. Brodmann, M. Greda, C. Mutascu, J. Roth, WO2011/069625A1, **2011**.
- [29] M. Brodmann, M. Greda, C. Mutascu, J. Neumann, U. Rost, J. Roth, A. Wildometz, WO2014/040746A1, **2014**.
- [30] M. Brodmann, C. L. Mutascu, P. Podleschny, U. W. Rost, J. Roth, C. Sagewka, F. J. Wirkert, WO2018/001543A1, **2018**.
- [31] J. Mo, Z. Kang, G. Yang, S. T. Retterer, D. A. Cullen, T. J. Toops, J. B. Green Jr., F.-Y. Zhang, *Appl. Energy* **2016**, *177*, 817.
- [32] Z. Kang, G. Yang, J. Mo, S. Yu, D. A. Cullen, S. T. Retterer, T. J. Toops, M. P. Brady, G. Bender, B. S. Pivovar, J. B. Green Jr., F.-Y. Zhang, *Int. J. Hydrogen Energy* **2018**, *43*, 14618.
- [33] T. Schuler, J. M. Ciccone, B. Krentscher, F. Marone, C. Peter, T. J. Schmidt, F. N. Büchi, *Adv. Energy Mater.* **2020**, *10*, 1903216.
- [34] P. Lettenmeier, R. Wang, R. Abouatallah, B. Saruhan, O. Freitag, P. Gazdzicki, T. Morawietz, R. Hiesgen, A. S. Gago, K. A. Friedrich, *Sci. Rep.* **2017**, *7*, 44035.
- [35] P. Lettenmeier, R. Wang, R. Abouatallah, S. Helmlly, T. Morawietz, R. Hiesgen, S. Kolb, F. Burggraf, J. Kalló, A. S. Gago, K. A. Friedrich, *Electrochim. Acta* **2016**, *210*, 502.
- [36] F. J. Hackemüller, E. Borgardt, O. Panchenko, M. Müller, M. Bram, *Adv. Eng. Mater.* **2019**, *21*, 1801201.
- [37] K. E. Ayers, J. N. Renner, N. Danilovic, J. X. Wang, Y. Zhang, R. Maric, H. Yu, *Catal. Today* **2016**, *262*, 121.
- [38] S. Siracusano, S. Trocino, N. Briguglio, V. Baglio, A. S. Aricó, *Materials* **2018**, *11*, 1368.
- [39] C. Rozain, E. Mayousse, N. Guilleta, P. Millet, *Appl. Catal., B* **2016**, *182*, 123.
- [40] M. Eikerling, A. A. Kornyshev, *J. Electroanal. Chem.* **1999**, *475*, 107.
- [41] J. K. Lee, C. H. Lee, K. F. Fahy, P. J. Kim, J. M. LaManna, E. Baltic, D. L. Jacobson, D. S. Hussey, S. Stiber, A. S. Gago, K. A. Friedrich, A. Bazylak, *Energy Convers. Manage.* **2020**, *226*, 113545.
- [42] H. Ito, T. Maeda, A. Nakano, A. Kato, T. Yoshida, *Electrochim. Acta* **2013**, *100*, 242.
- [43] G. Schmidt, M. Suermann, B. Benschmann, R. Hanke-Rauschenbach, I. Neuweiler, *J. Electrochem. Soc.* **2020**, *167*, 114511.
- [44] J. K. Lee, C. H. Lee, A. Bazylak, *J. Power Sources* **2019**, *437*, 226910.
- [45] J. K. Lee, A. Bazylak, *J. Electrochem. Soc.* **2020**, *167*, 013541.
- [46] J. T. Gostick, M. A. Ioannidis, M. W. Fowler, M. D. Pritzker, *J. Power Sources* **2007**, *173*, 277.
- [47] J. C. Garcia-Navarro, M. Schulze, K. A. Friedrich, *ACS Sustainable Chem. Eng.* **2019**, *7*, 1600.
- [48] G. Tsotridis, *JRC validated methods, reference methods and measurements report – EU Harmonised Polarisation Curve Test Method for Low Temperature Water Electrolysis, Joint Research Center (JRC)*, Brussels **2018**.
- [49] T. Malkow, A. Pilenga, G. Tsotridis, *JRC validated methods, reference methods and measurements report – EU harmonized test procedure: electrochemical impedance spectroscopy for water electrolysis cells, Joint Research Center (JRC)*, **2018**.
- [50] F. J. Wirkert, J. Roth, U. W. Rost, M. Brodmann, *Int. J. Smart Grid Clean Energy* **2017**, *6*, 171.
- [51] F. J. Wirkert, J. Roth, S. Jagalski, P. Neuhaus, U. Rost, M. Brodmann, *Int. J. Hydrogen Energy* **2020**, *45*, 1226.
- [52] J. Gostick, M. Aghighi, J. Hinebaugh, T. Tranter, M. A. Hoeh, H. Day, B. Spellacy, M. H. Sharqawy, A. Bazylak, A. Burns, W. Lehnert, A. Putz, *Comput. Sci. Eng.* **2016**, *18*, 60.
- [53] S. Bryant, S. Blunt, *Phys. Rev. A* **1992**, *46*, 2004.
- [54] C. H. Lee, B. Zhao, R. Abouatallah, R. Wang, A. Bazylak, *Phys. Rev. Appl.* **2019**, *11*, 054029.
- [55] C. H. Lee, R. Banerjee, N. Ge, J. K. Lee, B. Zhao, E. Baltic, J. M. LaManna, D. S. Hussey, D. L. Jacobson, R. Abouatallah, R. Wang, A. Bazylak, *Electrochim. Acta* **2018**, *279*, 91.